

1. Report No. FHWA/TX-98/1404-1	2. Government Accession No.	3. Recipient's Catalog No.	
4. Title and Subtitle MEASURED BEHAVIOR AND THERMAL GRADIENTS IN INNOVATIVE BRIDGE PIERS		5. Report Date May, 1998	
		6. Performing Organization Code	
7. Author(s) Valerie A. Andres, Wade S. Bonzon, Rodney T. Davis, John E. Breen and Michael E. Kreger		8. Performing Organization Report No. Research Report 1404-1	
9. Performing Organization Name and Address  Center for Transportation Research The University of Texas at Austin 3208 Red River, Suite 200 Austin, TX 78705-2650		10. Work Unit No. (TRAIS)	
		11. Contract or Grant No. Research Study 0-1404	
12. Sponsoring Agency Name and Address Texas Department of Transportation Research and Technology Transfer Section/Construction Division P.O. Box 5080 Austin, TX 78763-5080		13. Type of Report and Period Covered Research Report (9/96-8/97)	
		14. Sponsoring Agency Code	
15. Supplementary Notes Project conducted in cooperation with the Federal Highway Administration. Research study title: "Instrumentation of Precast Segmental Box Girder Bridges on US 183 in Austin"			
16. Abstract  Construction of the U.S. 183 elevated highway in Austin, Texas, provided a unique opportunity to investigate the behavior of two types of innovative concrete piers. Tied Y shape piers were used to support mainlane spans. They were cast in situ with steel pipes for the tensile ties between the arms of the Y. Force distribution and thermal gradients and effects were measured prior to and during construction of the superstructure. Force measurements were compared to conventional and to strut-and-tie model analyses. The second type of piers were tall segmentally constructed hollow box piers. Temperature gradient and strain data were obtained to evaluate design thermal gradients and thermal gradient design procedures. Recommendations for improvement in design specifications are presented.			
17. Key Words Field measurements, precast concrete piers, Y shape piers, segmental bridges, bridge instrumentation, thermal gradients, live load tests		18. Distribution Statement No restrictions. This document is available to the public through the National Technical Information Service, Springfield, Virginia 22161.	
19. Security Classif. (of report) Unclassified	20. Security Classif. (of this page) Unclassified	21. No. of pages 248	22. Price

**MEASURED BEHAVIOR AND THERMAL GRADIENTS IN  
INNOVATIVE BRIDGE PIERS**

by

**Valerie A. Andres, Wade S. Bonzon, Rodney T. Davis,  
John E. Breen and Michael E. Kreger**

Research Report 1404-1

Research Project 0-1404  
“Instrumentation of Precast Segmental Box Girder Bridges  
on US 183 in Austin”

conducted for the

Texas Department of Transportation

in cooperation with the

US Department of Transportation  
Federal Highway Administration

by the

**CENTER FOR TRANSPORTATION RESEARCH  
BUREAU OF ENGINEERING RESEARCH  
THE UNIVERSITY OF TEXAS AT AUSTIN**

**February 24, 1999**



This report was prepared in cooperation with the Texas Department of Transportation and the U.S. Department of Transportation, Federal Highway Administration.

## **DISCLAIMER**

The contents of this report reflect the views of the authors, who are responsible for the facts and the accuracy of the data presented herein. The contents do not necessarily reflect the official views or policies of the Federal Highway Administration or the Texas Department of Transportation. This report does not constitute a standard, specification, or regulation.

There was no invention or discovery conceived or first actually reduced to practice in the course of or under this contract, including any art, method, process, machine, manufacture, design or composition of matter, or any new and useful improvement thereof, or any variety of plant which is or may be patentable under the patent laws of the United States of America or any foreign country.

NOT INTENDED FOR CONSTRUCTION,  
BIDDING OR PERMIT PURPOSES

John E. Breen, Texas PE# 18479  
Michael E. Kreger, Texas PE# 65541

Research Supervisors

The contents of this report reflect the views of the authors, who are responsible for the facts and accuracy of the data presented herein. The contents do not necessarily reflect the views of the Texas Department of Transportation. This report does not constitute a standard, specification or regulation.

## **ACKNOWLEDGEMENTS**

The research studies reported herein involved a complex instrumentation program of an ongoing major bridge project. The report is based on portions of the University of Texas theses of Val Andres and Wade Bonzon as well as the dissertation of Rodney Davis. In addition to these co-authors of the report, the authors are indebted to a number of other graduate students who assisted on the project, particularly Bryan Wood of TxDOT who helped instrument many elements, and Keith Thompson who instrumented the balanced cantilever erection and provided some pier data from this phase. The overall project was greatly helped by the interest and cooperation of Mr. Tom Rummel of the Design Division, who was the TxDOT Project Director. He played an invaluable role in providing background information and in liaison with the casting yard and site operations. The TxDOT inspectors, the TxDOT District construction engineers and the two splendid contractors, Martin K. Eby Construction and Flatiron Structures Company provided substantial assistance to the project. We are most appreciative of their interest and in their willing cooperation in scheduling, communicating and putting up with interlopers on their time critical project.



## IMPLEMENTATION

The results of the instrumentation studies of these innovative bridge piers have two very practical applications to practice. The first of these is the indication of the procedures and advantage of using Strut-and-Tie Modeling (STM) for unusual structures. Even though STM is basically a strength design lower bound (thus conservative) design procedure and these piers were loaded only at the service load level, the conventional analysis results were not conservative when compared to measured values while the STM results were conservative and useful even at service levels. This example indicated the ability of STM to allow a designer to trace the flow of forces through the structure.

The second application is the detailed information concerning actual temperature gradients in the bridge piers. While the gradients measured were somewhat similar to those in superstructures, the effects were found to be minor and it is recommended that temperature gradients need not be considered in substructure service load design thus simplifying the task of the designer.



# TABLE OF CONTENTS

1. INTRODUCTION .....	1
1.1 General .....	1
1.2 US 183 Project Description .....	1
1.2.1 Project Location .....	1
1.2.2 Project Description.....	2
1.3 Mainlane Pier Description .....	5
1.4 Problem Statement and Objectives .....	7
1.5 Problem Statement and Objectives .....	10
2. BACKGROUND .....	13
2.1 Introduction.....	13
2.2 Strut-and-Tie Modeling (STM).....	13
2.2.1 General .....	14
2.2.2 History.....	14
2.2.3 Assumptions.....	17
2.2.4 Development of a Strut-and-Tie Model .....	17
2.2.5 Struts .....	19
2.2.6 Ties.....	20
2.2.7 Nodes .....	21
2.2.8 Summary of Design Procedure .....	21
2.2.9 Benefits of Strut-and-Tie Modeling.....	22
2.2.10 Limitations of Research .....	23
2.3 Thermal Gradients .....	23
2.3.1 Gradient Shape .....	24
2.3.2 Gradient Effects.....	25

2.4 Development of Current AASHTO Thermal Gradient Provisions.....	34
2.4.1 Potgieter and Gamble [20].....	34
2.4.2 NCHRP Report 276 [17].....	35
2.4.3 AASHTO LRFD Specification [8] Requirements .....	38
2.4.4 AASHTO Segmental Specification [7] Requirements.....	40
2.4.5 Roberts [19] .....	41
2.5 Previous Bridge Pier Temperature Studies .....	42
2.5.1 General.....	42
2.5.2 Stephenson [25] .....	42
2.5.3 Andres [2] .....	43
2.6 Precast Segmental Piers in North America.....	45
2.6.1 Long Key Bridge.....	45
2.6.2 Seven-Mile Bridge .....	45
2.6.3 Dauphin Island Bridge [29] .....	46
2.6.4 Sunshine Skyway Approaches .....	47
2.6.5 Neches River Bridge [5] .....	47
2.6.6 Linn Cove Viaduct.....	48
2.6.7 Wando River Bridge [34].....	49
2.6.8 James River Bridge [35] .....	49
2.6.9 Chesapeake and Delaware Canal Bridge [36].....	50
2.6.10 Louetta Road Overpass .....	51
2.6.11 Northumberland Strait Crossing .....	51
3. PIER INSTRUMENTATION.....	53
3.1 Introduction.....	53
3.2 Mainlane Pier .....	53
3.2.1 Instrumentation Systems.....	53
3.2.2 Instrumented Pier .....	53
3.2.3 Steel Strains - Strain Gauges.....	54
3.2.4 Steel Strains - Concrete Strain Devices .....	56
3.2.5 Concrete Strains - Demec Extensometer .....	58

3.2.6 Temperature Gradient - Thermocouples .....	62
3.2.7 Deformation of the “Y” - Linear Potentiometers and Thermocouples .....	63
3.2.8 Data Acquisition System.....	65
3.3 Segmental Pier Instrumentation.....	65
3.3.1 Instrumentation Objectives .....	65
3.3.2 Pier Selection .....	65
3.3.3 Pier Shaft.....	67
3.3.4 Pier Shaft.....	69
3.3.5 Capital PC16-8 Instrumentation plans .....	71
3.3.6 Capital PC16-8 Concrete Strain Gauges.....	72
3.3.7 Capital PC16-8 Steel Strain Gauges .....	75
3.3.8 Capital PC16-8 Thermocouples.....	77
3.3.9 Segmental pier Data Acquisition System .....	79
4. US 183 CONSTRUCTION AND DATA COLLECTION.....	81
4.1 Introduction.....	81
4.2 Mainlane Pier Construction .....	81
4.3 Mainlane Pier Data Collection.....	81
4.4 Segmental Pier Construction.....	85
5. MEASURED BEHAVIOR - MAINLANE PIER AND INTERPRETATION .....	91
5.1 Introduction.....	91
5.2 Background - Thermal Strains .....	91
5.2.1 Thermal Stresses in Mainlane Pier due to Temperature Gradient in Concrete.....	91
5.2.2 Thermal Stresses in Mainlane Pier due to Temperature Gradient in Pipes .....	92
5.3 Measurements on Mainlane Pier - Prior to Superstructure Erection .....	92
5.3.1 Temperature Measurements.....	94
5.3.2 Structural Steel Pipe Strains - Typical Sunny Day .....	96
5.3.3 Capital Strains - Typical Sunny Day .....	98
5.3.4 Shaft Strains - Typical Sunny Day.....	101

5.4 Measurements on Mainline Pier During Superstructure Erection .....102

    5.4.1 Temperature Measurements.....104

    5.4.2 Structural Steel Pipe Strains.....108

    5.4.3 Capital Strains.....111

    5.4.4 Shaft Strains.....114

5.5 Gravity Load Strains .....116

    5.5.1 Significance of Thermal Strains.....116

    5.5.2 Procedure for Extraction of Thermal Strains from Measured Strains.....117

5.6 Superstructure Dead Load Strains in Pier .....118

    5.6.1 Pipe Strains .....118

    5.6.2 Capital Strains.....119

    5.6.3 Shaft Strains .....121

5.7 Superstructure Dead Load Forces in the Mainlane Pier .....122

    5.7.1 Pipe Forces.....122

    5.7.2 Capital Forces .....122

    5.7.3 Shaft Forces .....122

5.8 Strut-and-Tie Model for US 183 Mainlane Pier .....124

    5.8.1 Strut-and-Tie Model Based on Measured Forces .....125

    5.8.2 Strut-and-Tie Model Based on an Elastic Frame Analysis.....127

5.9 Comparison of Forces and Force Paths .....127

**6. MEASURED BEHAVIOR - RAMP P SEGMENTAL PIER AND INTERPRETATION.....131**

6.1 General Temperature Trends .....131

    6.1.1 Daily Cycles.....131

    6.1.2 Seasonal Characteristics.....133

    6.1.3 Effects of Cover .....134

    6.1.4 Effects of Shading.....135

6.2 Thermal Gradients .....136

    6.2.1 Pier Shaft Gradients .....136

6.2.2 Capital Gradients .....	140
6.2.3 Capital Curing Gradients .....	141
6.3 Concrete Strain Gauge Measurements .....	144
6.3.1 Axial Strains.....	144
6.3.2 Transverse Strains .....	146
6.4 Pier Post-Tensioning Strains.....	147
6.4.1 General.....	147
6.4.2 Axial Strains.....	147
6.4.3 Transverse Strains .....	149
6.5 Stress/Strain Analyses - Hand Calculation Methods .....	150
6.5.1 Classical Method.....	150
6.5.2 Primary Bending Axis Method .....	155
6.5.3 Transverse Stresses .....	161
6.6 Finite Element Analysis.....	165
6.6.1 Pier Geometry Input.....	165
6.6.2 Material Properties Input .....	167
6.6.3 Temperature Loading Input .....	167
6.6.4 Analysis Results.....	170
6.6.5 Comments .....	178
6.7 Measured Response of Ramp P Segmental Pier to Superstructure Construction Loads .	179
6.8 Comparison of Measured and Analytical Results.....	182
6.8.1 Longitudinal Strains.....	182
6.8.2 Transverse Strains .....	189
6.8.3 General Comments Concerning Pier Thermal Gradient Effects.....	193
7. DESIGN IMPLICATIONS.....	197
7.1 Mainlane Pier Indications .....	197
7.1.1 Temperature Measurements.....	197
7.1.2 Superstructure Dead Load Measurements .....	198
7.1.3 Comparison of Measured Forces with Strut-and-Tie Models.....	198

7.2 Segmental Pier Indications .....	199
7.2.1 Load Cases .....	199
7.2.2 Comments on Load Cases.....	212
7.3 Suggested Revisions to <i>AASHTO Guide Specification</i> [7] .....	213
7.3.1 Thermal Gradients .....	214
7.3.2 Application of Thermal Gradients to Substructures .....	215
7.3.3 Suggestions for Future Study.....	216
8. SUMMARY & CONCLUSIONS.....	217
8.1 Introduction.....	217
8.2 Mainlane Bridge Pier .....	217
8.3 Segmental Ramp Pier.....	218
8.4 Conclusions.....	220
8.4.1 Mainlane Pier.....	220
8.4.2 Segmental Ramp Pier.....	221
References.....	223

## LIST OF FIGURES

Figure 1.1	US 183 segmental viaduct location.....	2
Figure 1.2	US 183 viaduct mainlane superstructure. ....	3
Figure 1.3	Typical access ramp superstructure. ....	4
Figure 1.4	(a) Mainlane “Y” pier; (b) small ramp pier; (c) large ramp pier.....	5
Figure 1.5	US 183 Mainlane Pier: Elevation view.....	6
Figure 1.6	US 183 Mainlane Pier: Plan view.....	7
Figure 1.7	Structural steel pipe assembly: Detail.....	7
Figure 1.8	Typical large ramp pier: elevation view. ....	8
Figure 1.9	Typical sections: large ramp pier. ....	9
Figure 2.1	Typical Uses of Strut-and-Tie Models [11]. ....	16
Figure 2.2	St. Venant's Principle [10]. ....	18
Figure 2.3	Strut Types [11]. ....	19
Figure 2.4	Design Procedure for Structural Concrete [9].....	22
Figure 2.5	Factors affecting thermal gradients (after Roberts [19]).....	24
Figure 2.6	A statically determinate member under a linear temperature gradient (after Roberts [19]).....	26
Figure 2.7	Arbitrary section with a non-linear temperature distribution.....	27
Figure 2.8	(a) Non-linear strain distribution assuming no interaction between section fibers (b) final linear strain distribution because plane sections remain plane (after Imbsen[17]). ....	27
Figure 2.9	Thermal gradient and stress distribution in a fully restrained member.....	28
Figure 2.10	Temperature-induced stress distributions (after Roberts [19]). ....	29
Figure 2.11	Application of thermal gradients to a two-span beam (after Potgieter and Gamble [20]).....	30
Figure 2.12	Application of thermal gradients to a three-span beam (after Roberts [19]).....	31
Figure 2.13	Temperature-induced response in a free-standing single pier bent.....	32
Figure 2.14	Temperature-induced response in a partially-restrained single pier bent. ....	32
Figure 2.15	Temperature-induced response in a fully restrained single pier bent. ....	33
Figure 2.16	Temperature-induced response of a multiple-pier bent. ....	34
Figure 2.17	Proposed maximum solar radiation zones (after Imbsen, et al [17]). ....	35
Figure 2.18	Proposed positive vertical temperature gradient (after Imbsen, et al [17]).....	36
Figure 2.19	Proposed negative vertical temperature gradient (after Imbsen, et al [17]).....	36
Figure 2.20	AASHTO LRFD Code [8] vertical positive gradient shape. ....	39
Figure 2.21	Bronze-encased steel bolt undergoing uniform temperature change. ....	44

Figure 2.22 Concrete pier model undergoing differential temperature change.....44

Figure 2.23 Unusual V-shaped piers, Long Key Bridge. ....45

Figure 2.24 Cross-section of precast segmental piers, Dauphin Island Bridge.....46

Figure 2.25 Segmental pylon cross-sections, Neches River Bridge.....47

Figure 2.26 Segmental approach pier cross-section, Neches River Bridge.....48

Figure 2.27 Pier cross-section - Linn Cove Viaduct. ....49

Figure 2.28 Cross-sectional dimensions of approach-span piers, Chesapeake and Delaware Canal cable-stayed bridge.....50

Figure 2.29 Segmental pier cross-section, Louetta Road Overpass. ....51

Figure 2.30 Elevation view of pier components, Northumberland Strait Crossing. ....52

Figure 3.1 Strain Gauge and Concrete Strain Device Layout: Elevation View. ....54

Figure 3.2 Strain Gauge Locations: Pipe Assembly.....55

Figure 3.3 - Strain Gauge and Concrete Strain Device Layout: Sections.....55

Figure 3.4 - Concrete Strain Device.....56

Figure 3.5 - Concrete Strain Device Locations in Shaft. ....57

Figure 3.6 Demec Extensometer .....58

Figure 3.7 Demec Point Installation.....59

Figure 3.8 Demec point locations on shaft.....60

Figure 3.9 Demec Point Locations on Side of Shaft and Capital.....61

Figure 3.10 Demec Point Locations on Inside Face of Capital.....62

Figure 3.11 Thermocouple locations.....63

Figure 3.12 Set-up to Read Deformation in the "Y." .....64

Figure 3.13 Bridge layout in the US 183 and IH-35 interchange area. ....66

Figure 3.14 Instrumented areas of pier P16 relative to surrounding structures' locations. ....67

Figure 3.15 Concrete gauge locations in base segment PC16-1. ....68

Figure 3.16 Concrete gauge locations in "top" segment PC16-7.....68

Figure 3.17 Concrete strain gauge positions, "gradient" segment PC16-5. ....69

Figure 3.18 Thermocouple locations in base segment PC16-1. ....69

Figure 3.19 Thermocouple locations in the "gradient" segment PC16-5.....70

Figure 3.20 Thermocouple locations in "top" segment PC16-7. ....71

Figure 3.21 Fixed moment connection during superstructure erection as designed to be achieved with DYWIDAG post-tensioned bars. ....72

Figure 3.22 Elevation view of concrete strain gauges in top half of capital segment. ....73

Figure 3.23 Plan view of concrete strain gauges located in top half of capital segment. ....73

Figure 3.24 Concrete strain gauge placement in compression strut between tie-down anchor plates and tendon anchorages.....74

Figure 3.25 Two layers of concrete strain gauges located near bottom face of capital segment coinciding with gauge distributions in segment PC16-7.....74

Figure 3.26	Location of steel strain gauges near the capital face.....	75
Figure 3.27	Locations of steel strain gauges near the top face of the capital. ....	76
Figure 3.28	Locations of strain gauges attached to DYWIDAG post-tensioned tie-downs. ....	77
Figure 3.29	Temperature gradient thermocouples located near base of capital segment. ....	77
Figure 3.30	Thermocouples located near top face of capital segment. ....	78
Figure 3.31	Thermocouples placed in compression strut areas.....	78
Figure 4.1	Casting of pier column concrete. ....	82
Figure 4.2	Construction of pier capital.....	82
Figure 4.3	Typical mainlane pier. ....	83
Figure 4.4	Pier bracket supporting truss.....	83
Figure 4.5	Construction procedure for typical span completion. ....	84
Figure 4.6	Completed pier segments in storage at the casting yard. ....	86
Figure 4.7	Typical segment-per-day casting sequence.....	87
Figure 4.8	Match cast segments fit together perfectly. ....	87
Figure 4.9	“U-turns” in tendon ducts located in pier foundation. ....	88
Figure 4.10	Steel support frame for segment prior to cast-in-place base construction. ....	88
Figure 4.11	Cast-in-place base forming a rigid moment connection between base segment PC16-1 and foundation.....	89
Figure 4.12	Sequence of final post-tensioning of pier P16 tendons.....	89
Figure 5.1	Temperatures over a typical day. ....	92
Figure 5.2	Temperature history. ....	93
Figure 5.3	Ambient temperatures for March 11, 1995.....	93
Figure 5.4	Structural steel pipe temperatures: typical sunny day.....	94
Figure 5.5	Temperature in concrete “shell”: typical sunny day. ....	95
Figure 5.6	Temperature lag to concrete “core”: typical sunny day. ....	95
Figure 5.7	Exposed pipe strain change and temperature change.....	96
Figure 5.8	Well embedded pipe strain change and temperature change. ....	97
Figure 5.9	Pipe embedded end strain change and temperature change. ....	97
Figure 5.10	Capital instrument locations. ....	98
Figure 5.11	Strain variation instruments located in top section of capital: typical sunny day. ....	99
Figure 5.12	Comparison of temperature change and strain variation for instruments located near the top of the capital. ....	101
Figure 5.13	Strain variation: top of column. ....	102
Figure 5.14	Comparison of column strain variation and surface temperature change: concrete “shell.” ....	103
Figure 5.15	Temperature readings during superstructure erection.....	105
Figure 5.16	Temperatures measured on the structural steel pipe during construction. ....	106

Figure 5.17	Concrete temperatures measured near the top of the capital during construction.....	107
Figure 5.18	Strain changes measured in the exterior structural steel pipe during construction.....	109
Figure 5.19	Strain change measured in the interior structural steel pipe during construction.....	110
Figure 5.20	Comparison of strain change "vertically" on capital during superstructure erection: shell near outside face of "Y.".....	112
Figure 5.21	Comparison of strain change "vertically" on capital during superstructure erection: core near outside face of "Y.".....	113
Figure 5.22	Comparison of strain changes "vertically" in shaft during construction of superstructure.....	115
Figure 5.23	Strains measured in capital due to superstructure dead load: thermal strains extracted. ....	119
Figure 5.24	Strain distribution across each section of the capital: thermal strains extracted. ....	120
Figure 5.25	Strains measured in the shaft due to superstructure dead load: thermal strains extracted. ....	121
Figure 5.26	Basic force path in the US 183 mainlane piers. ....	125
Figure 5.27	Calculation of the orientation of the compression strut in the capital based on measured compressive centroids.....	126
Figure 5.28	Comparison of measured forces and strut-and-tie model forces.....	128
Figure 6.1	Temperature gradient orientations at different times in the day. ....	132
Figure 6.2	Typical daily temperature cycle of selected outside-layer thermocouples in gradient segment PC16-5.....	132
Figure 6.3	Datalogger panel temperatures recorded during April 1996.....	133
Figure 6.4	Datalogger panel temperatures recorded during July 1996.....	134
Figure 6.5	Comparison of temperatures recorded through the thickness of the west wall on June 17, 1996. ....	135
Figure 6.6	Comparison of temperatures at locations along the height of pier P16. ....	136
Figure 6.7	One day cycle of thermal gradients along the east-west axis of the cross-section, June 17, 1996.....	137
Figure 6.8(a)	Maximum measured monthly positive temperature gradients.....	138
Figure 6.9(a)	Maximum measured monthly negative temperature gradients.....	139
Figure 6.10	One day cycle of thermal gradients along the east-west axis, capital segment PC16-8, June 17, 1996.....	140
Figure 6.11	Mechanism for cracking of large monolithic members during curing.....	141
Figure 6.12	Comparison of internal curing temperature to ambient air temperature, capital segment PC16-8. ....	142
Figure 6.13	Maximum gradient shape during curing of capital. ....	143
Figure 6.14	Map of cracks found during curing of capital segment PC16-8. ....	143

Figure 6.15	Temperature and strain changes on June 17, 1996: outer gauge locations, north-south sectional axis. ....	144
Figure 6.16	Temperature and strain changes on June 17, 1996: outer and inner gauges, north wall of pier P16. ....	145
Figure 6.17	Temperature and strain changes on June 17, 1996: outer and inner gauges, west wall of pier P16. ....	145
Figure 6.18	Temperature and strain changes on June 17, 1996: horizontally oriented gauges, east and west faces. ....	146
Figure 6.19	Pressure transducer readings during pier post-tensioning.....	147
Figure 6.20	Selected axial strains in segment PC16-1 during pier post-tensioning, north-south axis locations. ....	148
Figure 6.21	Comparison of strains along length of pier during post-tensioning.....	149
Figure 6.22	Comparison of axial and transverse strains during post-tensioning, north-south axis locations. ....	149
Figure 6.23	Calculation of self-equilibrating stresses induced by the maximum positive temperature gradient, April 1996. ....	150
Figure 6.24	Longitudinal strains due to self-equilibrating stresses induced by monthly maximum positive gradients, plotted on the east-west cross-sectional axis. ....	151
Figure 6.25	Longitudinal strains due to self-equilibrating stresses induced by design positive gradients, plotted on the east-west cross-sectional axis. ....	152
Figure 6.26	Calculation of self-equilibrating stresses induced by the maximum negative temperature gradient, April 1996. ....	153
Figure 6.27	Longitudinal strains due to self-equilibrating stresses induced by monthly maximum negative gradients, plotted on the east-west cross-sectional axis. ....	154
Figure 6.28	Longitudinal strains due to self-equilibrating stresses induced by design negative gradients, plotted on the east-west cross-sectional axis. ....	155
Figure 6.29	Final planar section orientation is dependent on temperature loading.....	156
Figure 6.30	Areas and assigned temperatures used for stress calculations. ....	157
Figure 6.31	Longitudinal strains due to self-equilibrating stresses induced by monthly maximum positive gradients, calculated by the primary bending axis method and plotted on the east-west cross-sectional axis. ....	158
Figure 6.32	Orientation of primary bending axis B-B calculated for each monthly maximum positive gradient load case. ....	159
Figure 6.33	Longitudinal strains due to self-equilibrating stresses induced by monthly maximum negative gradients, calculated by the primary bending axis method and plotted on the east-west cross-sectional axis. ....	160
Figure 6.34	Orientation of primary bending axis B-B calculated for each monthly maximum negative gradient load case. ....	160
Figure 6.35	Application of non-linear thermal gradient to individual pier walls.....	161

Figure 6.36	Frame model of pier cross-section used for redistribution of forces by computer frame analysis program.....	162
Figure 6.37	Temperature distributions and self-equilibrating transverse strains caused by positive temperature gradients for (a) April, (b) May, (c) June, (d) July. ....	163
Figure 6.38	Temperature distributions and self-equilibrating transverse strains caused by negative temperature gradients for (a) April, (b) May, (c) June, (d) July.....	164
Figure 6.39	(a) Actual pier geometry, (b) finite element model geometry, (c) element mesh longitudinal geometry, (d) actual cross-section geometry, and (e) element mesh cross-section geometry.....	166
Figure 6.40	“Octagonal shell” method of temperature estimation. ....	168
Figure 6.41	Maximum positive gradient load case: April 23, 1996.....	169
Figure 6.42	Nodal temperature change assignments: NCHRP 276 [5] positive design gradient. ....	169
Figure 6.43	Contour plots of temperature and longitudinal strain, April maximum positive gradient load case. ....	170
Figure 6.44	Finite element analyses strain projection plots on east-west cross-sectional axis from positive design temperature gradients. ....	171
Figure 6.45	Finite element analyses strain projection plots on east-west cross-sectional axis from maximum monthly positive temperature gradients. ....	172
Figure 6.46	Contour plots of temperature and longitudinal strain, April maximum negative gradient load case. ....	173
Figure 6.47	Finite element analyses strain projection plots on east-west cross-sectional axis from maximum monthly negative temperature gradients. ....	174
Figure 6.48	Finite element analyses strain projection plots on east-west cross-sectional axis from negative design temperature gradients. ....	176
Figure 6.49	Temperature loading and transverse strain from finite element analysis of maximum monthly positive gradients during (a) April, (b) May, (c) June, (d) July.....	176
Figure 6.50	Temperature loading and transverse strain from finite element analysis of maximum monthly negative gradients during (a) April, (b) May, (c) June, (d) July.....	178
Figure 6.51	Pier Segment PC16-1 stress changes from placement of superstructure Segment P16-17.....	180
Figure 6.52	Pier Segment P16-5 stress changes from placement of superstructure Segment P16-17.....	180
Figure 6.53	Tie down bar stress changes at the top of pier capital Segment P16-8 from placement of superstructure Segment P16-17.....	181
Figure 6.54	Pier Segment P16-7 stress changes from placement of superstructure Segment P16-17.....	181

Figure 6.55	Temperature changes along the east-west cross-sectional axis recorded by thermocouples in segment PC16-5. ....	184
Figure 6.56	Calculated strain changes and strain changes recorded by concrete strain gauges in segment PC16-5, east-west cross-sectional axis. ....	185
Figure 6.57	Comparison of C433 and C458 during several daily cycles of temperature. ....	186
Figure 6.58	Temperature changes along the east-west cross-sectional axis recorded by thermocouples in segment PC16-5. ....	187
Figure 6.59	Calculated strain changes and strain changes recorded by concrete strain gauges in segment PC16-5, east-west cross-sectional axis. ....	187
Figure 6.60	Daily cycles of strain recorded by C435 and C454. ....	188
Figure 6.61	Temperature changes along the north-south cross-sectional axis recorded by thermocouples in segment PC16-5. ....	188
Figure 6.62	Calculated strain changes and strain changes recorded by concrete strain gauges in segment PC16-5, north-south cross-sectional axis. ....	189
Figure 6.63	Transverse strain comparison in the west wall of segment PC16-5. ....	191
Figure 6.64	Transverse strain comparison in the south wall of segment PC16-5. ....	191
Figure 7.1	Unbalanced segment construction load case. ....	200
Figure 7.2	Stress components for load case excluding temperature effects. ....	201
Figure 7.3	Additional sectional stresses due to the application of the April maximum measured positive temperature gradient. ....	202

## LIST OF TABLES

Table 2.1	Proposed temperature coefficient magnitudes for positive gradients (after Imbsen, et al [17]). ....	36
Table 2.2	Proposed temperature coefficient magnitudes for negative gradients (after Imbsen, et al [17]). ....	37
Table 2.3	Proposed design values for concrete coefficient of thermal expansion (after Imbsen, et al [17]). ....	37
Table 2.4	Excerpt from AASHTO LRFD Specification [8] “Table 3.4.1-1 - Load Combinations and Load Factors.” ....	38
Table 2.5	AASHTO LRFD Code [11] positive gradient magnitude values. ....	39
Table 4.1	Mainlane pier data collection summary. ....	85
Table 4.2	Construction and instrumentation sequence for segmental pier P16. ....	90
Table 5.1	Superstructure erection sequence over Pier D6. ....	103
Table 5.2	Comparison of expected gravity strains and measured thermal strains .....	116
Table 5.3	Temperature differential locations compared for thermal strain extraction.....	117
Table 5.4	Relative temperatures for March 16 and March 30, 1995 .....	118

Table 5.5	Superstructure dead load strains measured in structural steel pipes: thermal strains extracted.....	119
Table 5.6	Average superstructure dead load strains measured in the capital: thermal strains extracted.....	120
Table 5.7	Forces measured in pipes due to gravity load.....	122
Table 5.8	Average measured strains in shaft due to superstructure dead load: thermal strains extracted.....	123
Table 5.9	Compressive forces measured on one branch of the capital due to superstructure dead load.....	123
Table 5.10	Forces measured in one-half of shaft due to superstructure dead load.....	124
Table 6.1	Maximum tensile and compressive strains by load case: positive gradients.....	171
Table 6.2	Maximum tensile and compressive strains by load case: negative gradients.....	174

## **SUMMARY**

Construction of the U.S. 183 elevated highway in Austin provided a unique opportunity to investigate the behavior of two types of innovative concrete piers. Tied Y shape piers were used to support mainlane spans. They were cast-in-situ with steel pipes for the tensile ties between arms of the Y. Force distribution and thermal gradients and effects were measured prior to and during construction of the superstructure. Force measurements were compared to conventional and to Strut-and-Tie Model analyses. The second type of piers were tall segmentally constructed hollow box piers. Temperature gradient and strain data were obtained to evaluate design thermal gradients and thermal gradient design procedures. Recommendations for improvement in design specifications are presented.



# CHAPTER 1

## *1. INTRODUCTION*

### **1.1 General**

The US 183 elevated freeway is a precast segmental post-tensioned box girder viaduct constructed in Austin, Texas. Researchers from the Phil M. Ferguson Structural Engineering Laboratory of The University of Texas at Austin conducted extensive field instrumentation studies on the bridge. These studies began in 1994 and are continuing through 1998. Phase I of the research program involved the instrumentation of one precast segmental mainlane superstructure span constructed by the span-by-span method. It will be reported on by Davis [1]. This report presents the results of Phase II, the instrumentation and monitoring of one cast-in-place mainlane pier [2] and one segmentally constructed hollow box bridge pier [3] respectively. Thompson [4] has reported on Phase III, a ramp superstructure span built by the balanced-cantilever method.

This chapter contains information concerning the US 183 segmental viaduct. A full description of the cast-in-place mainlane pier and the segmentally constructed ramp pier is presented, and the scope and objectives of their instrumentation are outlined.

### **1.2 US 183 Project Description**

#### *1.2.1 Project Location*

The route of US 183 bisects central Texas and ends just short of the Texas coast of the Gulf of Mexico near Corpus Christi. Its path jogs to the southeast as it passes through the northern end of Austin, and forms one segment of a loop of heavily traveled arteries around the central part of Austin (see Figure 1.1). The US 183 segmental viaduct project constitutes one of the last legs of this loop of limited-access freeway.

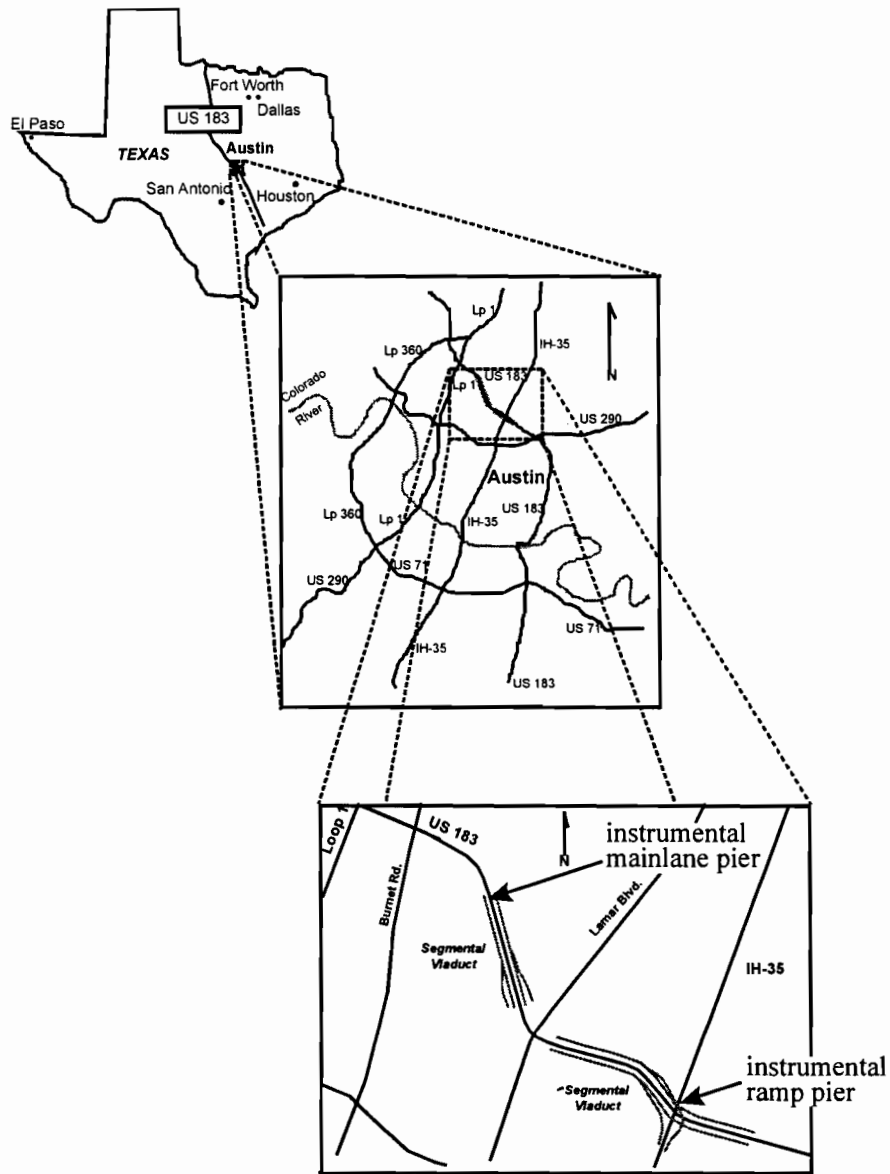


**Figure 1.1** *US 183 segmental viaduct location.*

**1.2.2 Project Description**

Originally, US 183 consisted of six lanes of full-access arterial in the area of the new viaduct. These existing lanes now serve as the frontage roads for the new limited-access elevated freeway. Limited right-of-way, extreme narrowness of the US 183 corridor, the need to mitigate traffic delays, and the desire to minimize construction time were crucial design considerations for the project. Much of the new bridge was required to overhang existing traffic lanes; therefore, overhead construction was a prime consideration as well. During the design process, engineers at the Texas Department of Transportation

(TxDOT) were allowed a great deal of freedom to create an aesthetically pleasing viaduct structure. Precast segmental construction methods fit these requirements well, and public attention to and acceptance of the new elevated freeway has been unusually positive.

The mainlanes of the new viaduct consist of twin bridge structures built using the span-by-span method of precast segmental construction. Each bridge carries three full lanes of traffic with provisions for a wide 3-meter outside shoulder and a narrow 1.2 meter inside shoulder (see Figure 1.2). The mainlane girders typically span 36 meters to 41 meters between piers. On average, each span consists of 14 superstructure segments weighing approximately 490 kN apiece. Anchorage segments located at the piers weigh approximately 620 kN. The mainlane superstructure segments feature unusually wide wings rather than the more traditional box girder design consisting of a wide box and short wings. This configuration is more appropriate for the single column supports chosen due to the limited right-of-way.



*Figure 1.2 US 183 viaduct mainlane superstructure.*

Four access ramp structures carrying one lane of traffic each complete the viaduct (see Figure 1.3). Three of the ramps were constructed span-by-span, while the high flyover ramp located at the interchange of US 183 and Interstate 35 was partly built in balanced-cantilever. Span lengths for the ramp structures vary between 30 meters and 41 meters. The two longest spans located on the balanced-cantilever ramp reach 55 meters.

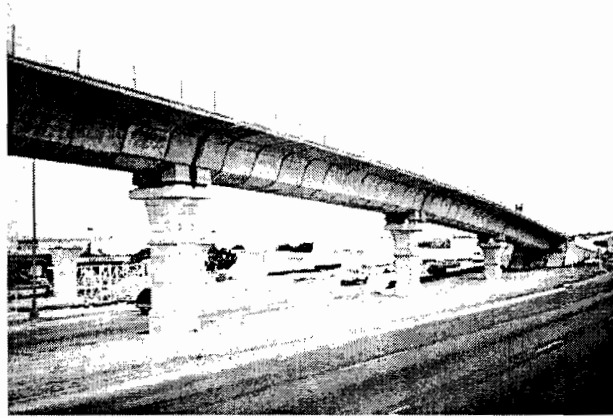


*Figure 1.3 Typical access ramp superstructure.*

A total of 3300 precast segments were produced at the contractor's casting yard. The total bid cost for the viaduct was approximately \$74 million. For comparison, this figure translates into about \$480/m<sup>2</sup> of bridge deck. The average cost of highway bridges in the state of Texas is about \$380/m<sup>2</sup> while the national average for the United States is approximately \$750/m<sup>2</sup>. These numbers by no means represent a comparison of typical segmental bridge costs to other types of construction. However, the US 183 price and the average figure for Texas do reflect the availability of good quality concrete, lack of seismic design requirements, and the large number of working days per year (i.e., good weather) typical of bridges constructed in Texas.

The US 183 segmental viaduct project was originally designed with three types of segmentally constructed piers covering 100% of the piers in the project (see Figure 1.4). However, the general contractor, Martin K. Eby, Inc., opted to cast in place two of the three pier types [5]. One of these cast-in-place types, the "Y" shaped mainlane pier [see Figure 1.4(a)], was instrumented in this study [2]. The second type, the small ramp pier [see Figure 1.4(b)], was not instrumented. The third type, known as the large ramp pier [see Figure 1.4(c)], was the only type to be constructed with precast segments. It was also instrumented in this study [3].

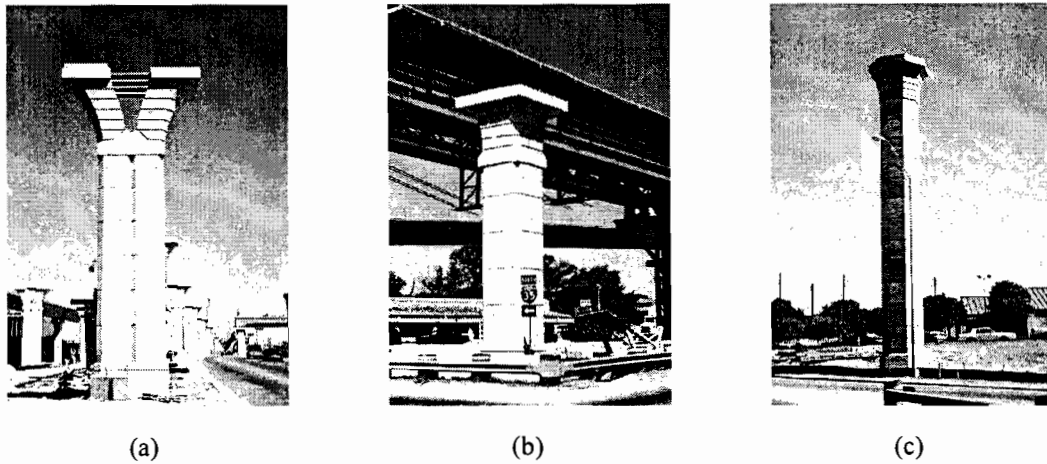


**Figure 1.4** (a) Mainlane “Y” pier; (b) small ramp pier; (c) large ramp pier.

The contractor’s decision to cast most of the piers on the project in place rather than use precast segmental construction was made due to several factors. First, the vast majority of the piers were relatively short (below 10 meters in height) and easy to reach with only small cranes. Also, access to the piers for construction vehicles was relatively simple: most of the mainlane piers were located in the median of the existing roadway where ground conditions were excellent (this fact can also be advantageous for segmentally constructed piers). Principally, contractor constraints on the precasting yard were decisive. The contractor had great difficulty locating a suitable facility with existing noise- and air-pollution control certification in the environmentally sensitive Austin area. The actual site selected was very cramped and priority was given to casting and storage facilities for the superstructure segments. The decision was made to use the large amount of land provided as the bridge right-of-way as the construction preparation area for the pier reinforcement cages.

### **1.3 Mainlane Pier Description**

The piers for the mainlane portion of US 183 Elevated are attractive “Y-shaped” reinforced concrete piers with structural steel tension ties across the top of the “Y,” as shown in Figures 1.5 and 1.6. The shaft of the piers is of variable height, “H.” The capital has a constant height of 3200 mm. The structural steel pipes are AASHTO Extra Strong M270 steel and are 203 mm in diameter. The pipes are anchored in the concrete by steel plates at two locations as seen in Figure 1.7.

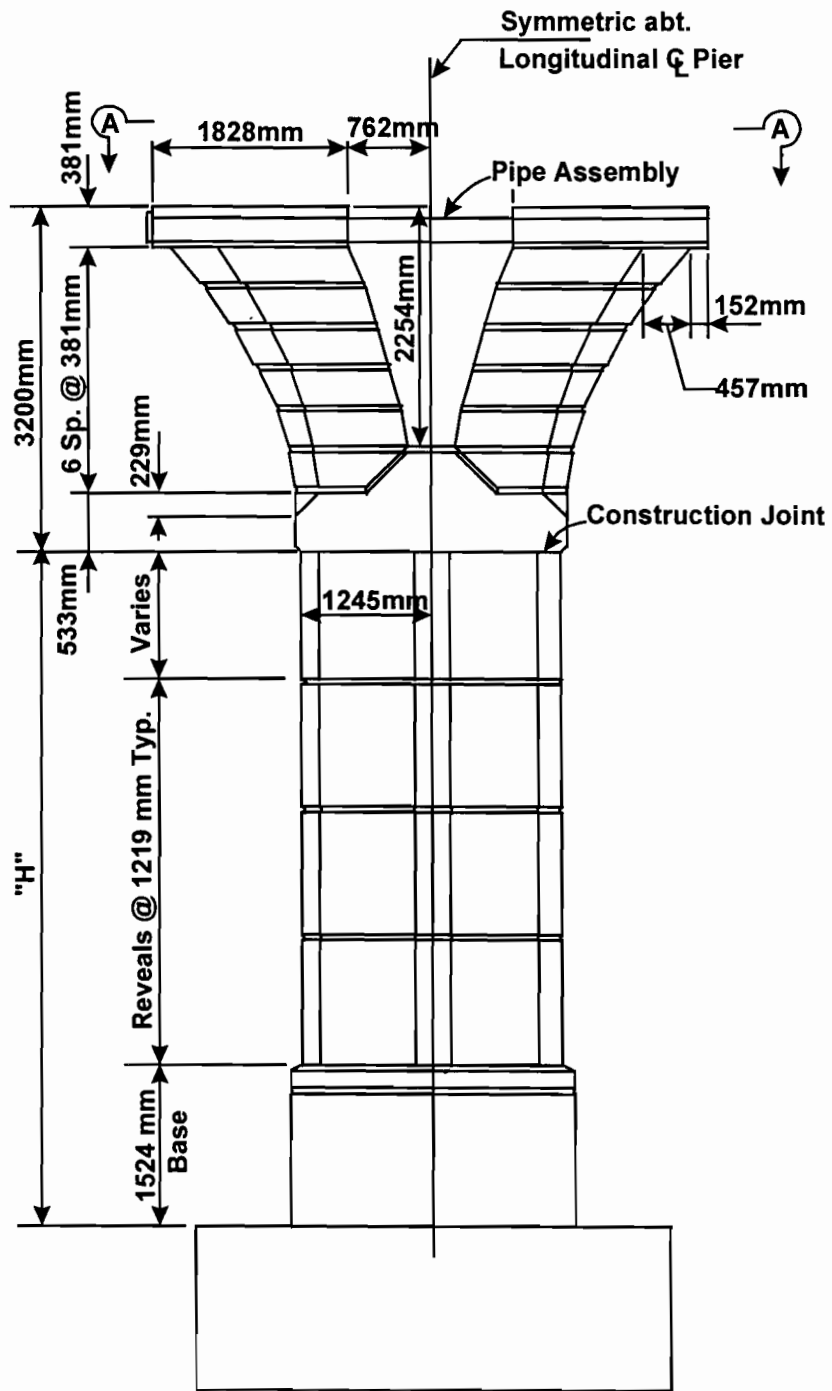


Figure 1.5 US 183 Mainlane Pier: Elevation view.

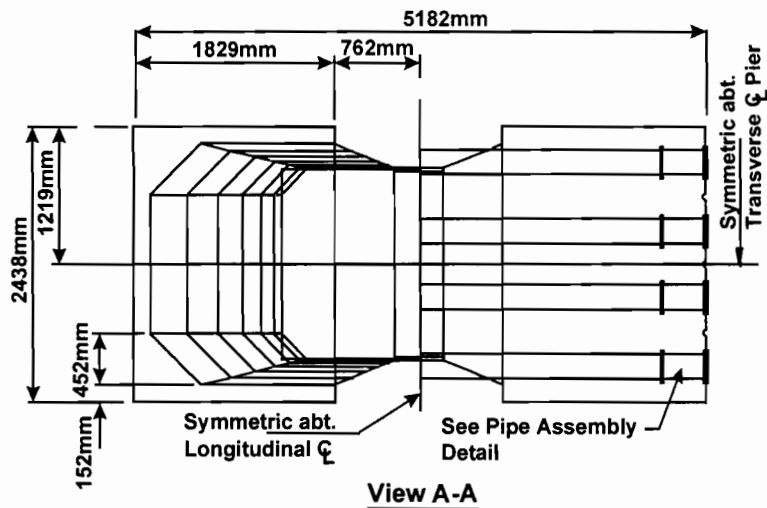


Figure 1.6 US 183 Mainlane Pier: Plan view.

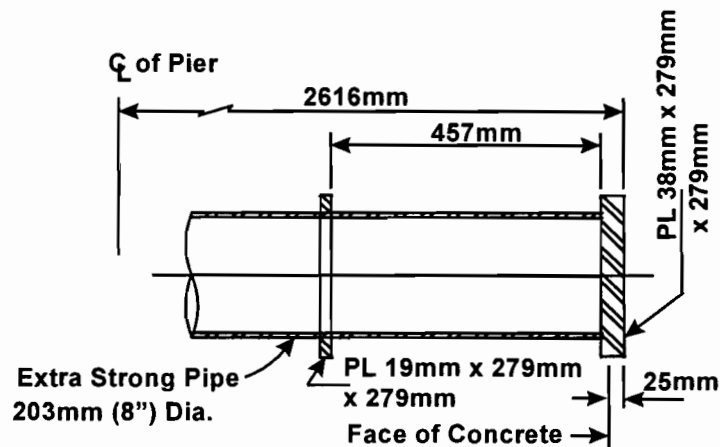
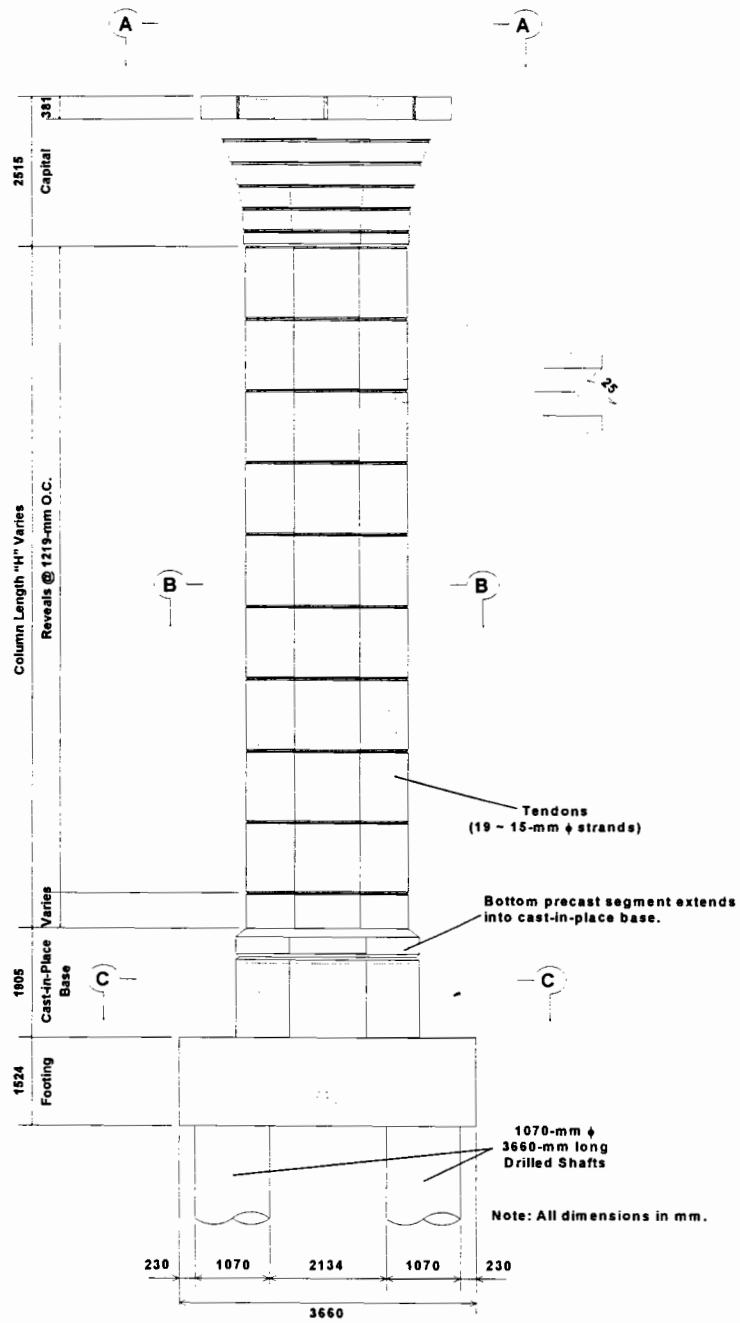


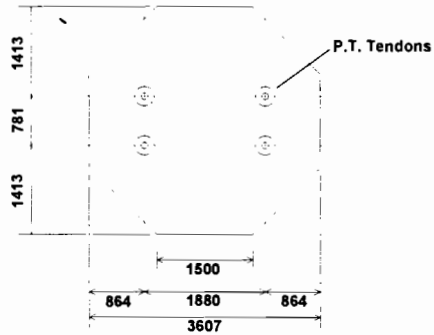
Figure 1.7 Structural steel pipe assembly: Detail.

#### 1.4 Problem Statement and Objectives

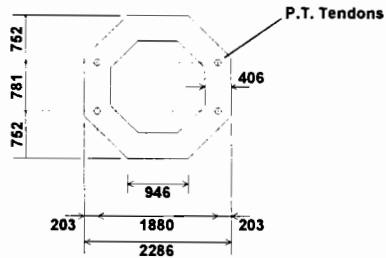
The large ramp pier was designed as a hollow, octagonal column cross-section with 406-mm thick walls. The column's shaft consisted of precast segments of 2.44-meter and 1.22-meter lengths. The hollow section reduced foundation costs and facilitated the transportation and erection of the pier segments. A solid "capital" segment located at the top of the column provided an anchorage zone for post-tensioning tendons. The capital also served as a bearing area for the ramp superstructure and an anchorage for tie-down bars connecting the superstructure to the capital during balanced-cantilever erection. Figure 1.8 and Figure 1.9 show the general configuration of the large ramp pier.



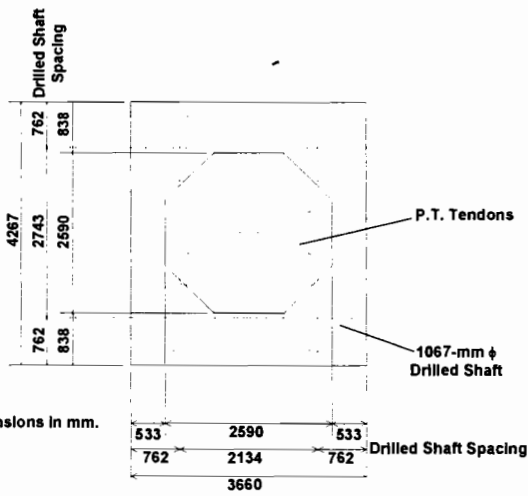
**Figure 1.8** Typical large ramp pier: elevation view.



SECTION A-A



SECTION B-B



Note: All dimensions in mm.

SECTION C-C

Figure 1.9 Typical sections: large ramp pier.

## **1.5 Problem Statement and Objectives**

The US 183 mainlane piers are an excellent candidate for use of strut-and-tie modeling (STM). This is a design method that is generally not taught in universities in the United States (USA) as a standard method for reinforced concrete design. However, interest in the use of STM in design is increasing in the USA. Since this type of modeling was only recently mentioned in USA codes, many engineers are unfamiliar with its possible uses and benefits. The deformation measurements made on the US 183 mainlane piers will be used to further evaluate the use of STM for reinforced concrete design and to familiarize designers with the concept of STM and its possible uses. Since STM is a plasticity based concept for ultimate limit state design, it has a limited capability to detect compatibility and constraint induced stresses. Therefore, the possibility of thermal induced deformations needs to be investigated by extensive monitoring of thermal gradients and associated deformations.

The effects of temperature gradients on concrete superstructure members with hollow cross-sections are well known and recognized by bridge design codes. However, present United States (US) codes offer no provisions for the application of thermal gradients in bridge piers. The increasing use of precast segmental substructures both in the US and worldwide coupled with the lack of guidance available to designers highlights the need for a closer examination of the shapes and magnitudes of the actual gradients that occur in order to provide input data for broader analytical studies. Such studies could indicate what types of substructures might be sensitive to differential temperature gradients. From the outset it was recognized that the effects of thermal gradients would be much less in a single-pier bent than in a multiple-pier substructure. However, only single-pier precast bents were available. It was felt that the opportunity to obtain measured temperatures in a hollow section justified the program even if the overall effects might be limited. The instrumentation of the large ramp pier can indicate whether design codes should treat hollow concrete substructures differently and whether differential temperature gradients should be applied to bridge piers.

The objectives of this project are as follows:

1. To instrument a US 183 mainlane pier in order to measure force distribution and thermal gradients through the pier;
2. To develop a strut-and-tie model of the pier in order to evaluate the use of STM for structural concrete design;
3. To compare measured force distributions with those predicted by strut-and-tie modeling;
4. To comprehensively instrument a precast segmental bridge pier with a hollow cross-section.

5. To determine the maximum differential temperature gradient across the pier's cross-section and the frequency of its occurrence during the service life of the pier.
6. To determine the typical shape of the differential temperature gradient.
7. To track the behavior of the pier due to changes in temperature gradients over time.
8. To measure the induced stresses in the pier caused by applied temperature gradients and determine their importance to the overall behavior of the pier.
9. To make recommendations for changes or additions to current bridge design codes.

The scope of work for this project included selection and extensive field instrumentation of two piers. The first was a cast-in-place mainlane pier. Construction and service load deformations were measured to determine force distribution throughout the pier. A detailed strut-and-tie model was used to compare analytical values with experimentally determined force distributions in order to further investigate the validity of STM for reinforced concrete design. Thermal gradients across the steel tension ties were monitored to identify additional forces induced in the pier due to this gradient.

The second was a precast, segmentally constructed bridge pier with a hollow cross section. Instruments were monitored hourly during the first five months of the service life of the pier. A finite element model was used to confirm measured response of the pier to applied temperature gradients. Analytical studies were performed to extend the results to multiple column bents. Comparisons of measured pier gradients to those specified for bridge superstructures in current bridge design codes were used to determine recommendations for modifications in current design practice.



## CHAPTER 2

### **2. BACKGROUND**

#### **2.1 Introduction**

The purpose of this chapter is to present background information. The significance of the US 183 mainlane bridge pier study is presented with emphasis on its relationship to strut-and-tie modeling. The general background of design for thermal gradients is summarized.

#### **2.2 Strut-and-Tie Modeling (STM)**

Previous research pertaining to overall load distribution throughout all components of a bridge and general behavior of bridge piers is minimal. Most previous load distribution studies have focused exclusively on distribution among the various superstructure elements. The many studies of load transfer between girders are examples of this trend.

Bridge pier design has become highly standardized. Designs for piers that have worked in the past are often used, and many designers minimize creativity in this area of bridge design as a means of minimizing cost. Piers are very conservatively designed, and minimum reinforcement ratios tend to govern. Due to these circumstances, structural problems with bridge piers do not often arise. Consequently, research in this area is lacking.

The US 183 mainlane bridge piers are not typical highway bridge piers. They are functional and are also innovative and aesthetically pleasing, as shown in Figure 1.2. As such, they provide an opportunity to investigate behavior of non-standard bridge substructures.

Through their form, these piers provide a visual representation of their structural behavior. Most observers will intuitively realize that as vertical load is placed on the bearings, the “Y” will tend to “spread apart,” placing the steel members across the “Y” into tension. Although this behavior is intuitive, detailing and dimensioning involved in the pier design may be quite difficult.

Structural failures have shown that detailing and dimensioning of structural concrete are of utmost importance to the integrity of a structure [1]. This is especially true in areas where geometric discontinuities and concentrated loads occur. However, until recently, no consistent method for detailing structural concrete had been codified in the US. Most detailing recommendations included in codes do not provide a conceptual model to aid the engineer in visualizing behavior. In order to insure structural integrity, the engineer’s focus must be redirected to the flow of forces and overall structural behavior. The introduction of rational, transparent models could greatly improve detailing [1]. This approach has been introduced in recent AASHTO specifications [7, 8].

Since the US 183 mainlane pier was accessible for instrumentation purposes during construction, researchers had the opportunity to measure deformations and deduce the flow of forces through the pier. Once obtained, these forces could be compared to forces predicted by a strut-and-tie model of the pier to evaluate the use of strut-and-tie modeling for design of structural concrete.

### ***2.2.1 General***

Strut-and-tie modeling utilizes struts, ties, and nodes to idealize the flow of forces through a structure. Struts represent the flow of compressive forces through three dimensional (3-D) stress fields in the concrete. Ties represent the flow of tensile forces provided by reinforcement or concrete tensile strength. For practical design purposes, concrete tensile strength is neglected. Nodes link the strut and tie forces together, and must be in equilibrium.

Strut-and-tie modeling provides a rational framework for a detailing method that can be applied to a variety of structural components [9]. With strut-and-tie models, the stress distribution is idealized as a static force system. Forces in the struts and ties are calculated and then used to evaluate compressive stresses in the concrete and to proportion the reinforcement [10]. Although a full study of strut-and-tie modeling is beyond the scope of this research, the following discussion is provided as background information.

### ***2.2.2 History***

Strut-and-tie modeling can trace its origin to 1899 with William Ritter's introduction of the truss model for shear design of reinforced concrete beams and Morsch's introduction of the truss analogy for design of web reinforcement in 1902. Strut-and-tie modeling is a generalized application of the truss analogy. Marti and Mueller created strut-and-tie model's scientific basis for a rational application working with Thürliman at the Swiss Federal Institute of Technology, using the theory of plasticity [11]. Leonhardt had advanced the practical use of STM at the University of Stuttgart and in his consulting practice [12]. Schlaich further developed STM as a consistent method by which structural concrete can be designed. His landmark PCI Journal paper was the first major introduction of STM into US literature [11]. A thorough history of strut-and-tie modeling can be found in Bergmeister [9].

Truss models for beams and STM for discontinuity regions are seen as attractive alternatives to empirical approaches for detailing structural concrete because of their transparency and adaptability to many design situations [9]. Strut-and-tie modeling is particularly useful for irregularly shaped zones and areas subject to high concentrated loads. Typical uses for strut-and-tie modeling include the design of corbels, deep beams, and walls with openings as shown in Figure 2.1. Strut-and-tie modeling is also frequently used in segmental bridge design in anchorage zones and deviator blocks.

Although strut-and-tie modeling is used in the situations listed above, it is by no means a widely used design method in the US. This may be attributed to the background of most US engineers. Sectional analysis is emphasized in US universities, and engineers therefore become comfortable and familiar with this type of analysis. While sectional analysis is very useful in many situations, it is not sufficient for detailing structural concrete in unusual circumstances where stress concentrations occur. Sectional analysis does not force an engineer to focus on the overall behavior of a structure. When unique conditions occur, lack of a consistent design method for all portions of a structure may cause problems.

US codes, other than the 1989 AASHTO Design Specification for Design and Construction of Segmental Concrete Bridges [7] and the 1994 AASHTO LRFD Bridge Design Specifications [8] do not currently contain a consistent design method for detailing and dimensioning structural concrete in areas of geometric discontinuity or areas where strain distribution becomes disturbed. This forces the designer to rely on empirical procedures, rules of thumb, and guess-work when dealing with these situations.

The ACI 318-95 Building Code Requirements [13] contains no information on strut-and-tie modeling. The AASHTO Specifications previously mentioned contain information concerning where the use of strut-and-tie modeling may be appropriate. These codes also contain some design examples. However, no consistent guidelines exist through which a designer can learn and apply strut-and-tie modeling.

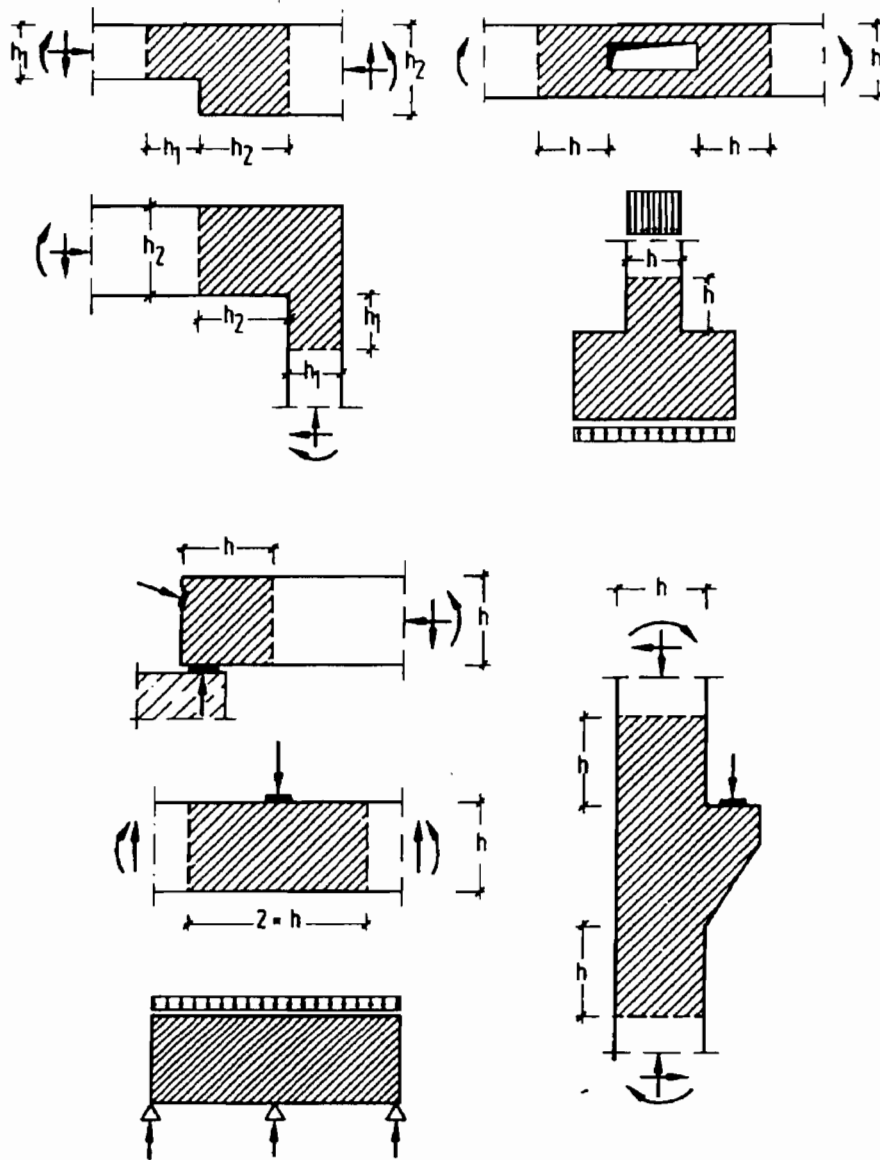


Figure 2.1 Typical Uses of Strut-and-Tie Models [11].

### **2.2.3 Assumptions**

The most important assumptions of which a designer should be aware when using strut-and-tie models are the following [9]:

- 1) Failure coincides with the formation of a mechanism caused by yielding of one or more of the ties.
- 2) Crushing of the concrete struts should not occur prior to yielding of the ties. Crushing is prevented by limiting the stress levels in the concrete.
- 3) All forces in the struts and ties are assumed as uniaxial.
- 4) All external loads are applied at the nodes of the strut-and-tie model. The model must be adequately formulated to realistically represent the load distribution when distributed loads are present.
- 5) Reinforcement must be detailed properly in order to prevent local bond or anchorage failure.

Also important is the adherence of strut-and-tie modeling to the lower bound theorem of the theory of plasticity. The lower bound theorem states that a load system which does not violate the yield condition and is based on a statically allowable stress field is a lower bound of the ultimate load. Equilibrium equations and statical boundary conditions must be satisfied by the statically allowable stress distribution. The lower bound theorem will be conservative in all cases [9].

### **2.2.4 Development of a Strut-and-Tie Model**

#### **2.2.4.1 B-regions and D-regions**

In order to apply the strut-and-tie modeling procedure to a structure, Schlaich [11] suggests dividing the structure into B-regions and D-regions. B-regions are those areas of a structure in which the Bernoulli hypothesis of plane strain distribution is assumed valid. D-regions are areas of a structure where strain distribution becomes disturbed; near concentrated loads, corners, and openings [11].

The size of D-regions can be estimated by using the principle of St. Venant. Stress distribution varies from nominal in regions of stress concentrations. St. Venant's principle states these localized effects disappear at some distance from the point of application of the load [14]. This distance is shown as "h" in Figure 2.2. A load on a structure can be replaced by a set of statically equivalent loads without changing the state of stress in the structure beyond the distance in which localized effects disappear. This distance is approximately equal to the distance between the statically equivalent applied loads.

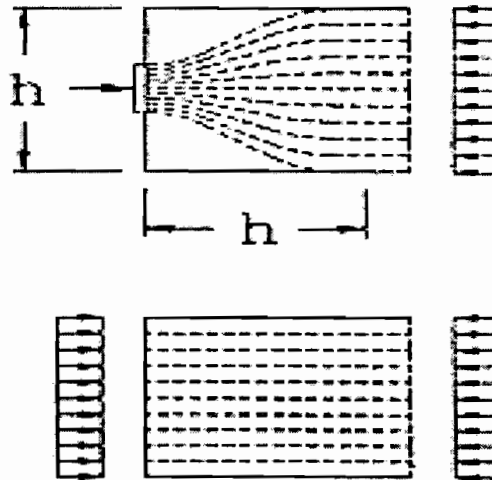


**Figure 2.2 St. Venant's Principle [10].**

#### 2.2.4.2 Layout of Struts and Ties

Two recommended methods exist for determining the orientation of struts and ties [11]. These are the load path method and the elasticity analysis method. The load path method can be easily used for structures in which the flow of forces is intuitive or known from previous experience. The elasticity analysis method is normally used in structures with very unusual configurations, where the flow of forces is not intuitive.

In the load path method, the outer equilibrium of the D-regions are determined. Once a structure has been divided into B- and D-regions, the forces in the B-regions can be found from flexural theory. The outer forces acting on a D-region are then the externally applied loads as well as these newly determined internal forces at the boundary between the B- and D-regions. Strut-and-tie models can be developed to determine the load paths in the D-region. A detailed approach for the load path method can be found in Bergmeister [9].

With the elasticity analysis method, the strut-and-tie model is based on the principal stress pattern as determined from an elastic analysis. An elastic finite element program may be used for unusual cases. The struts and ties are then located at the center of gravity of the corresponding stress fields [9].

There is no unique solution for a given structural problem. While developing and subsequently evaluating a strut-and-tie model, a designer should be aware that loads will tend to use the path of least resistance, or the path with the least forces and deformations. Therefore, the model with the least and shortest ties is the best since the steel ties are much more deformable than the concrete struts [11].

### 2.2.5 Struts

Compression forces are transferred from node to node through struts. Three basic strut types are suggested for use by Schlaich [11]. These are the “prism”, the “fan”, and the “bottle” struts as shown in Figure 2.3.

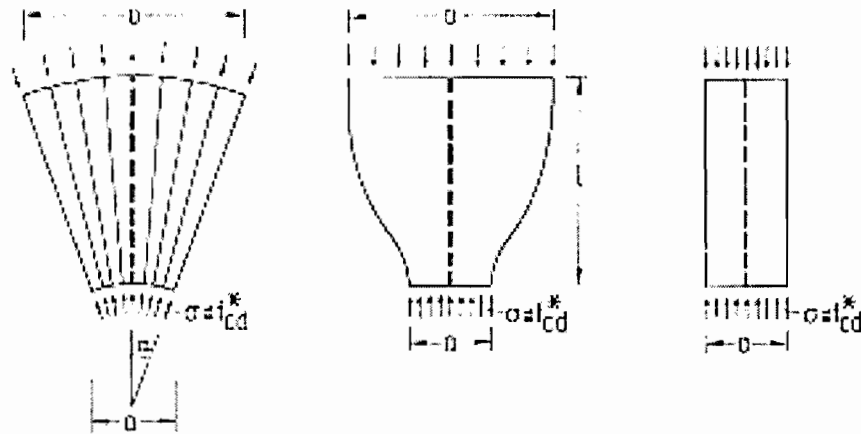


Figure 2.3 Strut Types [11].

Stress fields having uniform parallel stress trajectories are usually modeled by the prism strut. Fan shaped struts are used to model stress fields at supports or points of concentrated loading. In order to account for the possibility of stress fields narrowing near points of load application, a bottle shaped strut may be used.

In order to determine the effective strength of concrete compression struts, an efficiency factor is applied to the 28 day cylinder compressive strength of the concrete. This efficiency factor,  $\nu_e$ , takes into account several parameters. A few of these parameters are [9]:

- multiaxial state of stress
- cracking disturbances
- disturbances from reinforcement
- aggregate interlock after cracking
- time dependence

Recommended efficiency factors for different types of struts vary depending on the strut type. For a detailed discussion of efficiency factors, see Bergmeister [9].

The nominal load in the strut is represented as:

$$C_n = C_s + C_c$$

where

$$C_c = A_c f_{cd} = \text{concrete compression}$$

$$C_s = A_s f_s' = \text{steel compression}$$

where

$$A_c = \text{strut area}$$

$$f_{cd} = \text{effective concrete stress} = v_e f_c'$$

$$v_e = \text{concrete efficiency factor}$$

$$A_s = \text{steel area}$$

$$f_s' = \text{compressive stress in the steel}$$

Compatibility in concrete compression struts is important to consider. Large compressive forces may produce transverse tensile stresses in the bottle-shaped strut that may cause cracking and lead to loss of capacity [11].

### 2.2.6 Ties

The ties of a strut-and-tie model are tension carrying members provided by reinforcing steel or concrete tensile strength. Reliance on concrete tensile strength for ties should be approached with caution since previous loading conditions, such as shrinkage or thermal loads, may reduce the tension carrying capacity of the concrete. For most practical cases, concrete tensile strength is ignored.

Once the orientation of the ties is determined and forces in the ties are calculated from equilibrium analysis, reinforcing steel can be proportioned. The following relationship is used for this purpose:

$$T_n = A_s f_y$$

where

$$A_s = \text{the area of steel reinforcement}$$

$$f_y = \text{the yield stress of the steel}$$

Tie forces are usually resisted by placing the reinforcement symmetrically along the entire length of the tie and about the line of action of the force. Proper anchorage for the reinforcement at the nodes should be provided. Reinforcement should be provided such that the bars will just reach yield at ultimate load. Yielding of the reinforcing bars must occur prior to the crushing of the concrete.

In addition to proportioning reinforcement to resist the tie force, special attention should be given to assuring that brittle failures, such as stability failures, are precluded. To ensure satisfactory performance at service load levels, crack control reinforcement should supplement that required by strut-and-tie modeling. This additional reinforcement is not critical in terms of ultimate capacity as long as adequate reinforcement is provided for the primary load path [10].

### **2.2.7 Nodes**

Nodes are defined as the intersection points of three or more straight struts or ties [11]. They are points where forces change direction. The strut and tie forces that meet at a node must be balanced in equilibrium at the node. If the deviation of forces at a node is locally concentrated and the node is small, the node is referred to as a “singular node”. Where stress fields joined by the node are large, the node is referred to as a “smeared node”. Nodes are further classified depending on the type of elements they connect. The classifications are [9]:

- CCC: Compression-Compression-Compression
- CCT: Compression-Compression-Tension
- CTT: Compression-Tension-Tension
- TTT: Tension-Tension-Tension

Node dimensioning is limited by two constraints [9]:

1. The lines of action of struts, ties, and external loads must coincide.
2. The relative angles and widths of struts and ties restrict the geometry of the nodes.

The forces of a node balance each other in compression in most cases. An idealized tension tie, represented as a tie anchor, transfers load from “behind” the node. Detailed information on checking strength for various node types can be found in Schlaich [11] and Bergmeister [9].

### **2.2.8 Summary of Design Procedure**

Bergmeister [9] presents a generalized design procedure for structural concrete based on the utilization of strut-and-tie models. This procedure is shown in Figure 2.4.

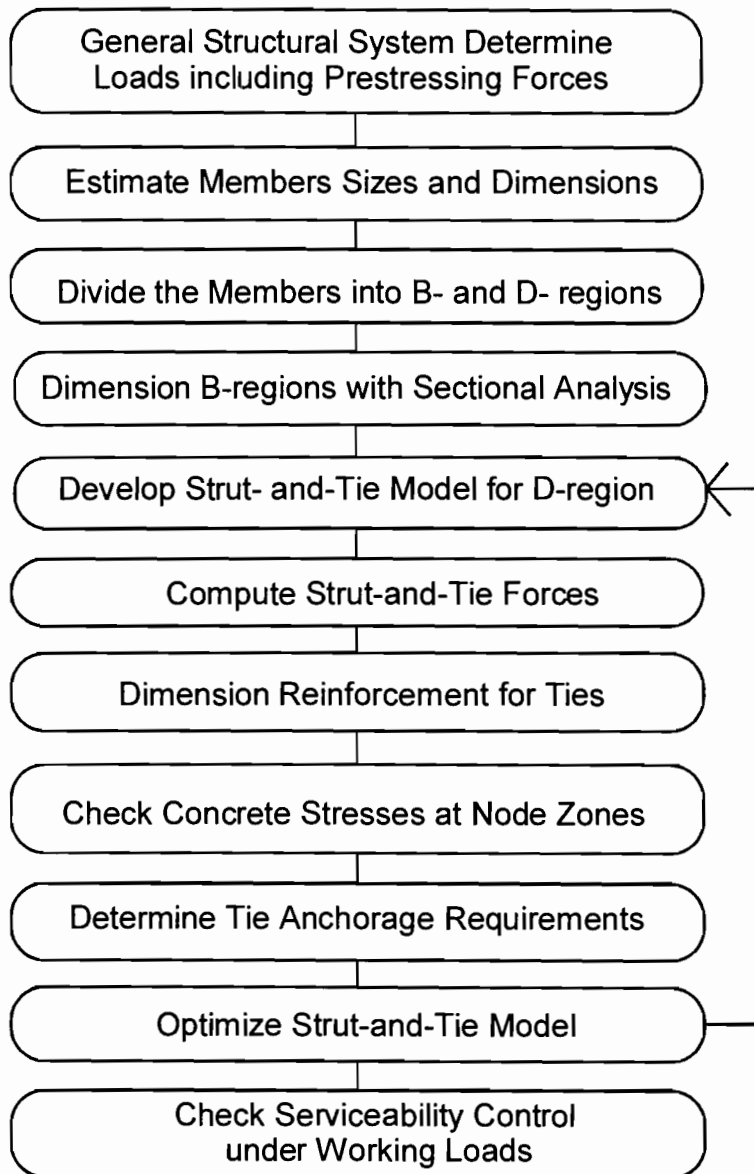


**Figure 2.4** *Design Procedure for Structural Concrete [9].*

### **2.2.9 Benefits of Strut-and-Tie Modeling**

Strut-and-tie modeling redirects the designer's focus to overall structural behavior. The method is rational and transparent. It allows the engineer to visualize the flow of forces through a structure. It provides a consistent design approach for an entire structure and is adaptable to many situations. Proportioning of reinforcing steel is simple with the use of strut-and-tie modeling.

Since STM is a lower bound plasticity model, it is conservative for design. STM is appropriate for design of structural concrete in areas where discontinuities occur because the behavior of the region in question is simplified into discrete load carrying members [11]. In summary, strut-and-tie modeling can lead to a better understanding of structural behavior. By providing a consistent method for detailing and dimensioning, STM can improve the integrity of concrete structures.

#### ***2.2.10 Limitations of Research***

The ultimate load of the US 183 mainlane pier could not be investigated in this study. The strut-and-tie model developed for research purposes is not the one used for pier design, which considered dead load, live loads, and wind loads. Since this study was limited to dead load conditions, a different STM was developed using dead loads only. The purpose of this STM was only to trace the flow of dead load forces through the pier in order to compare the model forces with forces deduced from field measurements.

### **2.3 Thermal Gradients**

Engineers have long known of the effects of ambient temperature variations on the superstructures of bridges. This fact is reflected in bridge designs which account for axial shortening and elongation in the superstructure through the use of elastomeric bearing pads, rollers, and expansion joints [15]. Recently, some sophisticated bridge designs eliminated such devices; more accurate analysis methods allowed designers to accommodate superstructure movements through deflections of the substructure [16].

The increased use of monolithic systems with restrained members highlighted a second and potentially serious environmentally-induced effect: strains due to temperature gradients through member cross-sections. The poor thermal conductivity of concrete tends to create large temperature differentials on opposite sides of members as they are heated and cooled in daily cycles [15]. These differentials in turn cause a corresponding strain distribution which can develop a significant amount of tensile stress in the member. The problem became especially apparent in bridge superstructures with hollow cross-sections: the Jagst bridge in Germany and several cast-in-place bridges in the State of Colorado exhibited cracking attributable in part to thermal differences between the top and bottom flanges [17].

To date, however, no investigations into the effects of non-linear thermal gradients on concrete bridge piers have been performed. According to a survey performed by Poston, Diaz, and Breen [18] in 1984 regarding 155,000 bridge bents, approximately 17% were single pier bent configurations. Of these, about 11% were designed with a hollow cross-section. Of the 129,000 bent configurations built with multiple piers, 1% were hollow in cross-section. Thus, in the period of 20 years between 1960 and 1980, approximately 2950 single-pier and 1420 multiple-pier bent configurations were built with hollow cross-

sections. Furthermore, respondents to the survey indicated that the number of single-pier bents (where hollow cross-sections are more often used) would likely increase to 20% of the planned total for the period from 1980 to 1990. Therefore it would seem that the use of hollow cross-sections is increasing in bridge piers built in North America. Additional anecdotal evidence of the increasing use of segmentally constructed hollow bridge piers is presented later in this chapter. Clearly, there exists a need for clarification of the code requirements concerning the effects of temperature gradients on hollow bridge piers.

### 2.3.1 Gradient Shape

Many factors influence the shape of thermal gradients across a member's cross-section. Environmental variations, material properties, and time all greatly affect the distribution of temperatures (see Figure 2.5).

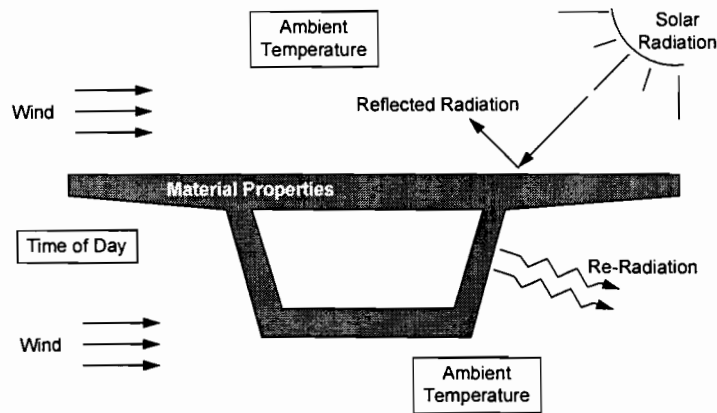


**Figure 2.5** Factors affecting thermal gradients (after Roberts [19]).

In general, the environmental influences on a bridge structure include radiation, convection, and conduction [16, 17]. The most important of these is solar radiation [17, 19, 20], which causes significant increases in temperature on surfaces directly exposed to sunlight, even on days when the ambient air temperature is relatively low. In addition to direct solar radiation, re-radiation of heat back into the surrounding environment can also occur, primarily at night [17]. Convection and conduction occur between the structure and the ambient air [16, 17]. These two processes are directly related to the difference in temperature between the air and concrete and can be affected by wind speed. Roberts [19] reported that air stirring caused by vehicular motion on the decks of bridges can influence temperatures near the top surface.

Weather patterns during certain times of the year and at particular geographic locations affect temperature distributions as well. During the months of March and April, the city of Austin, Texas typically experiences unstable weather patterns. Warm and cool fronts tend to arrive alternately every few days, causing large variations in the ambient air temperature on a day-to-day basis. Potgieter and Gamble [20] suggest that such variations in weather patterns can produce large temperature differences through bridge members. A warm weather pattern that immediately follows cold weather can produce a large “positive” gradient in bridge decks (i.e., the temperature of the bridge deck is higher than that of the soffit.) Cool weather following a warm front can have the opposite effect, producing “negative” gradients. The same researchers also cite ambient humidity as an important factor. In desert regions air temperature during the night can fall dramatically, whereas daytime temperatures can rise to very high levels. This large daily fluctuation can cause severe gradients in bridge structures. However, the effect may be less pronounced in humid climates where nighttime ambient air temperature drops relatively little; the bridge members never cool down sufficiently to create large temperature gradients when the sun rises the following morning.

The material properties of concrete greatly influence the distribution of temperatures through the bridge cross-section. Moorty and Roeder [16] cite density, specific heat, and conductivity as important factors in determining heat flow. The low conductivity of concrete is the most important material property which contributes to the shapes of measured gradients in bridges [15, 19, 20]. Heat absorbed into the outer layer of a concrete member will transfer through the section over a period of many hours. During thermal tests on concrete frame models, Vecchio and Sato [21] reported that steady-state temperature conditions finally occurred in the 300 mm thick sections of their models after 18 hours of constantly-applied thermal load. It can be concluded that the daily radiation and temperature fluctuations in the environment surrounding bridges will seldom if ever allow the structures to achieve steady-state equilibrium.

### ***2.3.2 Gradient Effects***

#### *2.3.2.1 Generalized Members*

The effects of temperature gradients on a structure are a function of the shape of the gradient and the determinacy of the structure [17]. In order to investigate the effects of thermal gradients, several assumptions must be made (from Imbsen, et al[17]):

1. The material is homogeneous and isotropic.
2. Material properties are independent of temperature changes.
3. The material behaves elastically (i.e., superposition is valid).
4. Plane sections remain plane.
5. Temperature varies only with the depth of the member.

The first and third assumptions limit the discussion of thermal response in concrete members to those in an uncracked state. The fifth assumption was confirmed to be approximately true by Hoffman, McClure, and West [22] during a thermal study on a model span in Pennsylvania.

The requirement that plane sections remain plane is the basis of all thermal gradient effects. As shown in Figure 2.6, when a statically determinate member undergoes a linear temperature distribution across its cross-section it will experience bending and elongation related to the slope of the linear gradient. No induced stresses will occur due to the linearity of the gradient [19].

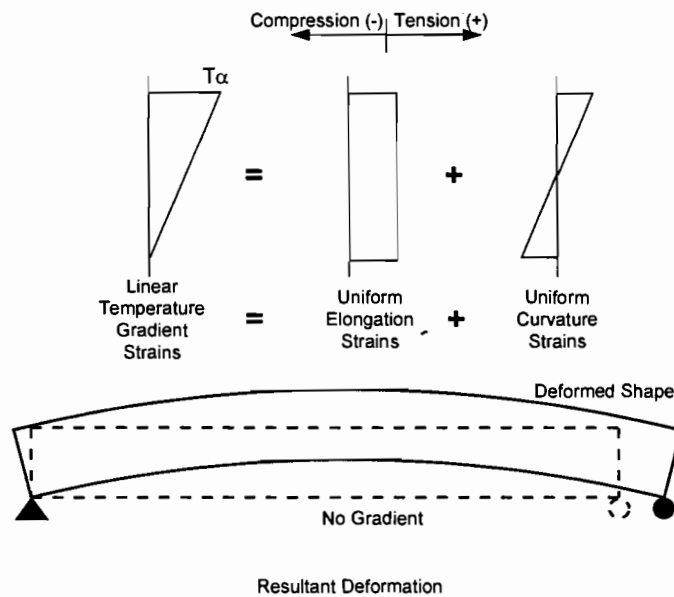


**Figure 2.6** *A statically determinate member under a linear temperature gradient (after Roberts [19]).*

The problem becomes more complicated with the application of a non-linear temperature gradient (see Figure 2.7). Temperature induced strain is a function of the temperature at any distance from the neutral axis of the member and the coefficient of thermal expansion  $\alpha$ :

$$\varepsilon_t(Y) = \alpha T(Y) \quad (2.1)$$

where  $Y$  is measured from the neutral axis of the member.

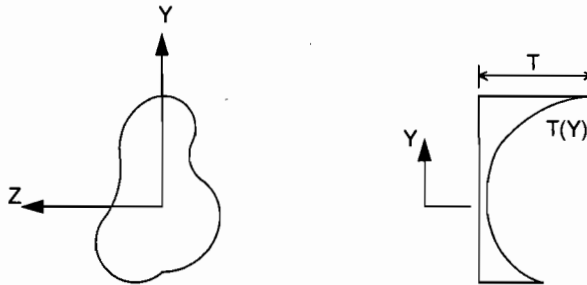


**Figure 2.7** *Arbitrary section with a non-linear temperature distribution.*

Figure 2.8(a) illustrates the strain distribution across the arbitrary section with a non-linear temperature gradient if plane sections do not remain plane and the section's fibers do not influence one another. In a monolithic structure this cannot be the case; there is an interaction and shear transfer between fibers and the actual strain distribution has been shown to be linear as shown in Figure 2.8(b). The induced stress distribution in a fully restrained member due to the non-linear gradient can be calculated as (see Figure 2.9):

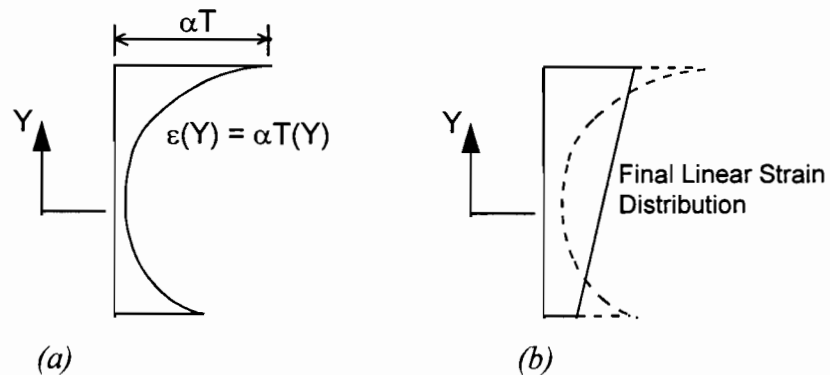


**Figure 2.8** *(a) Non-linear strain distribution assuming no interaction between section fibers (b) final linear strain distribution because plane sections remain plane (after Imbsen[17]).*

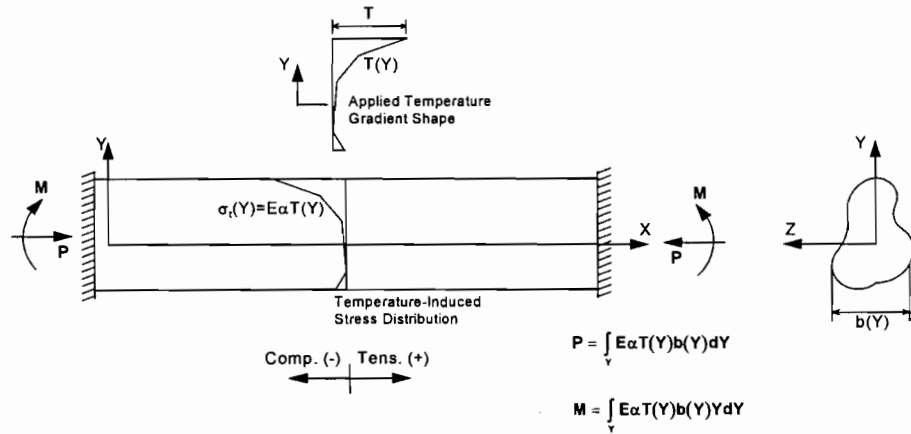


**Figure 2.9 Thermal gradient and stress distribution in a fully restrained member.**

The internal stresses needed to satisfy the requirement that plane sections remain plane are referred to as *self-equilibrating* stresses. They arise from the interaction of the member's fibers with one another and are analogous to residual stresses present in hot-rolled steel shapes [17,20]. To calculate their magnitude, one must first assume that the member is fully restrained [19]. The temperature-induced stress distribution (i.e. Equation 2.2) represents the sum of the self-equilibrating stresses and *artificial* stresses which represent the axial force and bending moment required to fully restrain the member [17]. Figure 2.10 illustrates this concept.

$$\sigma_t(Y) = E \alpha T(Y) \quad (2.2)$$

The restraining axial force is expressed as:

$$P = \int_Y E \alpha T(Y) b(Y) dY = \int_Y \sigma_t b(Y) dY \quad (2.3)$$

where  $b(Y)$  is the section width at any distance  $Y$  from the neutral axis [17, 19]. The axial stress can be written as:

$$\sigma_p(Y) = \frac{P}{A} \quad (2.4)$$

where  $A$  is the cross-sectional area of the member. It follows that the restraining moment is calculated as:

$$M = \int_Y E \alpha T(Y) b(Y) Y dY = \int_Y \sigma_t(Y) b(Y) Y dY \quad (2.5)$$

and the bending stresses are:

$$\sigma_m(Y) = \frac{MY}{I} \quad (2.6)$$

where  $I$  is the moment of inertia of the section about the neutral axis. Self-equilibrating stresses are then calculated by the following:

$$\sigma_{se} = \sigma_t - \sigma_p - \sigma_m = E\alpha T(Y) - \frac{P}{A} - \frac{MY}{I} \quad (2.7)$$

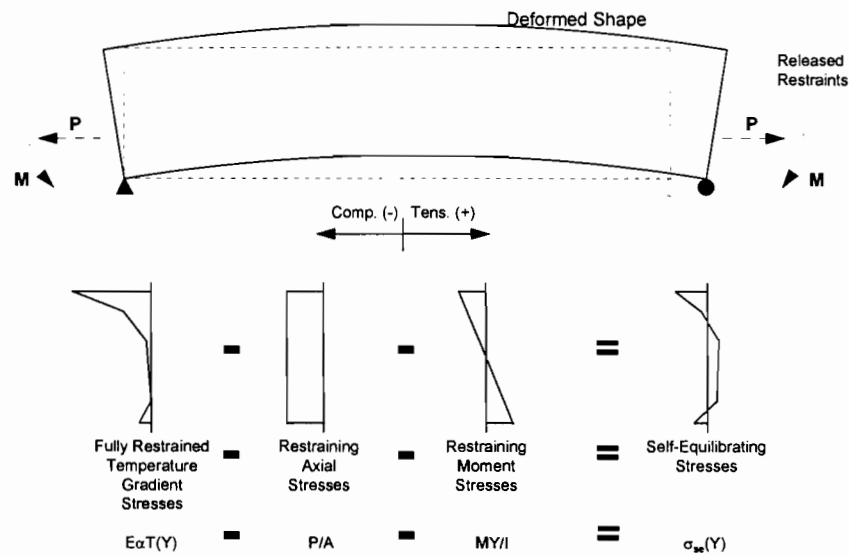


**Figure 2.10** *Temperature-induced stress distributions (after Roberts [19]).*

In summary, self-equilibrating stresses in a statically determinate member are determined in these steps:

- Artificially restrain the member
- Calculate the fully restrained stress distribution (Equation 2.2)
- Calculate the artificial moments and axial forces (Equations 2.4 and 2.6)
- Remove the artificial stresses from the total stress distribution (Equation 2.7)

The member's curvature can then be found by converting the sum of the stresses found in Equations 2.4 and 2.6 into strains and solving for the slope of the linear strain distribution [20].

Stress distributions in statically indeterminate members are found similarly. Potgieter and Gamble [20] present the example of a two span continuous beam (see Figure 2.11). As before, the fully restrained axial and bending stresses are calculated, and the member's curvature is found as stated above. Using the calculated value for curvature, the beam's unrestrained deflection (cambered upwards for positive gradients) can be found. A force is then applied at the middle support to satisfy boundary conditions, and the new restraint stresses (i.e., bending moment) are added to the self-equilibrating stresses found earlier.

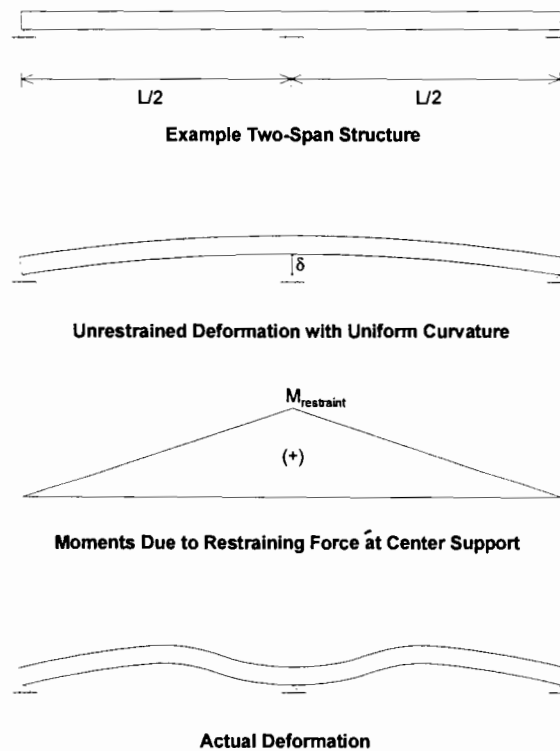


**Figure 2.11** *Application of thermal gradients to a two-span beam (after Potgieter and Gamble [20]).*

Roberts [20] illustrates the concept with a three-span continuous beam using the same process (see Figure 2.12). The temperature stresses are more critical in this example: the three-span beam undergoes a positive moment due to temperature stresses in the middle span, thus acting in concert with live load moments.

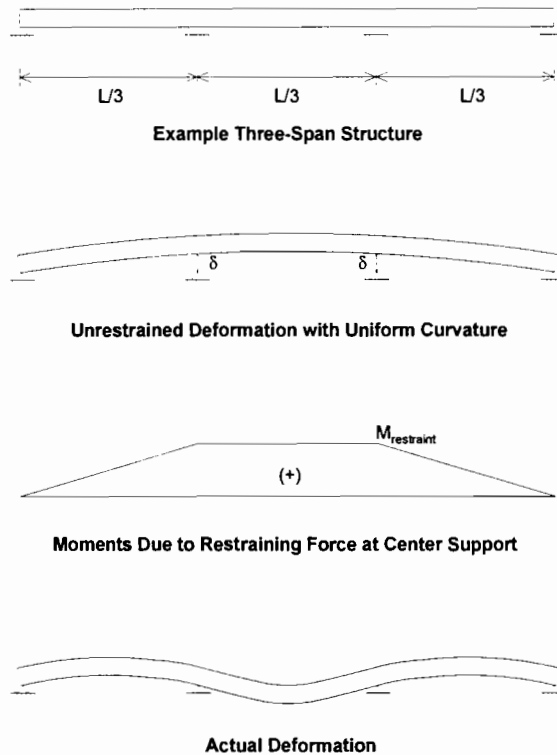


**Figure 2.12** *Application of thermal gradients to a three-span beam (after Roberts [19]).*

### 2.3.2.2 Effects on Bridge Piers

The effects on hollow bridge piers due to temperature gradients are assumed to be similar to those for the beam members in the previous section. However, different deflection patterns are possible due to the differences in support conditions. Figure 2.13 shows the expected deflection due to self-equilibrating stresses on the statically determinate free-standing single pier bent.

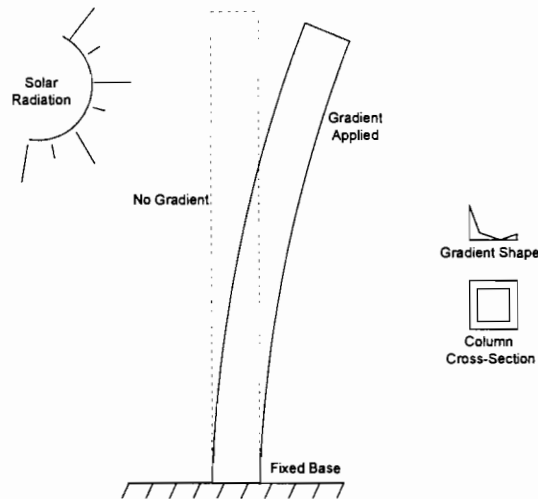


**Figure 2.13** *Temperature-induced response in a free-standing single pier bent.*

Restraint conditions would be imposed on the pier in various degrees depending on the type of interface between the pier and the superstructure. A simplistic idealization would be to model the pier as a fully restrained member (see Figure 2.14). This assumption requires that both the superstructure and the foundation exhibit infinite stiffness. Modeling the pier in this manner would produce an overly conservative estimate of the axial and flexural stresses induced by the non-linear temperature gradient.

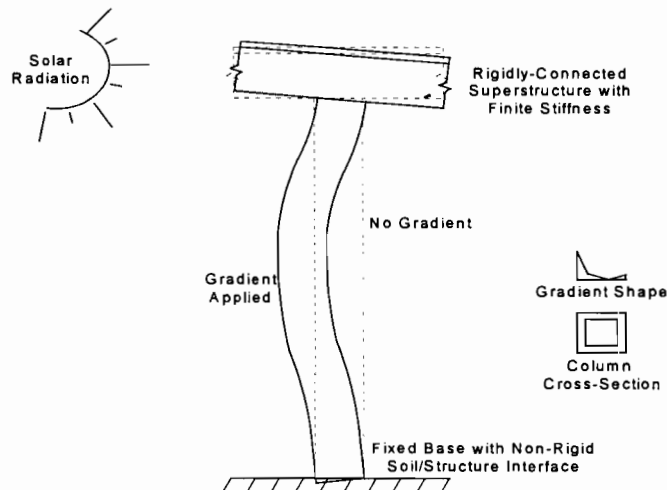


**Figure 2.14** *Temperature-induced response in a partially-restrained single pier bent.*

Modeling the pier as partially restrained by the superstructure and the foundation would give a more accurate representation of the induced stresses. The stiffness at each end of the pier could be modeled as finite. Therefore, some movement would be possible at the column's ends as shown in Figure 2.15.

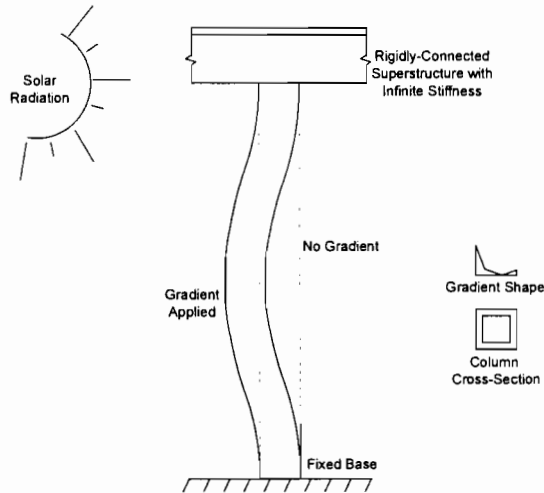


**Figure 2.15** *Temperature-induced response in a fully restrained single pier bent.*

Although their use is rare, bents consisting of multiple piers with hollow cross-sections would also respond to thermal gradients according to restraint conditions. For a bent with no superstructure attached, the response would be highly dependent on the orientation of the applied maximum temperature difference (see Figure 2.16). Various levels of rigidity in the superstructure-to-bent and foundation-to-column connections along with the temperature gradient orientation would also influence any induced stresses. Finally, the bent configuration itself would affect the response. The number of piers and horizontal braces would determine the magnitudes of strains and stresses induced by temperature.

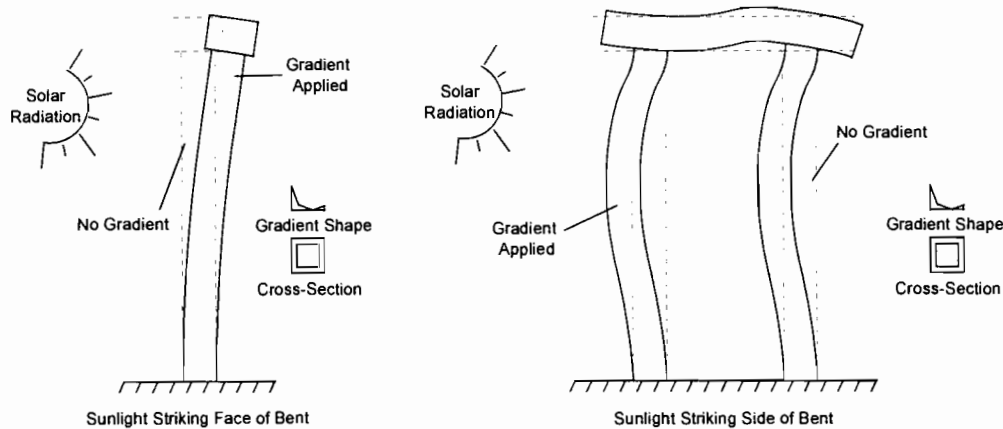


**Figure 2.16** *Temperature-induced response of a multiple-pier bent.*

## 2.4 Development of Current AASHTO Thermal Gradient Provisions

A comprehensive literature review of studies related to thermal gradient effects in bridge superstructures was performed by Roberts [19]. However, it is necessary to discuss two important studies [17, 20] that had a direct impact on the thermal effects provisions as stated in the American Association of State Highway and Transportation Officials (AASHTO) *LRFD Bridge Design Specifications* [8] and the *AASHTO Guide Specifications for the Design and Construction of Segmental Concrete Bridges* [7]. Findings indicated by a new study [19] are discussed in a subsequent section.

### 2.4.1 Potgieter and Gamble [20]

Researchers from the University of Illinois used a one-dimensional heat flow computer model to predict temperature distributions in concrete box-girder bridges. The program was run with a variety of cross-sectional shapes. Temperature data taken over a period of two days from the Kishwaukee River Bridge in northern Illinois were used to confirm the results found by the computer program.

In addition, measurements of solar radiation levels from 26 weather stations throughout the country were used as input for the computer model. From these data, researchers attempted to quantify the maximum possible gradient and the frequency of its occurrence in particular regions in the continental United States.

Potgieter and Gamble [20] noted that temperature-induced stresses were primarily a serviceability problem. The effects of these stresses on the ultimate strength of a structure were minimal. The authors found temperature stresses to be of the same order of magnitude as those caused by service live loads. Most importantly, the authors recommended the use of additional mild reinforcement to control crack widths, rather than additional prestressing to prevent the occurrence of tensile stresses.

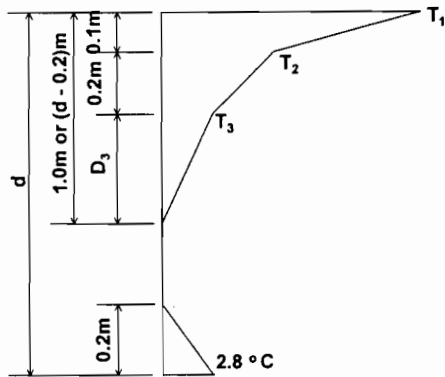
#### 2.4.2 NCHRP Report 276 [17]

This study's main objective was to develop specific guidelines intended for adoption into the AASHTO bridge design code. This extremely informative report provided an overview of (then) current design code provisions for temperature gradients from a variety of foreign sources. Case studies were examined to determine the magnitude of thermal effects on typical bridge types and configurations. Also, a comprehensive list of references was cited to aid designers. Several complete examples of calculations to determine temperature-induced stresses were included as well.

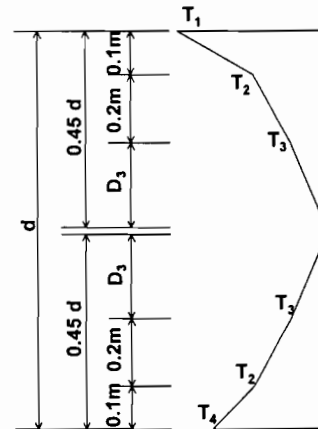
Design guidelines for the applications of thermal gradients in bridge superstructures were proposed that relied heavily on the research performed by Potgieter and Gamble [20]. The United States was divided into four zones of solar radiation intensity (see Figure 2.17). Both positive and negative temperature gradient shapes were proposed that varied in magnitude according to the radiation zone in which a particular project was located (see Figures 2.18 and 2.19). The temperature magnitudes corresponding to the gradient coefficients can be found in Tables 2.1 and 2.2. NCHRP Report 276 also recommended design values for the concrete coefficient of thermal expansion based on aggregate type (see Table 2.3).



**Figure 2.17** Proposed maximum solar radiation zones (after Imbsen, et al [17]).



Note: For superstructure depths greater than 0.61m



Note: For superstructure depths greater than 0.6 meters

**Figure 2.18** Proposed positive vertical temperature gradient (after Imbsen, et al [17]).

**Figure 2.19** Proposed negative vertical temperature gradient (after Imbsen, et al [17]).

Positive Gradients			
Plain Concrete Surface			
Zone	T <sub>1</sub> (°C)	T <sub>2</sub> (°C)	T <sub>3</sub> (°C)
1	30	8	2.8
2	26	7	2.2
3	23	6	2.2
4	21	5	1.7

50 mm Blacktop			
Zone	T <sub>1</sub> (°C)	T <sub>2</sub> (°C)	T <sub>3</sub> (°C)
1	24	8	2.2
2	20	7	2.2
3	18	6	1.7
4	16	5	1.0

100 mm Blacktop			
Zone	T <sub>1</sub> (°C)	T <sub>2</sub> (°C)	T <sub>3</sub> (°C)
1	17	5	1.7
2	14	5.6	1.7
3	13	6	1.1
4	12	6	1.1

**Table 2.1** Proposed temperature coefficient magnitudes for positive gradients (after Imbsen, et al [17]).

**Negative Gradients**

Plain Concrete Surface				
Zone	T <sub>1</sub> (°C)	T <sub>2</sub> (°C)	T <sub>3</sub> (°C)	T <sub>4</sub> (°C)
1	15.0	3.9	1.1	7.8
2	12.8	3.3	1.1	5.6
3	11.7	3.3	1.1	4.4
4	10.6	2.8	1.1	3.3

50 mm Blacktop				
Zone	T <sub>1</sub> (°C)	T <sub>2</sub> (°C)	T <sub>3</sub> (°C)	T <sub>4</sub> (°C)
1	12.2	3.9	1.1	8.3
2	10.0	3.3	1.1	6.1
3	9.4	3.3	1.1	5.6
4	8.3	2.8	0.6	4.4

100 mm Blacktop				
Zone	T <sub>1</sub> (°C)	T <sub>2</sub> (°C)	T <sub>3</sub> (°C)	T <sub>4</sub> (°C)
1	8.9	2.8	0.6	6.7
2	7.2	2.8	0.6	5.0
3	6.7	3.3	0.6	4.4
4	6.1	3.3	0.6	4.4

**Table 2.2** *Proposed temperature coefficient magnitudes for negative gradients (after Imbsen, et al [17]).*

Aggregate Type	Thermal Coefficient of Concrete (0.000001 per °C)
Quartzite	12.8
Quartz	11.5
Sandstone	11.7
Gravel	12.4
Granite	9.5
Dolerite	9.5
Basalt	9.0
Marble	4.3 to 7.4
Limestone	7.2

**Table 2.3** *Proposed design values for concrete coefficient of thermal expansion (after Imbsen, et al [17]).*

### 2.4.3 AASHTO LRFD Specification [8] Requirements

According to the 1994 edition of the *AASHTO LRFD Bridge Design Specification* temperature gradient effects are to be examined on a case-by-case basis under six different load combinations as shown in Table 2.4. The load factor  $Y_{TG}$  is to be chosen for each individual project. The commentary suggests basing the load factor on two items: the type of structure and the limit state being investigated. It suggests considering a lower factor for the strength limit states, but gives no example values. Menn [23] states, “Theoretically, no sectional forces due to restrained deformations (authors note ...including thermal effects) are present at ultimate limit state in ductile systems. In general, therefore, restrained deformations are only significant for the behaviour of the structure under service conditions, particularly with regard to cracking and deformations. The reinforcement required for crack control is practically independent of the magnitude of the restrained deformation.” The authors agree completely with Menn. Thermal gradients should be included only in the service load combinations of Table 2.4.  $Y_{TG}$  should be 0 for the strength limit states.

AASHTO LRFD Load Combinations and Load Factors

Load Combination	DC	LL	WA	WS	WL	FR	TU CR SH	TG	SE	Use One of These at a Time				
										Limit State	EQ	IC	CI	CV
STRENGTH-I	$Y_p$	1.75	1.00	-	-	1.00	0.50/1.20	$Y_{TG}$	$Y_{SE}$	-	-	-	-	
STRENGTH-II	$Y_p$	1.35	1.00	-	-	1.00	0.50/1.20	$Y_{TG}$	$Y_{SE}$	-	-	-	-	
STRENGTH-III	$Y_p$	-	1.00	1.40	-	1.00	0.50/1.20	$Y_{TG}$	$Y_{SE}$	-	-	-	-	
STRENGTH-IV	$Y_p$	1.35	1.00	0.40	0.40	1.00	0.50/1.20	$Y_{TG}$	$Y_{SE}$	-	-	-	-	
SERVICE-I	1.00	1.00	1.00	0.30	0.30	1.00	1.00/1.20	$Y_{TG}$	$Y_{SE}$	-	-	-	-	
SERVICE-III	1.00	1.00	1.00	-	-	1.00	1.00/1.20	$Y_{TG}$	$Y_{SE}$	-	-	-	-	

Table 2.4 Excerpt from AASHTO LRFD Specification [8] “Table 3.4.1-1 - Load Combinations and Load Factors.”

The AASHTO Code’s positive gradient shape is based on that of NCHRP Report 276 [17]. The code specifies the same solar radiation zones as the report, but the gradient shape is simplified to some extent (see Figure 2.20 and Table 2.5).

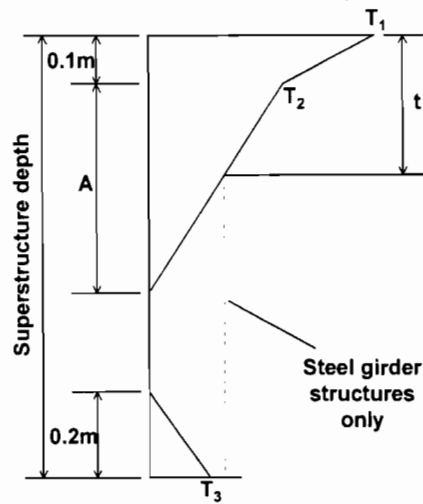


**Figure 2.20** *AASHTO LRFD Code [8] vertical positive gradient shape.*

Plain Concrete Surface		50mm Asphalt		100mm Asphalt		
Zone	T <sub>1</sub> (°C)	T <sub>2</sub> (°C)	T <sub>1</sub> (°C)	T <sub>2</sub> (°C)	T <sub>1</sub> (°C)	T <sub>2</sub> (°C)
1	30.0	7.8	23.9	7.8	17.2	5.0
2	25.6	6.7	20.0	6.7	13.9	5.6
3	22.8	6.1	18.3	6.1	12.8	6.1
4	21.1	5.0	16.1	5.0	12.2	6.1

**Table 2.5** *AASHTO LRFD Code [11] positive gradient magnitude values.*

The negative gradient shape values specified by AASHTO are the values in Table 2.5 multiplied by -0.5. For both positive and negative gradients, the dimension “A” is specified as:

- 300mm for concrete superstructures that are 400mm or greater in depth
- 100mm less than the actual depth for concrete sections shallower than 400mm
- 300mm for steel superstructures, where t = concrete deck thickness.

Furthermore, the code specifies that the “temperature value  $T_3$  shall be taken as 0.0, unless a site-specific study is made to determine an appropriate value, but shall not exceed 2.8°C for positive gradients and 1.4°C for negative gradients.” There are no code provisions or commentary relating to the use of thermal gradients of any kind in the design of bridge substructures.

#### **2.4.4 AASHTO Segmental Specification [7] Requirements**

The AASHTO specification relating to concrete segmental bridges contains the following provision for thermal gradients:

##### **7.4.4 Differential Temperature**

Positive and negative differential superstructure temperature gradients shall be considered in accordance with Appendix A of National Cooperative Highway Research Program Report 276 “Thermal Effects in Concrete Bridge Superstructures” [17].

It also amends the *AASHTO Standard Specifications* [24] load cases by adding the following service load condition:

$$(DL + SDL + EL) + \beta_E E + B + SF + R + S + (DT) \quad (2.8)$$

where: loads in parentheses are from the AASHTO segmental specification, all others are from *AASHTO Standard Specifications* [24].

DL = structure dead load	B = buoyancy
SDL = superimposed dead load	SF = stream flow pressure
EL = erection loads at end of construction	R = rib shortening
E = earth pressure	S = shrinkage
$\beta_E$ = earth pressure coefficient	DT = thermal gradient loading

The segmental specification states that for any load combination that includes full live load with impact the load DT may be reduced by 50%. Also, the load T (temperature loading) in the standard specification is redefined as:

$$T = (TRF + DT) \quad (2.9)$$

where TRF is equivalent to the original T loading. Table 8-1, “Allowable Tensile Stress for Construction Load Combinations,” allows for combinations including or excluding temperature loading, T, for analysis of substructure where a smaller allowable stress must be used if temperature effects are excluded.

#### **2.4.5 Roberts [19]**

A comprehensive set of temperature measurements were made with thermocouples installed in several segments of the downtown San Antonio “Y” segmental viaduct project. Readings were taken continuously from July 1992 through July 1993. Roberts reported a maximum positive gradient magnitude of 50% of the AASHTO segmental specification for a segment with no asphalt topping, and 78% of design values with a 50mm thick asphalt layer. The general shapes of the measured positive gradients were quite similar to those of the code specifications. The maximum measured negative gradient magnitude was about 65% of the design value for an untopped segment, but was reduced to only 50% after the addition of the 50mm topping. Again, the shape of the measured negative gradient was similar to that of the design gradient.

Based on this large set of measured temperatures, Roberts suggested the following temporary provisions to the AASHTO segmental specification requirements (with changes in italics):

#### **7.4.4 Differential Temperature**

Positive and negative differential superstructure temperature gradients *shall be taken as 80% of the values represented in Appendix A of National Cooperative Highway Research Program Report 276 “Thermal Effects in Concrete Bridge Superstructures” [17]. Alternatively, site specific thermal gradients, developed based on the climatic conditions in the area and the actual material properties of the structure, may be substituted for the current design gradients.*

Roberts also suggested an addition to the commentary section 7.4.4. as follows:

*The currently recommended design thermal gradients, both positive and negative, have not been substantiated with field data. The data collected to date indicate that the design gradients may be overly conservative.*

In addition to this new wording, Roberts also outlined suggested changes in allowable stress requirements. Current allowable stress levels force designers to use additional post-tensioning to eliminate small areas of tension in the top and bottom flanges of a member subjected to self-equilibrating stresses from negative temperature gradients. Roberts’ proposed changes would relieve designers of the requirement to account for these stresses.

Finally, Roberts recommended that stresses due to temperature gradients be eliminated from all ultimate strength load cases by the application of a load factor of zero to the DT term defined previously. Roberts highlighted the need for additional

field temperature measurements as well as thermal studies on cracked sections. However, no suggestions were made for the application of thermal gradients to hollow bridge piers.

## 2.5 Previous Bridge Pier Temperature Studies

### 2.5.1 General

A literature search performed by the authors provided no indication that studies on the effects of non-linear temperature gradients on hollow concrete piers have ever been performed in the United States. However, at least two previous authors addressed temperature effects on bridge piers with solid cross-sections.

### 2.5.2 Stephenson [25]

An early model for the flow of heat through a tall slender concrete pier and the induced forces it caused was provided by Stephenson [25]. From observations of solar radiation, Stephenson suggested that the variation of solar energy in a daily cycle was basically sinusoidal. Thus, the heat flow,  $H$ , varied according to:

$$H = \sqrt{\omega \frac{C}{R}} \quad (2.10)$$

where:

$$\omega = \frac{2\pi}{T}$$

$T$  = period of oscillation

$C$  = thermal capacity per unit area

$R$  = thermal resistance per unit area

The quantity  $\frac{C}{R}$  was a multiple of density, specific heat, and thermal conductivity.

Stephenson suggested that the sinusoidal variation of heat flow also involved a phase angle (given as  $45^\circ$  for good quality concrete) representing the time lag between a change in temperature and the flow of heat through the column. Surface absorptivity was also accounted for in the model.

Stephenson also suggested that the temperature through the column's section (i.e., the non-linear temperature gradient) could be described as an exponential function:

$$T(x) = T_0 e^{-ax} \quad (2.11)$$

where:  $T_o$  = variation of temperature from the mean temperature at the irradiated surface  
 $x$  = distance from the irradiated surface of the column

$$a = \sqrt{\frac{\omega CR}{2}}$$

The strain at any point in the column was then calculated using the equation:

$$\frac{\partial L}{L} = T\alpha = T_o\alpha e^{-ax} \quad (2.12)$$

Stephenson also recognized that plane sections must remain plane under strains induced by the exponential temperature distribution. This was accounted for by equating the moment of the strain diagram about the shaded side of the column's cross-section with depth "d":

$$T_o\alpha \int_0^d e^{-ax}(d-x)dx \quad (2.13)$$

with the moment of the area of the final, triangular strain distribution:

$$\alpha T_1 \frac{d^2}{3} \quad (2.14)$$

where  $T_1$  is the temperature at the irradiated side. This equation yielded an expression for the radius of curvature of the unrestrained member:

$$d \frac{L}{\partial L} = \frac{d}{T_1\alpha} \quad (2.15)$$

Stephenson then found the column tip deflection with:

$$\Delta_{tip} = \frac{H^2}{2r} \quad (2.16)$$

where  $r$  was the radius of curvature of the column under differential thermal load and  $H$  was the height of the column. The induced stress due to a longitudinal restraint at the top of the column could then be calculated as:

$$f_{bc} = \frac{3\Delta_{tip}yE}{H^2} \quad (2.17)$$

### 2.5.3 Andres [2]

Although primarily concerned with the flow of forces through an unusually-shaped concrete pier (see Figure 1.2), Andres also tracked the temperature characteristics and resulting stresses induced in that pier. The work was part of this report.

Andres described one model of the stresses induced in a monolithic pier section as analogous to the bronze-encased steel bolt shown in Figure 2.21. Each material responds differently to uniform temperature changes due to their differing coefficients of thermal expansion. Similarly, the pier's shaft can be described with two different material responses due to the extreme differences in temperature between the "core" and "shell" concrete (see Figure 2.22).

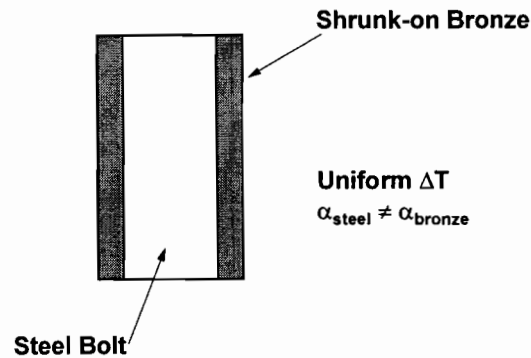


**Figure 2.21** *Bronze-encased steel bolt undergoing uniform temperature change.*

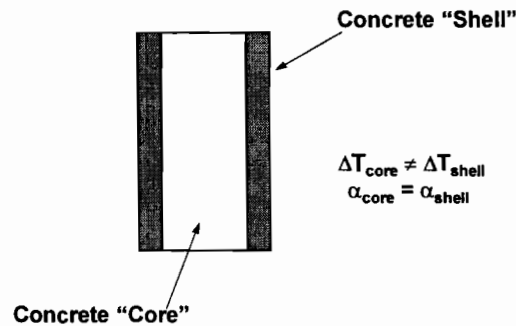


**Figure 2.22** *Concrete pier model undergoing differential temperature change.*

The outer shell will tend to expand due to heating, pulling the core along with it. Compressive stresses then occur in the shell while tension develops in the core area. Using this approach, Andres found that compressive stresses induced in the shell concrete due to temperature were of the same order of magnitude as those induced by the viaduct's superstructure dead load.

The data indicated large temperature gradients across the monolithic cross-section of the pier, but thermocouples were installed in only one quadrant of the pier's cross section, making determination of the gradient shape impossible.

## 2.6 Precast Segmental Piers in North America

Although no research into the effects of temperature gradients on hollow, precast bridge piers has been performed, construction of bridges with substructures of this type is increasing. An overview of projects involving precast, segmentally constructed bridge piers is presented here as anecdotal evidence of their importance. This list is representative but not inclusive.

### 2.6.1 Long Key Bridge

The Long Key Bridge, designed by Figg and Muller Engineers of Tallahassee, Florida, was completed in 1980 and featured 3701 meters of bridge deck consisting of 36-meter spans built by the span-by-span method [26]. The structure stands out as one of the first long over-water applications of precast segmental construction in North America. The piers had an unusual "V" shape and were precast at the contractor's casting yard (see Figure 2.23). The V-piers were post-tensioned to the bridge superstructure and were designed to act monolithically with it. Precasting the unusually shaped piers enhanced construction quality and eliminated the need for complex formwork to be installed over the water.

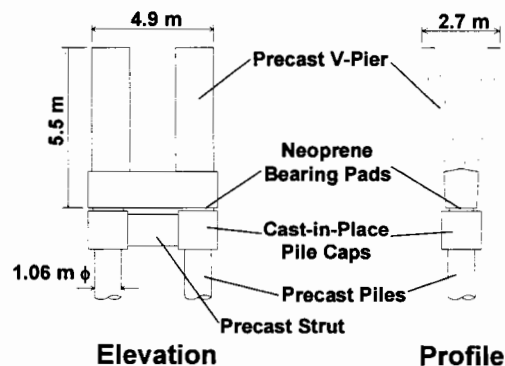


**Figure 2.23** *Unusual V-shaped piers, Long Key Bridge.*

### 2.6.2 Seven-Mile Bridge

The Seven-Mile Bridge, also designed by Figg and Muller Engineers, was completed in 1982. It featured 41-meter spans constructed by the span-by-span method. In an unusual move, the contractor decided to partially post-tension each span on a barge

before erection and then lift the entire span into place. This lengthy project stretched 10.9 km between two islands in the Florida Keys.

Most of the project's substructure consisted of cast-in-place twin-shaft units. Higher level piers on the project were constructed from precast concrete segments with rectangular cross-sections and post-tensioned vertically [27, 28]. Pier segments featured five voided cells in their cross-sections. Pier heights for the segmentally constructed piers ranged from 8.2 meters to 19.8 meters.

### 2.6.3 Dauphin Island Bridge [29]

The Dauphin Island Bridge is a 5430-meter long structure located about 80 km south of Mobile, Alabama. It serves to connect Dauphin Island in the Gulf of Mexico with the mainland United States, and replaced a 24-year-old bridge that was destroyed in a hurricane that struck the area in 1979. The new bridge was completed in 1982 after two years of construction. About 80% (4240 m) of the bridge's length consists of short-span (20 m) monolithically precast girder-and-deck segments. The bridge also features a 250-meter three-span unit built in balanced-cantilever with precast segments with a middle main span reaching 120 meters. The approaches for the main unit consist of twenty-six spans of 36 meters each built span-by-span with precast segments.

The designer, Figg and Muller Engineers, elected to use hollow, rectangular precast pier segments for the substructure of the segmentally constructed approach spans. Altogether, 174 precast box pier segments were used to construct piers ranging in height from 7 to 27 meters. Each pier segment was 4.88 x 2.44 x 2.74 meters high with 250 mm thick walls (see Figure 2.24). They were vertically match cast at the project's precasting plant located in Mandeville, Louisiana and barged to the bridge site. Epoxy was placed in the joints between segments during erection of the precast piers, which were then post-tensioned vertically.

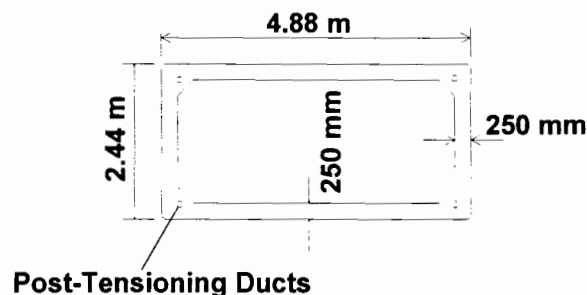


**Figure 2.24** *Cross-section of precast segmental piers, Dauphin Island Bridge.*

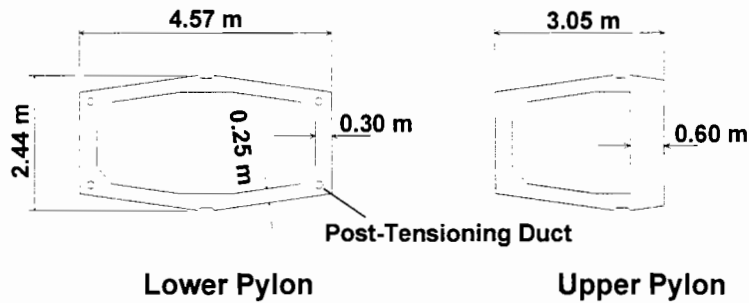


**Figure 2.25** *Segmental pylon cross-sections, Neches River Bridge.*

The designers chose to use precast pier segments to hasten construction. Pier segments could be precast in the yard and readied for erection concurrent with construction of the shorter monolithic spans. Also, shipment of precast segments was quite economical by barge, and prevented the need to transport large amounts of fresh concrete over water to the site.

#### **2.6.4 Sunshine Skyway Approaches**

The Sunshine Skyway Bridge is a cable-stayed structure featuring a concrete, trapezoidal box girder and a main clear span of 366 meters. It was designed by Figg and Muller Engineers. Construction of the 6.7 km long bridge was completed in 1987. It links St. Petersburg with Bradenton across Tampa Bay on the west coast of the Florida peninsula.

Most of the approaches to the cable-stayed main span were constructed with AASHTO girders, but higher level approaches were built with trapezoidal-box precast segments. The piers supporting these 41-meter spans were precast box segments. A total of 606 substructure segments were produced and used in piers ranging in height from 8 to 41 meters. All segments were cast at Port Manatee and barged approximately 6.4 km to the bridge site [30].

#### **2.6.5 Neches River Bridge [5]**

The Neches River Bridge is a cable-stayed structure located in southeastern Texas. It was originally designed as a box girder bridge by the Texas Department of Transportation but was redesigned for the contractor by Figg and Muller as a cable-stayed bridge which incorporated precast segmental piers. Several of the piers were only used temporarily during construction, and were therefore easier to dismantle than cast-in-place piers when the bridge was completed in 1986. Due to the remote location of the bridge site, precast substructures eliminated the need to build a large scale concrete batch plant on-site. Typical segments were 3 meters long, with approach pier heights reaching 40 meters. The main pylons were 96.6 meters high. The cross-sections for the pylons and the approach piers are shown in Figures 2.25 and 2.26.

### 2.6.6 Linn Cove Viaduct

Completed in 1983, the Linn Cove Viaduct formed the last link in the Blue Ridge Parkway located in a popular recreation area in North Carolina. The 379-meter long structure winds along the face of Grandfather Mountain, an environmentally-sensitive area in the Blue Ridge Mountains [31]. The bridge was designed by Figg and Muller Engineers and was constructed using the method of progressive placement. This method involved cantilevering the front of the bridge forward along the route by the addition of superstructure segments. When the location of a pier was reached, precast pier segments were placed by a crane located at the cantilevered tip

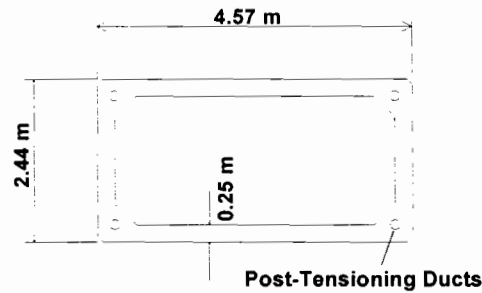


**Figure 2.26** *Segmental approach pier cross-section, Neches River Bridge.*

of the bridge superstructure. Because of the 55-meter length of several of the spans, temporary bents were placed in the same manner when the bridge superstructure reached midspan to reduce moments due to cantilever bending [32].

The pier segments were precast with an unusual cross-sectional shape (see Figure 2.27). The segments were match cast at a facility located at one end of the bridge. Segments were cast in both 1.8- and 2.7-meter lengths, and were bonded with epoxy during erection. After placement of the cap segment was complete, the pier was post-tensioned with eight tendons consisting of 12 ~ 13mm strands each. The tendons followed ducts from the top of the pier through and out the side of the cast-in place footing [33].

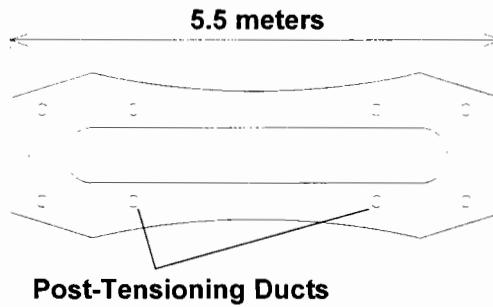


**Figure 2.27** *Pier cross-section - Linn Cove Viaduct.*

The use of precast pier segments greatly reduced the environmental impact of the construction activity. It also enabled the constructor to work completely from the top of the bridge during pier erection.

#### **2.6.7 Wando River Bridge [34]**

The Wando River Bridge is located on Interstate 526 near Charleston, South Carolina. It was designed by Figg and Muller. Construction of this 2500 meter long dual-span bridge was completed in 1988. Typical approach spans were 46 meters in length while the cantilevered main spans were 122 meters long.

The piers consisted of rectangular precast segments typically 3 meters in length. They were built in heights up to 41 meters to provide navigable clearance for ship traffic on the river. For piers located in the river, the hollow sections were filled with concrete in the bottom 15 meters. This provided additional resistance to ship impact. All precast segments were barged directly to the bridge site and lifted into place with a barge-mounted crane. For this project, the use of precast piers mitigated potential environmental problems in the surrounding wetlands.

#### **2.6.8 James River Bridge [35]**

This 1426 meter long bridge is located near Richmond, Virginia and was completed in 1989. This innovative cable-stayed structure features a 192-meter main span with 46-meter approach spans. Span-by-span construction was used to erect the approach spans, and the deck was cantilevered from the pylons outward during construction of the main span.

Precast, segmental piers with rectangular cross-sections were used for the approaches. Each segment had dimensions 2.4 x 5.5 x 4.3 meters high, and pier heights ranged from 19.5 to 43.9 meters. In addition, the main pylons were cast in place up to the level of the deck, with the remaining height comprised of precast segments.

### 2.6.9 Chesapeake and Delaware Canal Bridge [36]

This major new concrete cable-stayed bridge was completed in late 1995. It crosses the Chesapeake and Delaware Canal near St. Georges, Delaware on State Route 1. The main span is 229 meters in length, and the entire structure is 1417 meters long. The bridge consists of precast segmentally constructed 46 meter long approach spans built using the span-by-span method with an overhead gantry, as well as the main cable-stayed span comprised of the same trapezoidal segments.

While the main pylons were cast-in-place, the piers for the approach spans were constructed of precast rectangular box segments. The pier segments were 2.44 x 5.50 meters in size and were built in 1.22, 1.52, 1.83, and 3.05 meter lengths. Two pier segments were match-cast per day at the casting yard located 290 km to the south in Cape Charles, Virginia. Segments were barged directly to the bridge site. The approach span piers used a total of 463 precast segments and ranged in height up to 42 meters. The piers were post-tensioned after erection with 12 and 19 ~13 mm strand tendons (see Figure 2.28).

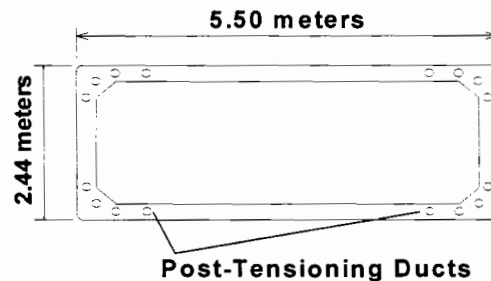


**Figure 2.28** *Cross-sectional dimensions of approach-span piers, Chesapeake and Delaware Canal cable-stayed bridge.*

The use of precast segmental piers enabled constructors to take advantage of the relatively inexpensive barging costs to transport segments. They also served to speed up erection time. The hollow cross-section of the piers allowed designers to reduce the number of precast piles supporting the piers and the size and cost of the foundations.

### 2.6.10 Louetta Road Overpass

The Louetta Road Overpass of State Highway 249, located in Houston, Texas, is an experimental bridge with several unique characteristics. Designed by the Texas Department of Transportation (TxDOT), it was completed in 1996. The bridge features the new “U54” precast, prestressed trapezoidal beam developed by TxDOT to increase span lengths and enhance aesthetics of urban highway bridges. In addition, the overpasses use precast, hollow, segmentally constructed piers. The entire project features extra-high-strength concrete with compressive strengths ranging from 70 to 90 MPa to decrease material usage and increase durability and impermeability [37].

The precast segmental piers consist of a small cast-in-place base, several 1.5-meter high column segments, and a 1.1-meter high ornamental capital segment. Pier heights range from 5.5 to 6.0 meters. The typical cross section of the pier is shown in Figure 2.29 [38]. According to Ralls and Carrasquillo [37], the use of this hollow section with thin walls was necessary to take full advantage of the extremely high concrete strength required for the project. In addition, this structure presented an opportunity for TxDOT to explore the feasibility of precast segmental piers in commonly used highway overpasses [5].

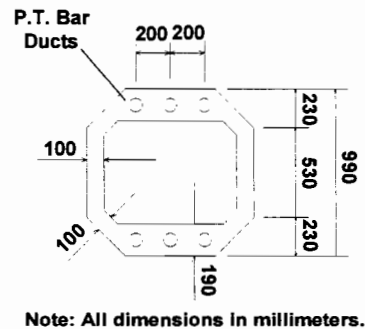


**Figure 2.29** *Segmental pier cross-section, Louetta Road Overpass.*

### 2.6.11 Northumberland Strait Crossing

This 12.9-km long structure is located between Prince Edward Island and the mainland at New Brunswick, in eastern Canada. The bridge was designed in a joint venture with J. Muller International and SLG/Stanley. When completed in 1997, it will be one of the longest over-water crossings ever built using precast segmental technology. The bridge was constructed with twenty-one precast segmental approach spans averaging about 90 meters in length and built in balanced-cantilever.

Also, the main bridge consists of 43 spans of 250 meters in length. The main spans were built using cast-in-place balanced cantilever techniques in the precasting yard, and lifted and placed as entire cantilever girder units weighing nearly 79,600 kN by a special floating crane supplied by Dutch contractors [39].

The piers were match-cast in the precasting yard in three large units: the pier base, the pier shaft with a conical ice shield, and a special “template” segment. Pier bases were cast in two separate sizes depending on the water depths at their locations and had maximum heights of 42 meters. The pier shafts were precast in heights up to 50 meters. They consisted of a 20-meter diameter conical ice shield located at the bottom of the shaft and a variable height shaft section. The pier shaft varied from an octagonal section at the ice shield to a rectangular section at the top. A rectangular “template” segment was match cast between the pier shaft and the massive cantilever girder unit described above. In this way, constructors could control the alignment of the bridge superstructure by simply varying the geometry of the template segment (see Figure 2.30). The piers were post-tensioned after their erection in the strait to provide structural continuity [40].

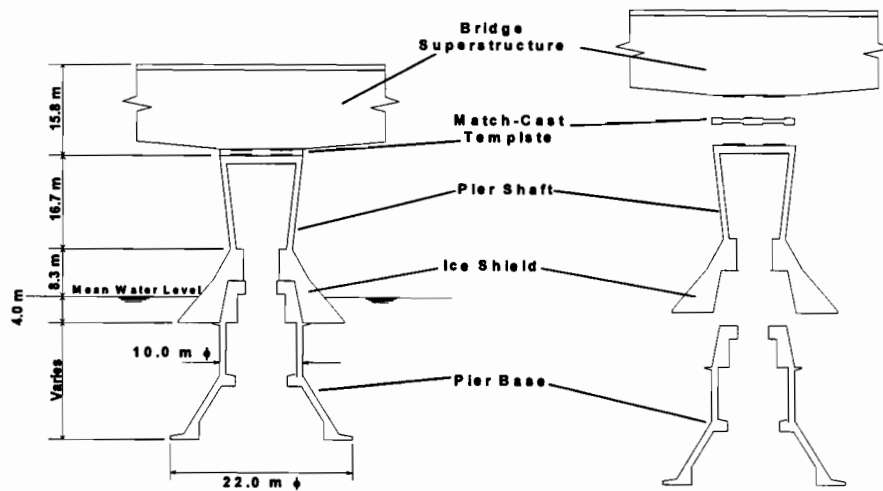


**Figure 2.30** *Elevation view of pier components, Northumberland Strait Crossing.*

The use of precast components for this massive structure enabled constructors to continue work even during the eight months of the year that the strait is icebound. The relatively short four-month window of opportunity for erection in the strait could therefore be used in an efficient manner. The entire bridge was completed within only four years in this particularly harsh construction environment [39].

## CHAPTER 3

### 3. *PIER INSTRUMENTATION*

#### 3.1 Introduction

This chapter describes the instrumentation of the US 183 mainlane bridge pier and ramp P segmental pier. Instrumentation systems and locations are discussed. A description of the pier selection process is also discussed.

#### 3.2 Mainlane Pier

##### 3.2.1 *Instrumentation Systems*

In order to measure the transfer of forces through the pier and to investigate the effects of thermal gradient in the pier, the following measurements were determined to be of importance:

- steel strains
- concrete strains
- temperature gradient
- deformation of the “Y”

Systems were chosen based on previous studies performed by Arréllaga [39] and from previous experiences of Roberts [19] on the instrumentation of the San Antonio “Y” segmental box girders.

##### 3.2.2 *Instrumented Pier*

The selection of the instrumented pier was based on several criteria; (1) the contractor’s schedule, (2) the research schedule, and (3) the height of the pier. In order to avoid compromising the research schedule, a pier was chosen which was located at the beginning of the first construction phase of the project. The pier was also chosen such that its location coincided with the instrumentation of a portion of the superstructure. The height of the pier was kept to a minimum in order to provide an accessible and safe working environment.

Pier D6, which supports superstructure spans 5 and 6, was chosen for instrumentation. This pier is located as shown in Figure 1.1. The dimension “H”, as shown in Figure 1.5, for pier D6 is 4572 mm (15’-0”). Only one quadrant of the pier was instrumented since the final loading is symmetrical.

### 3.2.3 Steel Strains - Strain Gauges

Electrical resistance strain gauges were used to measure steel strains. A 350 ohm strain gauge, as opposed to a standard 120 ohm strain gauge, was chosen for measuring the reinforcing steel strain. The gauge resistance was chosen so that the small strain variations expected could be read with accuracy. The signal to noise ratio is reduced with the use of a larger resistance strain gauge [19]. Strain gauges were bonded directly to the steel reinforcing cage of the pier and to the structural steel pipes at the construction site. Acrylic, rubber, and epoxy were layered on the gauges in order to protect them from exposure to water and from damage due to vibration of the concrete. The layout of strain gauges is shown in Figure 3.1 - Figure 3.3. Strain gauges are labeled with the designation "S."

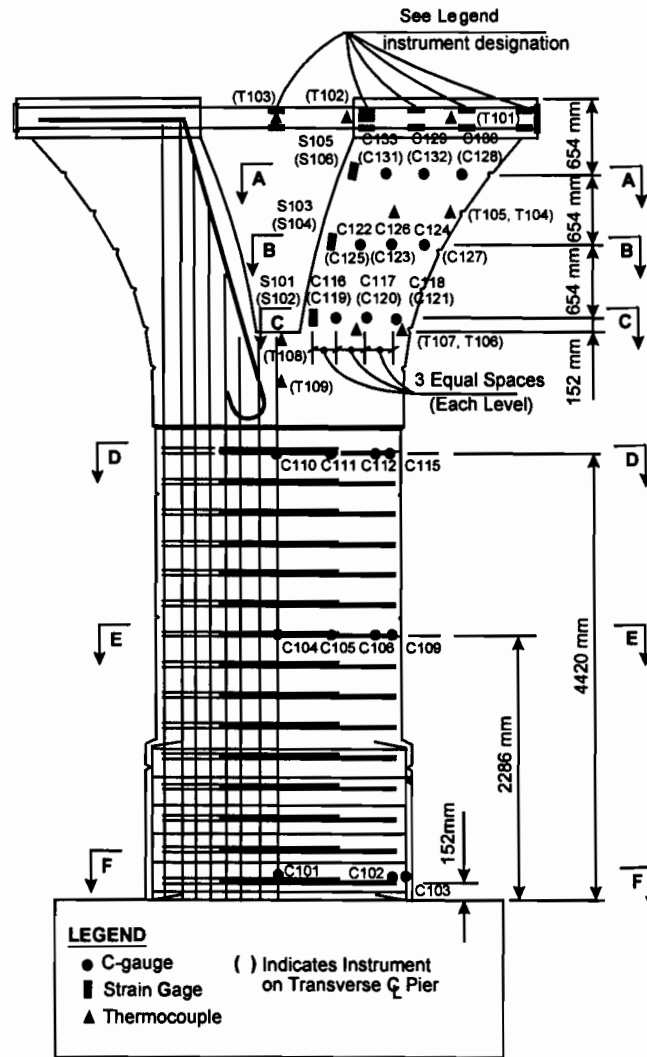


**Figure 3.1** *Strain Gauge and Concrete Strain Device Layout: Elevation View.*

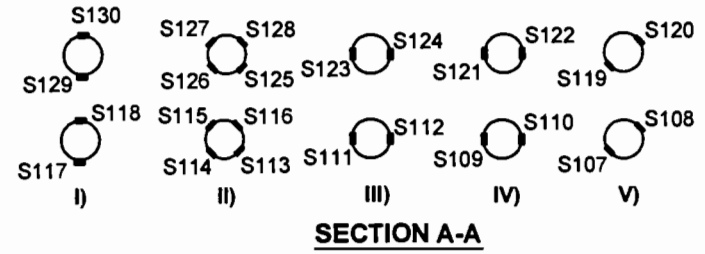
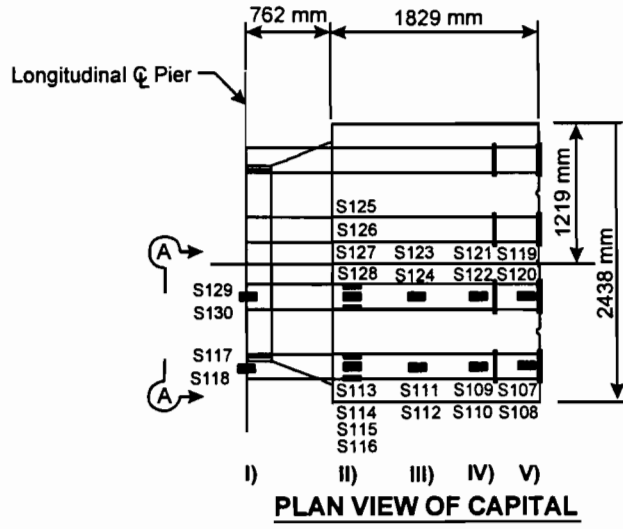


Figure 3.2 Strain Gauge Locations: Pipe Assembly.

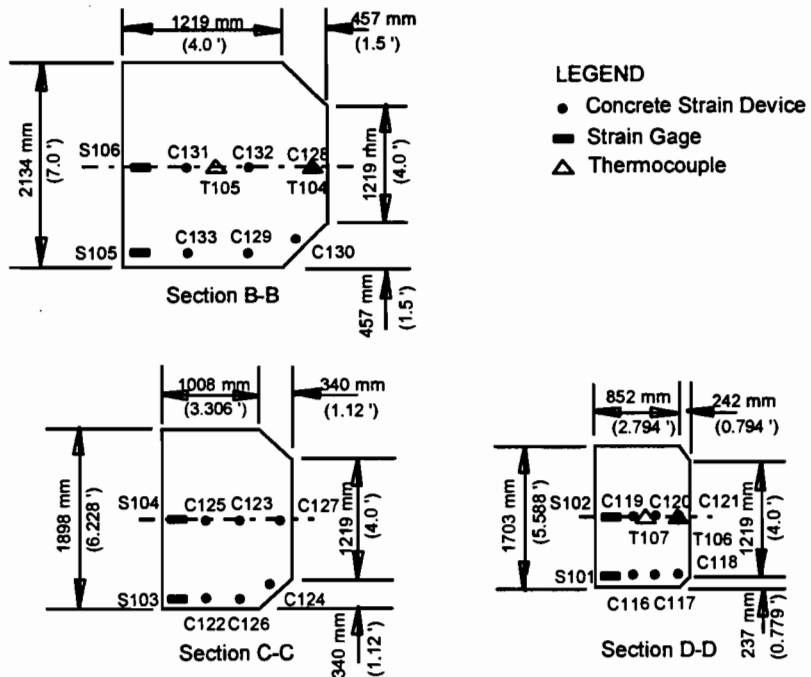
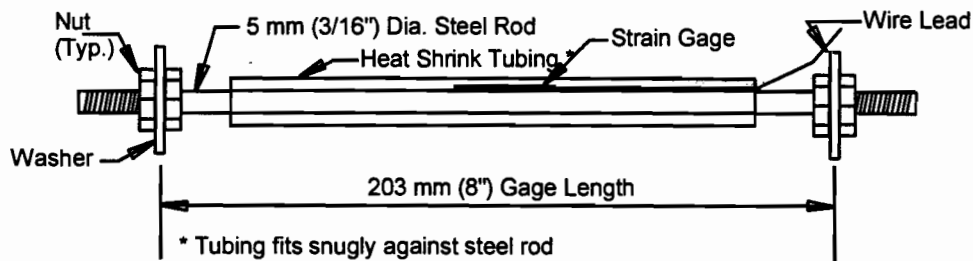


Figure 3.3 - Strain Gauge and Concrete Strain Device Layout: Sections.

### 3.2.4 Steel Strains - Concrete Strain Devices

A concrete strain device was manufactured in the laboratory in order to measure the strain in the concrete. The concrete strain device was selected to minimize the time required to place instruments in the field. Prefabrication of the devices in a controlled environment allowed for greater certainty that the strain gauge would be protected against infiltration by water and against various construction procedures that are detrimental to the gauges. A concrete strain measuring device was developed for this instrumentation project based on the modified Mustran Cell [39] and on research performed by Stone [40]. The concrete strain measuring device developed is shown in Figure 3.4. A washer and two nuts were placed at each end of the rod to insure strain compatibility and to minimize the inclusion effect. A series of tests were performed to verify performance. The shortest gauge length producing acceptable strain measurements was selected. Generally, excellent agreement was found between the concrete strain meters embedded in axially compressed concrete prisms and external strains measured on the face of the prisms with a mechanical extensometer[2].



**Figure 3.4 - Concrete Strain Device.**

For placement in the field, the devices were secured between two pieces of welded wire fabric for placement in the reinforcing cage. The wire cage allowed for ease of placement and greater options for placement. It also served to protect the instrument from the vibrator during casting and from adjustments to the reinforcing cage prior to concrete placement. Electrical wires were routed up reinforcing steel to the top of the pier. The locations for concrete strain devices are shown in Figures 3.1, 3.3, and 3.5. Concrete strain devices are labeled with the designation "C".

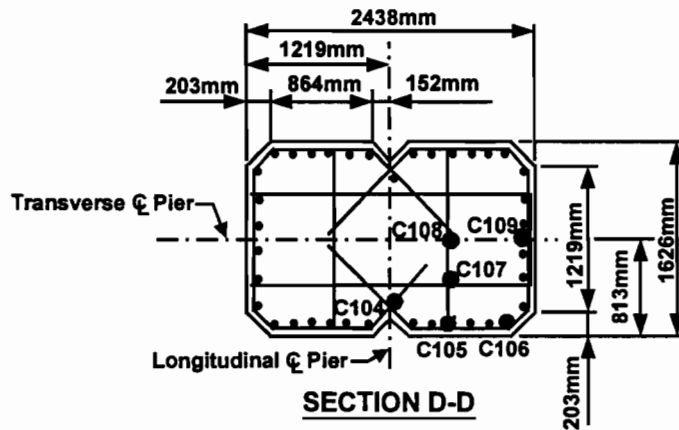
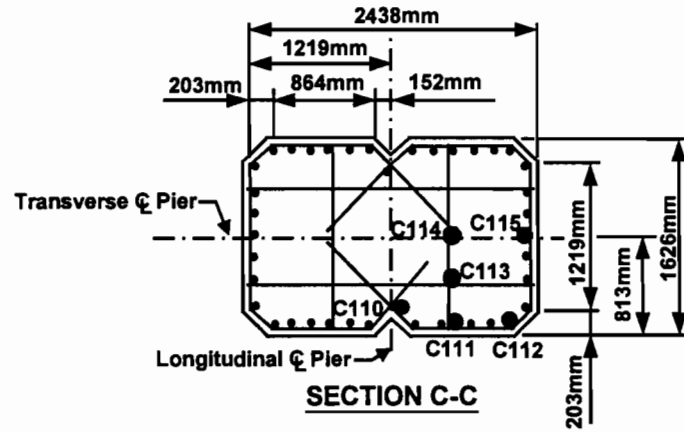
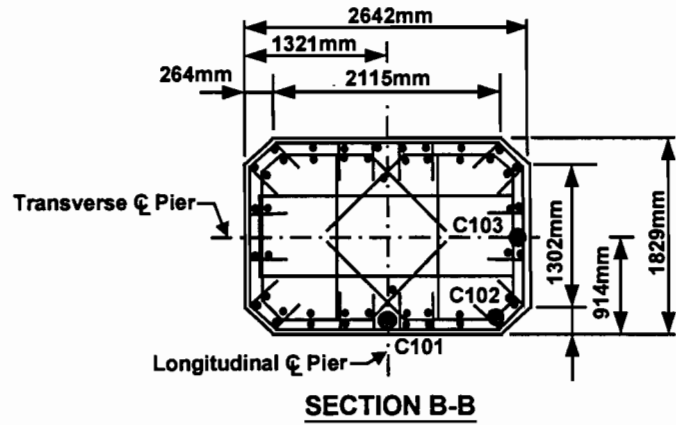
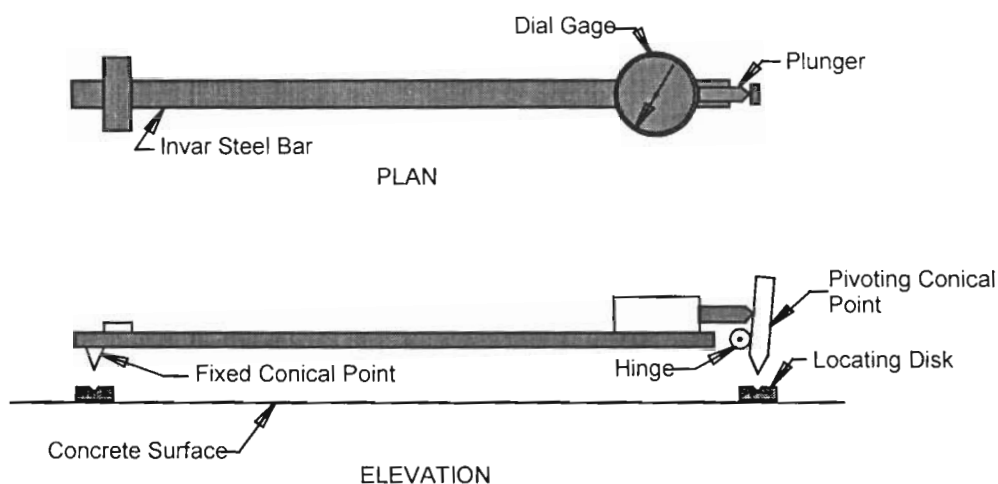


Figure 3.5 - Concrete Strain Device Locations in Shaft.

### 3.2.5 Concrete Strains - Demec Extensometer

A mechanical device known as a Demec extensometer was used to verify strain readings obtained from the embedded electronic devices in the calibration experiments and in field applications where instantaneous loads were applied to the structure. The Demec extensometer, as depicted in Figure 3.6, is a mechanical device which consists of an invar bar with conical locating discs at each end. An in-depth description of this measuring system can be found in Arréllaga [39].



**Figure 3.6** *Demec Extensometer*

The Demec extensometer is best used to measure strains due to instantaneous load. This is due to the fact that temperature effects cannot be accounted for through use of this device. The two metal locating discs are mounted on the surface of the test specimen. The modified installation method recommended by Arréllaga [39] was used as shown in Figure 3.7. An aluminum template was manufactured to insure proper spacing of the drilled holes for placement in the field.

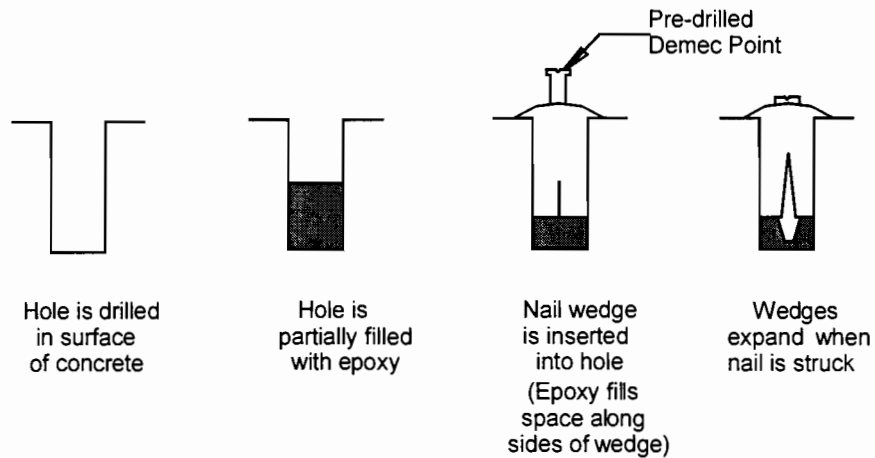


***Figure 3.7 - Demec Point Installation.***

The layout of the Demec points used on the studied pier is shown in Figures 3.8, Figure 3.9, and Figure 3.10. The points were placed at locations that corresponded to the elevations of the electronic strain measuring devices. The original Demec points placed at the lowest elevation on the pier had to be relocated to a higher elevation due to the grade at the base of the pier. Demec points are labeled with the designation “D.”

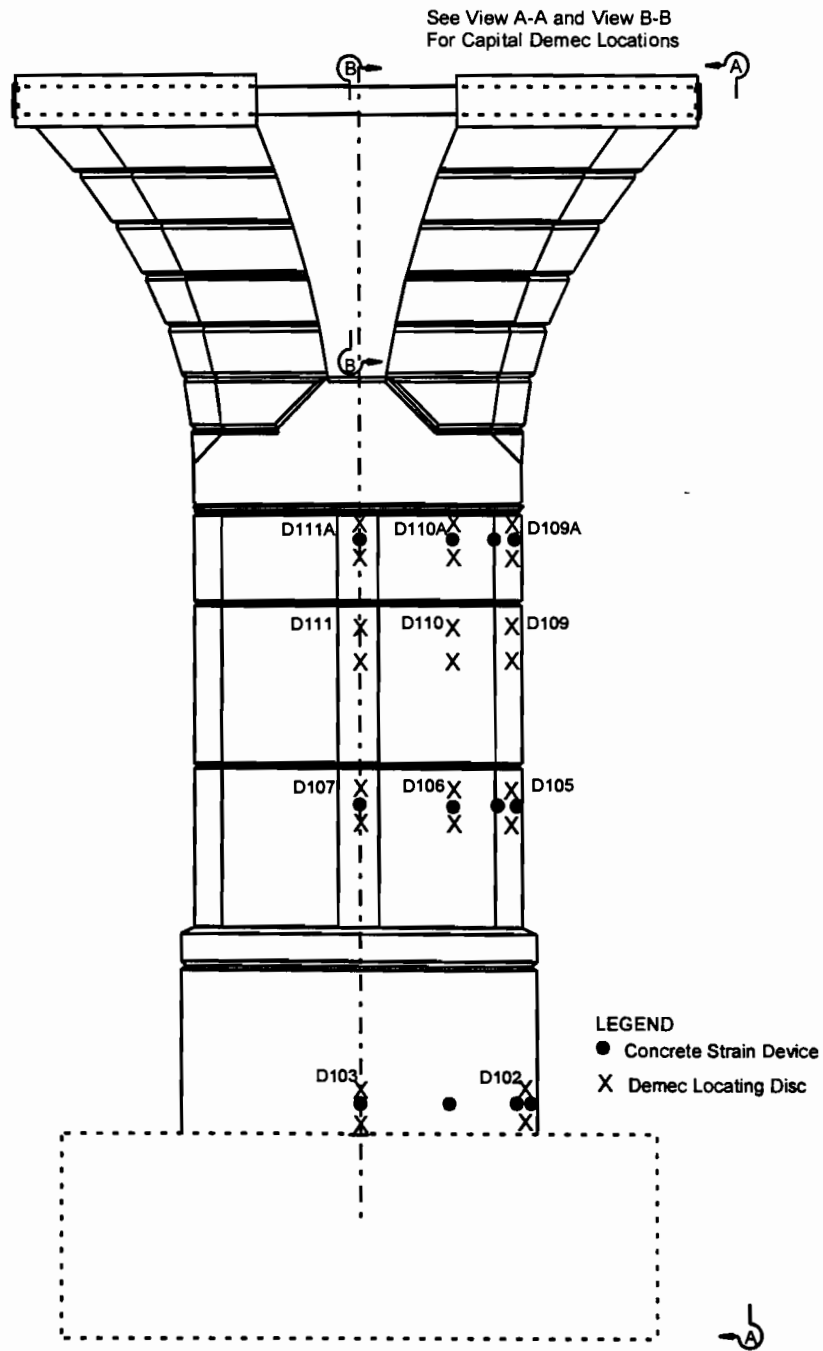


**Figure 3.8 - Demec point locations on shaft.**

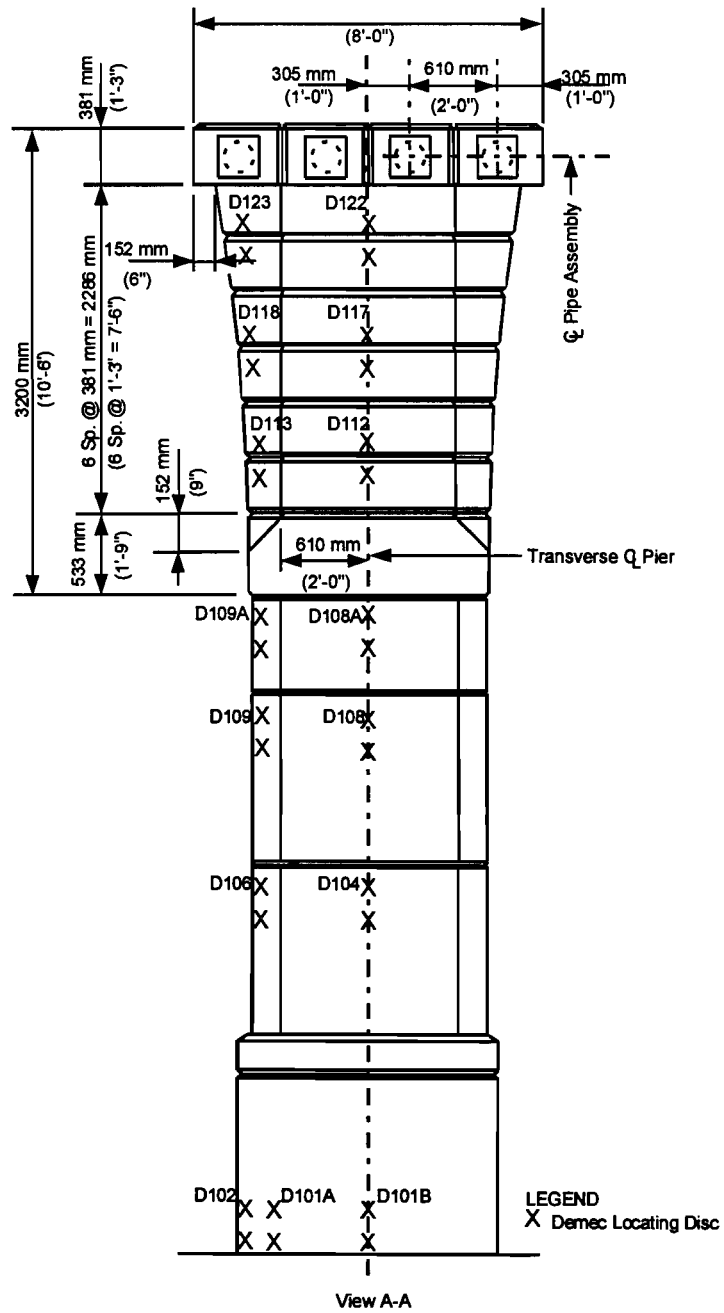
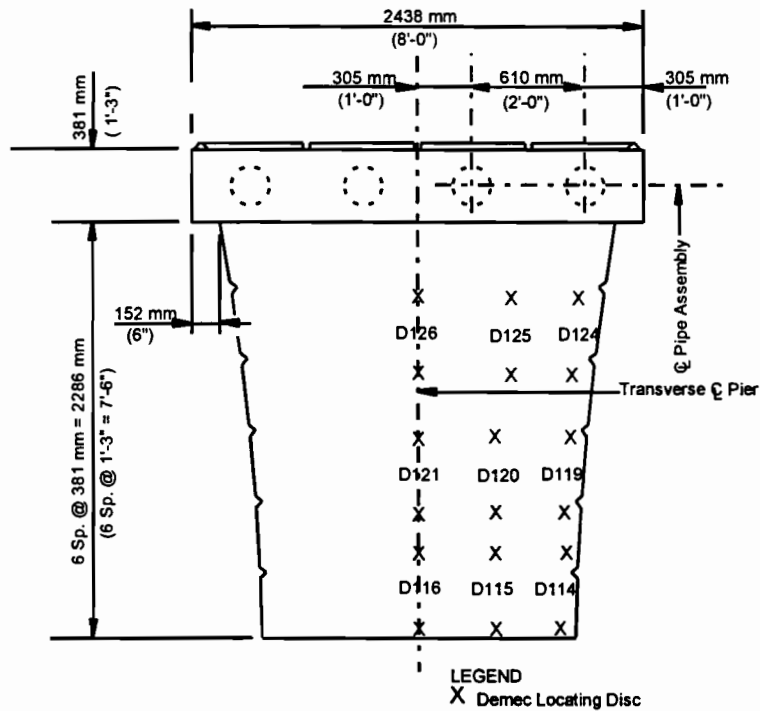


**Figure 3.9 - Demec Point Locations on Side of Shaft and Capital.**



View B-B

Figure 3.10 - Demec Point Locations on Inside Face of Capital.

### 3.2.6 Temperature Gradient - Thermocouples

The thermal characteristics of the pier were of particular concern in this study. The effects of thermal gradients across the structural steel tension ties and in the concrete were investigated. Type T thermocouples were used to measure temperatures on the steel pipes and in the concrete of the pier. Type T thermocouples are made of copper and constantan and are the most common type used for embedment in concrete [39] due to the fact that both of these materials only mildly oxidize in concrete. The thermocouples were placed on the steel pipe as well as inside the concrete as shown in Figure 3.11. Thermocouples were labeled with the designation "T."

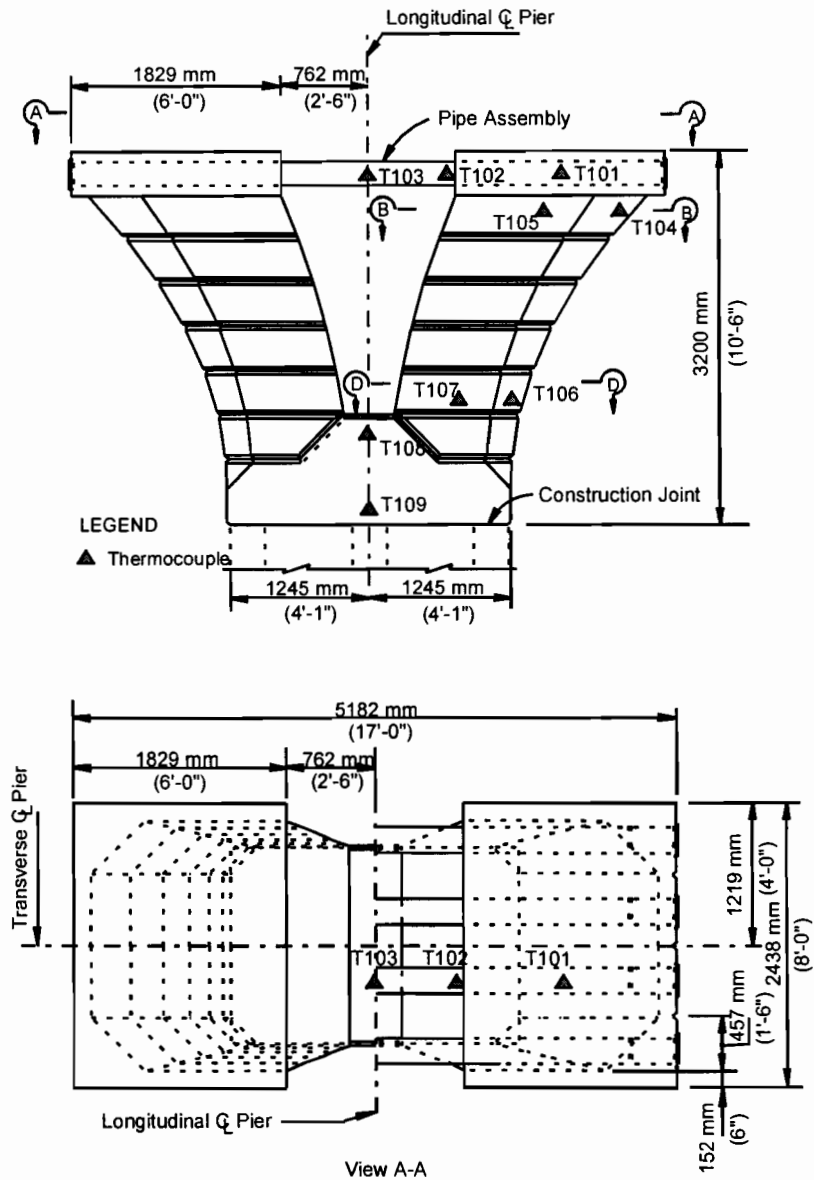


**Figure 3.11 - Thermocouple locations.**

### **3.2.7 Deformation of the “Y” - Linear Potentiometers and Thermocouples**

Measurement of the deformation of the “Y” under loading was done using linear potentiometers mounted on steel angles placed in the inner portion of the “Y.” The set-up for these measurements is shown in Figure 3.12. Deformation was measured at the face of each side of the pier. Thermocouples were used to measure the temperature gradient along the steel angles so that any temperature effects could be taken into account. Three thermocouples were placed on each angle as shown in Figure 3.12.

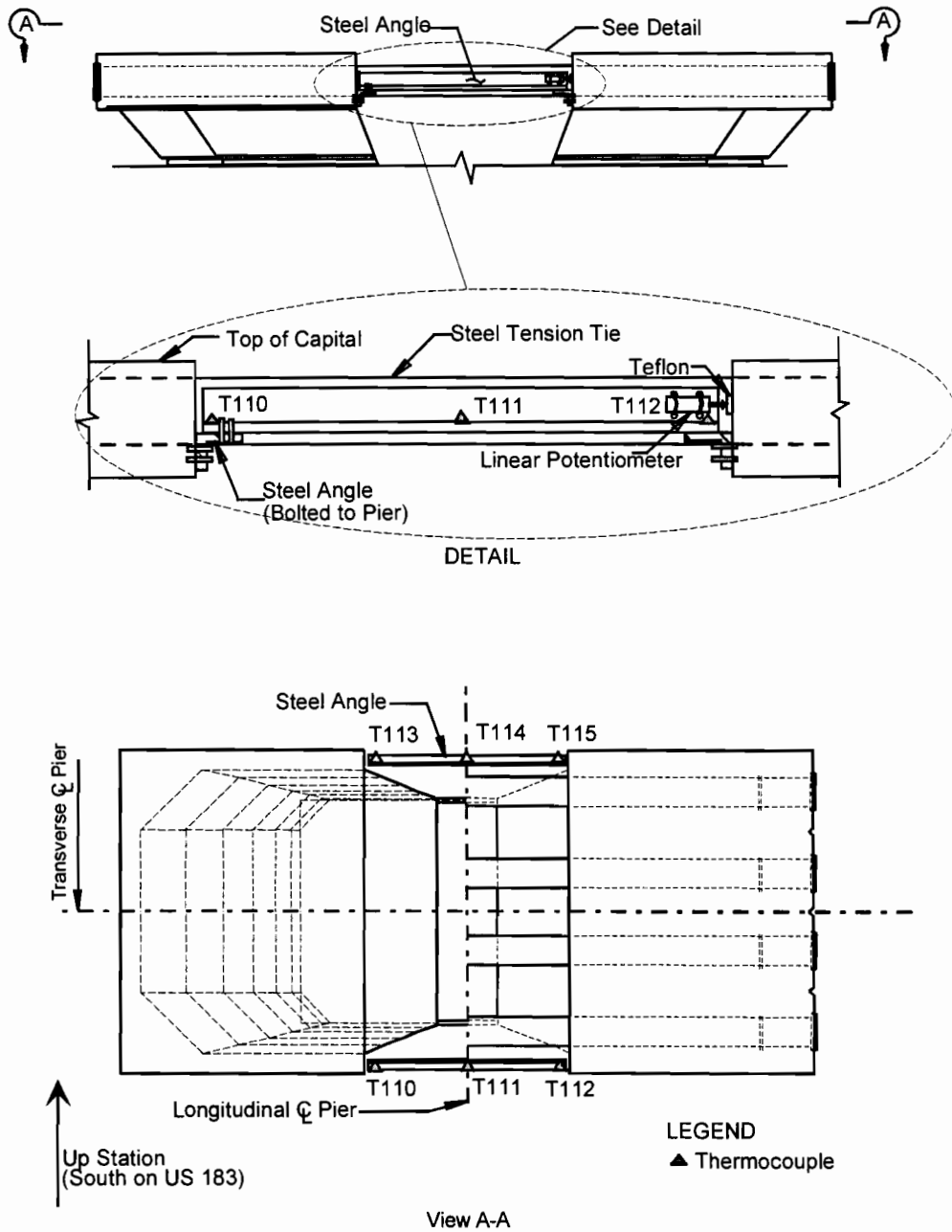


**Figure 3.12 - Set-up to Read Deformation in the "Y."**

### ***3.2.8 Data Acquisition System***

A data acquisition system was used to record measurements from the electronic instruments. The selection of this acquisition system was made based on studies by Arrélega [39]. The Campbell Scientific 21X Datalogger was used in conjunction with the Campbell Scientific AM416 Multiplexers to temporarily store data. Roberts [19] reported good performance of this system for the San Antonio “Y” project.

The wires from the electronic instruments were routed adjacent to a centrally located reinforcing bar and out the top of the pier. All measurements taken prior to the superstructure erection were taken using a temporary data acquisition system located at the bottom of the “Y.”

Once span D5 was erected, the wires were routed into the superstructure at the adjacent live end of the span and connected to a permanent acquisition unit which was mounted on the interior face of the box girder web.

## **3.3 Segmental Pier Instrumentation**

### ***3.3.1 Instrumentation Objectives***

The US 183 project provided an unusual opportunity to conduct research on a precast, segmentally constructed, hollow box, concrete bridge pier. The main objectives of the instrumentation of a segmental pier were as follows:

1. Measure the sunlight-induced temperatures across the hollow-box cross section.
2. Measure the corresponding strain changes due to the temperature gradients.
3. Determine the flow of forces from the post-tensioning of the pier.
4. Measure the strain changes in the pier during balanced-cantilever superstructure erection. (However, due to construction difficulties, the subsequent erection was done using two cranes and no unbalanced segments.)

### ***3.3.2 Pier Selection***

The only part of the US 183 project using the large ramp pier was ramp “P”, a high flyover ramp to be built using the balanced-cantilever method of construction. The highlight of the ramp was a 5-span unit with spans of 38.1m - 54.9m - 43.3m - 54.9m - 38.1m. As shown in Figure 3.13, pier P15 was located between a 54.9 meter span and the center 43.3 meter span, and was originally selected for instrumentation in order to track the most critical construction loads. However, pier P15 was not the optimal choice for temperature gradient effects because of its location between the north- and south-bound viaducts of the US 183 mainlanes; the new bridges would prevent most of the sunlight from striking the pier.

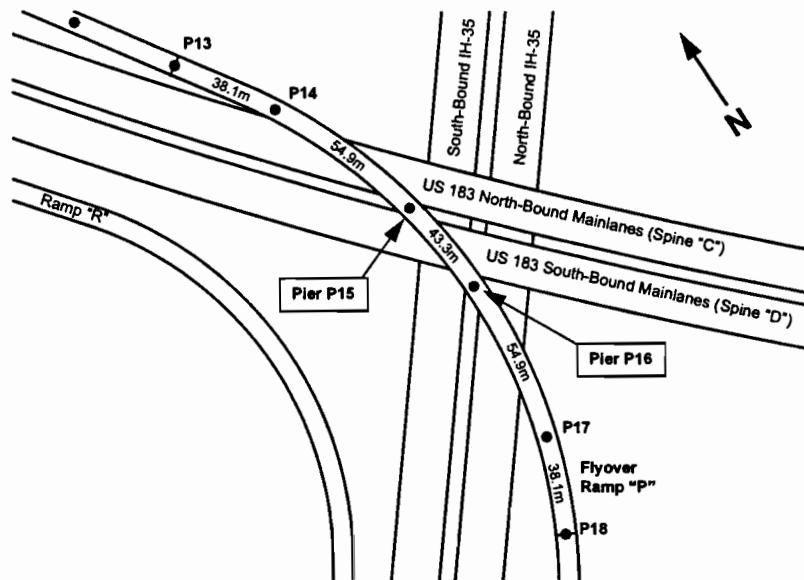


**Figure 3.13** *Bridge layout in the US 183 and IH-35 interchange area.*

Selection of the pier to be instrumented therefore involved a compromise between a location best for construction stresses and a location ideal for temperature gradients. Pier P16 was selected because it satisfied this compromise. It was located between the other 54.9-meter span and the middle 43.3-meter span where high bending moments would be introduced during balanced-cantilever erection of the ramp superstructure. It was situated just south of the south-bound US 183 mainlane viaduct, where sunlight could strike most of the length of the pier unhindered, providing the maximum possible temperature gradients. Thermocouples were placed in all three shaft sections and the capital. However, only the middle section located in segment PC16-5 has a sufficient distribution of thermocouples to measure temperature gradients across the pier section. This placement was the most practicable for assessing the maximum possible temperature gradient. A lower section would have had sunlight blocked by the IH-35 overpasses nearby; a higher section would have had sunlight blocked by the balanced-cantilever ramp superstructure. Figure 3.14 illustrates the sections of the pier that were instrumented and their relative positions to other structures nearby.

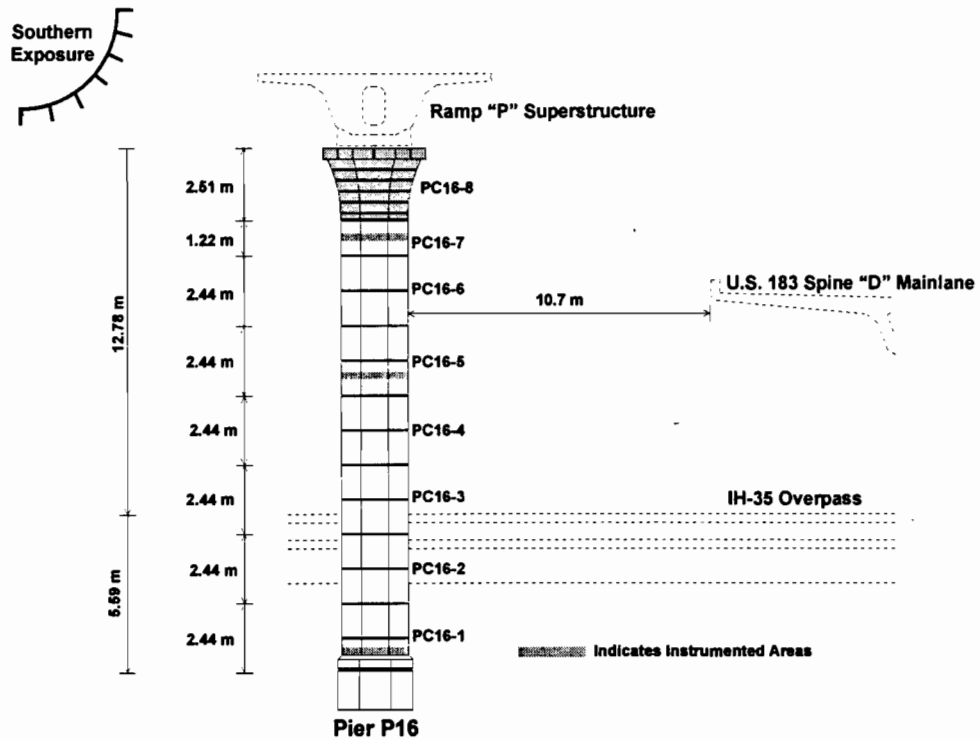


**Figure 3.14** Instrumented areas of pier P16 relative to surrounding structures' locations.

### 3.3.3 Pier Shaft

In areas where the concrete was not expected to crack, such as in the column or compression struts, strains were measured using the prefabricated concrete strain gauge described in Section 3.2.4. Concrete strain gauges were placed in the base segment PC16-1 in the configuration shown in Figure 3.15. The set of gauges was located just above the upper edge of the cast-in-place concrete base. In the “gradient” segment PC16-5, concrete gauge locations resembled those of the base segment, as shown in Figure 3.16. However, to reduce the number of gauges in this area, and due to their somewhat redundant nature, the off-axis gauges were omitted. The locations of instruments in the “top” segment PC16-7 were identical to those in the base segment PC16-1. Concrete gauge locations are shown in Figure 3.17.

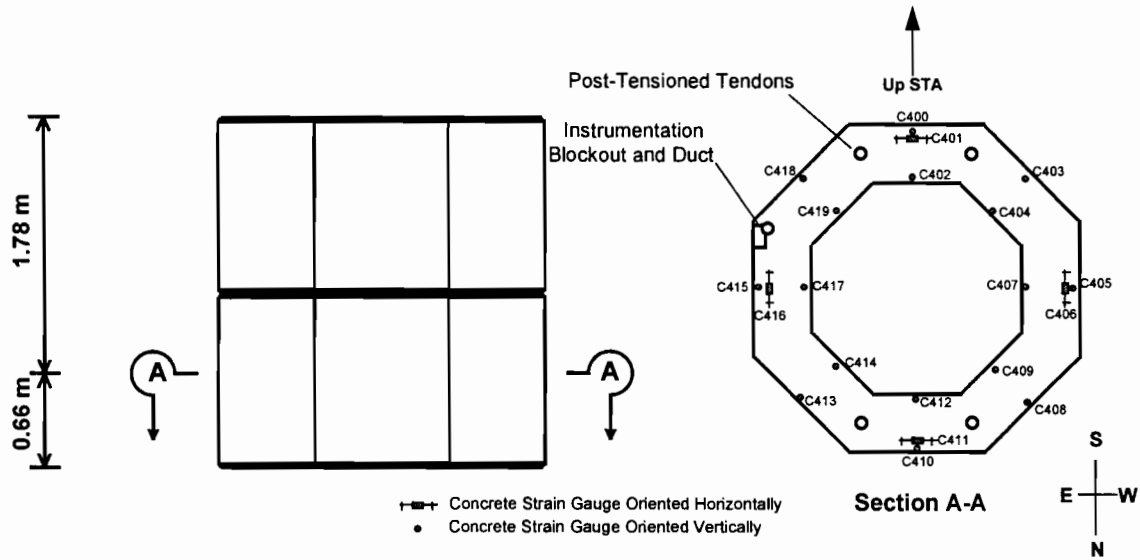


Figure 3.15 Concrete gauge locations in base segment PC16-1.

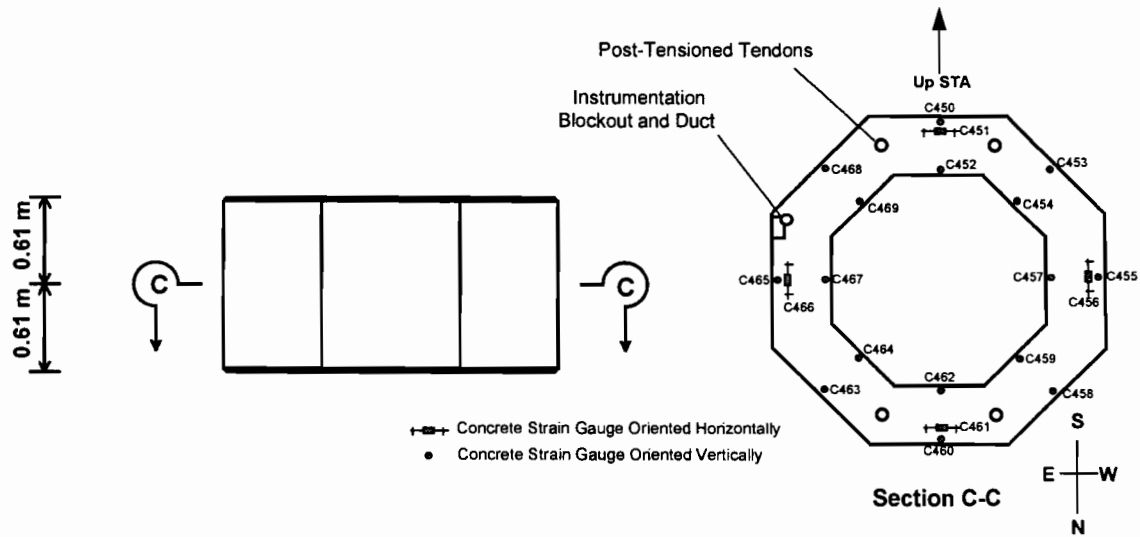


Figure 3.16 Concrete gauge locations in "top" segment PC16-7.

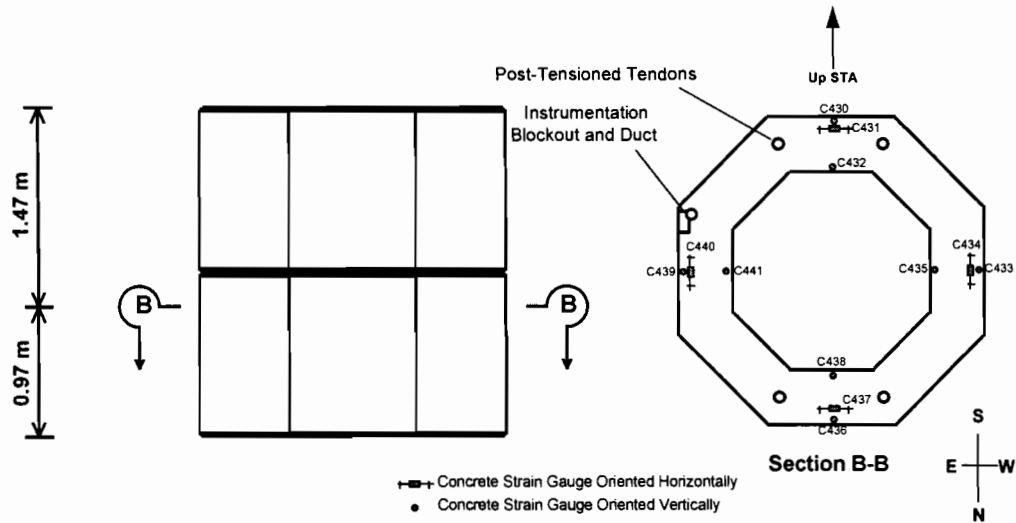


Figure 3.17 Concrete strain gauge positions, “gradient” segment PC16-5.

### 3.3.4 Pier Shaft

Thermocouples were numbered similarly to the concrete gauges. Thermocouples T400 through T407 were located in the base segment PC16-1 as shown in Figure 3.18. The fully shaded location of this instrument set was not conducive to measuring maximum temperature gradients. The thermocouples were placed such that they were always at least one inch from any rebar’s surface.

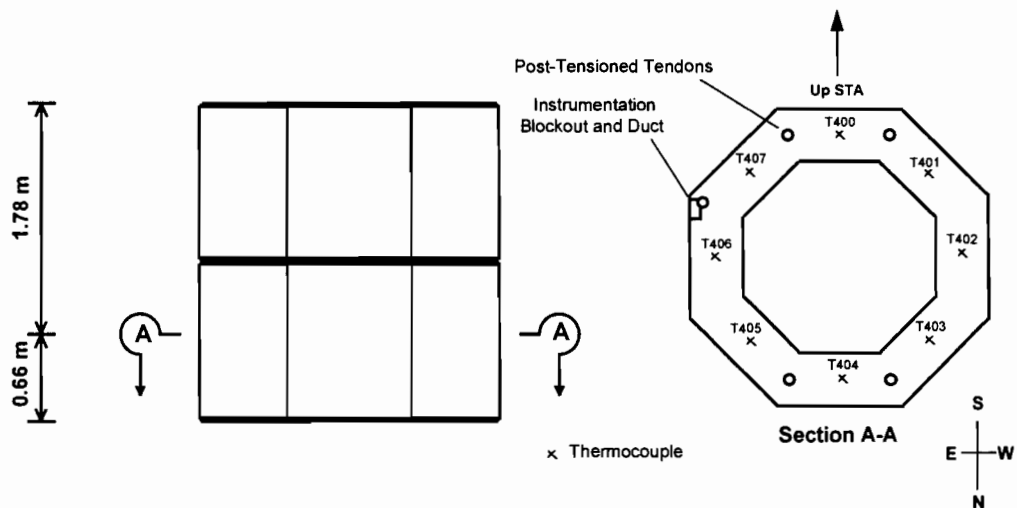
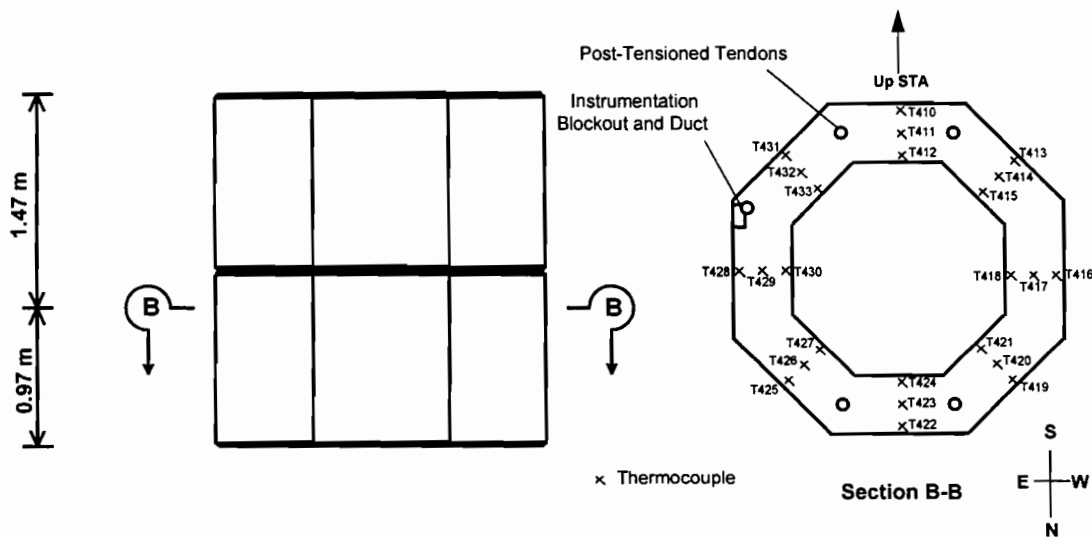


Figure 3.18 Thermocouple locations in base segment PC16-1.

The instrument cluster in segment PC16-5 was specifically positioned to measure the maximum possible temperature gradients occurring in the pier. For this reason, a section was chosen located at an elevation midway between the elevation of the top edge of the barrier wall on the IH-35 overpasses and the elevation of the bottom of the capital segment (see Figure 3.14). This location assured unobstructed sunlight at the level of the full gradient thermocouple set.

As shown in Figure 3.19, three thermocouples were installed on every side of the octagonal pier cross-section. The outer gauges were located at a cover of one inch, about the closest to the surface of the concrete as was thought possible and safe. The next ring of thermocouples was located at the middle of the 406mm thickness of the pier walls. The locations correspond with those thermocouples located in segment PC16-1 and PC16-7. Finally the inner ring was located again at a cover of 25mm from the inside faces of the pier walls.



**Figure 3.19** Thermocouple locations in the “gradient” segment PC16-5.

Like the concrete gauges, thermocouple placement in the “top” segment PC16-7 was identical to the base segment. However, this instrument section was located in an exposure to full sunlight. Figure 3.20 shows the locations of the thermocouples.

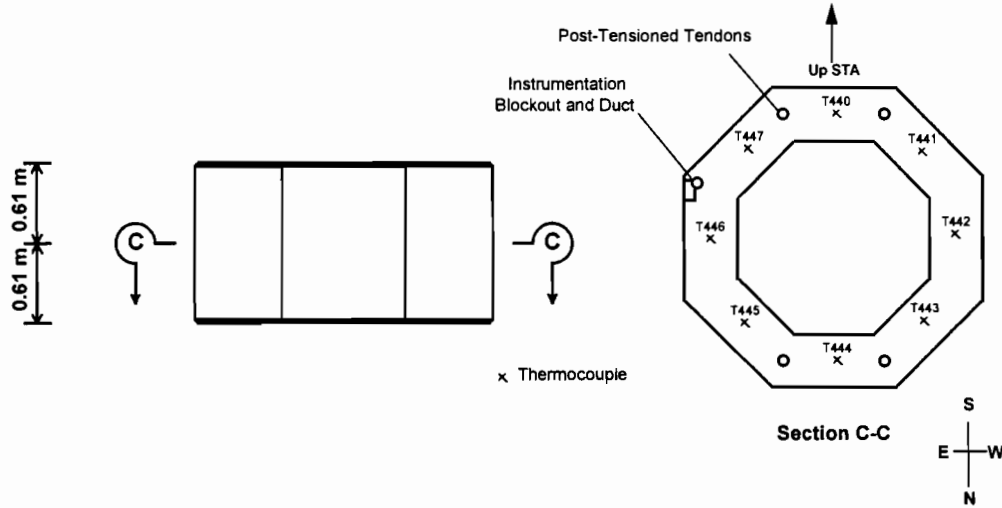


**Figure 3.20** Thermocouple locations in “top” segment PC16-7.

### 3.3.5 Capital PC16-8 Instrumentation plans

The capital segment PC16-8 serves as an anchorage zone for this post-tensioned segmental pier. In addition to its primary function, the capital also provides anchorage for post-tensioned “tie-down” bars used during the balanced-cantilever construction of the ramp superstructure. These bars were designed to provide the clamping force required to maintain a full moment connection between the superstructure and the pier during cantilevering (see Figure 3.21). Unfortunately, at the time of superstructure erection, the contractor did not have the proper jacking equipment to fully stress all of these bars. Thus only partial fixity was achieved and erection cranes were used to provide temporary support for the cantilevers on this set of spans. Much of the copious instrumentation provided thus proved superfluous since the loading conditions were both unknown and substantially less than the design conditions.

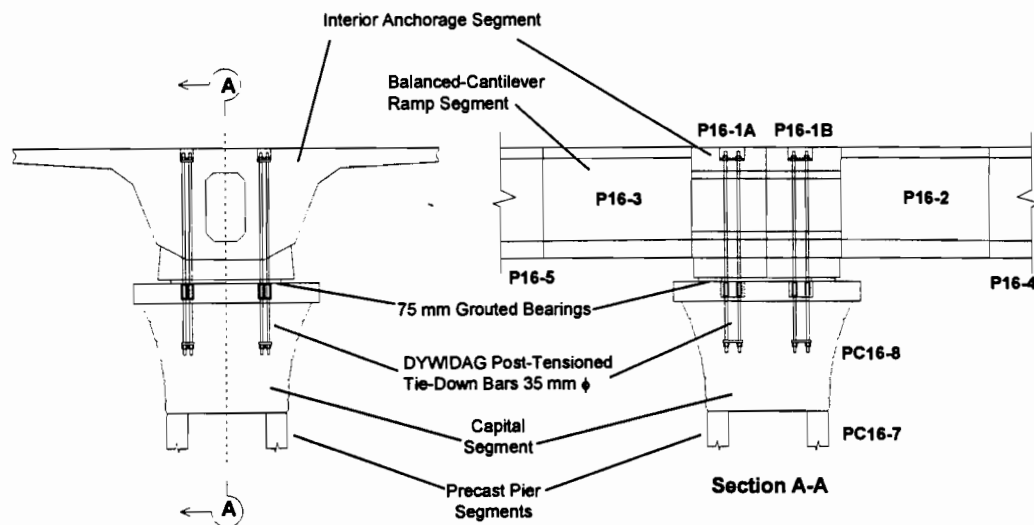
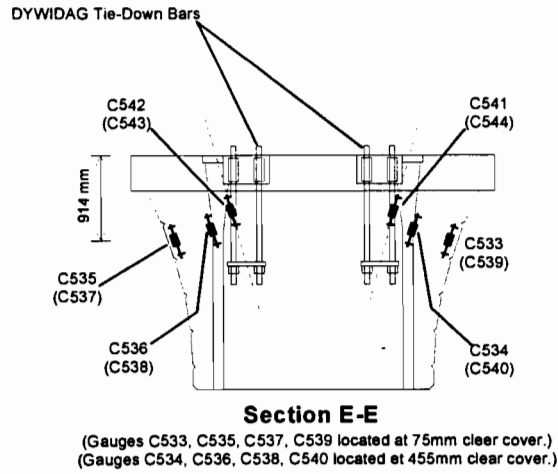


**Figure 3.21** *Fixed moment connection during superstructure erection as designed to be achieved with DYWIDAG post-tensioned bars.*

Extremely high construction loads could have been generated in the capital by the unbalanced erection process, and the strain distributions during this loading would probably not be linear. Thus, the capital seemed to provide an ideal opportunity for the use of strut-and-tie modeling to predict the flow of forces.

### **3.3.6 Capital PC16-8 Concrete Strain Gauges**

Concrete gauges were placed in the capital as shown in Figures 3.22 through 3.25). Gauges C533 through C544 were primarily located in areas where compression struts between anchor plates were predicted to form. C541 through C544 were placed such that their longitudinal axes coincided with the predicted compression struts' axes between the tie-down bar anchor plates and the anchor plates of the pier post-tensioning tendons.



Concrete Strain Gauge  
 (Oriented Along Compressive Struts)

Note: Gauges denoted by ( )  
 located "behind" gauges shown.

**Figure 3.22** Elevation view of concrete strain gauges in top half of capital segment.

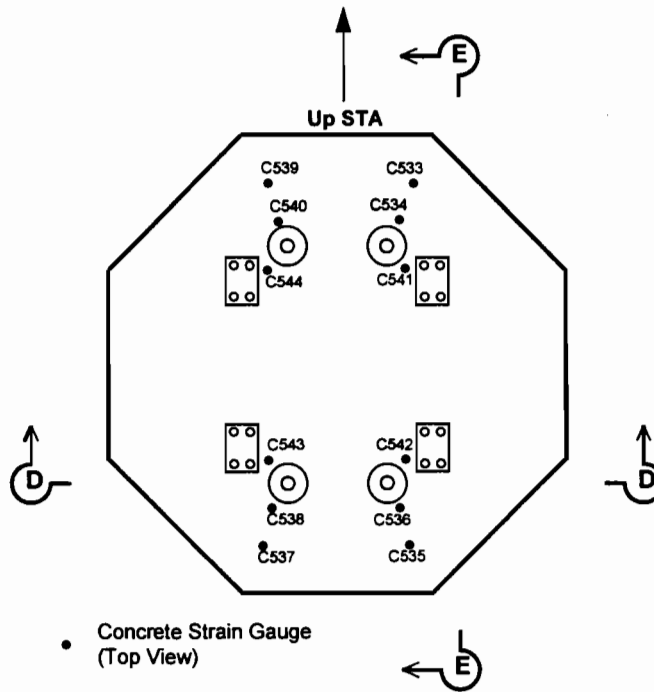
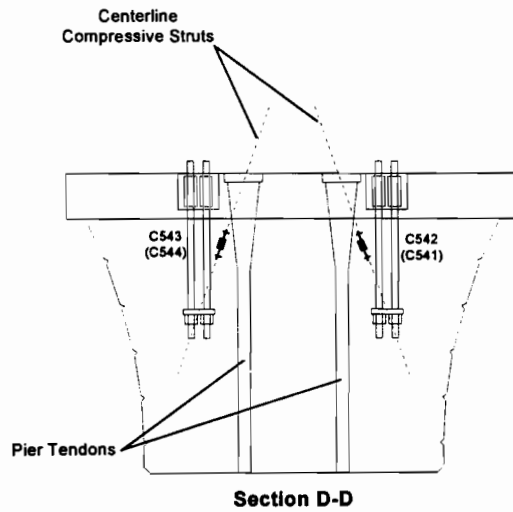


**Figure 3.23** Plan view of concrete strain gauges located in top half of capital segment.



- Concrete Strain Gauge  
 (Oriented Along Compressive Struts)
- Notes:**  
 Gauges denoted by ( ) located "behind" gauges shown.  
 Gauges C533-C540 omitted for clarity.

**Figure 3.24** Concrete strain gauge placement in compression strut between tie-down anchor plates and tendon anchorages.

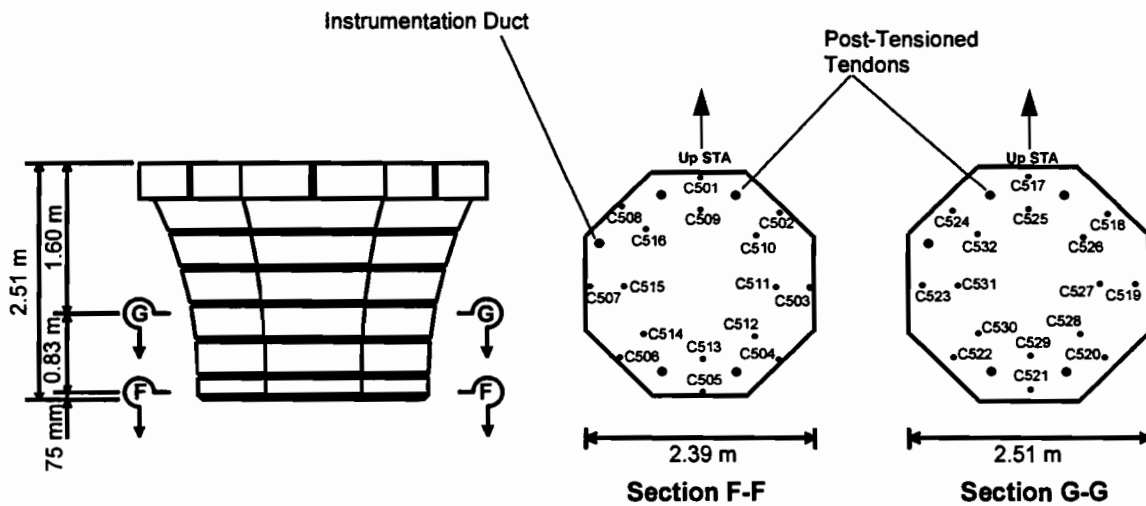


**Figure 3.25** Two layers of concrete strain gauges located near bottom face of capital segment coinciding with gauge distributions in segment PC16-7.

### 3.3.7 Capital PC16-8 Steel Strain Gauges

Strain gauges located directly on reinforcing steel were installed in the capital to coincide with possible tension ties predicted by strut-and-tie modeling. Steel strain gauges were installed in a section located about 75mm clear cover from the capital's bottom face (see Figure 3.26). The design required tensile steel reinforcement across the bottom face of the segment. Gauges S509 through S516 were attached to these tensile ties to determine their contribution to the flow of forces through the pier. Gauges S501 through S508 were also placed along the perimeter steel at this section. These gauges were intended to measure any hoop stresses present at the interface between the monolithic capital and the hollow, octagonal segment PC16-7 located just below it.

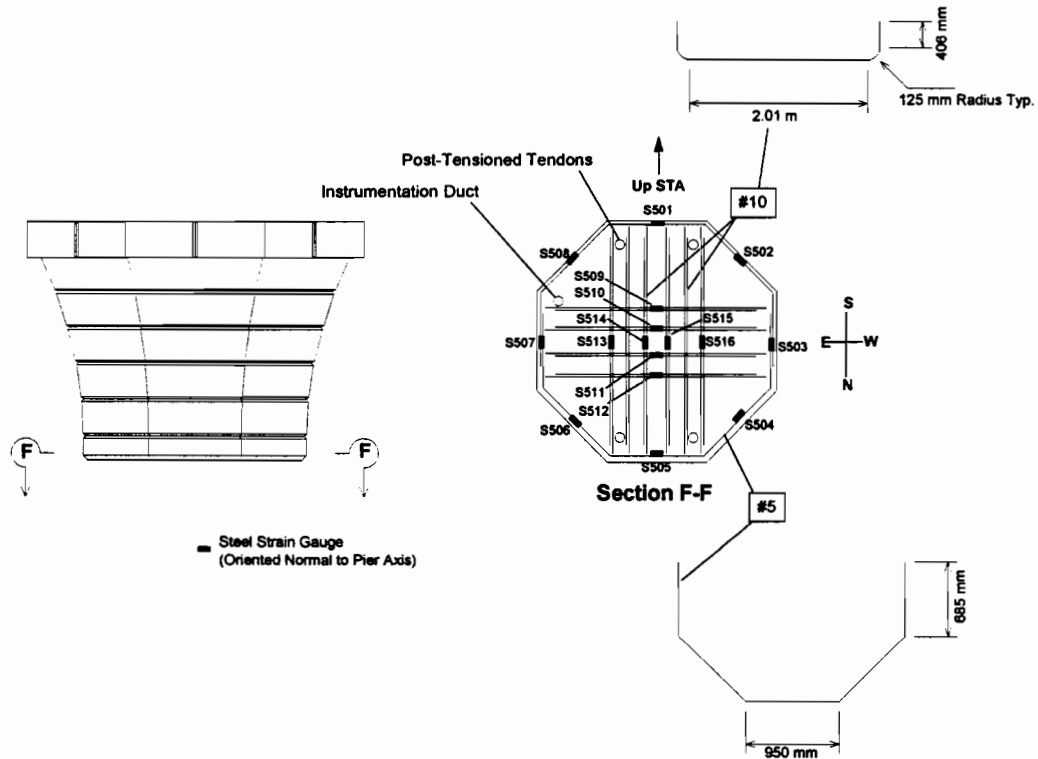


**Figure 3.26** Location of steel strain gauges near the capital face.

Steel gauges were also installed at tensile tie locations at the top face of the capital. Gauges S541 through S552 were located on the large #11 rebars running the full width of the capital at that section. These gauges would become critical during pier post-tensioning operations because tensile forces would likely develop between the tendon anchorages. Figure 3.27 illustrates the gauge locations.

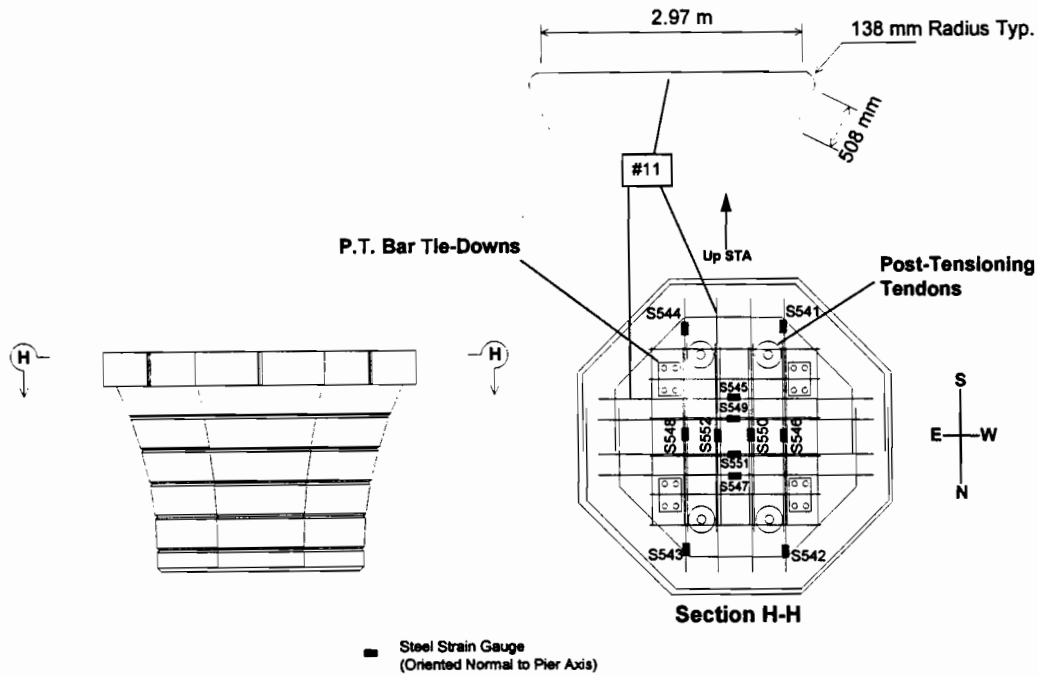


**Figure 3.27** Locations of steel strain gauges near the top face of the capital.

Finally, steel strain gauges were installed on the DYWIDAG post-tensioned tied down bars anchored in the capital. Figure 3.28 illustrates the configuration of the bars and gauges. The capital anchors four groups of four bars arranged so as to run from the capital to the top of the ramp superstructure as shown in Figure 3.21. Each of the DYWIDAG bars was instrumented with one gauge to measure the distribution of forces between the bars. In addition, one bar out of each four bar group had two more gauges added. Thus, four of the sixteen bars had three gauges distributed along them in order to measure the distribution of force along the bars and to determine how effectively the bars were anchored in the concrete.

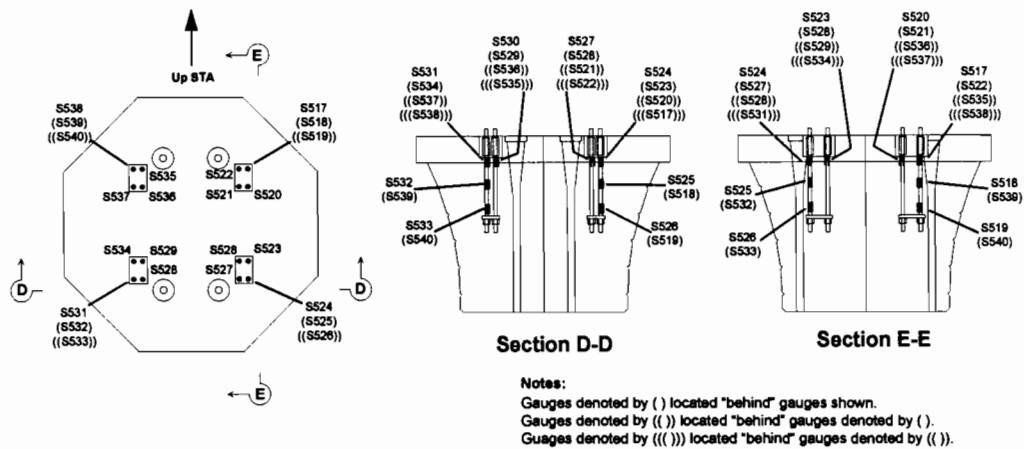


**Figure 3.28** Locations of strain gauges attached to DYWIDAG post-tensioned tie-downs.

### 3.3.8 Capital PC16-8 Thermocouples

The locations of thermocouples T501 through T572 were distributed throughout the capital segment. Two layers for measuring temperature gradients in the monolithic segment were located at sections 75mm and 915mm from the bottom face (see Figure 3.29). These gauges would measure a temperature gradient shape that would probably differ from that of the hollow cross-section of segment PC16-5.

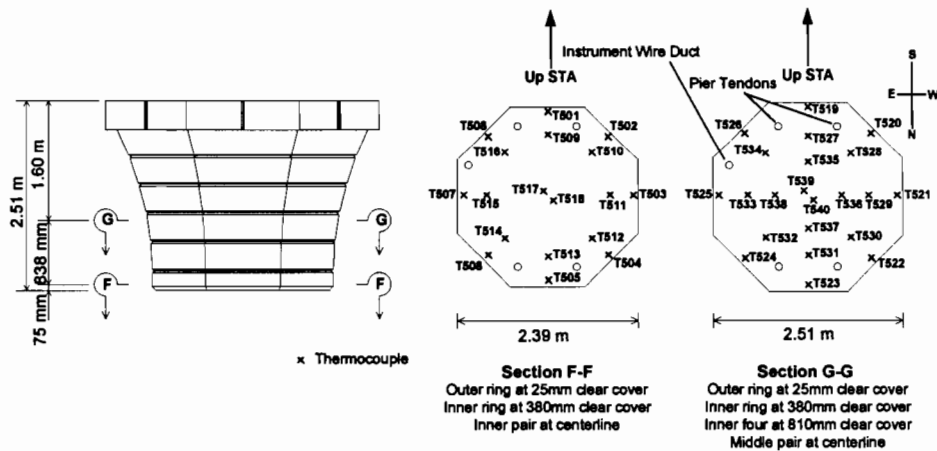


**Figure 3.29** Temperature gradient thermocouples located near base of capital segment.

Thermocouples were also installed to measure gradients in two sections near the top face of the capital. Figure 3.30 shows the distribution of gauges in sections 50 mm and 330 mm below the top face. Together these two sections would provide readings for horizontal temperature gradients as well as gradients oriented vertically through the capital. This information on vertical gradients was augmented by the placement of several thermocouples in various locations coinciding with the compression struts discussed previously. Figure 3.31 shows the locations of these gauges.

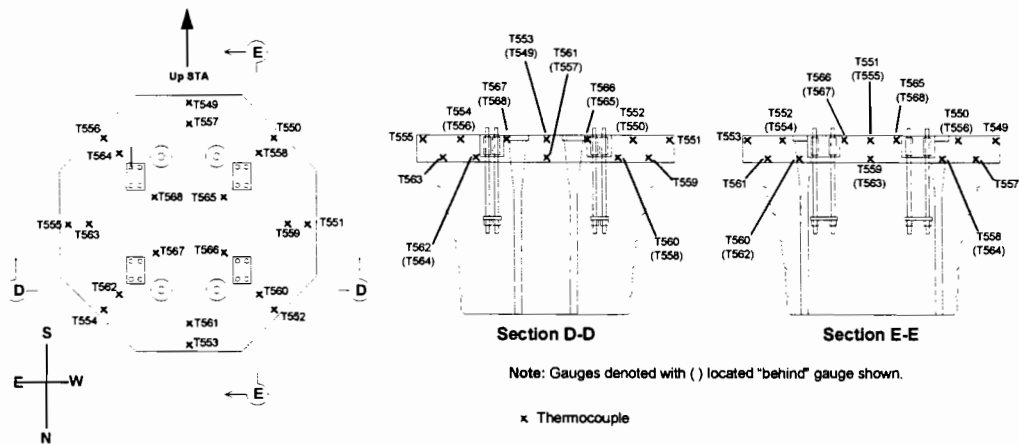


**Figure 3.30** Thermocouples located near top face of capital segment.

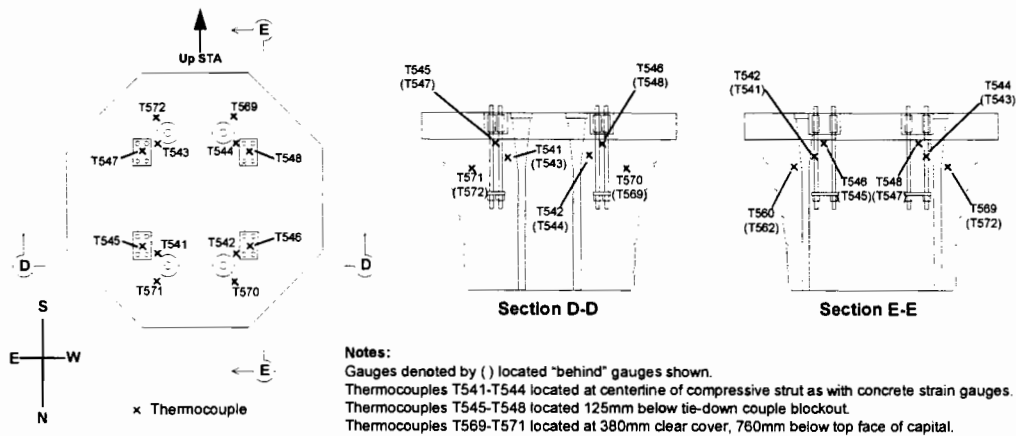


**Figure 3.31** Thermocouples placed in compression strut areas.

The distribution of thermocouples throughout the capital segment allowed a comprehensive measurement of thermal distributions during curing. Large, monolithic capitals previously cast during the course of the bridge construction had undergone curing temperature differentials large enough to cause some superficial cracking. In addition, the thermocouples in the capital could provide more information concerning sunlight-induced temperature gradients on solid concrete elements.

### ***3.3.9 Segmental pier Data Acquisition System***

All gauges in the pier were connected by means of the 100mm diameter instrument wire conduit to an instrument box located at the top of the pier. Positioning the data recorders at the top of the pier facilitated their future installation inside the ramp superstructure.

The data recorders used for the long-term data collection on this project were two Campbell 21X Data Loggers. Connected to each 21X unit were several Campbell AM416 Multiplexers. The memory capacity of the 21X units reading gauges on the hour required researchers to download data from them to an Intel 386 based laptop computer once every five days.

The Campbell equipment was compact and reliable. With a 12 volt marine battery to supply power, the 21X units could be left to run continuously at the top of the pier. Researchers did not need to access the top of pier P16 to download data: serial cables for data transfer and a power cable for battery charging followed the instrumentation conduit back down to the base of the pier for easy access.



## CHAPTER 4

### *4. US 183 CONSTRUCTION AND DATA COLLECTION*

#### **4.1 Introduction**

The purpose of this chapter is to describe the mainlane and segmental pier construction and related superstructure erection. Collection of data throughout these procedures is also discussed.

#### **4.2 Mainlane Pier Construction**

The US 183 Mainlane piers were constructed in two concrete lifts. The first lift consisted of the column portion of the pier, "H" (see Figure 1.5), and is shown in Figure 4.1. Subsequent to the hardening of the column concrete, the capital reinforcing steel was tied, the structural steel tension ties placed, and the concrete cast for the capital. Figure 4.2 shows the capital during construction. A completed typical mainlane pier is shown in Figure 4.3.

The superstructure consisted of a simple span precast concrete segmental box girder system erected by the span-by-span method. The piers were used to support a truss system which in turn supported the superstructure while under construction. In order for the piers to support the steel truss system, a steel "pier bracket" was mounted in the "Y" of the pier. The truss system was supported on the bracket as shown in Figure 4.4. The basic construction procedure is shown schematically in Figure 4.5.

#### **4.3 Mainlane Pier Data Collection**

All instruments were monitored weekly after installation until approximately one month prior to construction of the superstructure. At that time, a temporary data acquisition system was assembled and placed in a ventilated water-resistant box. This system was placed in the "Y" of the pier. Prior to pier bracket placement, this box was moved to the top of the capital and left in place until the segments of span 5 were epoxied and temporarily tensioned together.

The acquisition system was then disconnected for approximately three days while the instrumentation of span 5 was performed. During those three days, all construction activity was stopped. Pier instrument wires were re-routed into the box girder and connected to a permanent acquisition system mounted to the wall of the box girder.

During construction of span 5, all instruments were monitored more frequently during the stressing procedure. The instruments were observed frequently until span 5 was placed on the bearings of pier D6. Subsequent to span 5 placement on pier D6, regular hourly readings were resumed. A data collection summary can be found in Table 4.1.

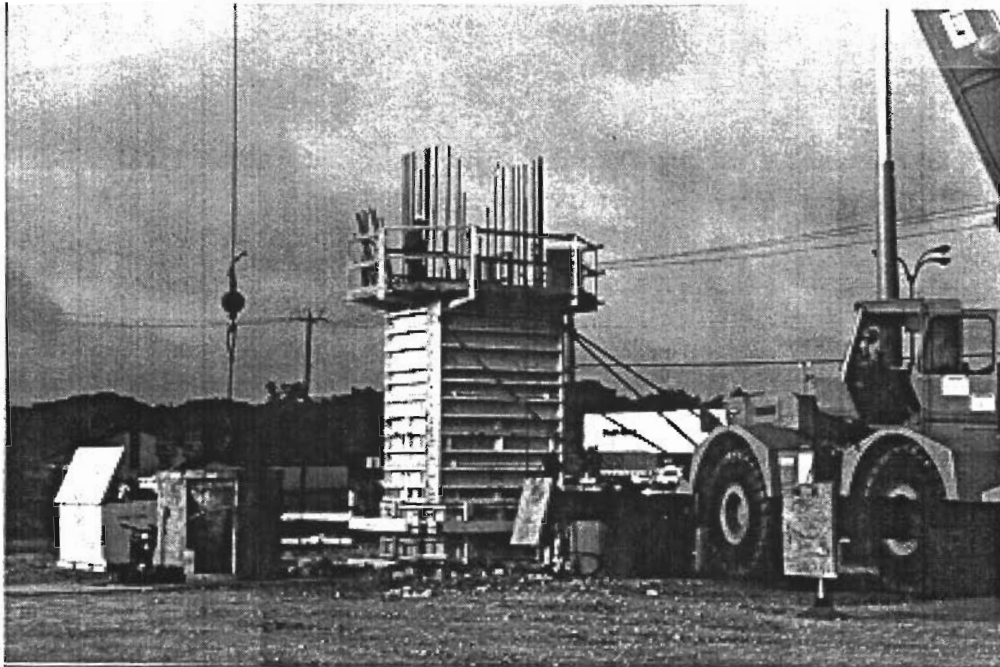


*Figure 4.1 Casting of pier column concrete.*

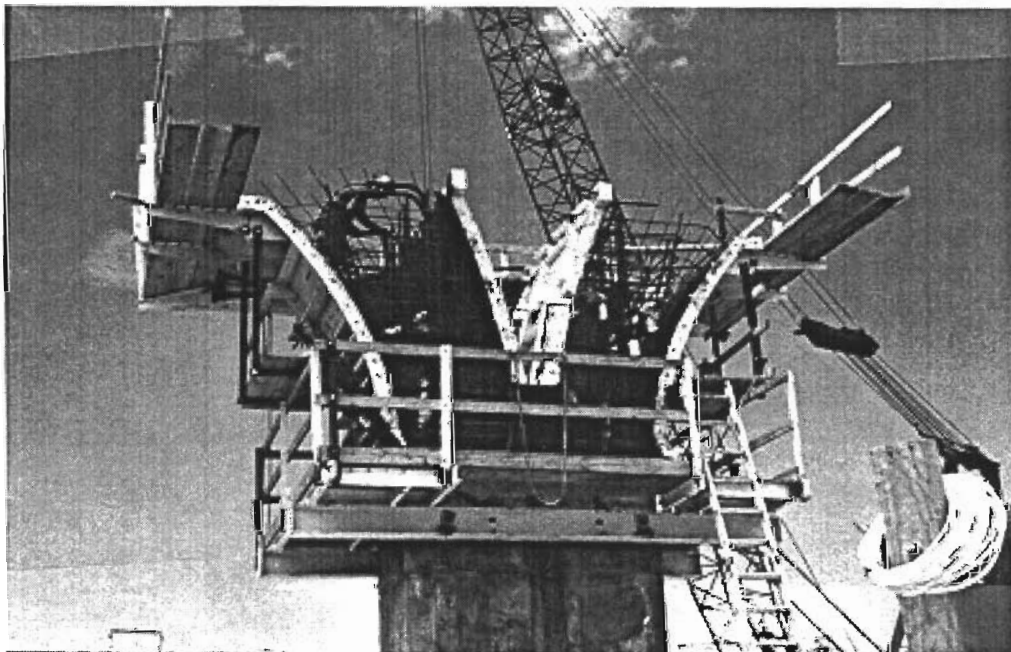


*Figure 4.2 Construction of pier capital.*



*Figure 4.3 Typical mainlane pier.*



*Figure 4.4 Pier bracket supporting truss.*

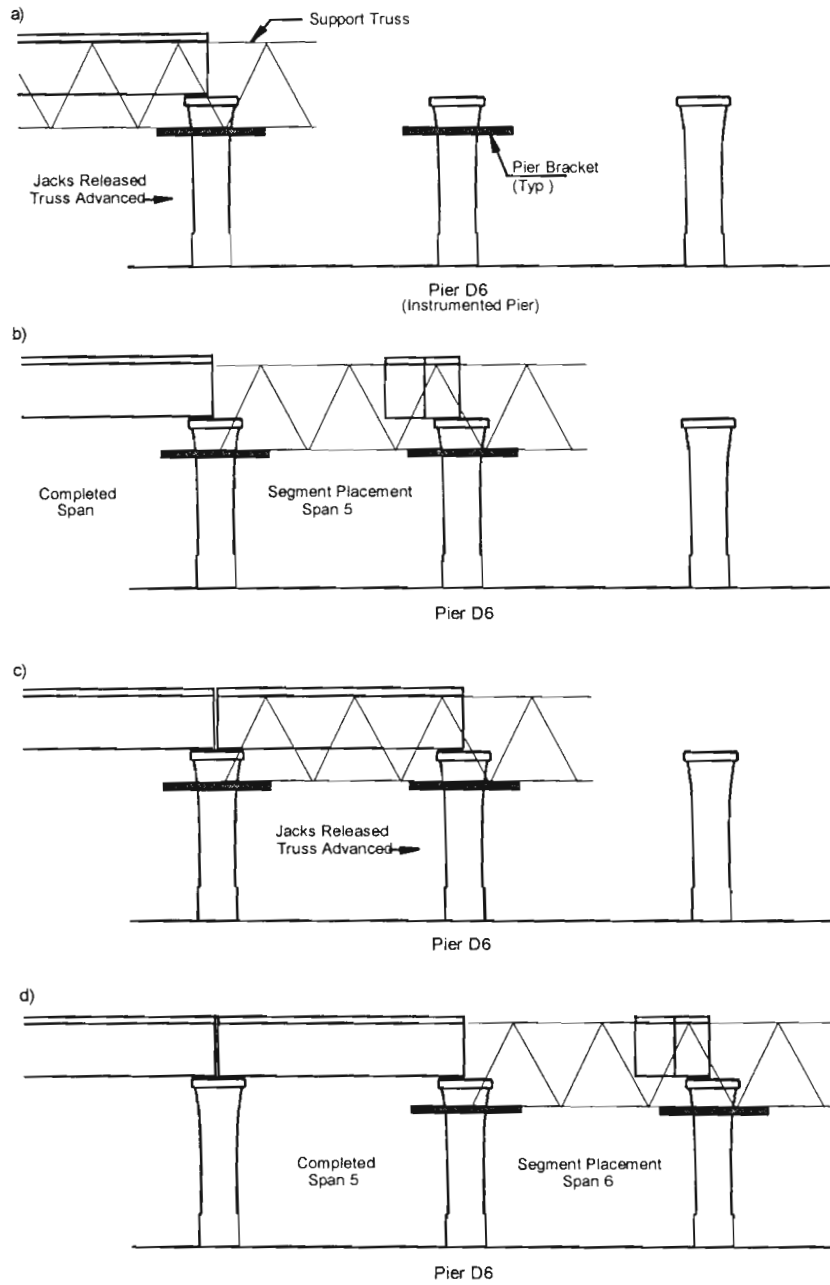


**Figure 4.5** Construction procedure for typical span completion.

**Table 4.1 Mainlane pier data collection summary.**

<b>EVENT</b>	<b>DATE</b>	<b>READINGS</b>
<b>Pier Finished</b>	8/23/94	<i>Each Week</i>
<b>Prior to Span 5 Erection</b>	12/1/94 - 4/19/95	<i>Each Hour</i>
<b>Instrumentation of Span 5</b>	4/19/95 - 4/21/95	<i>None</i>
<b>Stressing of Span 5</b>	4/22/95	<i>Each Minute</i>
<b>After Stressing</b>	4/22/95	<i>Each Half Hour</i>
<b>After Placement on Bearings</b>	4/22/95 - Present	<i>Each Hour</i>

#### **4.4 Segmental Pier Construction**

All of the segments for pier P16 were cast during the summer of 1995 at the constructor's precasting yard. The segments were placed in storage until pier erection activities began in March of 1996 (see Figure 4.6).

Precast pier segments were cast in a specially designed casting bed with tandem casting platforms at the precasting facility. Figure 4.7 illustrates the typical cycle for casting pier segments. The match-cast technique ensures a perfect fit between segments, and reduces or eliminates any systematic alignment errors (see Figure 4.8). A detailed description of the process is given in Reference 3.



*Figure 4.6 Completed pier segments in storage at the casting yard.*

The segmental piers were designed to be post-tensioned from the top of the capital segment. For this reason the post-tensioning ducts were designed with a “U-turn” at the base of the pier. Figure 4.9 shows this duct configuration at the pier’s foundation. It was necessary to cast in place this foundation and ductwork after the construction of the drilled piers supporting the pier were complete. After completion of the cast-in-place foundation, an adjustable steel frame was installed atop the foundation to support the base segment PC16-1 (see Figure 4.10).

The steel leveling frame provided only a temporary support for PC16-1. After alignment and leveling of the bottom segment, a concrete base was cast around it. During construction of the cast-in-place base, the concrete was mechanically vibrated and forced to flow up against the bottom face and into the core void of segment PC16-1, ensuring good contact between the base and the bottom segment and solidifying the moment-resisting connection at the column base. A pier of any height could be constructed with standard segments and base sizes in this manner by simply varying the elevation of the top of the cast-in-place base with respect to the bottom precast segment. Figure 4.11 shows the cast-in-place base after completion of the pier.

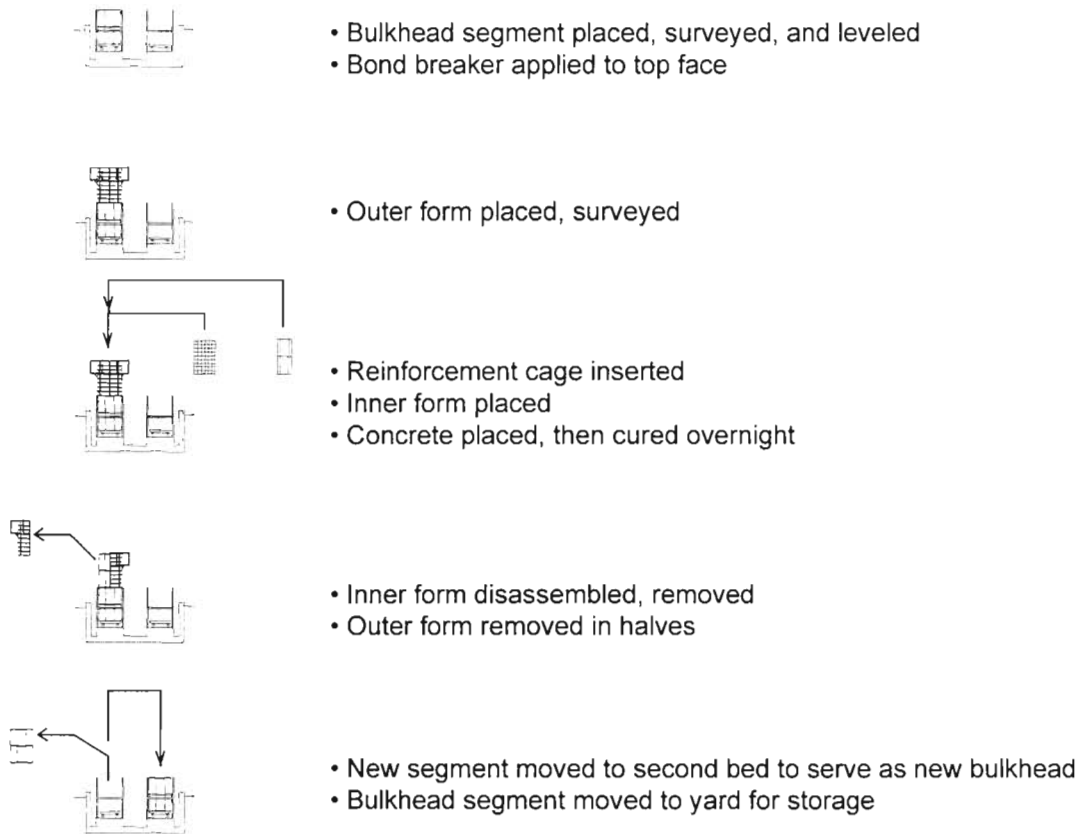


**Figure 4.7** *Typical segment-per-day casting sequence.*

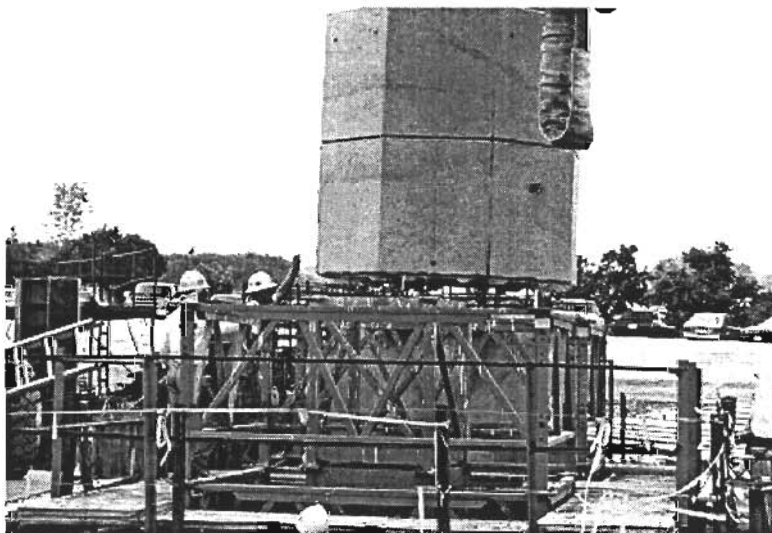


**Figure 4.8** *Match cast segments fit together perfectly.*

Subsequent segments were placed using a crane situated on the north-bound overpass of Interstate Highway 35. Segments were placed with “wet” joints; two-part bridge epoxy was spread over the adjoining segment faces before the segments were installed permanently. After each segment was placed and epoxied, a portable scaffold was lifted to the top of the new segment. From here, DYWIDAG post-tensioning bars were stressed to ensure complete contact between segments as the epoxy cured.

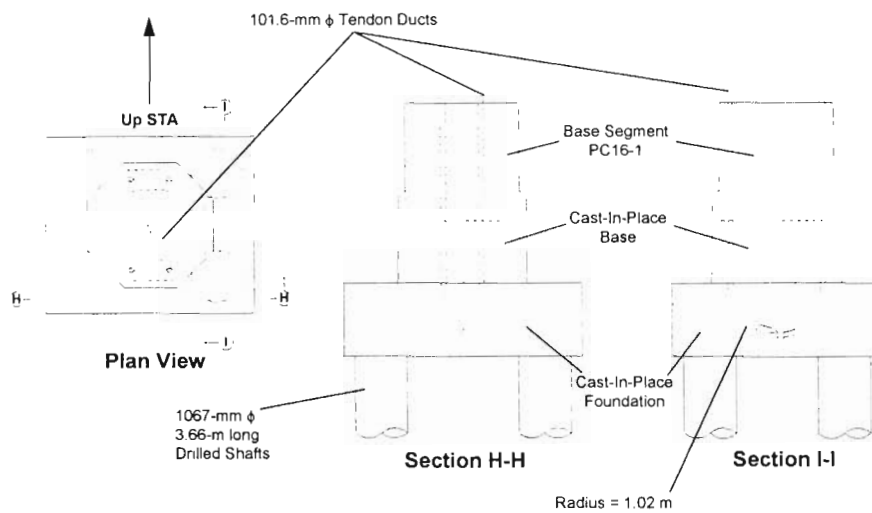


**Figure 4.9** “U-turns” in tendon ducts located in pier foundation.

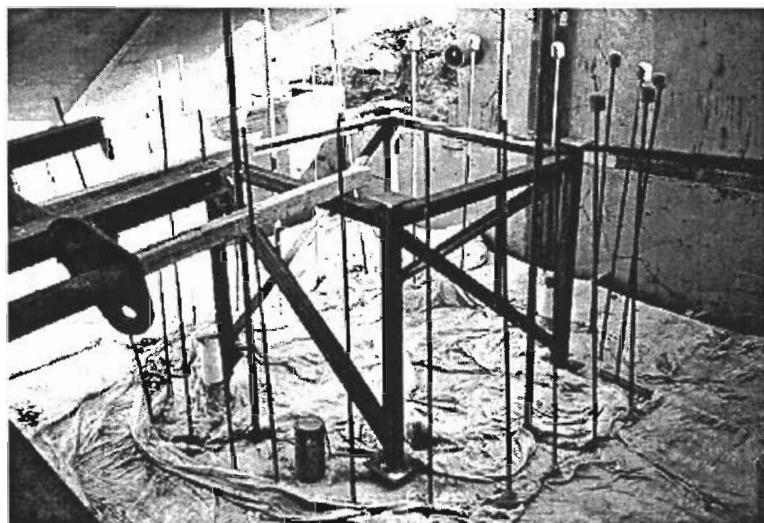


**Figure 4.10** Steel support frame for segment prior to cast-in-place base construction.

Post-tensioning of the pier's tendons followed the placement of the capital segment PC16-8. Tendons consisting of 19 ~ 15-mm  $\phi$  strands were cut to an approximate length, lifted by crane to the top of the pier, and inserted into the tendon ducts. The crane was then used to pull the tendons through the full lengths of the ducts. After installation of the post-tensioning anchorage heads and wedges, the tendons were stressed in the order shown in Figure 4.12.

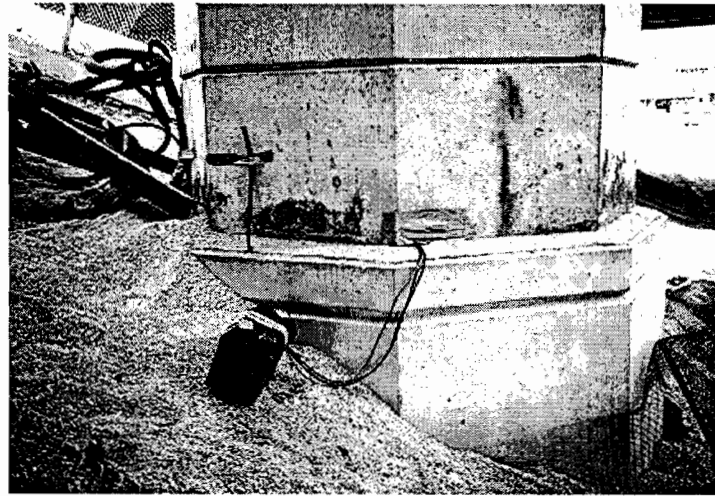


**Figure 4.11** *Cast-in-place base forming a rigid moment connection between base segment PC16-1 and foundation.*

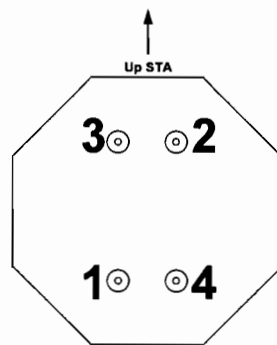


**Figure 4.12** *Sequence of final post-tensioning of pier P16 tendons.*

For the first pull the hydraulic jack was placed at the live end position 1 and position 2 served as the dead end. In a frictionless duct, no further stressing from position 2 would be needed, but the 180° angle change at the “U-turn” in the duct at the base of the pier caused about a 50% loss of post-tensioning force due to friction. Based on measured forces, the calculated frictional coefficient  $\mu$  of the post-tensioning ducts in pier P16 was 0.23, or slightly less than the typical design value of  $\mu = 0.25$ .

The alignment of the ducts was quite good, as the accepted value for a duct with no wobble (unintentional angle change) is  $\mu = 0.221$ . However, a pull at position 2 was needed to stress the complete length of the tendons to the specified level. The same procedure then followed for pulls 3 and 4. After tendon post-tensioning was complete, the tendons were grouted and the anchor heads were covered with a grout shell for corrosion protection. Table 4.2 outlines the entire precasting, erection, and instrumentation process for pier P16.

**Table 4.2 Construction and instrumentation sequence for segmental pier P16.**

Date	Time	Event
24-May-95	1:00 PM	Bottom segment PC16-1 instrumented and cast.
25-May-95	1:00 PM	Segment PC16-2 cast.
26-May-95	1:00 PM	Segment PC16-3 cast.
31-May-95	1:00 PM	Segment PC16-4 cast.
2-Jun-95	1:00 PM	Segment PC16-5 instrumented and cast.
3-Jun-95	1:00 PM	Segment PC16-6 cast.
6-Jul-95	1:00 PM	Top segment PC16-7 instrumented and cast.
18-Sep-95	10:00 AM	Capital segment PC16-8 instrumented and cast.
Sep 18 - Sep 25	hourly	Collection of capital segment PC16-8 curing temperatures.
15-Mar-96	3:00 PM	Segment PC16-1 placed, cast-in-place base constructed.
2-Apr-96	12:00AM - 5:00AM	PC16-2 through PC16-4 placed.
5-Apr-96	12:00AM - 5:00AM	PC16-5 through PC16-7 placed.
8-Apr-96	2:00 AM	Capital PC16-8 placed.
12 Apr - 30 Apr	hourly	Collection of pier temperature data.
Apr 30, May 1	10:00PM - 5:00AM	Pier Post-Tensioning Operations
Apr 30, May 1	every minute	Collection of post-tensioning data.
May 4 - present	hourly	Permanent collection of temperature and strain data.

A detailed description of the casting and erection process for the balanced-cantilever ramp segments is given in Report 1404-2. Detailed reporting of the pier behavior under cantilever erection and live load tests is given in Report 1404-3F.

## CHAPTER 5

### 5. *MEASURED BEHAVIOR - MAINLANE PIER AND INTERPRETATION*

#### 5.1 Introduction

The purpose of this chapter is to present background information, and comparison with theory data, in order to describe the behavior of pier D6 under temperature and gravity loads. Major trends and selected data are reported herein. Further detail is given in Reference 2.

#### 5.2 Background - Thermal Strains

Equilibrium based STM cannot predict compatibility and constraint-induced stresses. Thus in evaluating STM, strains induced due to thermal loading must be investigated and separated from those due to gravity loading. In addition, stresses computed from thermal gradients are often important in design of structures. While AASHTO does not specifically require thermal gradients to be used in design of substructures, it is implied. The background on thermal stresses and gradients was developed in Section 2.3.

##### *5.2.1 Thermal Stresses in Mainlane Pier due to Temperature Gradient in Concrete*

The shaft or “column” portion of the US 183 mainlane pier closely resembles the bolt example given in Section 2.5.3. Rather than consisting of two materials of differing  $\alpha$  and a uniform  $\Delta T$  as shown in Figure 2.21, the column consists of a core and a shell of the same material but with a differing  $\Delta T$ . This concept is shown in Figure 2.22. Since the concrete is so massive, it does not heat and cool uniformly with ambient temperature change. An outer “shell” of concrete tends to heat and cool more rapidly than the inner core, which stays more constant in temperature. Evidence of this behavior over a typical day can be seen in Figure 5.1.

If the concrete shell undergoes a greater  $\Delta T$  than the core, then the shell will want to expand more than the core. Assuming no pre-existing stresses exist on the member, the shell will then be placed in compression due to restraint from the core. Like the brass encased steel bolt, the core will be in tension for this case. If stress is present prior to the temperature change, then the shell will undergo a compressive strain change. However, the final state of stress may not necessarily be compression. Each branch of the “Y” portion of the capital would be expected to behave in a similar fashion, perhaps with a smaller effect since the concrete is less massive in this area.

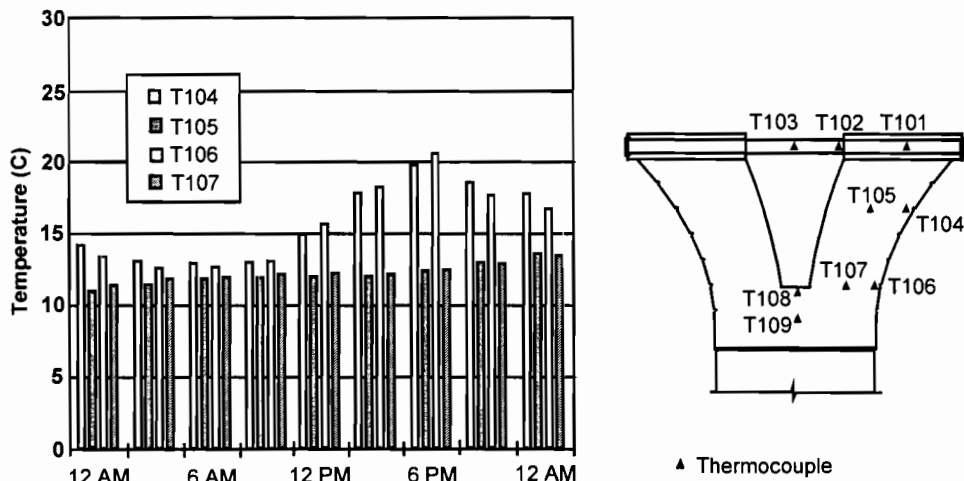


**Figure 5.1** *Temperatures over a typical day.*

### **5.2.2 Thermal Stresses in Mainlane Pier due to Temperature Gradient in Pipes**

Thermal stresses in both the structural steel pipes and the concrete of the pier may also be induced due to temperature change along the structural steel pipes. If the temperature of the pipes increase, the steel will want to expand. If the steel expansion is restrained by the concrete at the pipe ends, the full desired expansion will not be reached, and a thermal stress will be set up in the structural steel pipes.

The concrete will also be affected by this pipe expansion. As noted, the concrete is trying to resist the expansion of the steel. This action causes the concrete to accumulate bending stresses due to the temperature changes in the pipes.

### **5.3 Measurements on Mainlane Pier - Prior to Superstructure Erection**

This section presents field measurements made prior to the erection of the superstructure. Thus there is no shading effect. This emphasizes the effects of thermal gradients across the concrete and across the structural steel pipes. For behavior prior to the superstructure erection, March 11, 1995, was chosen as a typical sunny day. As seen in Figure 5.2, temperature patterns prior to this time were not consistent from day to day due to weather fluctuations. Figure 5.3 shows ambient temperatures as reported by the National Oceanic and Atmospheric Administration [41] for March 11, 1995. Also shown in Figure 5.3 are the pipe temperatures at midlength of the pipe. The temperatures show excellent correlation with the ambient temperatures. Therefore, thermocouple T103 can be used as a “local thermometer” at the project site.

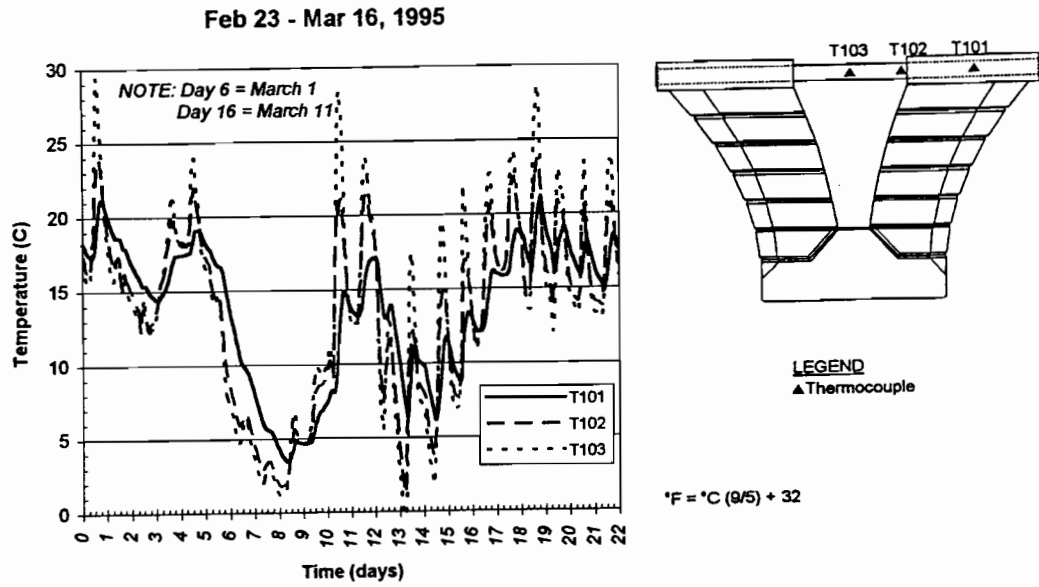


*Figure 5.2 Temperature history.*

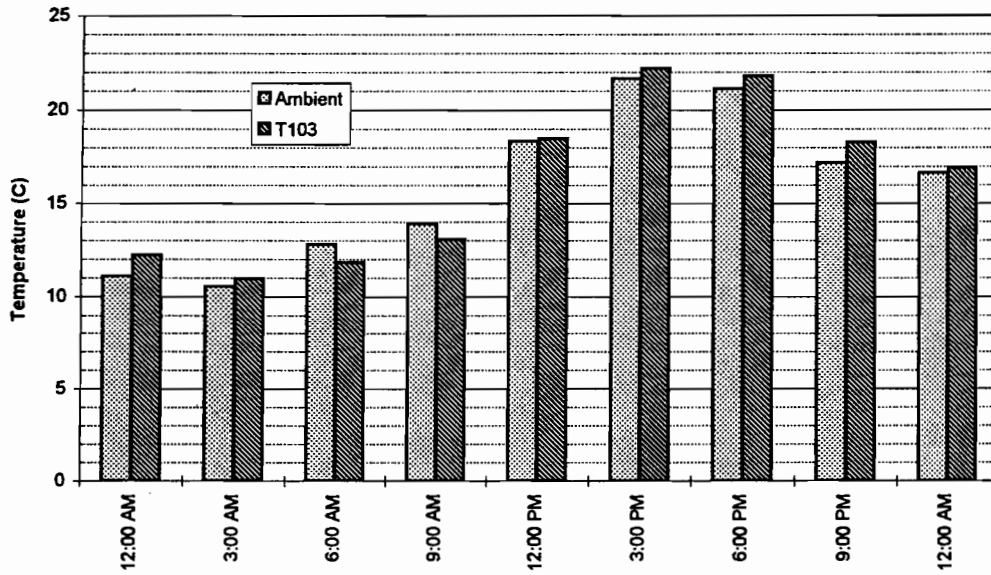


*Figure 5.3 Ambient temperatures for March 11, 1995.*

### 5.3.1 Temperature Measurements

Thermocouples were placed in the concrete “Y” portion of the pier and on the structural steel pipes as shown in Figure 3.11. Temperature variation along the structural steel pipes can be seen in Figure 5.4. As the day progresses, the pipe undergoes a cooling trend in the morning followed by a heating trend in the afternoon. In the evening, the pipes begin to cool. The greatest difference between the temperature on the fully exposed portion of the pipe and the fully embedded pipe occurs at 3:00 P.M. and is approximately 8 °C (11.5 °F). Although the entire length of the pipe shows similar trends, thermocouple T103 (located at the midlength of the pipe) undergoes a more drastic temperature change than thermocouple T102 (located at the concrete to steel interface). This trend indicates that the concrete is absorbing heat from the pipe. Thermocouple T101 shows the pipe is insulated from the sun’s radiation by the concrete.

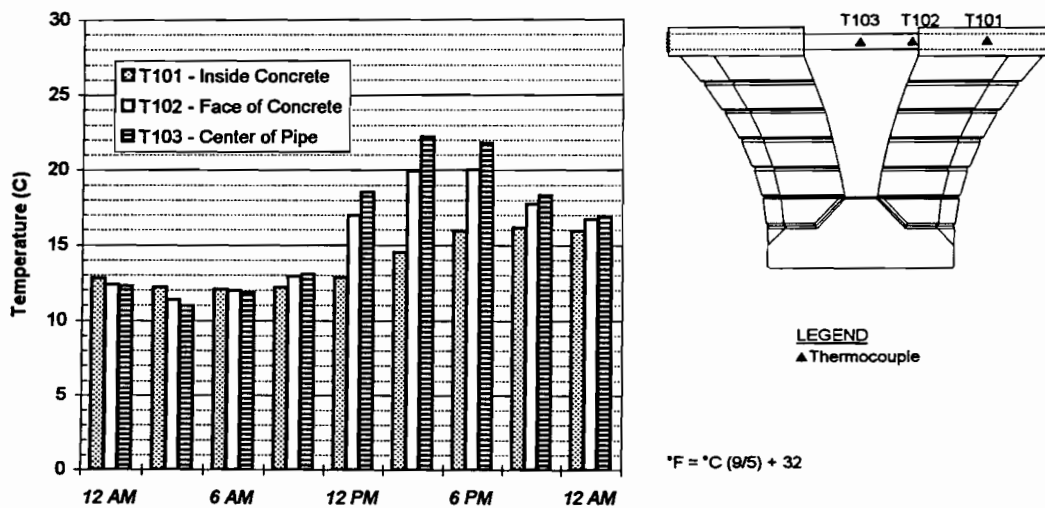


**Figure 5.4** Structural steel pipe temperatures: typical sunny day.

Temperatures near the surface of the concrete are shown in Figure 5.5. Again, a morning cooling trend, afternoon heating trend and evening cooling trend can be observed. Thermocouple T108 begins a cooling trend earlier in the evening than T104 and T106 which are located on the southwest corner of pier D6. As such, they are directly exposed to the setting sun. Thermocouple T108 is shaded by the “Y” during this time, allowing it to begin cooling earlier.

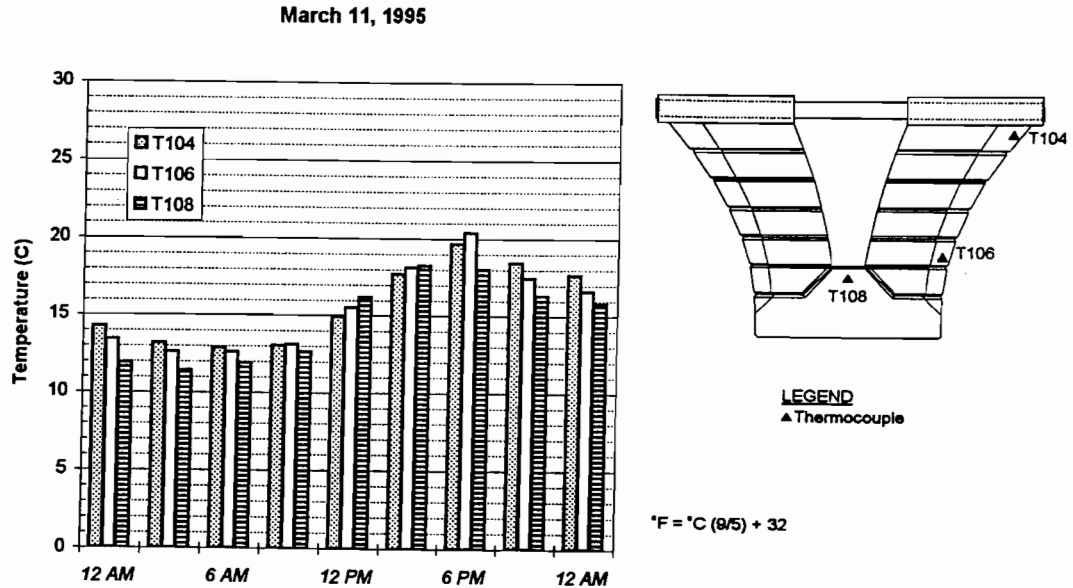


**Figure 5.5** Temperature in concrete “shell”: typical sunny day.

Temperatures in the core of the concrete are shown in Figure 5.6. They are not exposed directly to the environment and are not as immediately affected by ambient temperature changes as other thermocouples due to the massiveness and low conductivity of the concrete. These core thermocouples exhibit only a slight heating trend over the course of a typical day. Assuming thermocouple T103 represents the ambient temperature, the temperature ‘lag’ in the concrete “core” is shown in Figure 5.6.

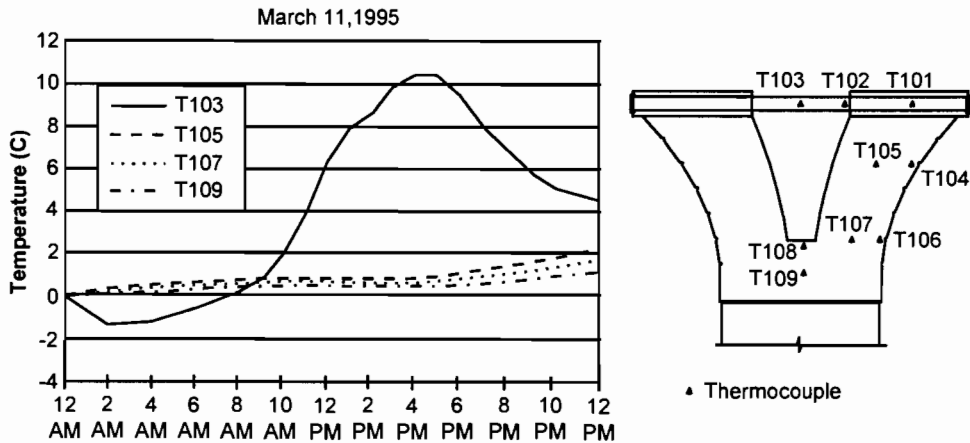


**Figure 5.6** Temperature lag to concrete “core”: typical sunny day.

In contrast Ref [2] shows that on a cloudy day with a general cooling trend, ambient temperatures varied only 3.5 C. Again, the temperatures measured by T103 at the center of the pipe are in excellent agreement with the ambient temperatures. Thermocouples indicated that heat stored in the concrete from previous warmer days was transferred to the pipe. “Shell” and “core” showed that the temperature of the concrete core was higher than the concrete shell.

### 5.3.2 Structural Steel Pipe Strains - Typical Sunny Day

Strain gauges were mounted along the length of two of the structural steel pipes as shown in Figure 3.2. Strain variations measured on March 11, 1995, along the pipes can be seen in Figures 5.7 through 5.9. These plots indicate that although the gravity load on the pier is unchanged during this time period, pipe strains are changing throughout the day due to temperature effects. Interestingly the maximum strain measured is the same at the pipe section exposed to the sun (Figure 5.7), well embedded in the concrete (Figure 5.8), and near the end anchor (Figure 5.9). The maximum changes would correspond to pipe stress changes of  $\pm 2.8$  MPa ( $\pm 400$  psi), which are relatively unimportant when compared to the pipe allowable stress.

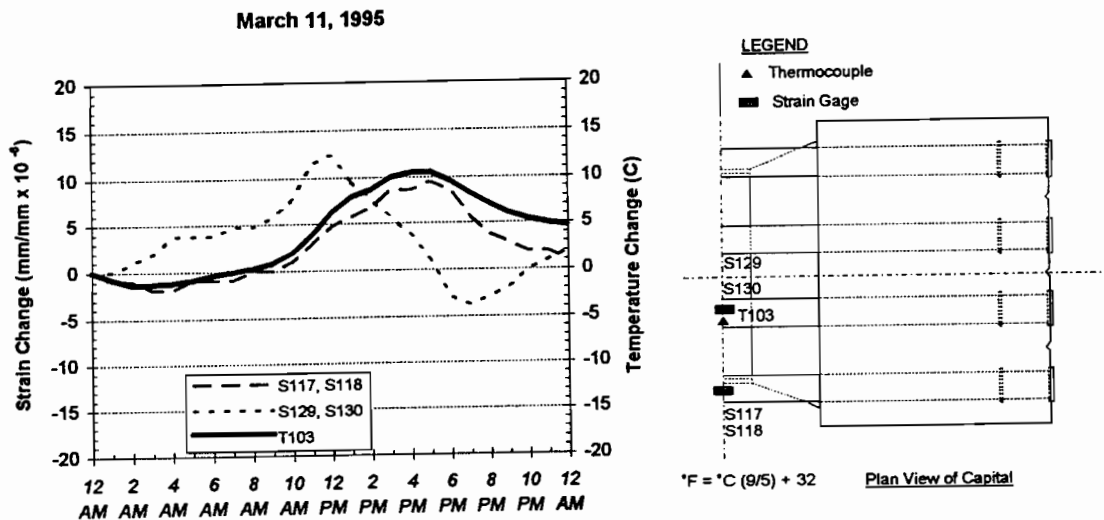


**Figure 5.7** Exposed pipe strain change and temperature change.

Both pipes show similarities in behavior along their lengths. In general, as the temperature increases over a day, tensile strain changes occur. As the temperature decreases, compressive strain changes occur. These tensile and compressive strain changes occur at different times over the course of the day.

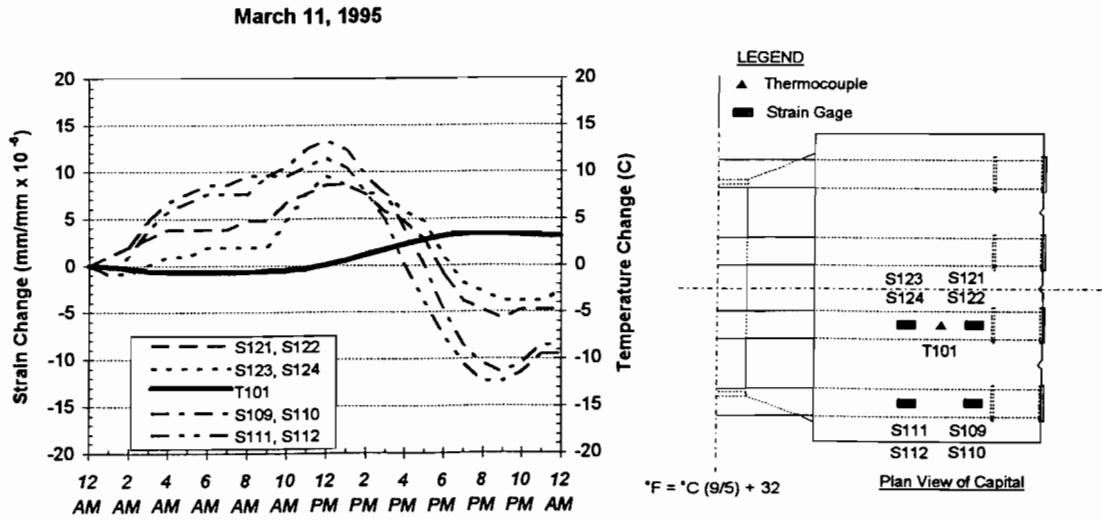


**Figure 5.8** Well embedded pipe strain change and temperature change.

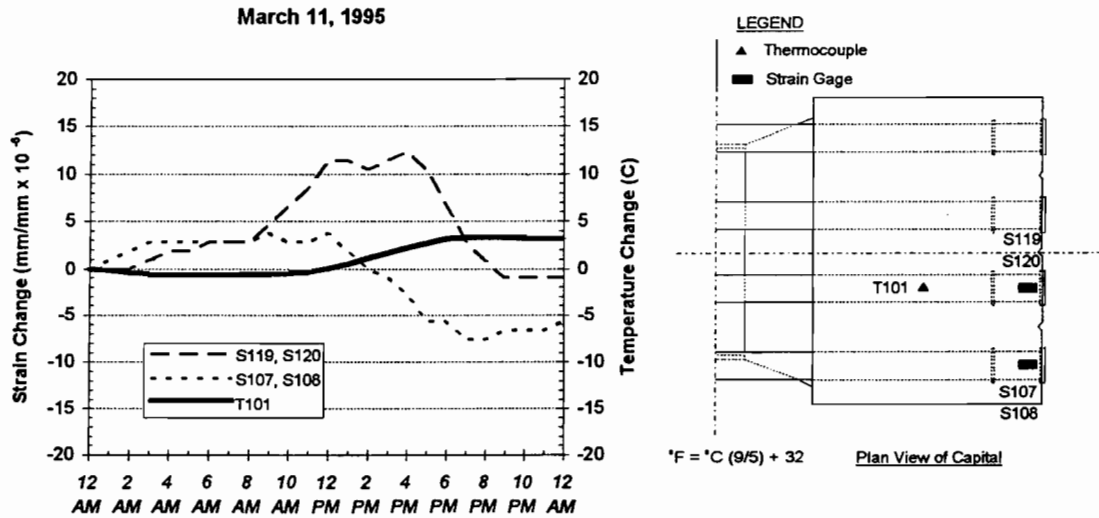


**Figure 5.9** Pipe embedded end strain change and temperature change.

### 5.3.3 Capital Strains - Typical Sunny Day

Concrete strain device, strain gauge, and thermocouple locations for the concrete portion of the capital are shown in Figure 5.10. Concrete strain device variations over the course of March 11, 1995, are shown in Figure 5.11 for the top section which had the highest strains. Negative strains are compressive. Devices located near the surface on the outside face of the “Y” exhibited much larger strain changes throughout the day than the devices located on the shell near the side face of the “Y” and in the core of the capital. This supports the idea discussed in Section 5.2.2 concerning the effect of the expansion and contraction of the structural steel pipes due to temperature changes. In the morning, the temperature of the pipe is cooling. The pipes contract as they cool, pulling the “Y” together. Flexural tensile strains may be caused on the outside face of the “Y” due to this pulling. As the day progresses and pipe temperatures increase, the outside face of the “Y” experiences compressive strain changes due to the expansion of the “Y.”

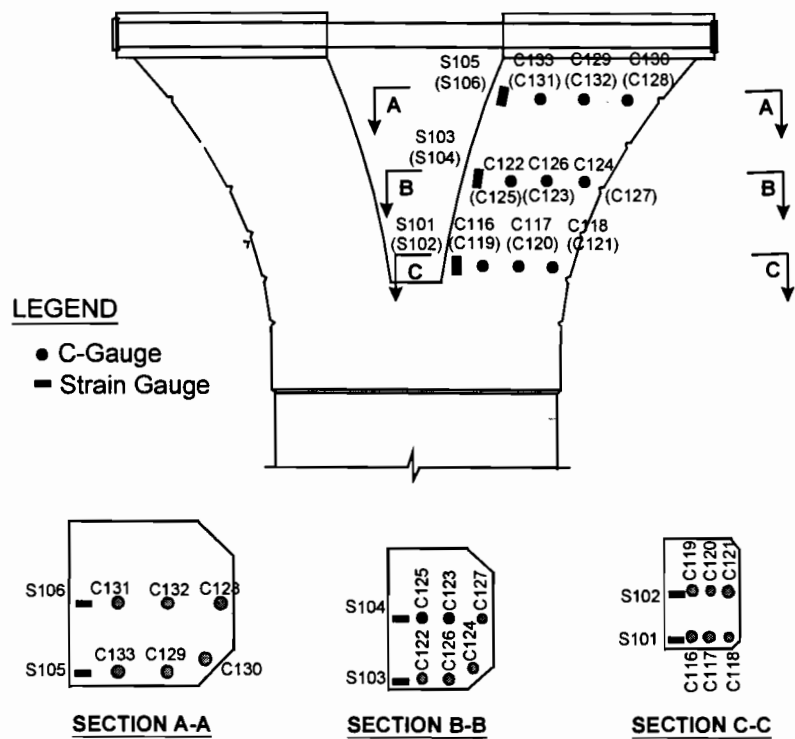
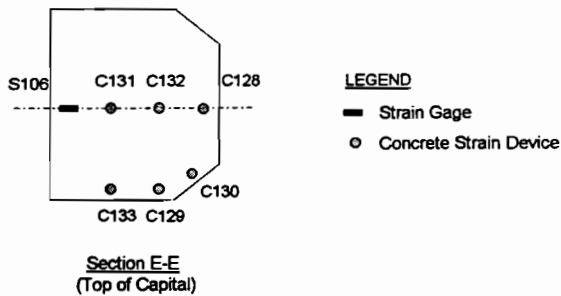
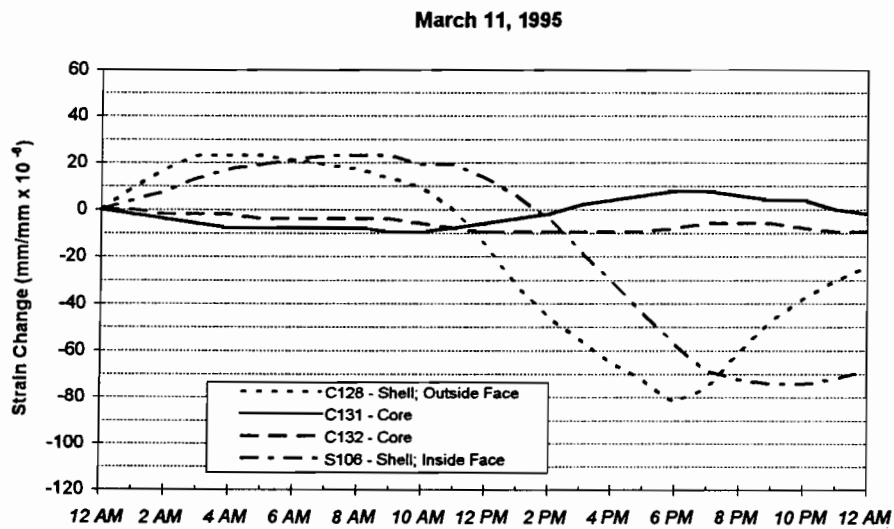
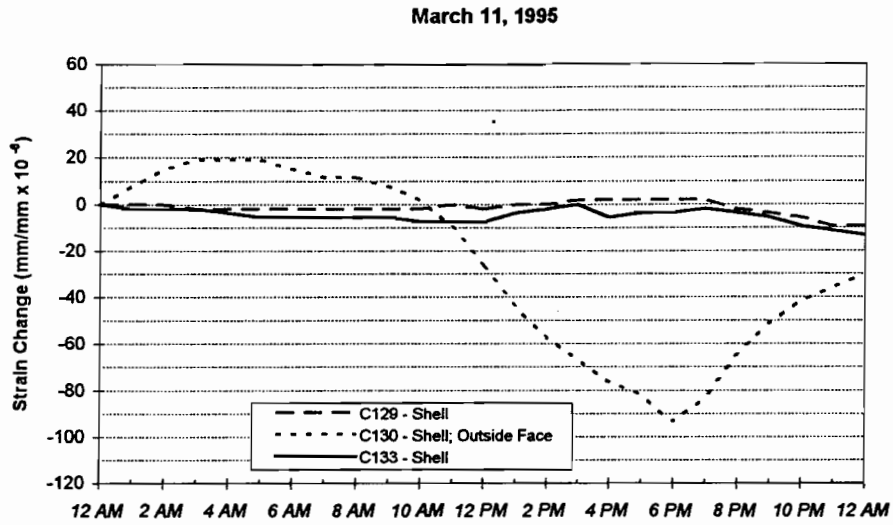


Figure 5.10 Capital instrument locations.



**Figure 5.11**      *Strain variation instruments located in top section of capital: typical sunny day.*

The concrete strain devices located in the core of the “Y” exhibit compressive strain changes during temperature decreases and tensile strain changes during temperature increases. The devices located in the shell exhibit behavior opposing the core devices. Decreases in temperature cause tensile strain changes, and increases in temperature cause compressive strain changes. This is consistent with the concept discussed in Section 5.2.1 that states that an ambient temperature increase causes the concrete located in the shell to undergo compressive strain changes and the concrete in the core to undergo tensile strain changes. Again, this is caused by the temperature lag existing across a given concrete section due to the massiveness and poor insulating properties of the concrete.

Figure 5.12 compares strain variation over March 11 with temperature change. In each case, the temperatures depicted are measurements from thermocouples located very close to the strain devices from which strain variation was measured. As the surface concrete is cooling during the early morning, the core concrete is heating up. This indicates a lag of heat transfer across the cross section of the pier due to the low conductivity of concrete. The surface concrete undergoes a large temperature increase in the afternoon. During this time, the core concrete is maintaining a fairly steady temperature. By the evening, the surface concrete is beginning to cool down. The core concrete is heating up in the evening; the afternoon heating trend of the surface is reaching the core at this time. As the core heats slightly in the early morning, compressive strains occur. As the shell concrete undergoes substantial temperature increase during the afternoon, the core is “pulled” along and tensile strains are induced in the core.

Depending on the time of day, the surface and core concrete are restraining each other from undergoing the desired expansion or contraction. This effect is indicated by the strain variation observed for each location. Strain gauges located near the surface of the concrete exhibit compressive strain changes during heating of the concrete surface and tensile strain changes during cooling of the concrete surface. If the expansion or contraction of the concrete due to temperature changes were free, heating would cause tensile strain changes and cooling would cause compressive strain changes.

Assuming an approximate modulus of elasticity for the pier concrete of 28.3 Gpa (4100 ksi), the maximum measured compressive strains of approximately  $90 \times 10^{-6}$  and tensile strains of approximately  $20 \times 10^{-6}$  would correspond to stress changes of only 2.6 MPa (370 psi) compression and 0.6 MPa (370 psi) compression and 0.6 MPa (80 psi) tension. These are of fairly low magnitude in terms of design significance.

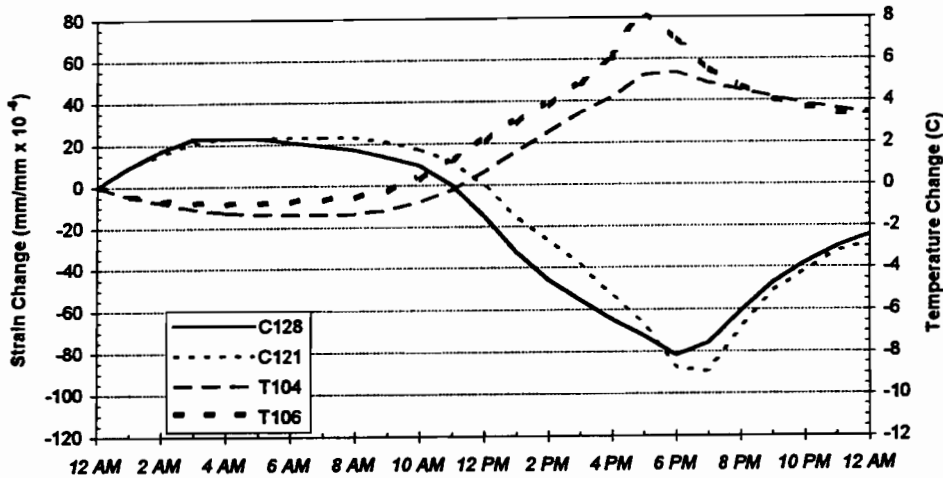


**Figure 5.12 Comparison of temperature change and strain variation for instruments located near the top of the capital.**

Vertical strain variations were consistent along each “vertical” line down the capital [2]. This indicates that temperature effects are fairly consistent at each cross section.

### 5.3.4 Shaft Strains - Typical Sunny Day

The locations of concrete strain devices in the column portion of pier D6 are shown in Figures 3.1 and 3.5. Strain changes for selected devices for March 11, 1995, are shown in Figures 5.13 and 5.14. Negative strain variations indicate compressive strains.

Figure 5.13 shows strain changes over the course of a typical day for concrete strain devices located near the top of the column or “shaft” portion of the pier where the largest strains were measured. The devices located in the shell of the pier exhibit tensile strain changes during temperature increases and compressive strain changes during temperature decreases. Compressive strain changes occur in the core during temperature increases. As temperatures decrease, core devices indicate tensile strain changes. Core strains are quite low.

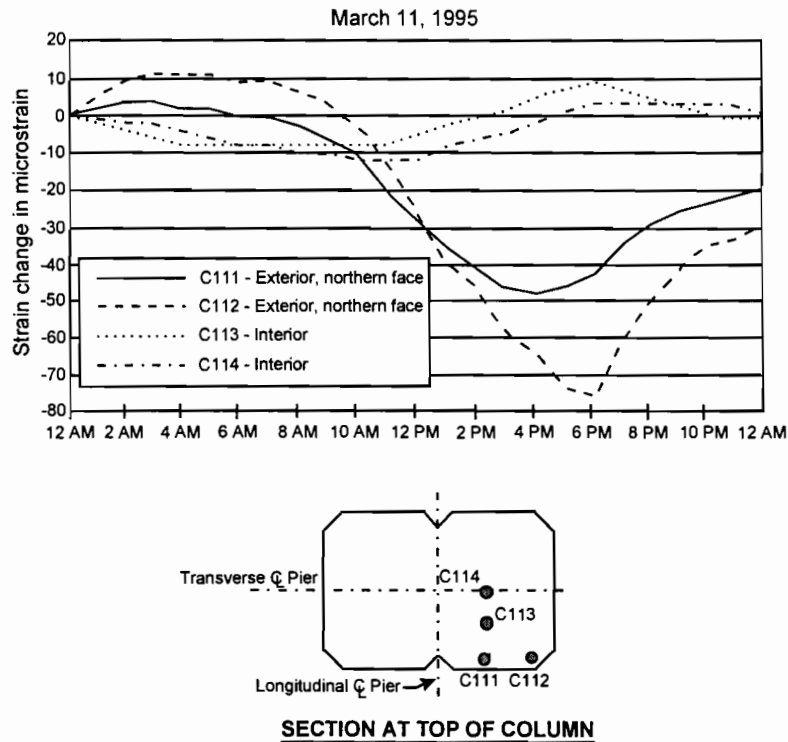


**Figure 5.13 Strain variation: top of column.**

Concrete strain devices located at the bottom of the column which was below grade showed substantially less strains.

Assuming that the surface temperature of the column is approximately the same as the surface temperature of the capital, Figure 5.14 shows a comparison of shaft shell strain and surface temperatures during March 11. As the surface of the concrete heats up in the afternoon, a compressive strain change takes place. As mentioned in Section 5.3, this is due to the uneven heating and cooling trends across the section of the concrete. The magnitudes of related stresses are lower than the capital stresses in the previous section.

#### **5.4 Measurements on Mainline Pier During Superstructure Erection**

This section presents field measurements made during the erection of Spans 5 and 6, both of which are supported by Pier D6. The total strains on Pier D6 are due to combined thermal and gravity loads during erection of the superstructure over a period of eleven days. Separation of thermal strains from total measured strains in order to compare measured forces with those predicted by a strut-and-tie model is discussed subsequently.

March 11, 1995

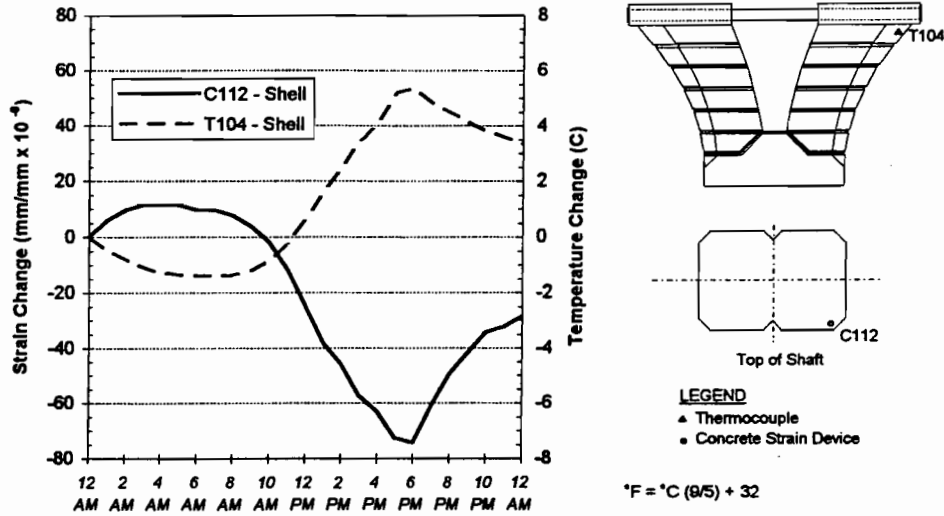


**Figure 5.14** Comparison of column strain variation and surface temperature change: concrete "shell."

**Table 5.1** Superstructure erection sequence over Pier D6.

EVENT	DATE
Truss advanced to Pier D6 for Span 5 Erection	March 17, 1995
Span 5 segments placed on truss	March 17 - 19, 1995
Instrumentation of Span 5 (Data acquisition system disconnected)	March 19 - 22, 1995
(Data acquisition system re-connected)	March 22, 1995
Span 5 segments post-tensioned	
Hydraulic jacks released - Span 5 placed on Pier D6 bearings	March 22, 1995 (Approximately 8:00 P.M.)
Truss advanced for Span 6 erection; segments placed on truss and post-tensioned	March 23 - 26, 1995
Hydraulic jacks released - Span 6 placed on Pier D6 bearings	March 26, 1995 (Approximately 8:00 P.M.)

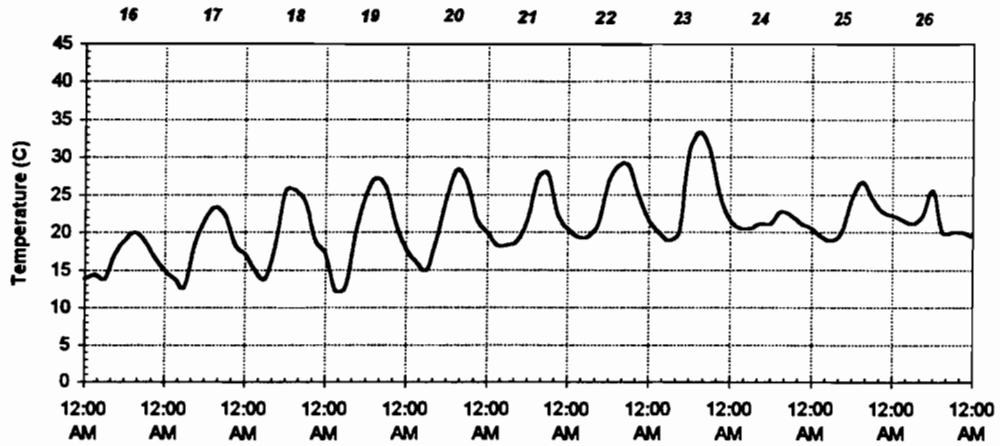
Span 5 was the first span erected and placed on the bearings of the instrumented pier. The erection process was monitored closely during all operations. Hourly readings continued through the erection of Span 6. The erection schedule for Spans 5 and 6 is shown in Table 5.1. The initial load on the shaft occurred on March 17 with the placement of the truss for erection of Span 5. The initial load on the capital and on the structural steel pipes occurred on March 22 with the stressing of the post-tensioning tendons in Span 5 when the spans begin to be supported on the bearings.

#### ***5.4.1 Temperature Measurements***

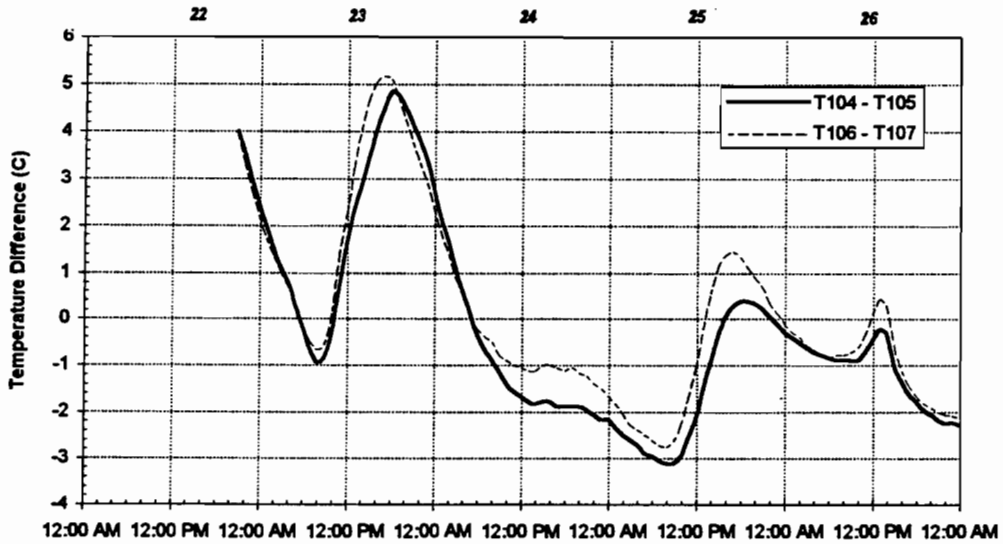
Ambient temperatures measured during the erection of the superstructure are shown in Figure 5.15(a). A slight warming trend occurred during the time period from March 16–26. Temperature measurements across the concrete capital section as measured for the 5 days of erection operations indicate that the daily maximum temperature gradient as shown in Figure 5.15(b) across the concrete capital section varied from +5 °C (9 °F) to -3 °C (5.4 °F). A positive gradient indicates that the shell is warmer than the core. Measurements from all thermocouples are given in Reference 2.

Temperatures measured from thermocouples located on the structural steel pipe are shown in Figure 5.16. Thermocouple T103, located at midspan of the structural steel pipe, was most directly affected by ambient temperature change. Thermocouple T102, located at the concrete/steel interface, experienced less temperature change. Thermocouple T101, embedded in the concrete, exhibits the least temperature change. This temperature trend is consistent with thermal trends of Section 5.3.

Temperatures from thermocouples T104 and T105, located near the top of the capital, are shown in Figure 5.17. Daily temperature fluctuations for thermocouple T104 (concrete shell) are greater than those for T105 (concrete core). Very similar temperatures were measured by thermocouples located near the bottom of the capital. Very small temperature variations were measured by the thermocouples embedded in the base of the capital.

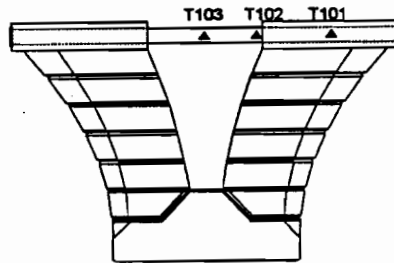
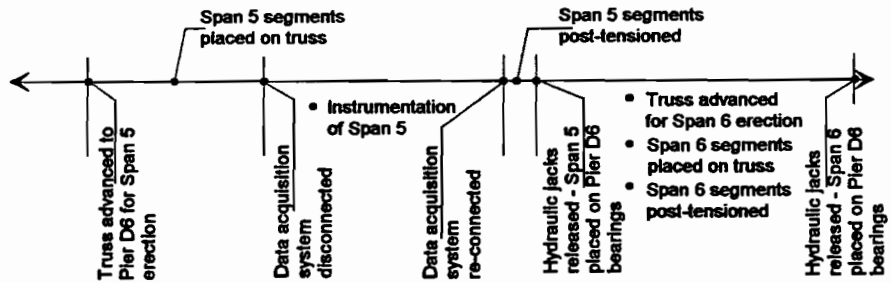
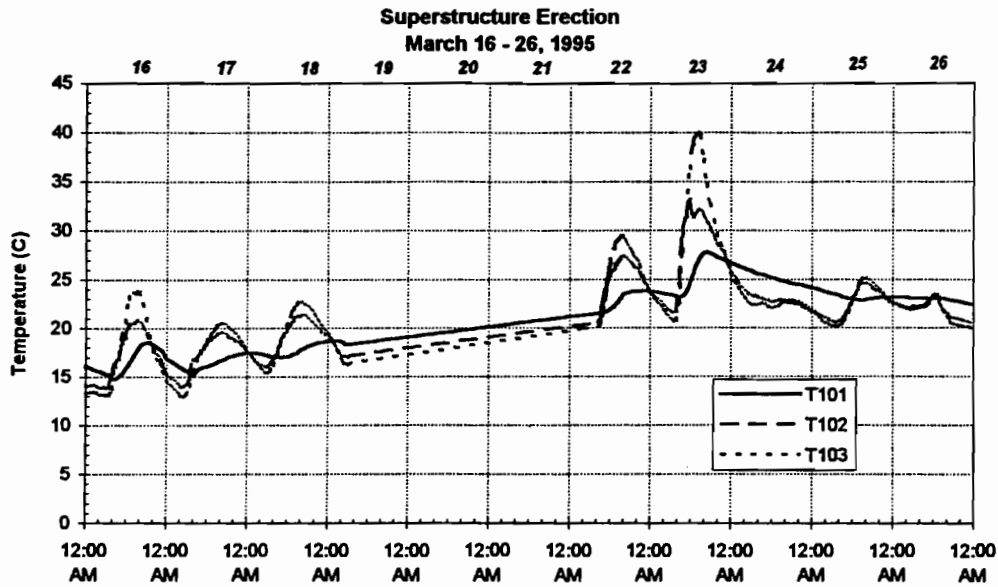


a) Ambient Temperatures - Superstructure Erection, March 16-26, 1995



b) Temperature Gradient Across Concrete, March 22-26, 1995

Figure 5.15 Temperature readings during superstructure erection.



**LEGEND**  
▲ Thermocouple

$$^{\circ}\text{F} = ^{\circ}\text{C} (9/5) + 32$$

**Figure 5.16** Temperatures measured on the structural steel pipe during construction.

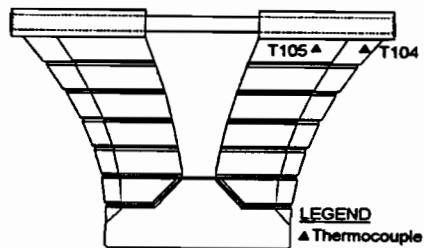
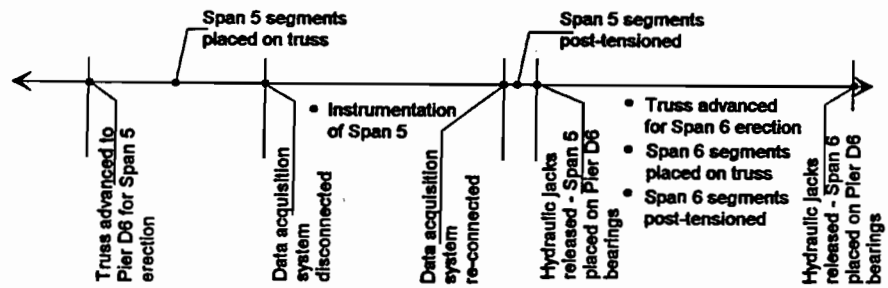
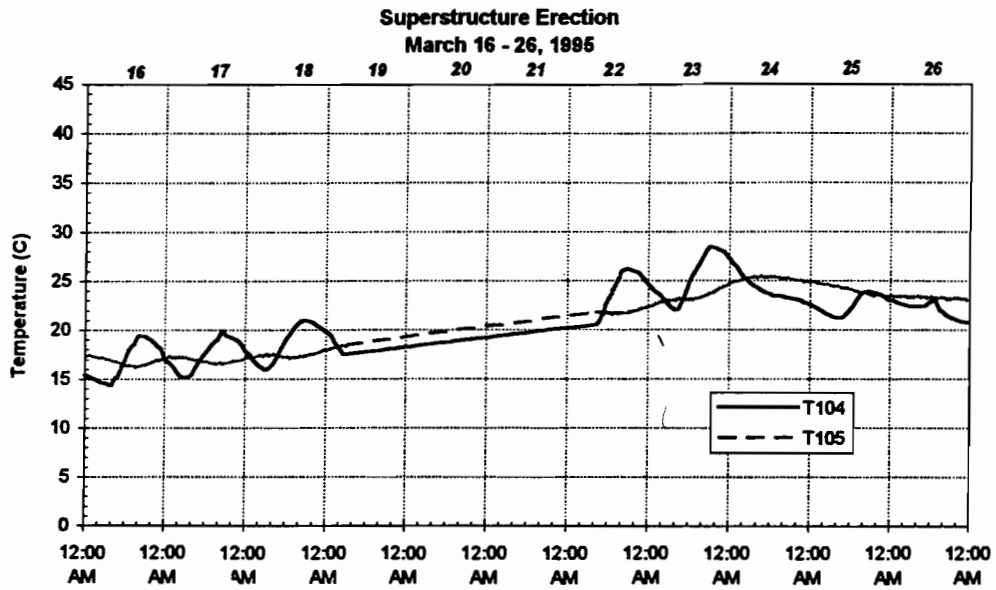


**Figure 5.17** Concrete temperatures measured near the top of the capital during construction.

#### ***5.4.2 Structural Steel Pipe Strains***

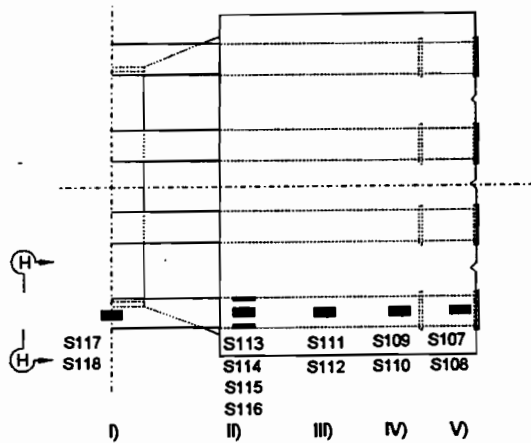
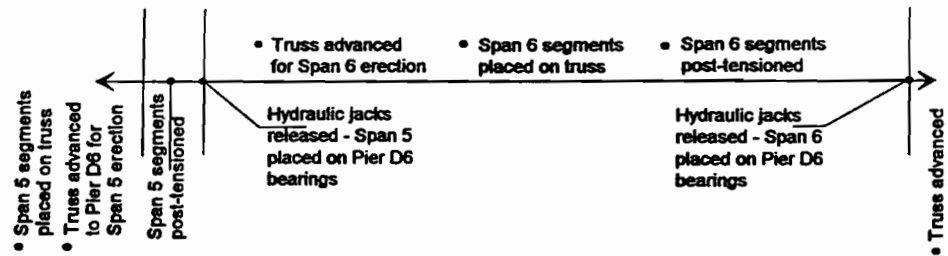
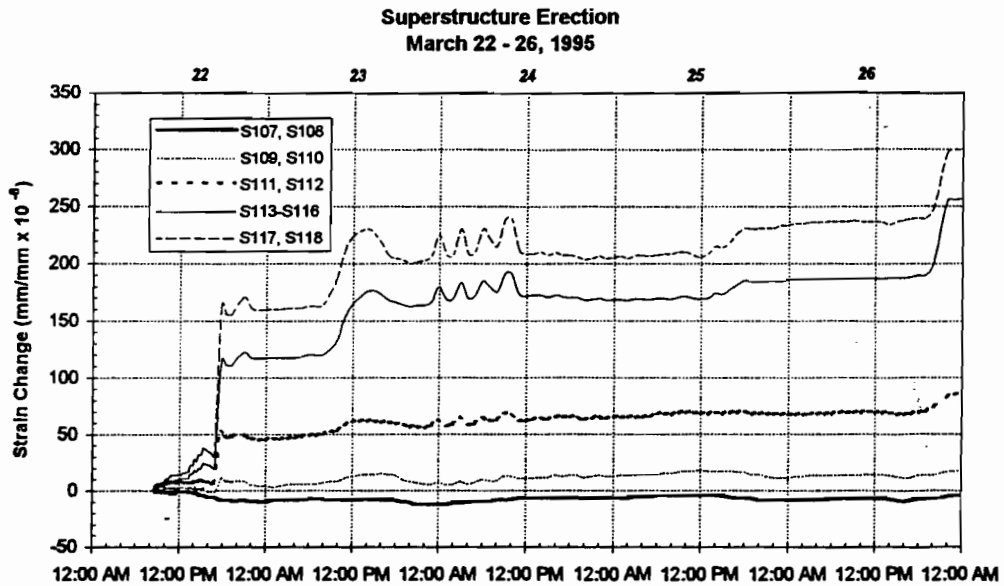
The total gravity load and thermal strain change measured on the structural steel pipes during the superstructure erection is shown in Figures 5.18 and 5.19. The initial point of these plots was taken immediately prior to stressing, before any load had been transferred to the bearings of the pier. Before this the Span 5 segments were supported by the erection truss, which was in turn supported on the brackets below the capital.

During stressing of the tendons in Span 5, some load is transferred to the pipes. A small tensile strain change is exhibited during this time period in all locations except at the ends of the pipes.

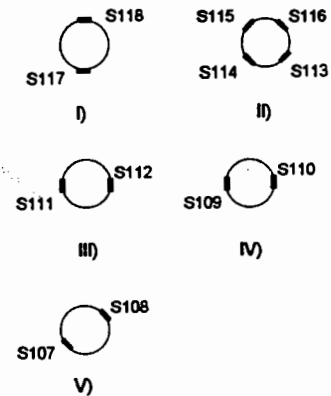
As Span 5 is placed on the bearings of the pier, a tensile strain change occurs along the pipes. Midspan of the pipes exhibits the largest strain changes. With somewhat less at the concrete/steel interface. The force due to loading is rapidly dissipated along the entire pipe length as the load is transferred to the concrete along the length of the pipe. Beyond midpoint of the pipe embedment, the strain change due to loading is very close to zero.

As Span 6 was placed on the bearings, the strain gauges at the pipe midpoint and at the concrete/steel interface exhibited approximately the same tensile strain change. The strain change due to Span 5 loading was larger than that due to Span 6 since the instrumented pipes are located on the Span 5 side of the pier. The strain gauges located at the ends of the pipes exhibited virtually no strain change due to Span 5 or 6 loading.

Both pipes exhibit similar total strain changes along their lengths. Trends in strain change during construction are also similar. Total strain change measured due to thermal and gravity loading is less for the interior pipe. This could be due to the fact that the interior pipe is more insulated by the concrete.



**Plan View of Capital**



**Section H-H**

**Figure 5.18** Strain changes measured in the exterior structural steel pipe during construction.

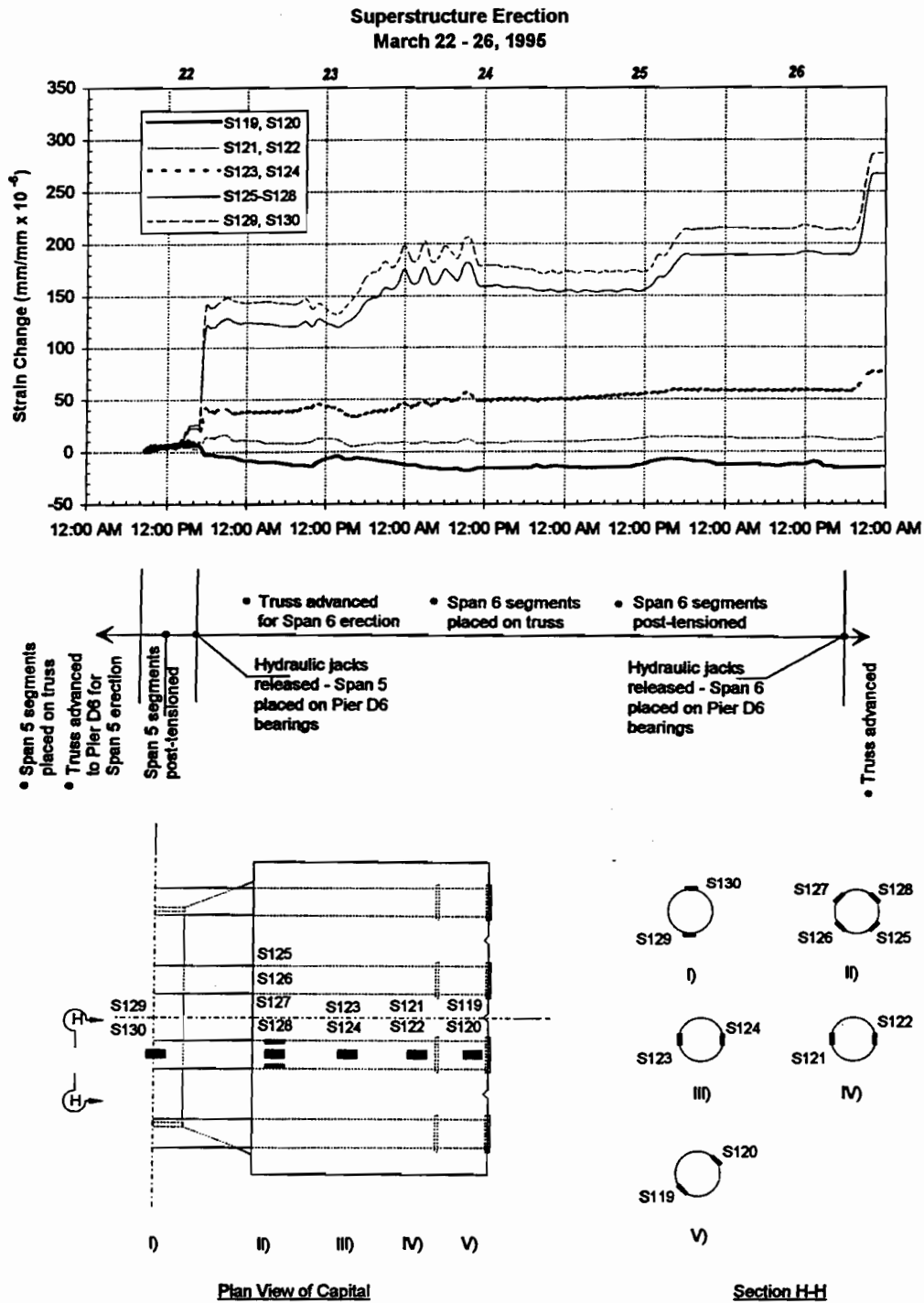


**Figure 5.19** Strain change measured in the interior structural steel pipe during construction.

### ***5.4.3 Capital Strains***

Typical concrete strain measurements made in the capital are shown in Figures 5.20 and 5.21, assuming an initial point directly prior to stressing of Span 5 tendons.

Prior to stressing, the erection truss and the segments are supported at the bottom of the "Y." Strain change in the compressive direction occurred for most strain devices as the tendons of Span 5 were stressed. This indicates that the span is being partially supported by the capital during stressing.

When the hydraulic jacks are released and Span 5 or 6 is placed on Pier D6 bearings, a significant compressive strain change is seen in strain devices along the centerline of the pier.

Consistently, strain devices located closer to the transverse centerline of the pier (See Figure 5.21) show a lower compressive strain change than those devices located toward the outside face of the capital (See Figure 5.20). This is partly due to the temperature changes. Strain devices located in the concrete core show small fluctuation in daily strain change due to what appears to be thermal strains. On March 23, the load on the capital is approximately constant. During the second half of the day, as ambient temperature is increasing, device C120 (Figure 5.21) shows small tensile strain change. Device C121, which is located in the shell of the concrete (Figure 5.20), shows a large compressive strain change during the same period.

These trends in strain change follow thermal effects discussed in Section 5.2. Across a section of the concrete, as ambient temperature increases the shell is put into compression and the core into tension. This is due to the temperature lag across the section caused by the fact that the concrete is so massive. The expansion of the pipe during this time period causes large compressive strains in devices located on the outside face of the "Y."

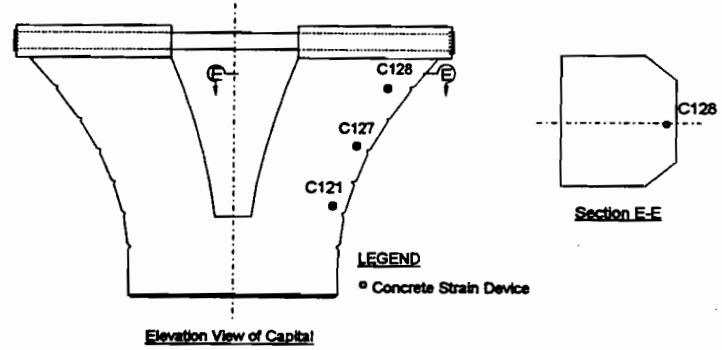
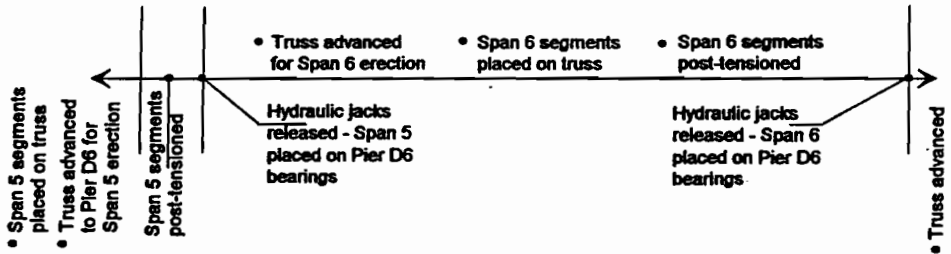
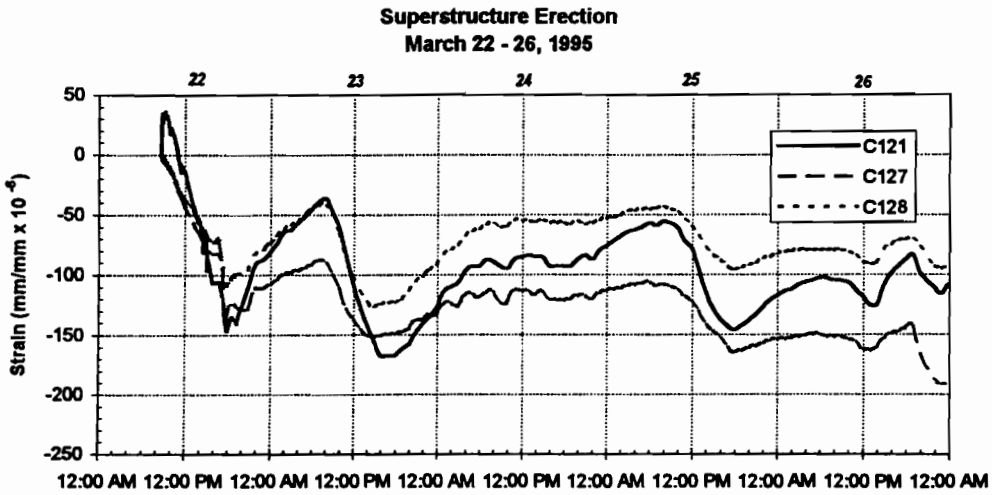


**Figure 5.20** Comparison of strain change "vertically" on capital during superstructure erection: shell near outside face of "Y."

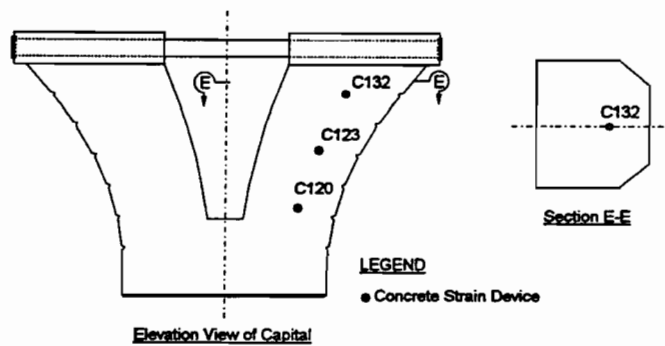
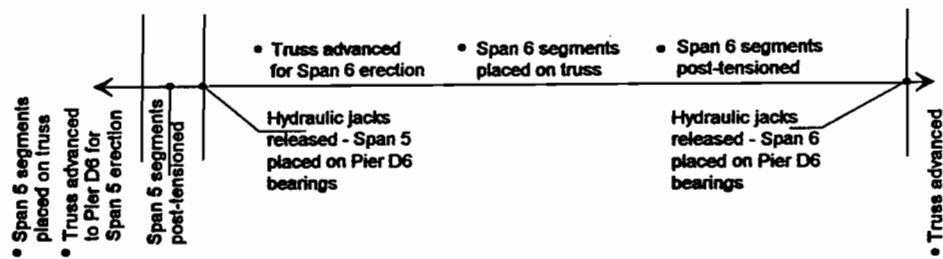
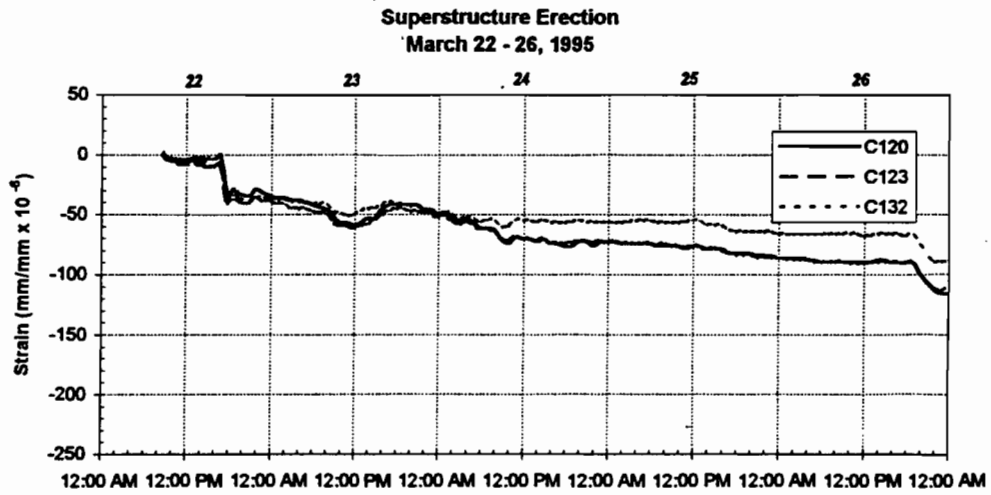


**Figure 5.21** Comparison of strain change "vertically" on capital during superstructure erection: core near outside face of "Y."

#### **5.4.4 Shaft Strains**

A sampling of total strains due to gravity load and thermal changes which were measured in the shaft of the pier are shown in Figure 5.22 [2]. Strain change was referenced to March 16 which preceded advancement of the erection truss to Pier D6 and hence is prior to any load placement on the shaft.

As the tendons of Span 5 were stressed, strain devices in the shaft exhibited strain change, indicating that the load was partially transferred from the bottom of the “Y” to the capital during the stressing operation. Strain devices located on the Span 5 side of the centerline of the pier (C101, C104, C106; C112) experienced compressive strain changes. Strain devices located on the transverse centerline of the pier (C108, C114) experienced tensile strain changes. This intuitively makes sense due to the fact that the bearings for Span 5 are not centered on the shaft centerline, but are placed on the Span 5 side of the pier. Bending is induced in the pier, causing tensile strain changes along the transverse centerline of the pier.

When the hydraulic jacks are released and Span 5 is placed on the bearing, a noticeable compressive strain change occurs in devices located on the Span 5 side of the pier. Devices located along the transverse centerline of the pier (C108, C114) do not exhibit a corresponding strain change.

The placement of Span 6 on the bearings has an effect which is the reverse of that caused by placement of Span 5 on the bearings. When Span 6 is placed on the bearings of the pier, devices C101, C104, C106 and C116 exhibit a distinct tensile strain change. Devices C108 and C114 experience a compressive strain change. When Span 6 is placed on the bearings, devices located in the shell of the shaft (C104, C106, C112) exhibit a tensile strain change approximately equal to the compressive strain change caused by placement of Span 5 on the bearings.

Figure 5.22 shows a comparison of devices located in the same relative position in the cross section of the shaft. Devices C104 and C101 experience less strain change due to the superstructure load than do devices C112 and C106. All of these devices located in the shaft of the concrete exhibit a distinct compressive strain change when Span 6 is placed on the bearings. Strain devices C114 and C108 are located in the core of the concrete. They do not exhibit a distinct strain change when Span 5 is transferred from the bottom of the “Y” to the bearings.

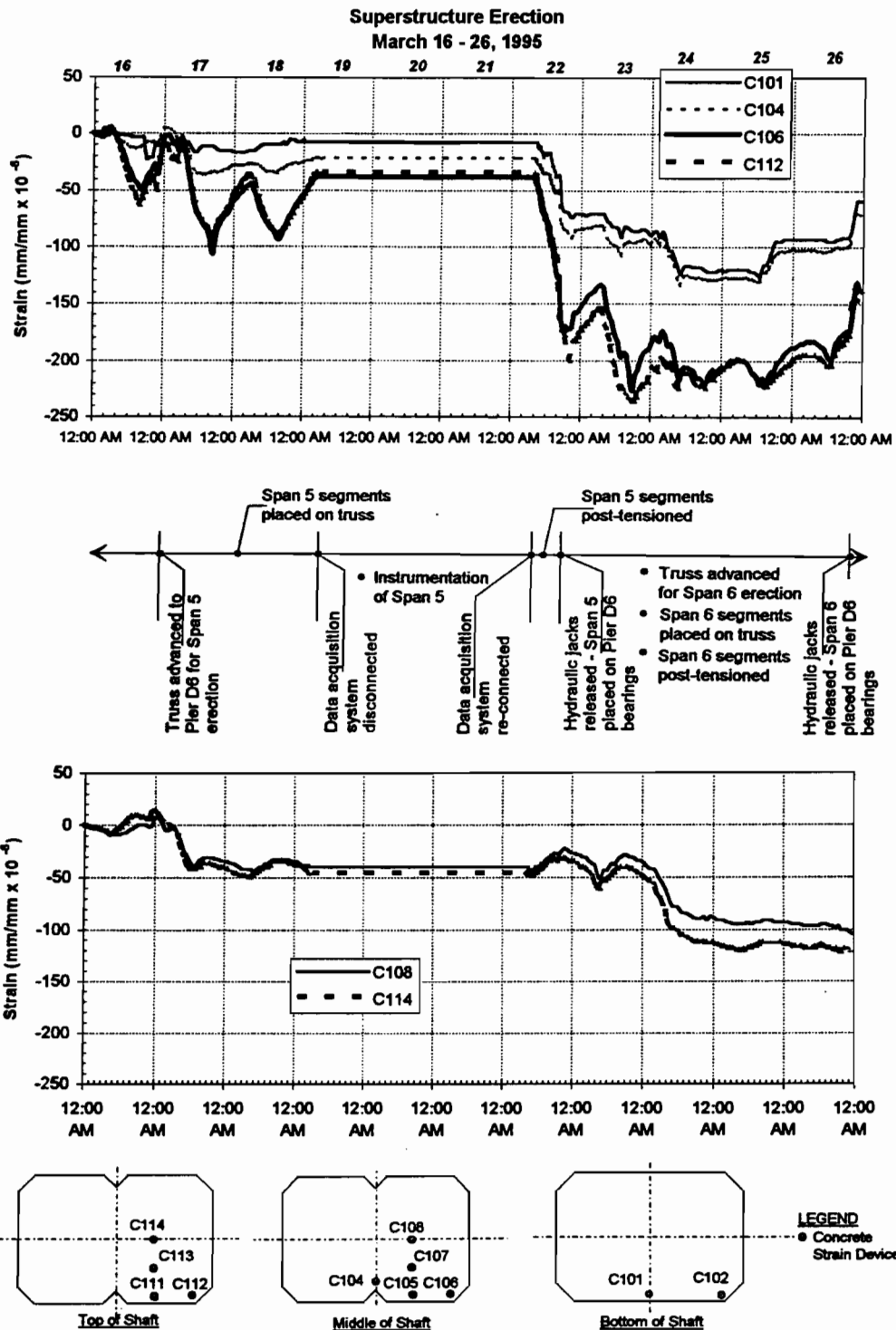


**Figure 5.22** Comparison of strain changes “vertically” in shaft during construction of superstructure.

As mentioned previously, the strain changes presented in this section contain thermal as well as gravity load effects. In order to compare the measured loads due to gravity to the loads predicted by a strut-and-tie model, thermal strains must be separated from the total measured strains presented in this chapter. A procedure for separating thermal strains from total strains is discussed in the next section.

## 5.5 Gravity Load Strains

As indicated in Section 5.2, temperature changes induce thermal strains in the mainlane piers of US 183. The following sections describe the significance of thermal strains as related to the total measured strains due to the superstructure dead load, suggest a procedure for separating these thermal strains from the total measured strains, and present a strut-and-tie model for the US 183 mainlane pier which is used to compare predicted and measured forces.

### 5.5.1 Significance of Thermal Strains

A comparison of expected gravity strains due to placement of the superstructure dead load,  $\mu_{\text{gravity}}$ , and measured thermal strains during these construction operations,  $\mu_{\text{thermal}}$ , is given in Table 5.2. Expected gravity strains were calculated based on the gross cross-sectional area of the concrete and a simplified load distribution of P/A (gravity load/cross-sectional area). Calculations can be found in the Appendix of Ref (2). Measured thermal strains were taken from data presented in Section 5.3 for March 11, 1995.

**Table 5.2 Comparison of expected gravity strains and measured thermal strains**

	<i>Pipe</i>	<i>Capital</i>		<i>Shaft</i>	
		<i>Shell</i>	<i>Core</i>	<i>Shell</i>	<i>Core</i>
$\epsilon_{\text{gravity}} (\mu\epsilon)$	210	40-80	40-80	70	70
$\epsilon_{\text{thermal}} (\mu\epsilon)$	10	80-95	20	70	10-50
$(\epsilon_{\text{thermal}} / \epsilon_{\text{gravity}}) \times 100$	5	40-200	25-50	100	15-70

Although  $\mu_{\text{thermal}}$  is only approximately 5% of  $\mu_{\text{gravity}}$  for the structural steel pipe, it ranges from 15 to 200% of  $\mu_{\text{gravity}}$  for the capital and the shaft. Thermal strains can be expected to be the same order of magnitude as gravity strains in certain cases. For this reason, the extraction of thermal strains from the total strains which were presented in Section 5.4 as measured during superstructure erection must be addressed.

### ***5.5.2 Procedure for Extraction of Thermal Strains from Measured Strains***

As indicated in Section 5.2, temperature differentials across the concrete section and between the concrete and the structural steel pipes induce thermal strains in the pier. If temperature differentials on the pier are the same for two separate times, the induced thermal strains should be the same for the two times regardless of the individual temperatures at each thermocouple location.

Data collected immediately prior to and subsequent to Span 5 and Span 6 erection over Pier D6 was investigated to determine if temperature differentials on the pier were the same for any two times. Several relative locations for temperature comparisons were considered to be of importance and are listed in Table 5.3.

**Table 5.3**      ***Temperature differential locations compared for thermal strain extraction***

<b><i>Thermocouple Designation</i></b>	<b><i>Location in Pier</i></b>
T103 - T101	Exposed Pipe - Embedded Pipe
T103 - T105	Exposed Pipe - Concrete Core
T103 - T104	Exposed Pipe - Concrete Shell
T104 - T105	Concrete Shell - Concrete Core
T106 - T107	Concrete Shell - Concrete Core

Stable temperature trends were observed on March 15-16, prior to superstructure erection, and March 30-31, subsequent to superstructure erection. During these times, no significant heating or cooling trends occurred, and the gravity load was constant. Relative temperatures were calculated for thermocouples located as indicated in Table 5.3 for these days. Temperature differentials prior to and subsequent to superstructure erection were compared. Close inspection of the differentials indicated that at 4:00 A.M. on March 16 and 4:00 A.M. on March 30, the variance in the differentials was less than 1 °C (1.8 °F) for each location comparison. These relative temperatures are shown in Table 5.4.

**Table 5.4** *Relative temperatures for March 16 and March 30, 1995*

<i>Date</i>	<i>Time</i>	<i>Differential (°C)</i>				
		T103-T101	T103-T105	T103-T104	T104-T105	T106-T107
March 30	4:00 A.M.	-1.83	-3.28	-0.98	-2.30	-2.22
March 16	4:00 A.M.	-2.33	-3.92	-1.59	-2.33	-2.22
Variance	4:00 A.M.	0.50	0.64	0.61	0.03	0

Since the temperature differentials for these times are very close, the assumption was made that the strains measured at 4:00 A.M. on March 16 prior to the superstructure erection could be directly subtracted from the strains measured at 4:00 A.M. on March 30 subsequent to the placement of Spans 5 and 6 on Pier D6, and thermal strains would in effect be negated.

## **5.6 Superstructure Dead Load Strains in Pier**

As mentioned previously, strut-and-tie modeling has a limited capability to detect compatibility and constraint induced stresses. For this reason, the procedure discussed in Section 5.5.2 was used to correct the total measured strains induced in the pier due to the total superstructure load in order to eliminate any thermal effects. The known weight of the superstructure produced a load on each branch of the pier capital of 4430 kN (996 kips). The following sections present these strains after they were adjusted for temperature effects.

### **5.6.1 Pipe Strains**

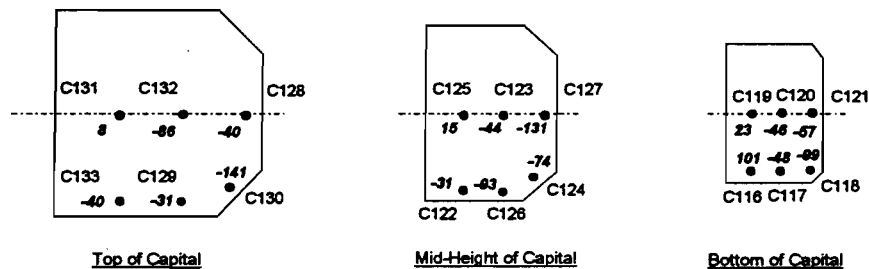
The superstructure dead load induced strains measured on the structural steel pipes are shown in Table 5.5. Thermal strains have been extracted from these strains. Both pipes show very similar trends along their lengths. Strain gauge locations are shown in Figure 5.17 and 5.18. The force is greatest in the exposed portions of the pipes. Once the pipes enter the concrete, force begins to rapidly transfer to the concrete through the steel/concrete bond. At the ends of the pipes, negligible strains exist.

**Table 5.5 Superstructure dead load strains measured in structural steel pipes: thermal strains extracted.**

<i>Single Exterior Pipe</i>		<i>Single Interior Pipe</i>	
<i>Strain Gauge</i>	<i>Strain</i> ( $\mu\epsilon$ )	<i>Strain Gauge</i>	<i>Strain</i> ( $\mu\epsilon$ )
S107, S108	-12	S119, S120	3
S109, S110	12	S121, S122	22
S111, S112	58	S123, S124	85
S113 - S116	230	S125 - S128	266
S117, S118	251	S129, S130	258

### 5.6.2 Capital Strains

Concrete strain devices were used in the capital to measure strains. Strains due to total superstructure dead load after thermal strains are shown in Figure 5.23. For evaluation purposes, strains were averaged as shown in Table 5.6. As the distance from the inside face of the “Y” increases, the strains are increasingly compressive.



NOTE: Measured strains are indicated in italics in  $\mu\epsilon$ .

**Figure 5.23 Strains measured in capital due to superstructure dead load: thermal strains extracted.**

**Table 5.6** Average superstructure dead load strains measured in the capital: thermal strains extracted.

<i>Bottom of Capital</i>		<i>Mid-Height of Capital</i>		<i>Top of Capital</i>	
<i>Concrete Strain Device</i>	<i>Strain (μϵ)</i>	<i>Concrete Strain Device</i>	<i>Strain (μϵ)</i>	<i>Concrete Strain Device</i>	<i>Strain (μϵ)</i>
C119, C116	-17	C125, C122	-8	C131, C133	62
C120, C117	-58	C123, C126	-69	C132, C129	-47
C121, C118	-90	C127, C124	-102	C128, C130	-78

**Average Strains Across Capital Sections**

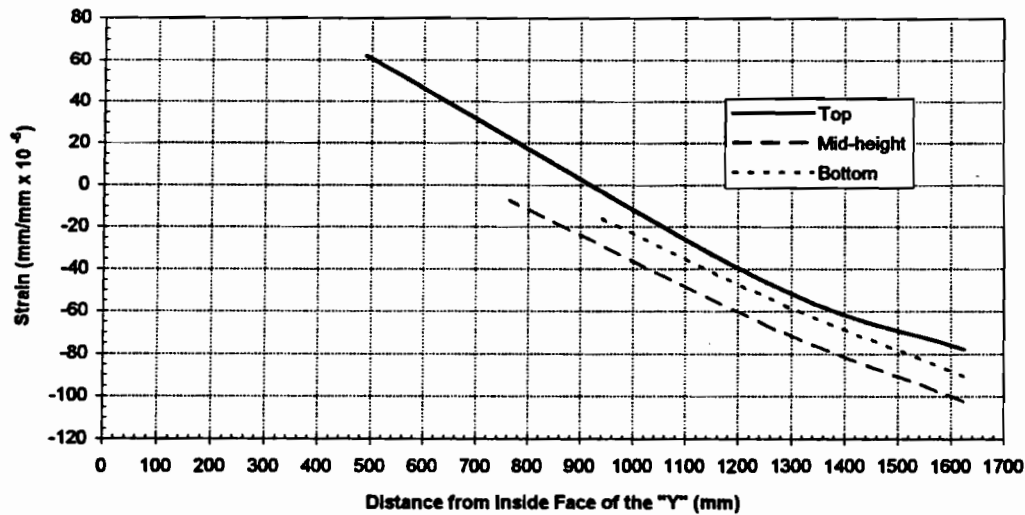


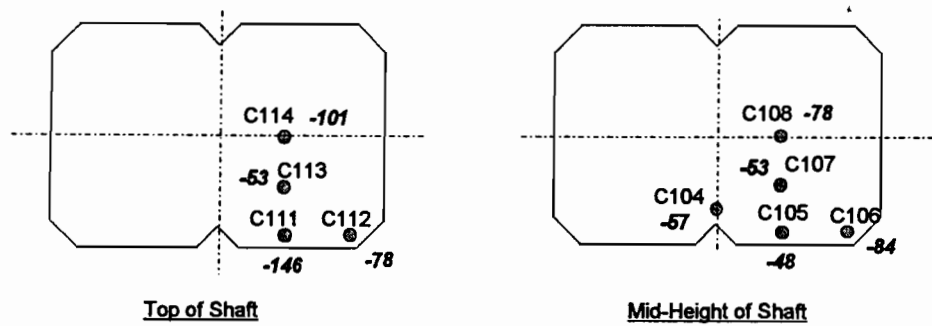
**Figure 5.24** Strain distribution across each section of the capital: thermal strains extracted.

The strain distribution across each section is shown in Figure 5.24. The outside face at each section is in compression. Strain distribution is approximately linear for both the mid-height and bottom sections. Although the strain gauges located on the inside face of the “Y” were damaged during construction, extrapolation of the measurements indicates that the inside face of the “Y” at both of these latter sections would also be in tension.

Measurements along the top section of the pier indicate a more non-linear strain distribution than those at the mid-height and bottom sections. This may be due to the fact that the strain gauges at this level are located closer to the points of load application. The load may not have fully dissipated across the section at this location.

### 5.6.3 Shaft Strains

Strains measured in the shaft of the pier due to the superstructure dead load are shown in Figure 5.25. All strains are compressive. Average strains are shown in Table 5.7. Average strains at the top of the shaft are substantially larger than at mid-height. After the correction for thermal strains was made, calculated strains at the bottom of the shaft were highly erratic and unexplainable. Therefore, they were neglected.



**NOTE:** Measured strains are indicated in italics in  $\mu\epsilon$

**Figure 5.25** *Strains measured in the shaft due to superstructure dead load: thermal strains extracted.*

**Table 5.7 Forces measured in pipes due to gravity load.**

<i>Single Exterior Pipe</i>		<i>Single Interior Pipe</i>	
<i>Strain Gauge</i>	<i>Force</i> kN (kips)	<i>Strain Gauge</i>	<i>Force</i> kN (kips)
S107, S108	-19.8 (-4.5)	S119, S120	4.89 (1.1)
S109, S110	19.8 (4.5)	S121, S122	36.3 (8.2)
S111, S112	95.6 (21.5)	S123, S124	140 (31.6)
S113 - S116	380 (85.4)	S125 - S128	399 (98.7)
S117, S118	415 (93.2)	S129, S130	426 (95.8)

## 5.7 Superstructure Dead Load Forces in the Mainlane Pier

Strains measured in the pier were converted to forces and are shown in this section. Calculations are presented in the Appendix to Reference 2.

### 5.7.1 Pipe Forces

Pipe forces were calculated from the strains presented in Table 5.5 using a Young's modulus of 199,955 MPa (29,000 ksi) and a cross sectional area of 8258 mm<sup>2</sup> (12.8 in<sup>2</sup>). The forces are shown in Table 5.8 for the single pipes instrumented. The effective pipe force of the tension tie would be the sum of the forces in the four pipes.

### 5.7.2 Capital Forces

Compressive forces measured in the capital due to gravity load were calculated from the averaged concrete strains presented in Table 5.6 and are shown in Table 5.9. Only compressive stress areas were used in calculations since the tensile capacity of concrete is neglected in strut-and-tie modeling. These forces were calculated based on a Young's modulus of 28,270 MPa (4100 ksi). This modulus was measured in the laboratory using concrete specimens taken from the casting of the capital for Pier D6.

### 5.7.3 Shaft Forces

Shaft forces were calculated from the averaged measured strains presented in Table 5.3 using a Young's modulus of 24,130 MPa (3500 ksi). This modulus was measured in the laboratory using test specimens taken from the concrete during casting of the shaft for

Pier D6. Forces were calculated based on the average core strains and one half the cross sectional area of the shaft at the location of the instrumented section. Forces are presented in Table 5.10.

**Table 5.8** *Average measured strains in shaft due to superstructure dead load: thermal strains extracted*

<i>Top of Shaft</i>		<i>Mid-Height of Shaft</i>	
<i>Average Strain Across Section (μϵ)</i>	-95	<i>Average Strain Across Section (μϵ)</i>	-64
<i>Average Strain in "Core" (μϵ) (C113, C114)</i>	-77	<i>Average Strain in "Core" (μϵ) (C107, C108)</i>	-66
<i>Average Strain in "Shell" (μϵ) (C111, C112)</i>	-112	<i>Average Strain in "Shell" (μϵ) (C104, C105, C106)</i>	-63

**Table 5.9** *Compressive forces measured on one branch of the capital due to superstructure dead load.*

<i>Compressive Force</i>	
kN (kips)	
<i>Mid-Height of Capital</i>	2215 (498)
<i>Bottom of Capital</i>	1637 (368)
<i>Average</i>	1926 (433)

**Table 5.10** *Forces measured in one-half of shaft due to superstructure dead load.*

<i>Force</i>	
kN (kips)	
<i>Top of Shaft</i>	3683 (828)
<i>Mid-Height of Shaft</i>	3157 (710)
<i>Average</i>	3420 (769)

### 5.8 Strut-and-Tie Model for US 183 Mainlane Pier

A strut-and-tie model (STM) was developed for the US 183 mainlane pier to compare predicted forces with measured service load forces. Strut-and-tie modeling is an *ultimate load model* developed for reinforced concrete design. Strut-and-tie modeling serves the designer by allowing efficient proportioning of reinforcement in patterns and quantities that satisfy equilibrium assuming that predicted force paths are followed by the applied load. Since STM is strictly speaking only applicable to ultimate load conditions, the only purpose of comparing the strut-and-tie model with *measured service load* forces is to investigate the general agreement of strut-and-tie modeling in predicting the basic flow of forces in a structure. A detailed discussion of strut-and-tie modeling can be found in Chapter 2.

The US 183 mainlane piers provide an excellent opportunity for the use of strut-and-tie models. A STM typical for a reinforced concrete wall subjected to two widely spaced concentrated loads is shown in Figure 5.26(a). Dashed lines represent compression struts, and solid lines represent tensile ties. The US 183 pier is shown in Figure 5.26(b) with the same general force path illustrated as for the wall. In areas of the reinforced concrete wall where the concrete is not necessary for the flow of forces, the concrete has been removed to form the US 183 pier. The flow of forces is easily visualized due to the shape of the structure. Figure 5.26 shows the efficiency of the basic shape chosen for the US 183 mainlane piers. The basic force path of Figure 5.26(b) was used to develop a strut-and-tie model for the instrumented pier.

In Figure 5.26(b), the superstructure dead load is assumed to be evenly distributed across the bearing pads. For this reason, the assumption is made that the compressive struts transferring the force through the capital must pass through the centroid of the applied load at the center of the bearing pad, or at node (A). The load is assumed to be evenly distributed at the bottom

of the shaft. Therefore, the compressive struts in the shaft must pass through the location of the half-pier force resultants of the distributed load at the bottom of the pier, or node (B). The location of the intermediate node (C) is somewhat arbitrary and will vary according to the particular model assumed. Thus, the angle  $\theta$  is a variable assumed by the designer in choosing a STM. Node (C) should be chosen so that the force centroid on the path between nodes (A) and (C) lies well within the concrete capital cross section.

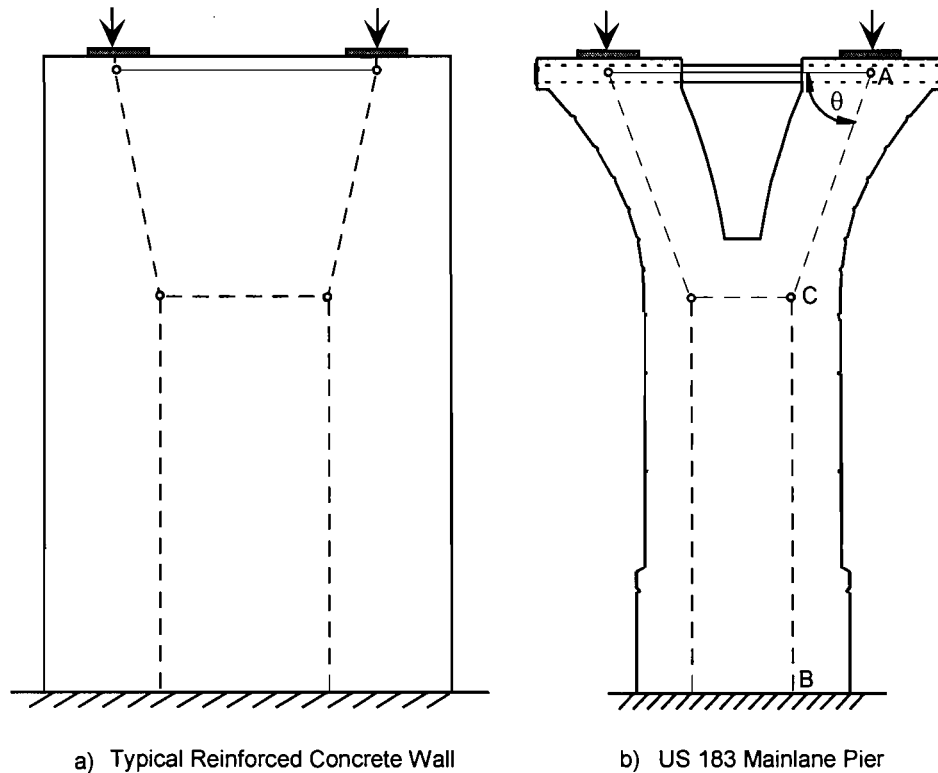


**Figure 5.26 Basic force path in the US 183 mainlane piers.**

### 5.8.1 Strut-and-Tie Model Based on Measured Forces

Two approaches were investigated for selection of a strut-and-tie model of the pier based on measured forces. These approaches are discussed in the following sections.

#### 5.8.1.1 Strut-and-Tie Model Based on Compressive Force Resultants in the Capital

In order to investigate the actual force path as indicated by measured compression strains, the force path in the pier was determined by assuming that the compression strut of the capital follows the location of the compressive force resultant at each instrumented level. The compression strut of the capital is also assumed to meet the tension tie of the pipe directly below the center of the bearing.

A graphical representation of this procedure is shown in Figure 5.27. In Figure 5.27(a), a strain diagram for each instrumented section is shown. These strain diagrams were obtained by using the average measured strains across each section as shown in Figure 5.24. The average strain at the outside face of the “Y” was assumed to be valid. An approximate linear fit was made through the measured data, and the linear fit was extrapolated to the inside face of the “Y.”

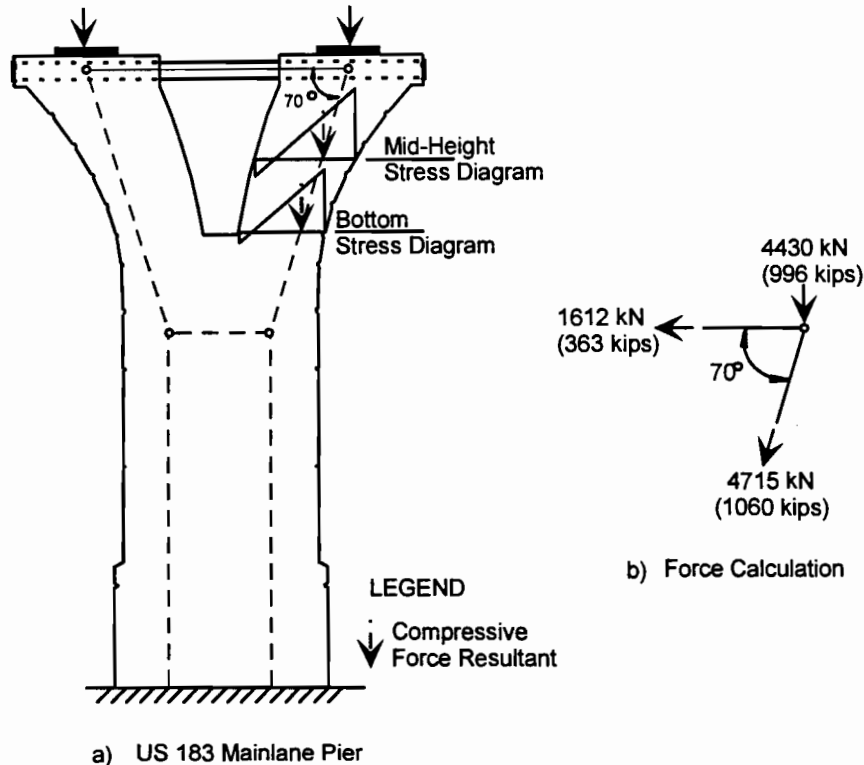


**Figure 5.27** Calculation of the orientation of the compression strut in the capital based on measured compressive centroids.

The neutral axis was then graphically measured, and the location of the compressive force resultants were calculated for each section assuming that the resultant force acts at a centroid located at the “1/3 points” of the compressive portion of the stress diagram. This assumption assumes the section is rectangular in shape, which is a reasonable approximation for the capital section. This measured “1/3 point” at the mid-height of the capital was calculated to be approximately 330 mm (13 in) from the outside face of the “Y.” The “1/3 point” at the bottom of the capital was similarly calculated to be about 356 mm (14 in) from the outside face of the “Y.” These calculations are given in the Appendix of Reference 2.

In order to calculate the angle  $\theta$ , through which the compressive strut of the capital acts, a line was drawn through these points as shown in Figure 5.27(a). The angle was measured to be approximately  $70^\circ$ . As shown in Figure 5.27(b) if the angle  $\theta$  is  $70^\circ$  for an applied superstructure dead load of 4430 kN (996 kips), from geometry the pipe force is 1612 kN (363 kips) and the compressive strut force is 4715 kN (1060 kips). These forces are also shown in Figure 5.28(a).

#### **5.8.1.2 Measured Force Distribution**

The previous section indicated that from measured superstructure dead load compressive force paths, the angle  $\theta$  is  $70^\circ$ . Individual measured pipe forces were presented in Table 5.8. The total pipe force across the tension tie was calculated to be 1681 kN (378 kips) by adding these measured forces and multiplying them by two. The compressive force in the compression strut of the capital as measured by the embedded strain devices, as shown in Table 5.9, was 1926 kN (433 kips), the average of the compressive forces at the mid-height and bottom of the capital. Table 5.10 shows the compressive force in each compressive strut in the shaft as measured by the embedded strain devices to be 3420 kN (769 kips). These forces do not satisfy equilibrium at any node and thus the basic accuracy of the measurements is questionable. These forces are also shown in Figure 5.28(b).

#### **5.8.2 Strut-and-Tie Model Based on an Elastic Frame Analysis**

An elastic frame analysis was performed for the capital of the pier to estimate the force in the structural steel pipes. Varying stiffnesses were used for the “Y” branch of the capital. The base of the “Y” was assumed to be fixed. The superstructure dead load of 4430 kN (996 kips) was applied on each branch of the “Y.” Calculations for section properties and dimensions for the model are shown in the Appendix to Reference 2. The total force across the tension tie was determined by the elastic frame analysis of the capital as 1368 kN (308 kips). Based on this force and the known superstructure dead load, the angle  $\theta$  was determined from equilibrium to be  $73^\circ$ . This would be possible since the compression strut path would still fall within the capital branch concrete section. The corresponding compression force in the compression strut along the capital was calculated from equilibrium to be 4635 kN (1042 kips). These forces are also shown in Figure 5.27(c).

### **5.9 Comparison of Forces and Force Paths**

Figure 5.28 shows a comparison of the measured forces with the forces determined from the various strut-and-tie analyses. Figure 5.28 shows the STM with forces in equilibrium based on an angle  $\theta$  of  $70^\circ$  as indicated from the centroids of the measured compressive force path.

Figure 5.28 shows the measured forces. These measured forces do not satisfy equilibrium, and particularly the inclined compressive strut force is questionable. Figure 5.28 also shows a STM with the forces in equilibrium. This STM is based on an assumed angle  $\theta$  of  $73^\circ$  as indicated from the elastic frame analysis results.

The measured pipe forces, shown in Table 5.8, show very similar trends across the pipe lengths. Also, similar forces were measured in both pipes. For these reasons, the measured pipe forces are thought to be very reliable. The very close agreement (within approximately 4%) of the measured pipe force shown in Figure 5.28 with that predicted by the strut-and-tie model in Figure 5.28 appears to confirm the validity of the  $70^\circ$  STM.

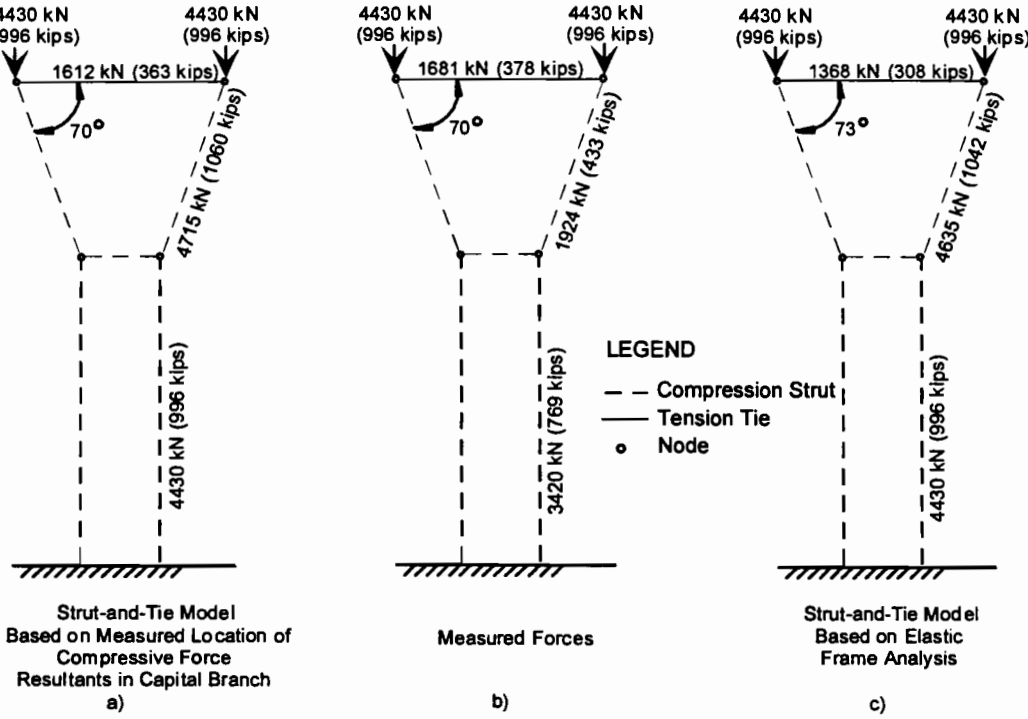


**Figure 5.28 Comparison of measured forces and strut-and-tie model forces.**

Assuming the measured pipe force due to superstructure dead load is known with reasonable certainty, the pipe force predicted by the strut-and-tie model of Figure 5.28 differs only 4 percent from the actual force in the pipe while the pipe force predicted by the elastic frame analysis shown in Figure 5.28 differs by 19 percent, both unconservative.

The point should be made that the strut-and-tie model presented in Figure 5.28 was developed by basing the design variable,  $\theta$ , somewhat on measured forces. A designer would obviously not have these measured forces on which to base a selection of  $\theta$ . However, the

selection of the location of the compressive strut in the branch of the capital by an experienced designer would likely be fairly close to  $70^\circ$  based on the geometry of the pier. A smaller  $\theta$  would require the compressive strut to approach an area of the capital branch where, intuitively, tensile forces are quite possible. A larger  $\theta$  would allow the compressive strut to approach the exterior face of the “Y” and eventually exit the concrete capital cross section, which is inadmissible.

The STM strut forces in Figure 5.28, calculated based on the compressive strut orientation indicated by the location of the measured compressive force resultants, do not agree with the measured strut forces shown in Figure 5.28. The measured concrete strains are substantially lower than those calculated based on an angle  $\theta$  of  $70^\circ$ . The calculated pipe force of 1612 kN (363 kips) agrees very well with the measured pipe force of 1681 kN (378 kips).

Several observations may explain the fact that the measured concrete forces do not agree with those predicted by the strut-and-tie model shown in Figure 5.28. Figure 5.23 shows the strains measured in the capital. These individual strain measurements are somewhat erratic and do not present any general trends across the sections. Figure 5.25 shows that the strains measured in the shaft also exhibit unexplainable erratic behavior. Strain devices located directly above one another do not agree at most locations. These behaviors may be due to lack of instrument sensitivity in reading the low strains produced in the concrete due to the superstructure dead load. Such low strain readings are difficult to measure electronically and can be affected by slight resistance changes.

The difference in the forces measured in the capital and those predicted by the strut-and-tie model may also be explained by assumptions inherent to strut-and-tie modeling. Strut-and-tie modeling is an ultimate load model. The strut-and-tie model presented in this chapter for the US 183 mainlane pier was based on service loads. As indicated by the strains measured at each section of the capital, tensile strains are present at levels below those needed to crack the concrete. The tensile capacity of the concrete is neglected for most practical cases with the use of strut-and-tie modeling. The concrete can be assumed to be carrying tensile loads in those areas where tensile strains were measured. The strut-and-tie model does not account for this concrete tensile capacity.

Strut-and-tie modeling is a design tool and is not intended for use in analysis. As such, exact agreement between measured forces and strut-and-tie model forces is not expected. The force path used for the strut-and-tie model of Figure 5.28 was very close to the measured force path. Thus, the angle  $\theta$  used in the STM agrees very well with reality. The calculated tie force is in close agreement with the measured tie force when this angle is used, indicating the ability of a strut-and-tie model to accurately determine the key reinforcement (the structural steel pipes in this case) needed in a structure.



## CHAPTER 6

### ***6. MEASURED BEHAVIOR - RAMP P SEGMENTAL PIER AND INTERPRETATION***

#### **6.1 General Temperature Trends**

Thermocouples measured temperatures in pier P16 beginning on April 12, 1996, and continuing hourly through May 1, 1996. After a brief interruption following pier post-tensioning operations, data were again recorded hourly from May 4, 1996, to August 1, 1996. The thermocouples appear to be extremely reliable and consistent, and from their measurements several general trends in temperature became apparent. Highly detailed comments and further data are given in Reference 3. Only major trends are reported herein.

##### ***6.1.1 Daily Cycles***

The general assumptions regarding the effects of thermal gradients on members made in Chapter 2 are valid for bridge piers and superstructures. However, predicting the characteristics of temperature gradients in bridge pier sections is more complex due to the pier's physical orientation.

Bridge superstructures, especially winged trapezoidal box girders, will typically experience well-defined gradients during the course of any given day. The sun's path across the sky causes it to directly heat the top slab of the girder, while the webs and bottom flange see virtually no solar heating. The thermal gradients always occur most significantly along the depth of the girder. Therefore the induced stresses also act in a well-defined manner.

However, bridge piers do not undergo a thermal gradient in only one direction over the course of a day. Due to the pier's orientation with respect to the sun's path across the sky, the largest temperature gradients occur at any given time along an axis oriented towards the sun's location (see Figure 6.1). Gradients in other directions will also be present, but will exhibit smaller temperature differences. Thus the pier's response changes over the course of the day.

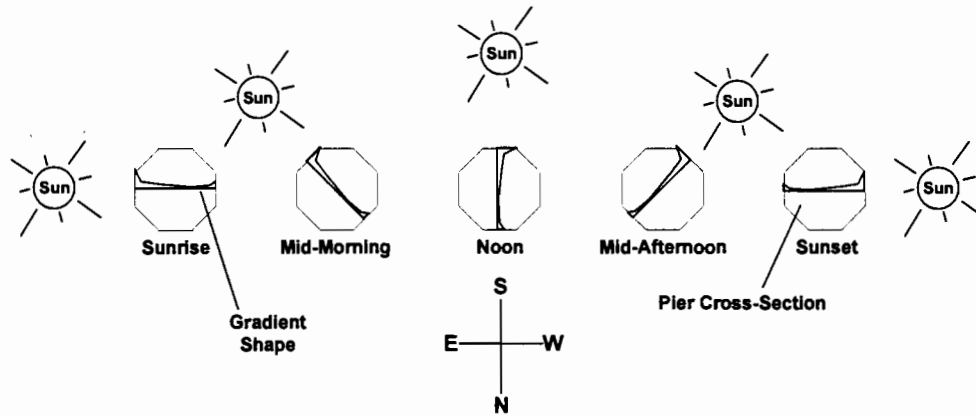


**Figure 6.1** Temperature gradient orientations at different times in the day.

The thermocouples located in the “gradient” segment PC16-5 were ideally placed to record the daily change in gradient orientation as the sun moved across the sky and heated progressive faces of the pier’s surface. Figure 6.2 illustrates this concept with temperatures recorded on June 17, 1996. This date was chosen to represent a typical summer day because it occurred in the middle of several consecutive days that exhibited steady daily cycles of temperature. Each thermocouple is located within 25 mm of the pier’s outer surface. After the sun heats each outer face, the corresponding thermocouple records a peak in temperature. The thermocouple then cools slightly while the subsequent face is heated.

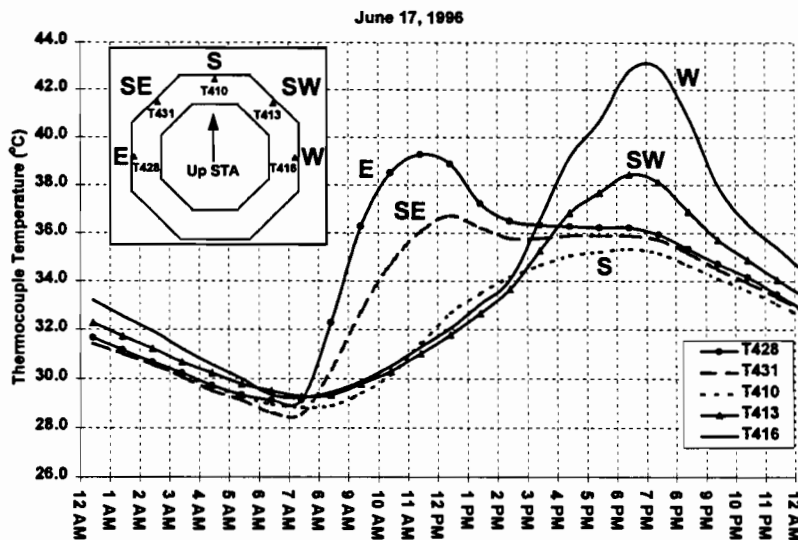


**Figure 6.2** Typical daily temperature cycle of selected outside-layer thermocouples in gradient segment PC16-5.

These data indicate that the east- and west-facing sides of the pier undergo the largest daily fluctuations in temperature. It is most likely, therefore, that the largest temperature gradients across the pier's section will occur along an axis running east to west. Gradients occurring along other axes could also be important, though, depending on bridge geometry.

### 6.1.2 Seasonal Characteristics

Environmental effects such as prevailing weather patterns can strongly influence the shape and magnitude of thermal gradients in bridge members. Alternating warm and cold fronts cause wide fluctuations in daily ambient temperatures and can mitigate solar radiation with cloud cover. Conditions that vary in this manner have a greater potential to produce large temperature gradients than more stable and cyclical patterns.

Figures 6.3 and 6.4 illustrate seasonal characteristics of weather as measured on top of the pier. The month of April (Figure 6.3) is characterized by particularly variable weather patterns with a maximum temperature change in a 24-hour period of about 18° C on April 29. This time of the year is typically the rainy season in Austin and often marked by the arrivals of alternating warm and cold fronts to the area every few days.

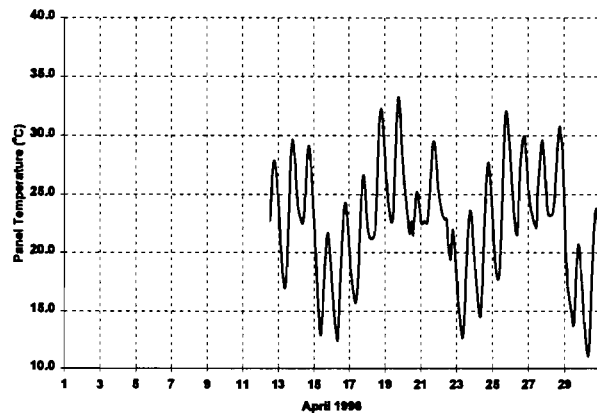


**Figure 6.3** *Datalogger panel temperatures recorded during April 1996.*

In contrast, the month of July exhibits very stable weather patterns (see Figure 6.4). Daily high and low temperatures changed very little. The largest temperature change in 24 hours is about 10° C. Thus, it appears that large short-term changes in ambient temperature, and possibly large section temperature gradients, will most likely occur during the spring in Austin. The summer months are too hot and humid (humidity prevents rapid cooling at night) to undergo large variations in temperature, and tend to exhibit very regular, stable characteristics. Likewise, the winter months are too cold to

allow significant heating of the pier to produce large gradients. The fall season may again bring weather patterns conducive to producing large daily temperature differentials and the large thermal gradients associated with those variations.

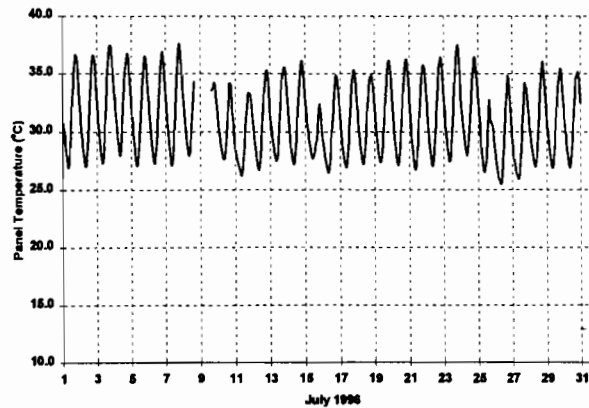


**Figure 6.4** *Datalogger panel temperatures recorded during July 1996.*

### **6.1.3** *Effects of Cover*

The extremely low thermal conductivity of concrete insulates gauges located away from surfaces exposed to sunlight. This effect produces severe temperature gradients. The effects of concrete cover over the course of a typical summer day (June 17, 1996) are shown in Figure 6.5. It is readily apparent that the outermost gauge T416 undergoes relatively large fluctuations in temperature on a daily basis. During this particular day, a maximum temperature change of about 14° C occurred at the location of T416. In contrast, the temperature changes are much smaller at the middle (5.5°C) and inner (2.5°C) faces of the pier's west wall. The temperatures here range from about 31.5° C at midday to just over 36° C at 9:00 PM. A comparison of the peak temperatures of the three gauges also illustrates the time lag associated with the concrete's thermal properties. The peak reading near the outer face occurred at 7:00 PM. This is also the peak temperature gradient with about 10° C difference between outer and inner face. The midwall temperatures peaked about 3 hours later while the inner face peaked about 8 hours after the outer face. The difference in temperature between T416 and T417 is greater than that between T417 and T418, indicating a nonlinear temperature distribution through the wall.

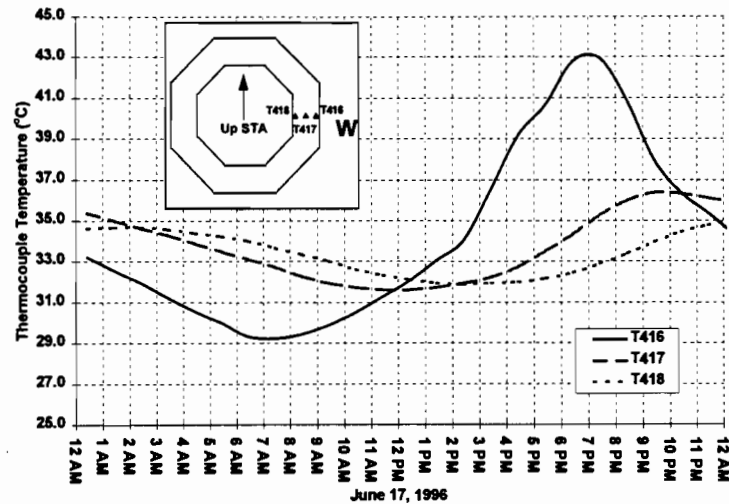


**Figure 6.5** Comparison of temperatures recorded through the thickness of the west wall on June 17, 1996.

#### 6.1.4 Effects of Shading

Thermocouples were distributed in segment PC16-5 to measure the shapes of temperature gradients occurring there. However, only a minimal number of thermocouples were placed in segments PC16-1 and PC16-7. The arrangements of instruments in these segments are not adequate to directly measure the thermal gradient shapes.

One can approximately deduce the gradient shapes in these segments by comparing thermocouple measurements at corresponding locations in each segment. Figure 6.6 shows temperatures recorded on June 17, 1996, in similar positions at the base, two-thirds height, top segment and capital (see Figure 3.14). The temperature tracks for segments at two-thirds and full height are almost identical because the two segments are both fully exposed to sunlight during the day. The base segment is continually shaded by the two overpasses of Interstate Highway 35 (see also Figures 3.13 and 3.14). The temperatures it experiences are lower overall and vary less than those of the upper segments exposed to direct sunlight. The capital thermocouple T511 should exhibit a similar curve to those of segments PC16-5 and PC16-7 due to the capital's full exposure to sunlight. However, T511 is located at a position of slightly more cover, causing it to experience smaller variations in temperature throughout the day. Therefore, it can be assumed that temperature gradients will exhibit similar shapes along the entire sunlit portion of the pier's shaft. The magnitudes of gradients in the shaded portion of the shaft and in the solid capital will undoubtedly be lower.

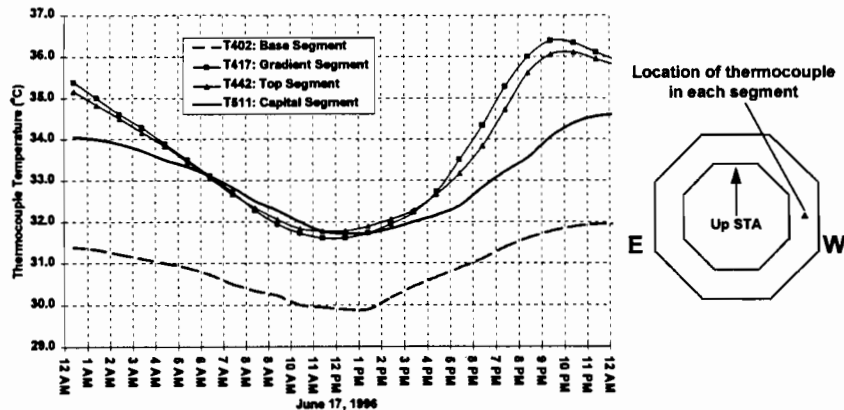


**Figure 6.6** Comparison of temperatures at locations along the height of pier P16.

## 6.2 Thermal Gradients

### 6.2.1 Pier Shaft Gradients

The shapes of thermal gradients occurring in the hollow, octagonal pier shaft cross-section can be directly obtained from the thermocouple measurements in segment PC16-5. Three thermocouples were placed through the thickness of each wall of the shaft. This distribution allows gradient shapes to be determined along four axes normal to the pier's longitudinal axis. A careful examination of all thermal data was carried out by Bonzon [3] to determine these gradients. Gradients along each axis are given in Reference 3. Only the maximum gradient is given herein.

Figure 6.7 shows a typical measured gradient for June 17, 1996, a day with hot, sunny weather and a little cloud cover.

The east-west axis of the pier's cross-section had the largest variations in temperature over the course of a day (see Figure 6.7). At 6:00 AM the outer surfaces of the pier are several degrees cooler than the interior. Throughout the morning the eastern face undergoes rapid heating as radiation from the rising sun strikes it directly. By mid-afternoon the east and west face temperatures have equalized, but the outer surfaces are much warmer than the pier's interior. The largest differential gradient occurs around 7:00 PM, when the west face is 10° C warmer than the interior, and 7° C warmer than the eastern face. High afternoon air temperatures and direct sunlight combine to heat the western face to a much higher level than along the rest of the axis. Note that the shape of this gradient is very similar to that of the AASHTO Code design gradient discussed in Chapter 2.

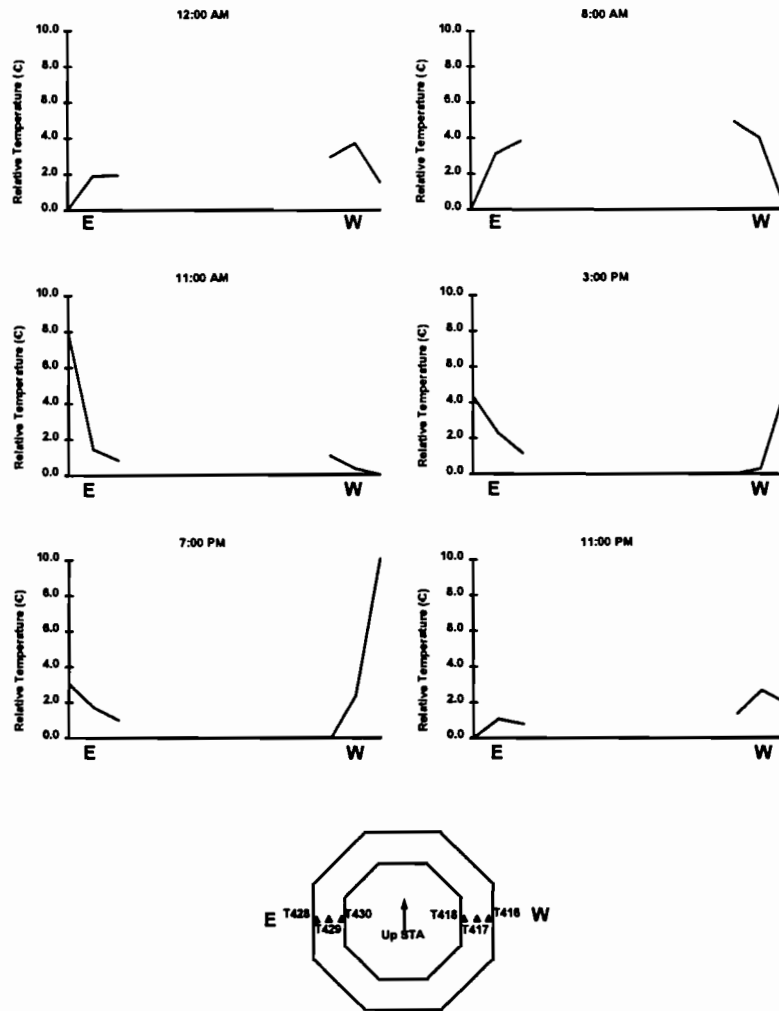


**Figure 6.7** *One day cycle of thermal gradients along the east-west axis of the cross-section, June 17, 1996.*

The Spring of 1996 was the most severe in terms of differential gradients as compared to all measurements made until January 1998. Maximum positive temperature gradients as measured from thermocouples located in segment PC16-5 at any time during the respective months are shown in Figure 6.8(a) for April through July 1996. The April values are the largest. All maximum positive gradients occurred along the east-west cross-sectional axis of the pier. For the purposes of comparison, the design gradient shapes from the *AASHTO LRFD Bridge Design Specifications* [8] and NCHRP Report 276 [5] are presented in Figure 6.8(b), along with the measured maximum value in the pier. Design code temperature values are plotted for the pier's location in Zone 2, Austin, Texas. The design code gradients plotted in Figure 6.5 were significantly larger than even the largest measured gradient. The maximum measured positive gradient's

highest temperature change was only 51% of the maximum temperature specified by both the AASHTO LRFD Code [8] and NCHRP Report 276 [17]. The LRFD Code gradient also has a sharp temperature difference between the outside fibers and the area a few centimeters from the surface. The NCHRP gradient's shape more closely follows that of the observed temperature gradient. Both design gradients, however, are larger in magnitude and more severe in shape. The maximum negative temperature gradients ever measured are shown in Figure 6.9(a). Again, April 1996 and the east-west axis are the highest. Comparisons with the design code values is shown in Figure 6.9(b).

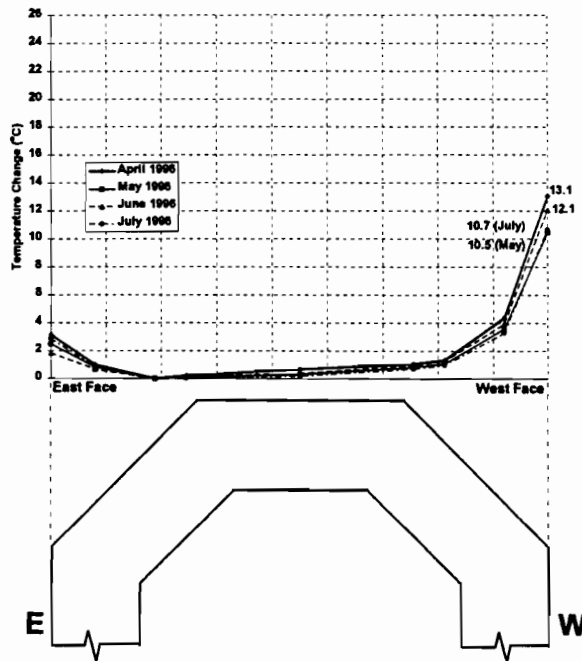


**Figure 6.8(a) Maximum measured monthly positive temperature gradients.**

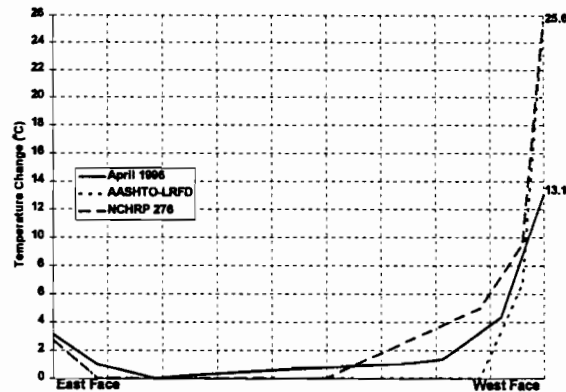


**Figure 6.8(b) Design code positive temperature gradients.**

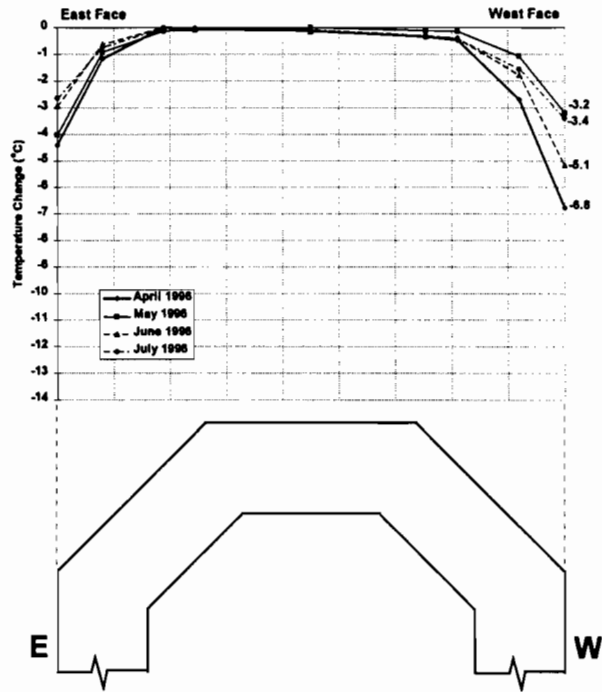


**Figure 6.9(a)** Maximum measured monthly negative temperature gradients.

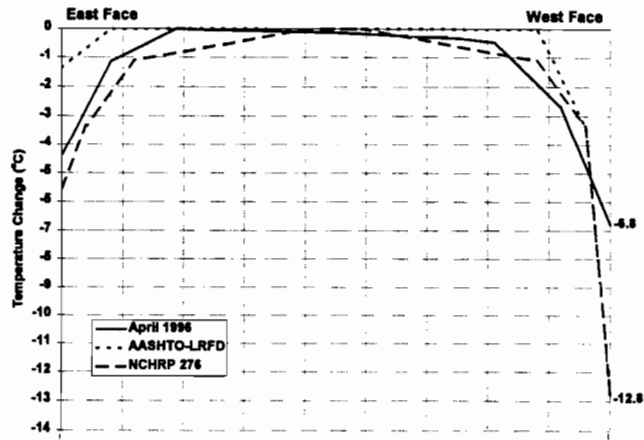


**Figure 6.9(b)** Design code negative temperature gradients.

## 6.2.2 Capital Gradients

Thermocouples were also installed to determine thermal gradients along 4 axes in the monolithic capital segment PC16-8 (see Figure 3.29). Data for all axes are given in Reference 3. Figure 6.10 shows plots of thermal gradients on the east-west axis as measured by the bottom layer of thermocouples. This was the axis with highest gradients.

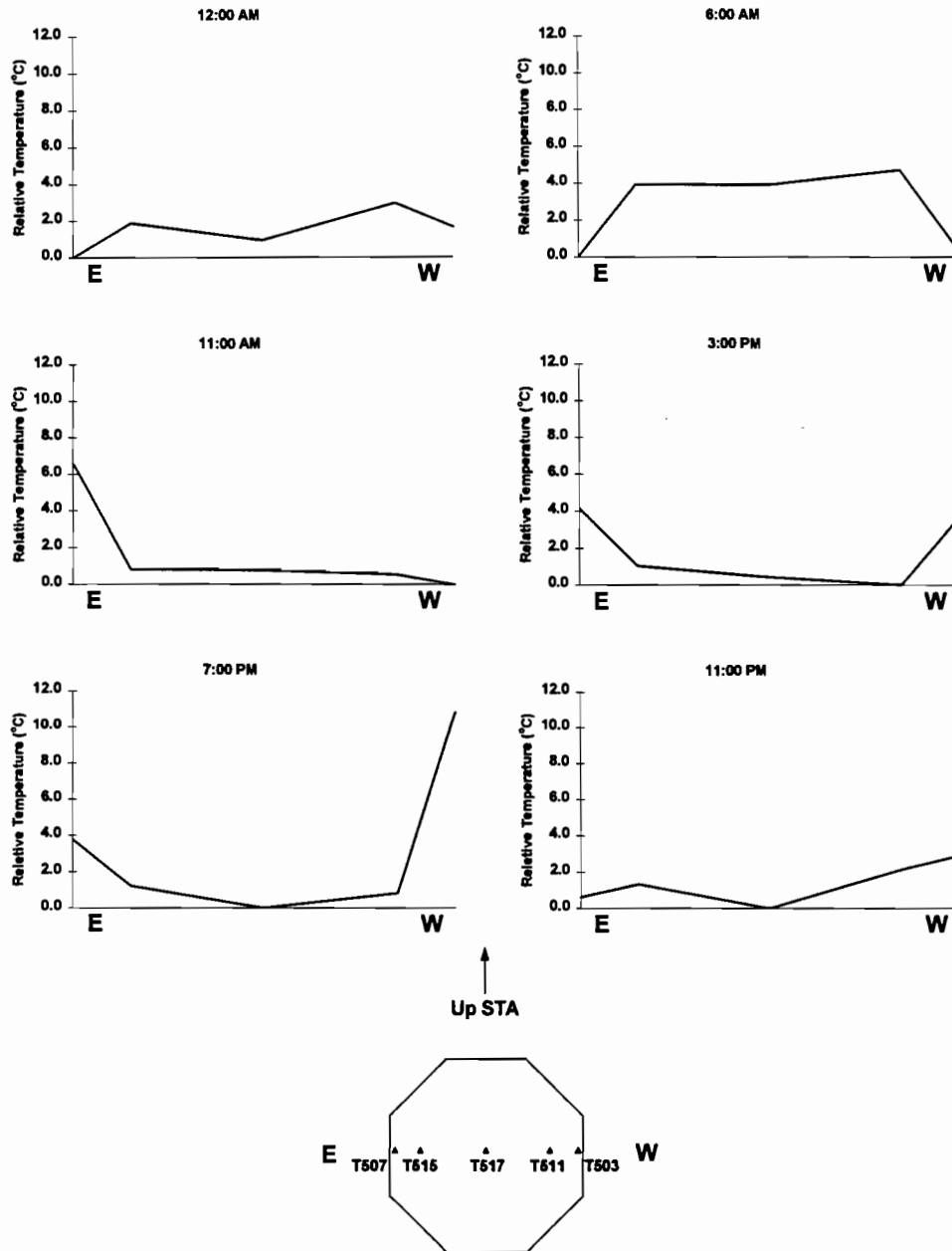


**Figure 6.10** One day cycle of thermal gradients along the east-west axis, capital segment PC16-8, June 17, 1996.

The maximum relative temperature recorded along the east-west axis is approximately 11° C, slightly larger than that found in the hollow shaft on the same day. This is most likely due to the well-insulated location of T517 deep within the concrete at the centerline of the capital's cross-section.

### 6.2.3 Capital Curing Gradients

Large thermal gradients can be induced during the construction of large monolithic concrete members. One of the byproducts of the concrete curing process is waste heat. Because of concrete's poor thermal conductivity, waste heat generated in the middle of a large monolithic member is trapped in the interior by the surrounding concrete, producing large thermal differences between the hot inner core and the cooler outer surface. During production of the capital segments, the contractor noticed small cracks along locations of reentrant corners such as reveals and blockouts. These fractures were already present when the forms were removed, indicating that they were not induced by shrinkage. Also, the cracks tended to close after several days when the capitals reached an equilibrium temperature with the ambient air. Therefore it was postulated that the cracking was due to large thermal differences between the inner core and outer surface of the capitals during curing (see Figure 6.11).

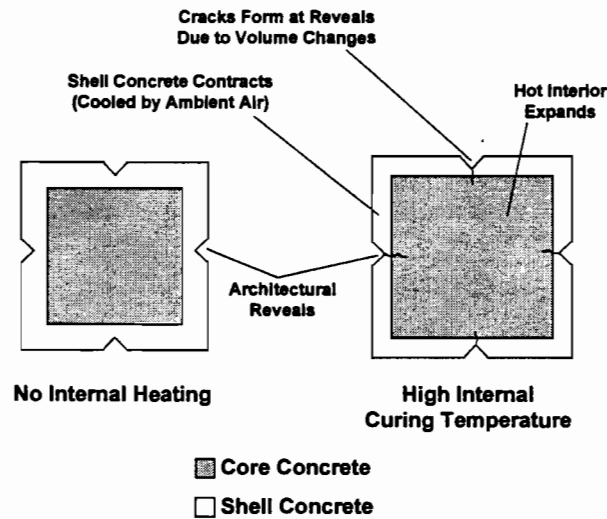


**Figure 6.11** Mechanism for cracking of large monolithic members during curing.

Temperatures in the capital segment PC16-8 were monitored during and after casting to determine the thermal gradients present during the curing process. As shown in Figure 6.12, the inner core temperature increased quickly after the placement of concrete was complete. The core temperature peaked about 26 hours after concrete placement and

steadily declined over a period of 7 days. Meanwhile, the ambient air temperature rose and fell over the course of several daily cycles. The maximum difference between the core and ambient temperatures occurred around 11:00 PM on September 19. At this point, the temperature difference reached almost 55° C. However, this value is much higher than the largest temperature gradient in the concrete because of the concrete's ability to store heat and dissipate it slowly (the concrete's surface is warmer than the ambient temperature).

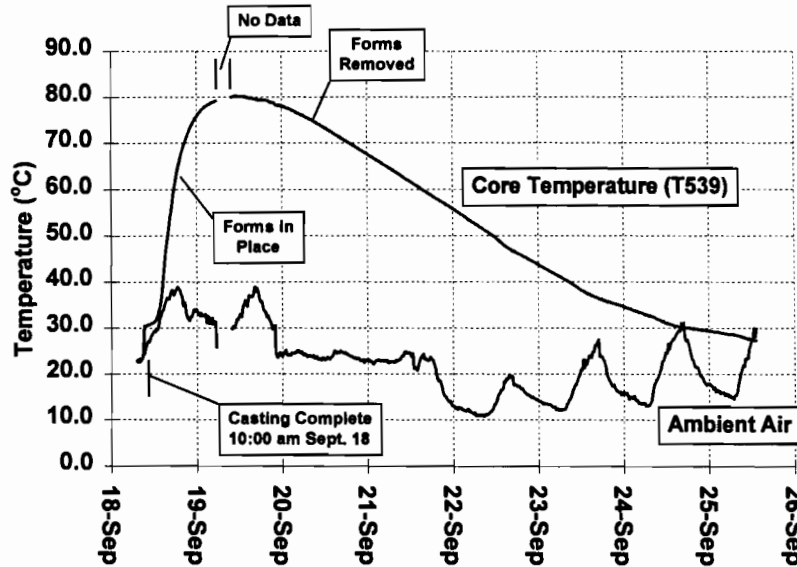


**Figure 6.12** Comparison of internal curing temperature to ambient air temperature, capital segment PC16-8.

The maximum temperature gradient in the concrete occurred at noon on September 20. The gradient shape produced by the high internal curing temperatures was similar to those typically found during the early morning hours in the pier after erection. It is distinguished by a high internal core temperature with relatively cool outer surfaces (see Figure 6.13). Note, however, that the temperature difference during curing of almost 36°C is much greater than the typical differentials measured after erection (see Figure 6.10).

Temperature differentials like those measured during curing of the capital can cause superficial cracking by the mechanism shown in Figure 6.11. To gauge the effects of the high temperatures measured in the capital segment during the curing process, the capital was inspected for cracks 24 hours after casting was completed. This was also very close to the time when the maximum difference between the inner core and ambient air temperature was observed. The cracks found during the inspection tended to follow architectural reveals, corners, and other surface irregularities as these were areas of stress concentrations (see Figure 6.14).

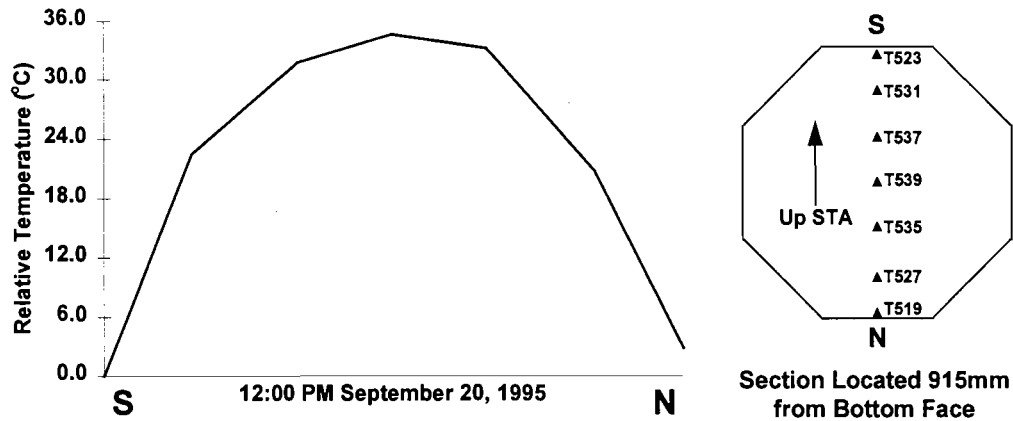


**Figure 6.13** Maximum gradient shape during curing of capital.

To prevent surface cracking of large monolithic members, the effects of temperature differences between the inner core and outside surfaces must be mitigated. This can be accomplished in three ways: the internal core temperature can be reduced, the outer surface temperature can be raised, or a combination of the two can be applied. High internal temperatures can be reduced by providing ventilation through ducts running through the interior of the member. This provides a mechanism for the escape of heat into the surrounding air. In large concrete dams, water in pipes imbedded in the concrete provide cooling. A simpler solution could be achieved by carefully insulating the outside of the member. This not only would prevent the ambient air from severely cooling the outer concrete, but would serve to hold the interior heat in the concrete, thus providing a more uniform temperature throughout the cross-section. However, merely insulating the member may be inadequate due to the extremely high internal temperatures. A combination of the two methods would produce the best results.

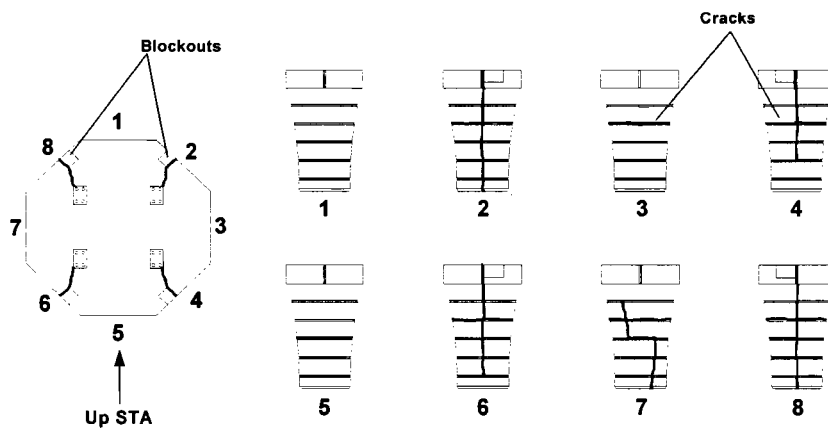


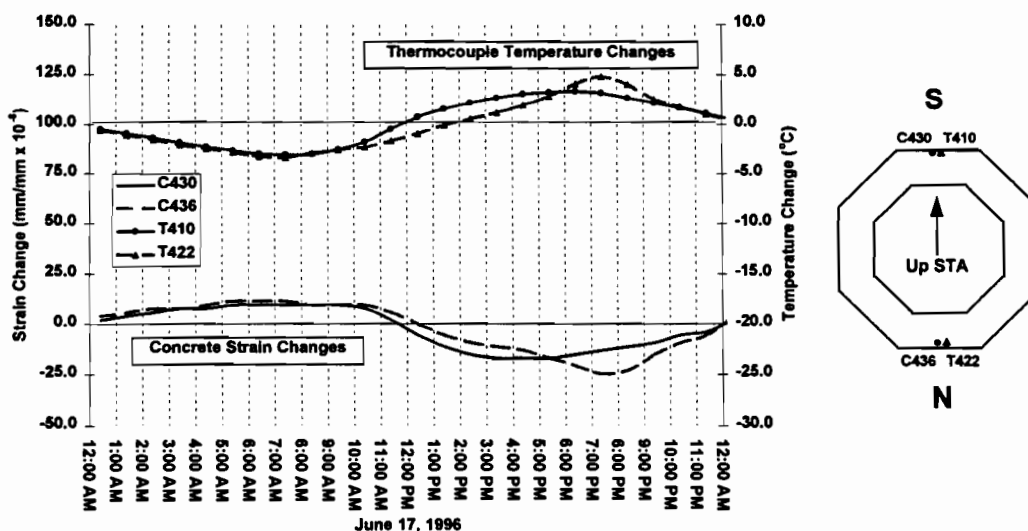
**Figure 6.14** Map of cracks found during curing of capital segment PC16-8.

## 6.3 Concrete Strain Gauge Measurements

### 6.3.1 Axial Strains

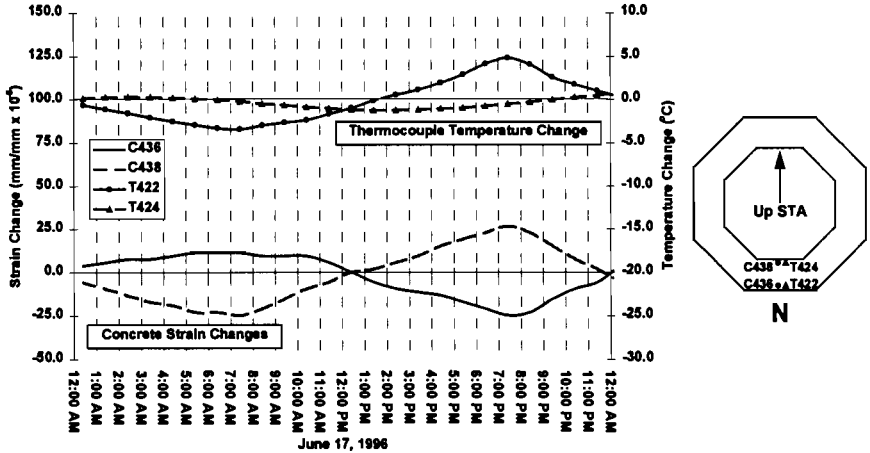
Concrete strain gauges located in the hollow column of pier P16 were oriented to measure strains parallel with as well as normal to the longitudinal axis of the pier. Axially oriented strain gauges were placed to measure strains from thermal effects and bending strains from externally applied loads about each of the four axes normal to the pier's length (see Figures 3.15 to 3.17).

Figure 6.15 shows a plot of temperature and strain changes throughout the day on June 17, 1996. The measurements were taken by instruments located along the north-south axis of the pier's cross section in segment PC16-5. Both the strain gauges and thermocouples were located near the outside of the north and south faces of the section. It should be noted that the electronic strain gauges automatically remove any strain effects due to temperature change in the concrete. The thermal strains from concrete expansion or contraction are removed internally: all strain measurements reflect strains due to stresses only. From the graph, it is apparent that strain changes occur simultaneously with the changing temperatures at the same locations. The strain gauges indicate compressive strains as the temperature increases, while tensile strains occur as the temperature drops. The theory discussed in Section 2.5.3 which predicts that compressive strains occur during a rise in temperature seems to match the measured strains at the locations in Figure 6.15 quite well.



**Figure 6.15** *Temperature and strain changes on June 17, 1996: outer gauge locations, north-south sectional axis.*

It is also interesting to note the strain distribution through the thickness of each wall of the pier's shaft. Figures 6.16 and 6.17 show that differences in strain exist between the inner and outer strain gauges in the north and west walls of the pier, respectively. As before, the strain changes match the temperature changes throughout the day.



**Figure 6.16** *Temperature and strain changes on June 17, 1996: outer and inner gauges, north wall of pier P16.*

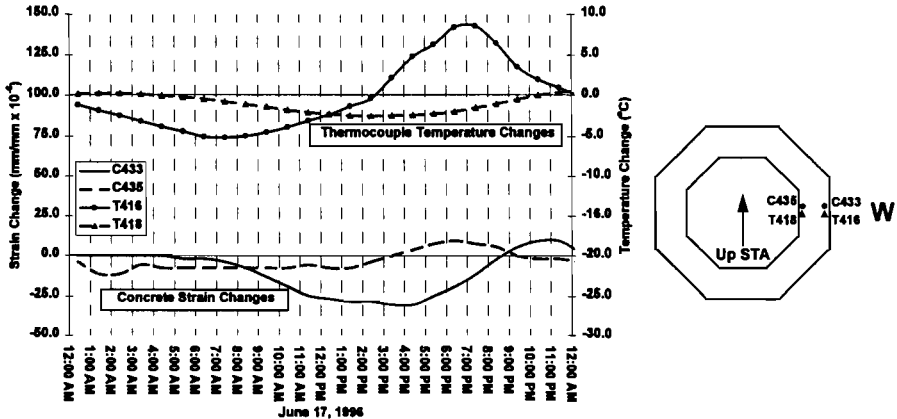


**Figure 6.17** *Temperature and strain changes on June 17, 1996: outer and inner gauges, west wall of pier P16.*

The strain changes in the north wall of the pier exhibit well defined opposing changes (see Figure 6.16). Again, a mechanism like that described in Section 2.5.3 may cause the measured strains. As the outside of the pier heats up, the outer strain gauge records a compressive change while the inner gauge undergoes tension. This reflects the

hypothesis that the core concrete is pulled in tension by the heated and expanding outer concrete shell. The shell, in turn, undergoes compressive strains caused by the restraint imposed by the cooler core concrete.

The west face of the pier (see Figure 6.17) does not exhibit such well defined patterns through the course of the day. The strain and temperature changes do not coincide directly like those in the north wall. In general, though, the strain gauges exhibit compressive strain changes during periods of heating. Gauge C433 recorded a tensile strain change corresponding to a drop in temperature at its location after sunset.

The largest longitudinal strain changes occurred along the east-west cross-sectional axis of the pier. This behavior corresponds to the axis along which the maximum differential temperatures were observed. The observations made concerning strains using data from segment PC16-5 also correlate with the measurements of gauges located in segment PC16-1 and PC16-7. Thus, the state of strain in the entire pier appears to be influenced by temperature distributions changing within it throughout the day. However, because the pier is not restrained, all induced stresses are internally balanced.

### 6.3.2 Transverse Strains

Strain gauges oriented normal to the pier's longitudinal axis also exhibit large changes in strain due to temperature changes. Horizontally oriented strain gauges in the east and west faces of the pier follow recognizable patterns through the course of the day (see Figure 6.18). Concrete strain gauge C440, located on the east face, appears to exhibit strains coinciding well with the temperatures recorded at that location. Similarly, C434 undergoes compressive strain changes as the temperature at the west face of the pier rises in the afternoon. Both gauges produce data that are consistent with theoretical expectations.

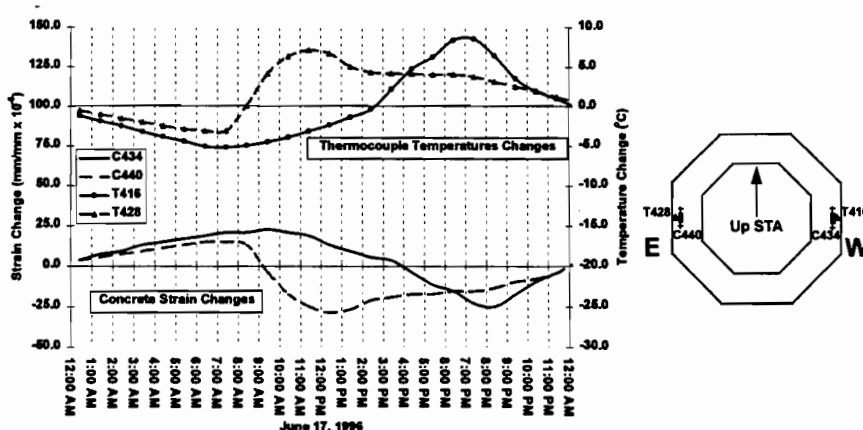


**Figure 6.18** *Temperature and strain changes on June 17, 1996: horizontally oriented gauges, east and west faces.*

## 6.4 Pier Post-Tensioning Strains

### 6.4.1 General

Pier P16 was erected during the month of April 1996, and was post-tensioned during the early morning hours of May 1, 1996. Temperature and strain data were recorded once every minute during the post-tensioning process. In addition, a pressure transducer was attached to the hydraulic ram to measure jacking forces at four locations. Pier P16 was post-tensioned with four tendons each with 19 strands of 13 mm diameter running from the pier capital through a 180° bend in the footing and ending at an adjacent anchorage (see Figure 4.9). The tendons were initially stressed to 80% of the strands' guaranteed ultimate tensile strength of 1860 MPa.

Figure 6.19 shows a plot of the readings taken by the pressure transducer over the course of the post-tensioning process. The tendons were stressed in the order indicated. Note that the plots for pulls 2 and 4 show an almost vertical initial increase in pressure to about 50% of the highest measurement. This reflects the fact that pulls 2 and 4 were already partially stressed by pulls 1 and 3.

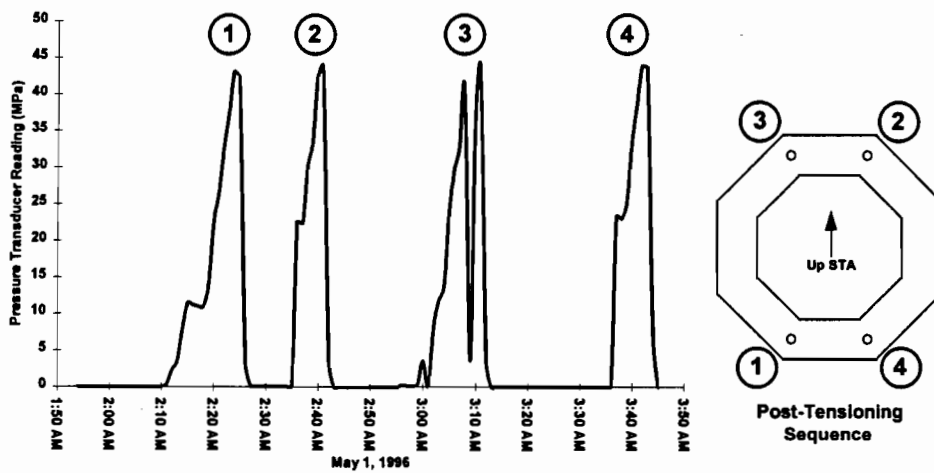


**Figure 6.19** *Pressure transducer readings during pier post-tensioning.*

### 6.4.2 Axial Strains

Strains were measured in the hollow shaft of the pier along the longitudinal axis. Figure 6.20 shows the measurements of strain gauges oriented along the vertical axis of the pier in segment PC16-1.

As shown in Figure 6.20, gauges located along an axis running north-south through the pier's cross-section show several well-defined trends during post-tensioning. After stressing takes place at position 1, the formerly uniform strains exhibit large differences between the north and south side of the pier. This differential strain is caused by a large load (i.e., the jacking force at position 1) eccentrically located with respect to the section's east-west centroidal axis.

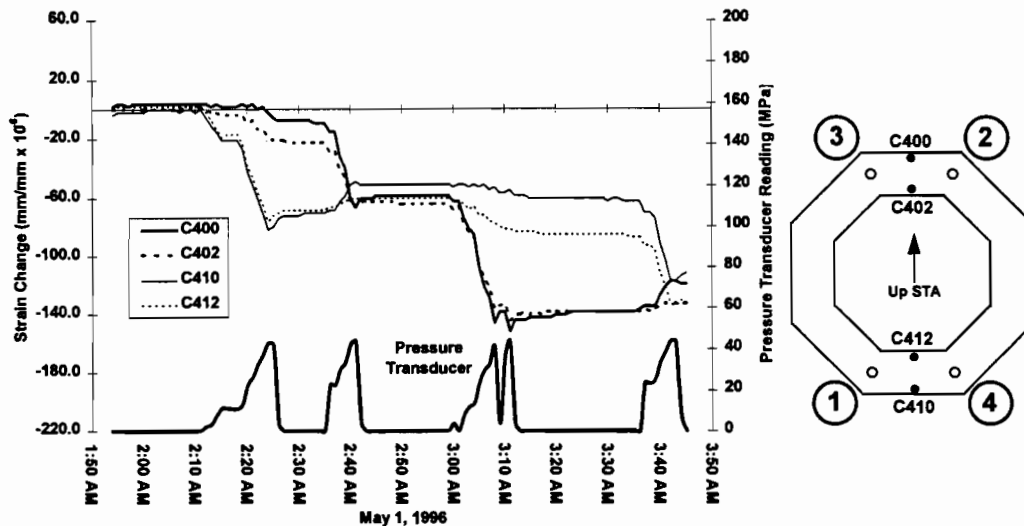


**Figure 6.20** Selected axial strains in segment PC16-1 during pier post-tensioning, north-south axis locations.

Conversely, after stressing at position 2 is complete, the post-tensioning loads experienced by the pier are symmetric about the east-west axis. This is reflected in the plots of strains after stressing at position 2: the strain levels are almost uniform in magnitude. The loads become unbalanced again after stressing at position 3. The gauges located directly under anchor position 3 experience large compressive strains, while the gauges located on the opposite side of the section (the north wall) undergo comparatively lower compressive strain changes. Again, strains are reasonably uniform after stressing at position 4.

Unfortunately, incomplete data was obtained for gauges along the east-west axis due to gauge malfunction.

Figure 6.21 shows a comparison between strains at the south face for the three instrumented shaft segments. Throughout the post-tensioning process, strains along the length of the pier at the south face are nearly equal in magnitude. They change in unison, reflecting the activities taking place at the top of the pier.

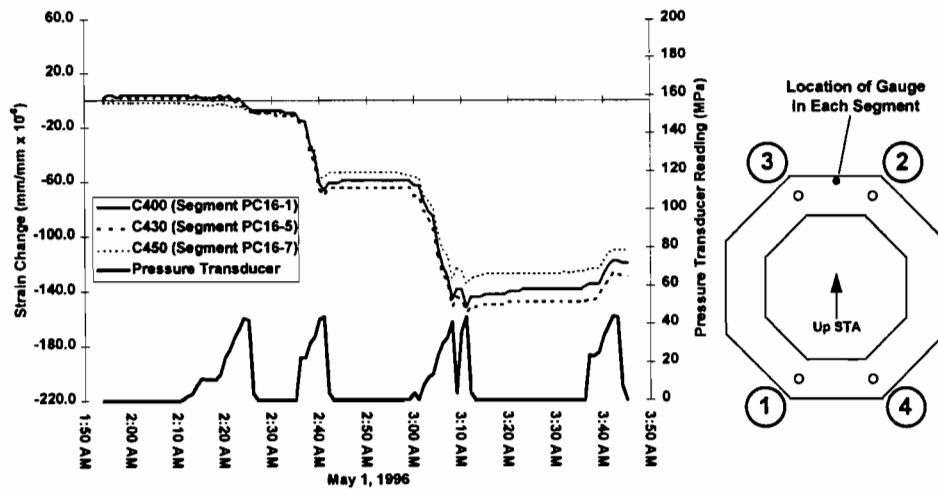


Figure 6.21 Comparison of strains along length of pier during post-tensioning.

#### 6.4.3 Transverse Strains

Gauges were also positioned to measure strains occurring normal to the pier's longitudinal axis. In some cases, longitudinal and horizontal gauges are located in the same area, allowing a determination of the ratio of axial to transverse strains at a given point (i.e., Poisson's ratio). The graph in Figure 6.22 illustrates this relationship for gauges located on the north-south cross-sectional axis. As expected, tensile strain changes occur in the horizontal direction (gauges C401 and C411) as the pier is loaded axially. The magnitudes of transverse strains are much less than the corresponding axial strains, reflecting the Poisson effect.

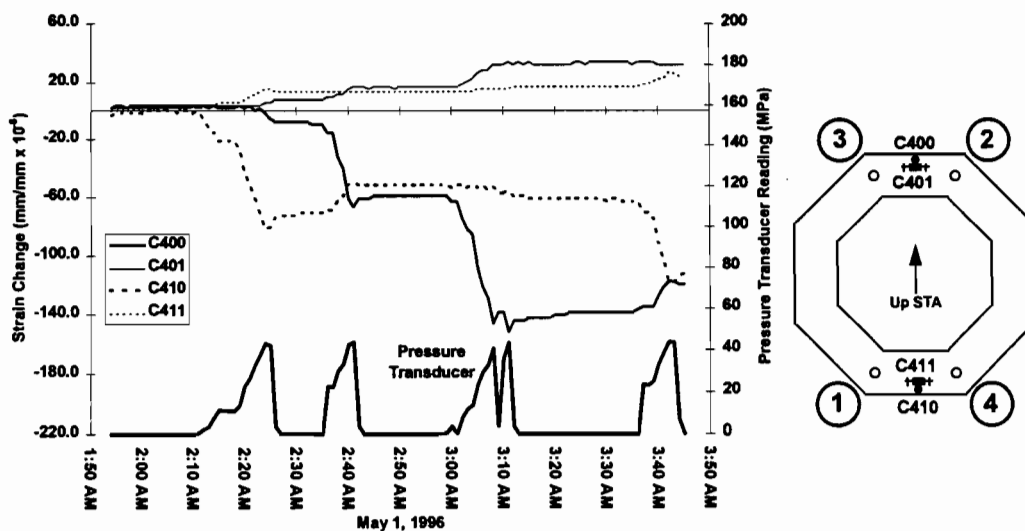


Figure 6.22 Comparison of axial and transverse strains during post-tensioning, north-south axis locations.

## 6.5 Stress/Strain Analyses - Hand Calculation Methods

### 6.5.1 Classical Method

The calculation methods outlined in Chapter 2 used by Imbsen, et al [17] and Roberts [19] were also employed to determine the longitudinal stress and strain distributions along the depth of the pier induced by the non-linear temperature gradients measured in the field. This method is commonly used during superstructure design to locate potential areas of tensile stress. Example calculations for the segmental pier's cross-section can be found in the Appendix of Reference 3.

#### 6.5.1.1 Positive Gradients

Figure 6.23 shows the temperature and stress distributions calculated for the maximum positive gradient for the month of April, 1996. As discussed in Chapter 2, the pier is initially assumed to be fully restrained. The stress distribution in this state is computed

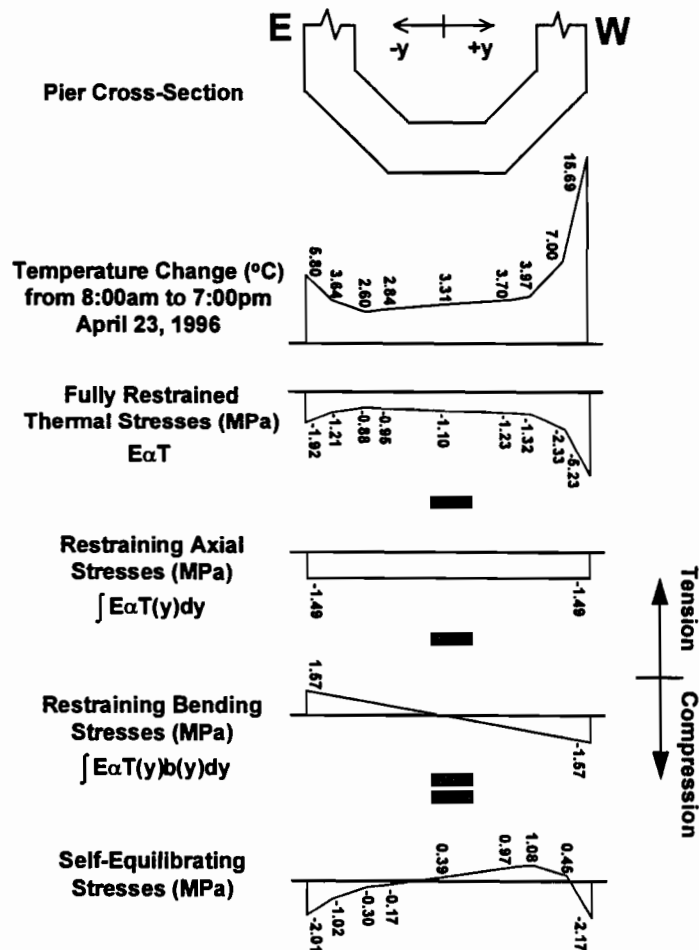


**Figure 6.23** Calculation of self-equilibrating stresses induced by the maximum positive temperature gradient, April 1996.

from the temperature distribution measured in the pier. Using the methods outlined in Chapter 2, the restraining axial force and moment are then calculated. To find the self-equilibrating stress distribution in the statically-determinate pier, the restraining forces are released and the axial and bending stresses are subtracted from the fully restrained stress distribution (see Figure 6.23).

For the sake of comparison with measured strains and the finite element model presented in Section 6.6, the longitudinal stresses calculated using this method are expressed as strains in the following figures. The calculation method illustrated in Figure 6.23 assumes that the longitudinal and transverse stress components due to temperature distributions are separable. The stresses calculated above do not include effects due to transverse stresses, which will be calculated later in this section. Thus, the strains plotted in the following figures are calculated using Hooke's law:

$$\epsilon_{\text{longitudinal}} = \frac{\sigma_{\text{longitudinal}}}{E} \quad (6.1)$$

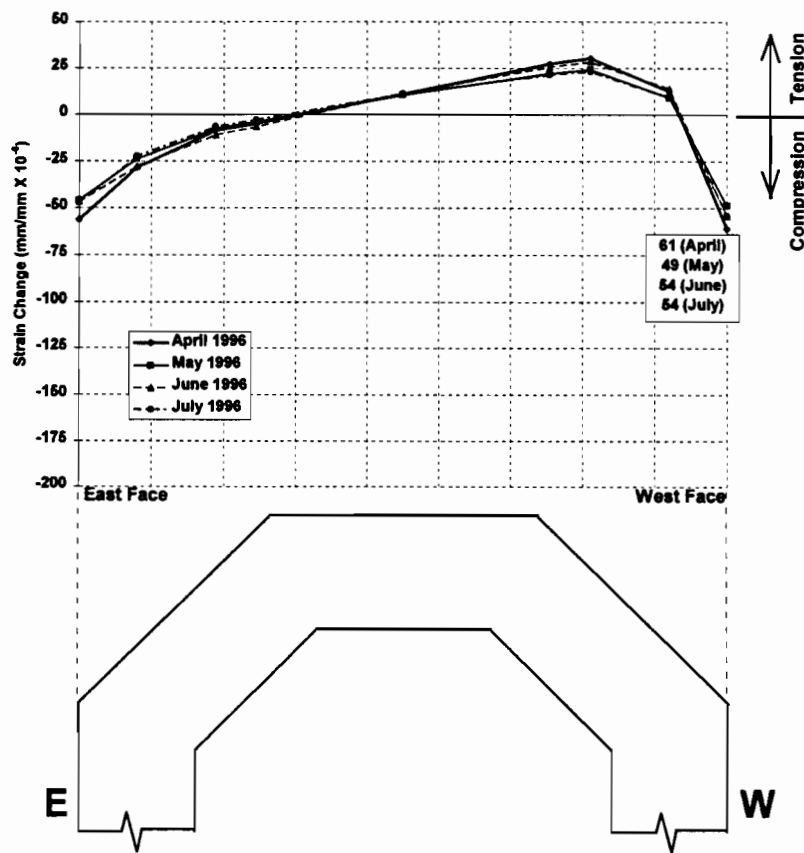


**Figure 6.24** Longitudinal strains due to self-equilibrating stresses induced by monthly maximum positive gradients, plotted on the east-west cross-sectional axis.

The method shown in Figure 6.23 was used to calculate the strain distributions induced by the monthly maximum positive temperature gradients (see Figure 6.24). All strain distributions are plotted on the east-west cross-sectional axis as they coincide with the temperature distributions shown earlier. Regions of high temperature in the pier's cross-section are marked by compressive self-equilibrating stresses. For positive gradients, the interior areas undergo tensile stresses associated with the relatively low temperatures there. This behavior is consistent with the theory discussed in Section 2.5.3. Figure 6.25 shows the longitudinal strains calculated from the application of the design positive gradients on the pier's cross-section as compared to those calculated from the maximum measured gradient. A striking difference exists on the west face where the strains calculated from the measured gradient are only one-third of those calculated from the design code gradients. Relatively large tensile strains in the interior fibers were calculated using the AASHTO-LRFD gradient. Tensile strains in that location induced by the April maximum gradient and the NCHRP gradient were approximately the same magnitude.

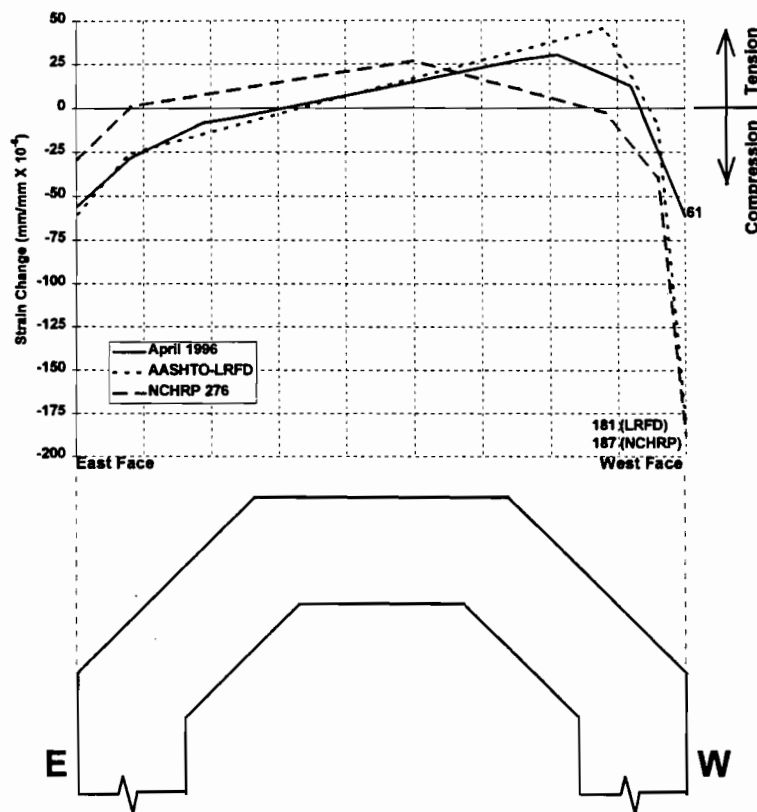


**Figure 6.25** Longitudinal strains due to self-equilibrating stresses induced by design positive gradients, plotted on the east-west cross-sectional axis.

### 6.5.1.2 Negative Gradients

The same longitudinal strain calculation method was used to determine the sectional strains occurring due to the largest negative gradients. Negative temperature gradients, where the outer surfaces are cool compared with the interior, cause tensile strains to develop at the outer faces of the pier. Figure 6.26 shows the stress calculation method for the maximum monthly negative gradient for April 1996. The longitudinal stress component is then converted to strain using Hooke's law as before. The monthly maximum self-equilibrating strain distributions are shown in Figure 6.27. All maximum negative gradients are plotted along the east west cross-sectional axis for comparison purposes. Figure 6.28 illustrates the strain distributions calculated from the application of the design negative temperature gradients to the pier cross-section.

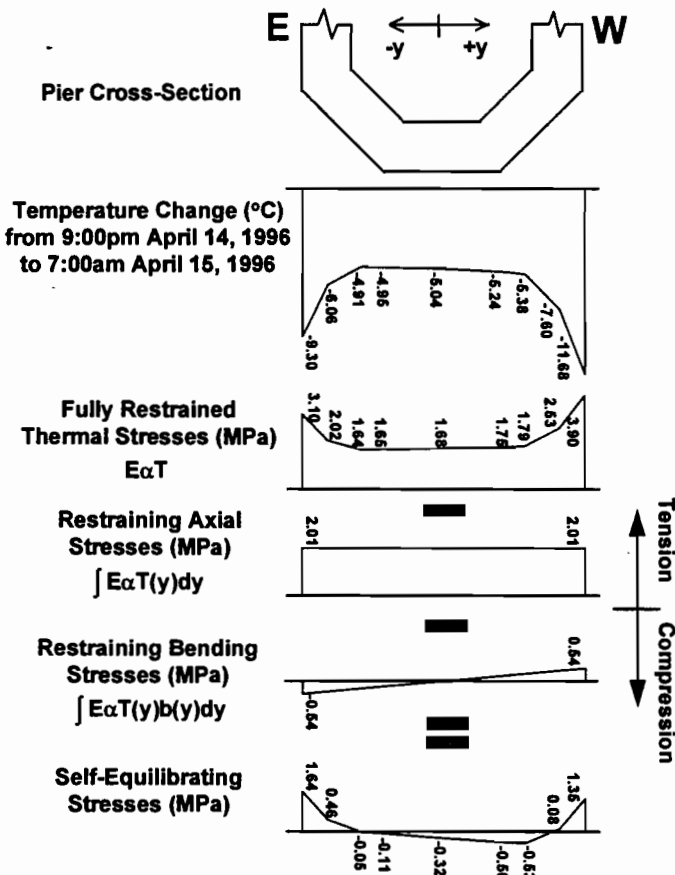


**Figure 6.26** Calculation of self-equilibrating stresses induced by the maximum negative temperature gradient, April 1996.

The maximum tensile strain changes due to the measured negative gradients occurred at the east face of the pier for each of the four months computed. However, the tensile strains at the east and west faces of the pier were very close in magnitude, indicating almost symmetrical temperature loading. The April maximum negative gradient produced the largest tensile and compressive strain changes in the pier's cross-section.

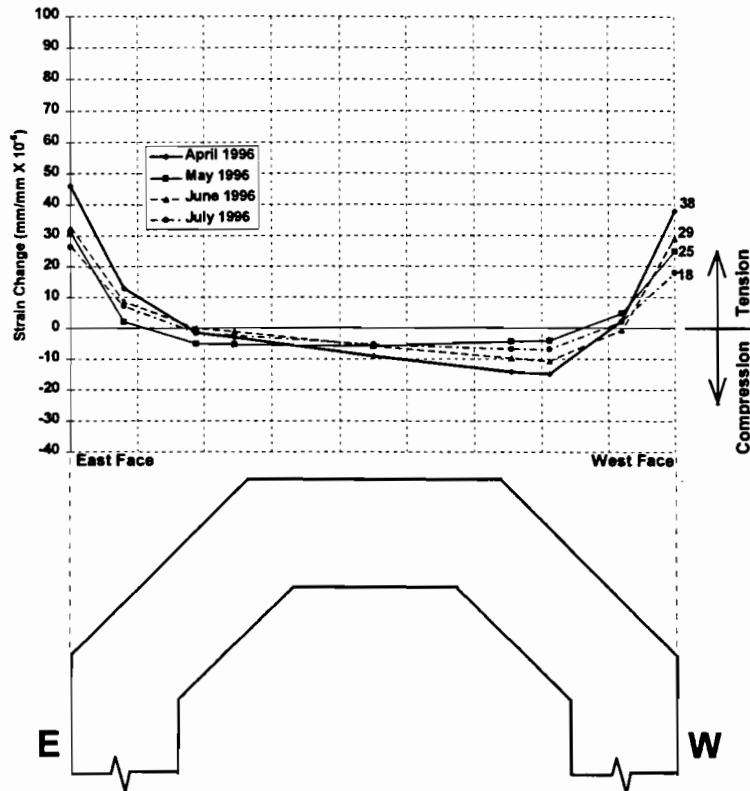


**Figure 6.27** *Longitudinal strains due to self-equilibrating stresses induced by monthly maximum negative gradients, plotted on the east-west cross-sectional axis.*

The design code negative temperature gradients produced large tensile strain changes at the west face of the pier. The maximum tensile strain change calculated from the April observed negative gradient was only 42% of the tensile strains induced by the AASHTO-LRFD Code negative gradient, and 38% of those from the NCHRP negative design gradient.

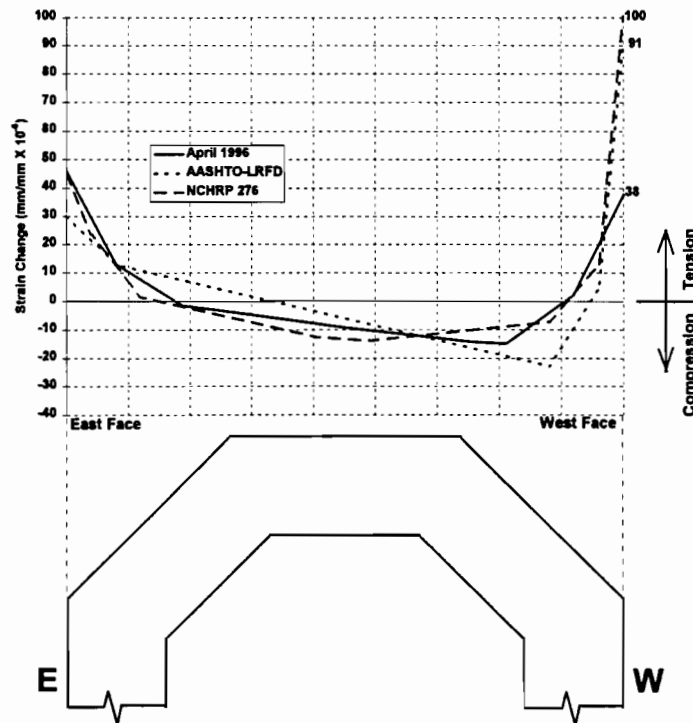


**Figure 6.28** Longitudinal strains due to self-equilibrating stresses induced by design negative gradients, plotted on the east-west cross-sectional axis.

### 6.5.2 Primary Bending Axis Method

The classical method described in the previous section works well for estimating the longitudinal self-equilibrating stresses at any depth in a bridge member. The method is useful only for a one-dimensional distribution of temperatures through the section, as it does not account for any temperature distributions in the transverse direction across the section. Bridge piers, as stated earlier, pose a slightly more complicated problem because they are not heated from a single direction. Thus, the self-equilibrating stresses induced by temperature changes will vary along both the depth and width of the pier's section.

A more general approach to the determination of temperature-induced stresses in a member involves a process similar to that of the classical method used previously. In this general method, temperatures are assumed to be constant over discrete *areas* of the cross-section, rather than at discrete *depths*. Thus, the member is loaded with a set of temperatures that can be visualized as a three-dimensional surface bounded by the geometry of the cross-section.

The assumption that plane sections remain plane requires the addition of an intermediate step in the process. The orientation of the axis about which bending occurs (i.e. the neutral axis) is assumed to be known in the classical method used previously in this chapter. However, the two-dimensional temperature loading applied to the pier causes it to bend about an axis that does not necessarily coincide with the neutral axis (see Figure 6.29). The bending axis, which is dependent on the temperature distribution, must be determined before a calculation of the restrained axial and bending stresses can be performed.

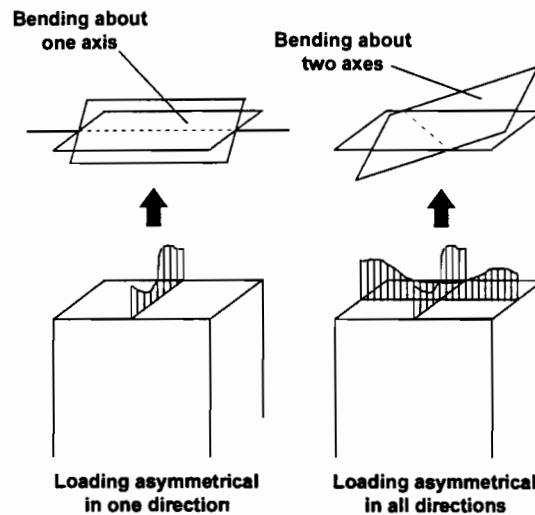


**Figure 6.29** *Final planar section orientation is dependent on temperature loading.*

To determine the bending axis orientation, the cross-section is divided into areas of constant temperature. Bonzon [3] used areas defined by the measured temperatures in the pier's cross-section as shown in Figure 6.30. A distribution of smaller areas of constant temperature would have produced more refined results, but temperatures were only known at the points indicated. He then used the primary bending axis method to recalculate the stresses caused by thermal strains. Full details are included in Reference 3. The primary bending axis method for calculating the self-equilibrating stress at a given point on the cross-section of the pier is analogous to methods used to determine the principal stresses at a point under a set of applied normal and shear stresses. In this case, however, the primary bending axis orientation is determined by the temperature distribution across the section.

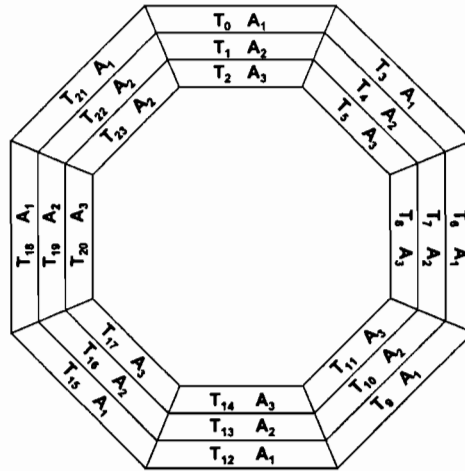


**Figure 6.30** Areas and assigned temperatures used for stress calculations.

### 6.5.2.1 Positive Gradients

The stress distributions found using the primary bending axis method are expressed in terms of longitudinal strain for comparison purposes. The self-equilibrating strain distributions found from the primary bending axis method for each monthly maximum positive temperature gradient are illustrated in Figures 6.31. The orientation of the primary bending axis for each set of temperatures is shown in Figure 6.32. Note that the primary bending axis is located very close to the east-west cross-sectional axis, and that the strain distributions are plotted along the east-west axis for comparison to other distributions discussed earlier in this chapter.

The longitudinal strain distributions produced by the primary bending axis method are consistent with those produced by the classical method of self-equilibrating strain calculation shown in Figure 6.24. The magnitude of the peak strains are about 15% higher in the primary bending method. The plots for all four months are virtually identical, with only small variations in the magnitudes of strain changes (see Figure 6.31). As calculated previously, the maximum positive gradient during April induced the largest self-equilibrating strains.

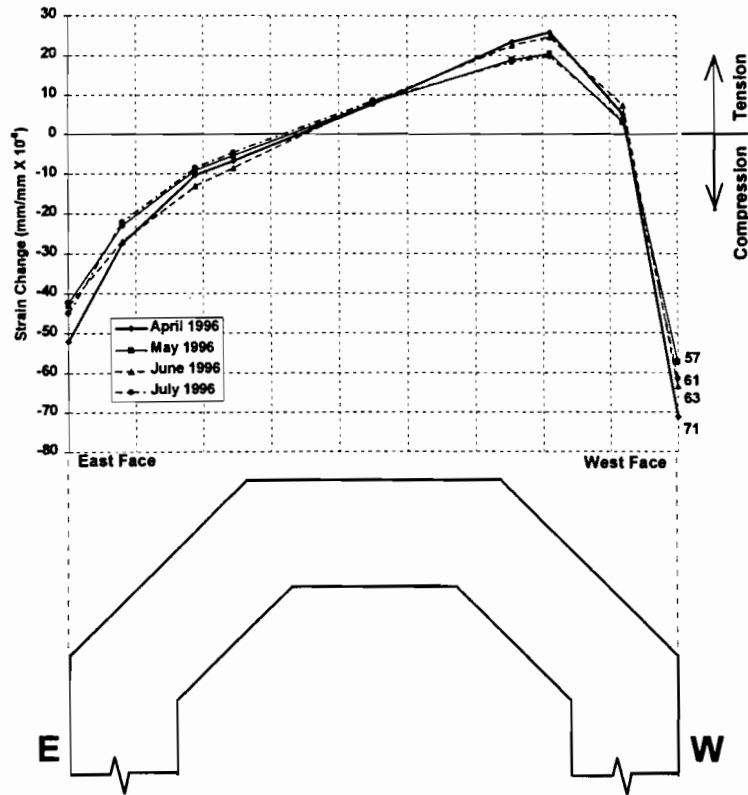


**Figure 6.31** *Longitudinal strains due to self-equilibrating stresses induced by monthly maximum positive gradients, calculated by the primary bending axis method and plotted on the east-west cross-sectional axis.*

The orientation of the bending axis B-B is quite similar for all four load cases (see Figure 6.32). This seems to confirm the observations made previously that the largest temperature differences primarily occur along the east-west axis of the pier's cross-section. For the positive gradient temperature distributions, the bending axis B-B almost directly corresponds with the north-south cross-sectional axis.

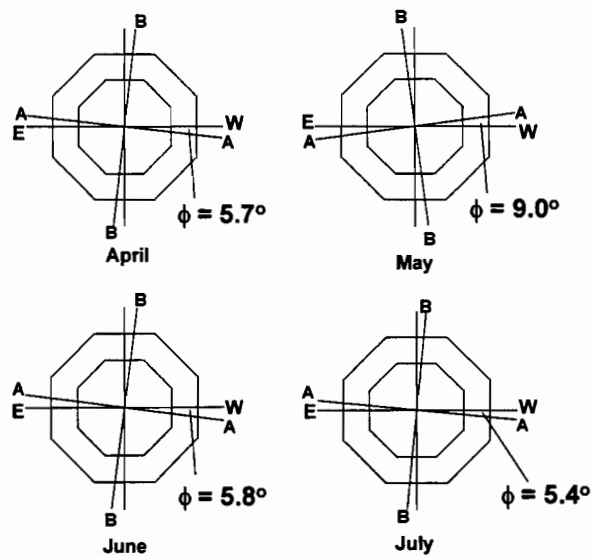


**Figure 6.32** *Orientation of primary bending axis B-B calculated for each monthly maximum positive gradient load case.*

### 6.5.2.2 Negative Gradients

The longitudinal strain distributions found by the primary bending axis method corresponding to the maximum monthly negative temperature gradients are shown in Figure 6.33. All distributions are projected along the east-west cross-sectional axis using the octagonal shell projection method for comparison with previously calculated self-equilibrating strains. Comparison with Figure 6.27 shows the peak values (on the east face) are almost identical for the two calculation methods.

The strain distributions calculated by the primary bending axis method produced consistent results between all four monthly temperature load cases. The maximum negative gradient from April produced the largest outer fiber tensile strain changes, and the maximum tensile strain change occurred at the east face of the pier.

The orientations of the bending axes B-B for the maximum monthly negative gradients varied greatly (see Figure 6.34). This indicates that the locations of the maximum temperature changes occurring during a negative temperature gradient are extremely difficult to predict.

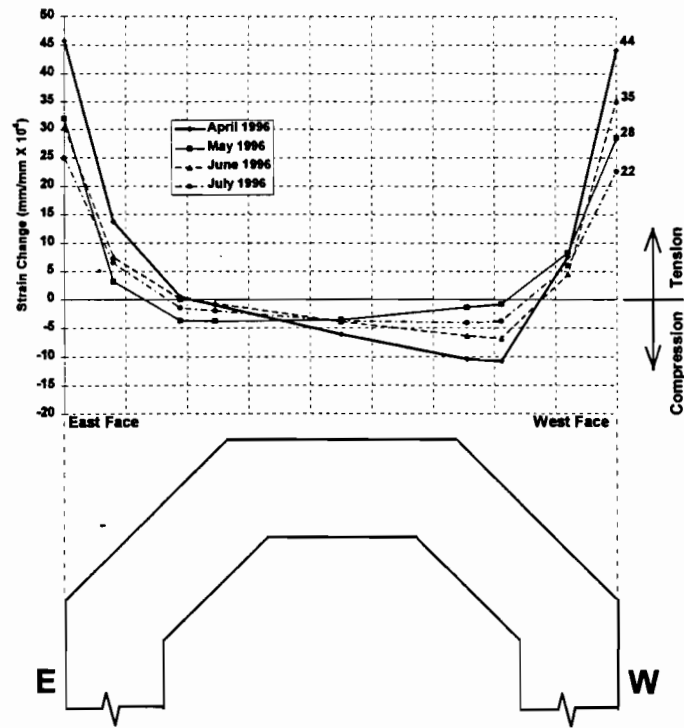


**Figure 6.33** Longitudinal strains due to self-equilibrating stresses induced by monthly maximum negative gradients, calculated by the primary bending axis method and plotted on the east-west cross-sectional axis.

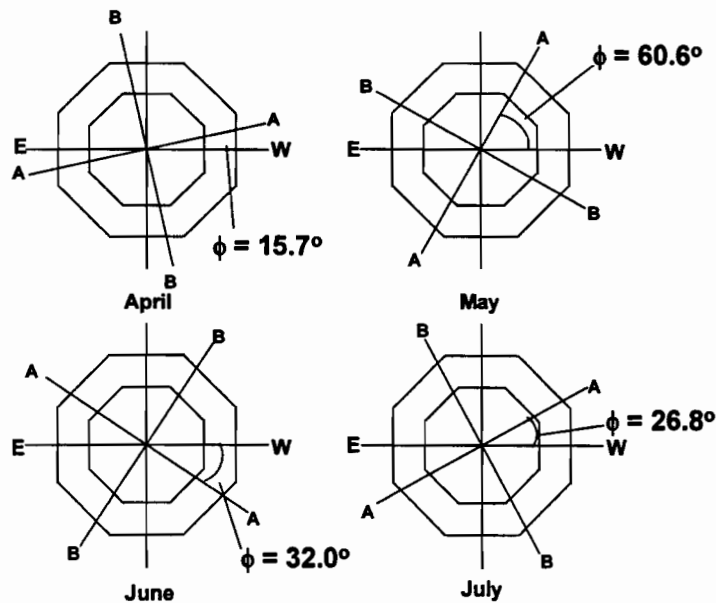


**Figure 6.34** Orientation of primary bending axis B-B calculated for each monthly maximum negative gradient load case.

### 6.5.3 Transverse Stresses

The longitudinal stresses calculated previously in this chapter do not describe the complete state of stress induced in the pier during temperature changes. Transverse stresses are also present due to the local effects of non-linear temperature gradients through the pier walls. During the analysis of most superstructures, local gradients across the thickness of flanges and webs are assumed to be linear. However, for walls with thickness greater than about 28 mm, the linear temperature gradient assumption no longer adequately describes the temperature distribution through the wall [17].

For the purposes of this project, the transverse stresses induced in the pier's walls can be analyzed with a method suggested by Imbsen, et al [17] (see the appendix of Reference 3 for an example transverse stress calculation). First, the walls of the cross-section are treated separately. Each wall is artificially restrained, and the corresponding non-linear temperature gradient through the thickness is applied (see Figure 6.35).

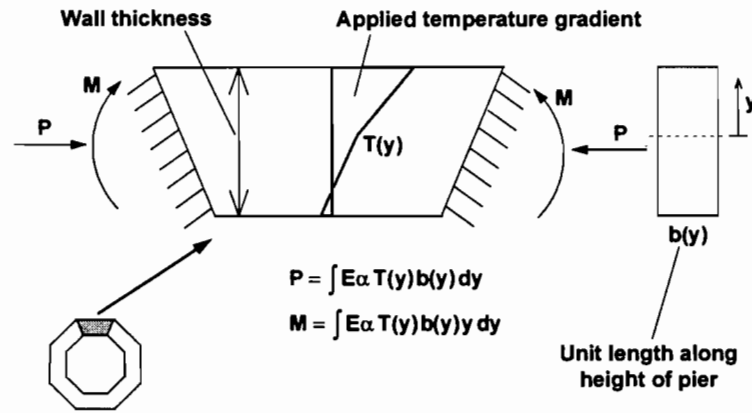


**Figure 6.35** Application of non-linear thermal gradient to individual pier walls.

The fully-restrained stress distributions as well as the restraining axial forces and moments are found by the method used earlier in this chapter. The axial force is expressed as:

$$\int E\alpha T(y) b(y) dy \quad (6.2)$$

where  $b(y)$  can be assumed to be a unit width of pier wall. Similarly, the restraining moment per unit width of wall along the pier's length is:

$$\int E\alpha T(y) y dy \quad (6.3)$$

The unit width term  $b(y)$  is dropped from the calculation. The geometry of the section is idealized as a frame and the *opposites* of all the axial forces and moments found above are applied as loads in a frame analysis computer program (see Figure 6.36). The program then redistributes the applied forces around the cross-section. Finally, the stresses associated with the redistributed forces found by the computer solution are *added* to the fully-restrained stress distributions in each wall found earlier (essentially the same as subtracting the restraining stresses as done previously for the longitudinal analyses). See the appendix of Reference 3 for example calculations.

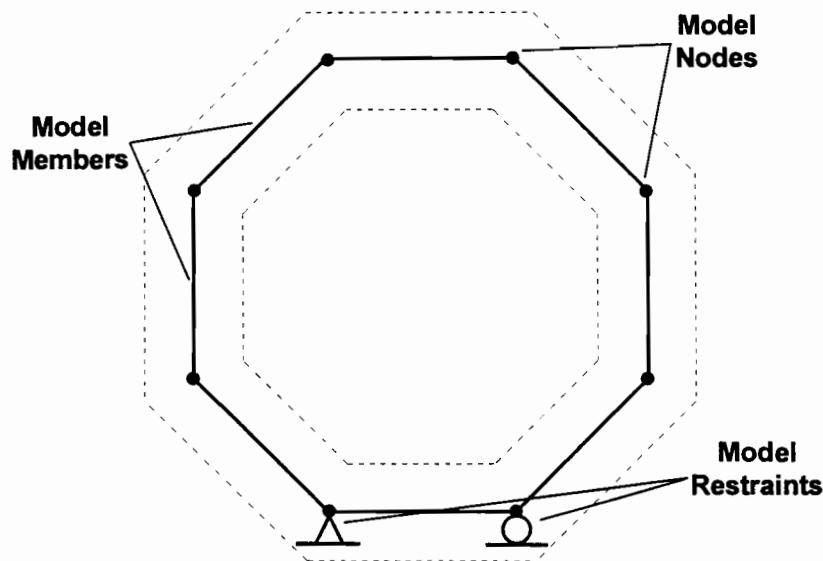


**Figure 6.36** *Frame model of pier cross-section used for redistribution of forces by computer frame analysis program.*

### 6.5.3.1 Positive Gradients

Transverse stresses and their associated strains were computed at mid-length of each wall of the pier. The temperatures measured by the thermocouples located in segment PC16-5 were used to determine the non-linear temperature gradients indicated through each wall of the pier for the monthly maximum temperature gradient load cases. Figures 6.37(a) through 6.37(d) illustrate the applied temperature distributions and their associated self-equilibrating transverse stresses for each month's maximum positive gradient. Note that for all load cases, relatively warm outside temperatures induced transverse compressive strains at the walls' outer faces.

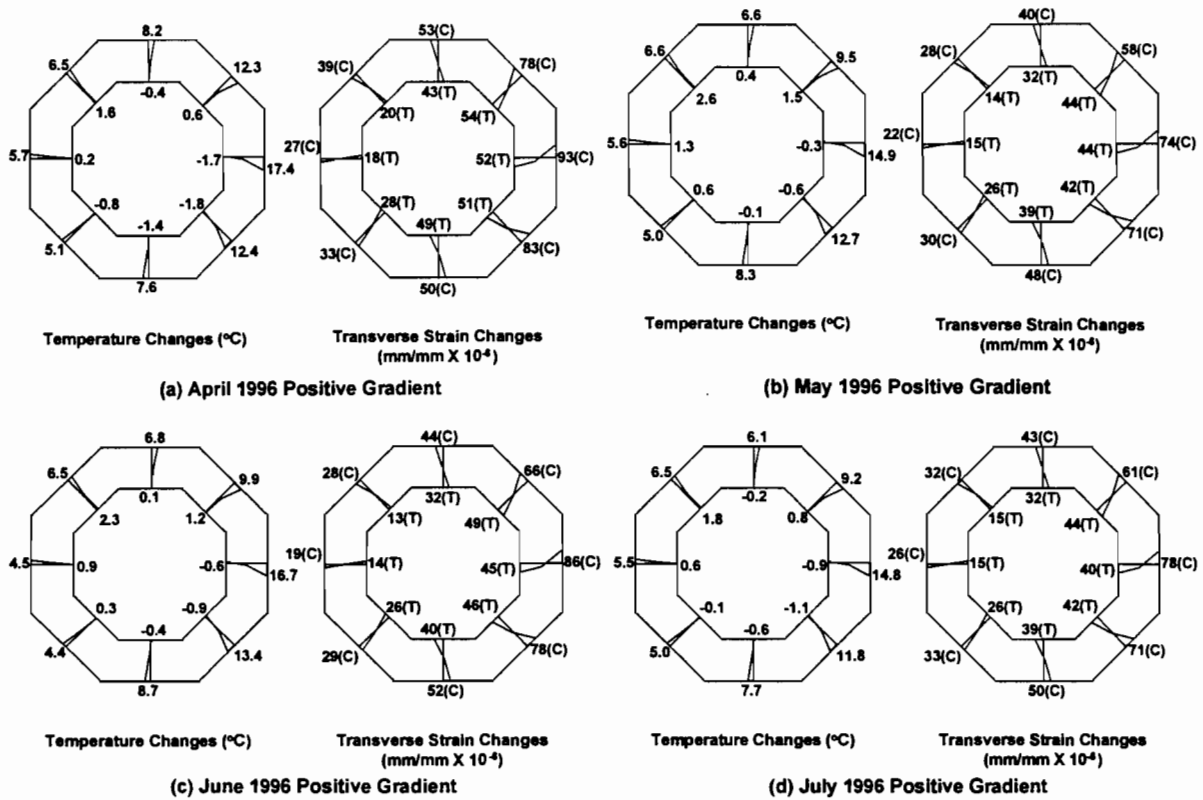


**Figure 6.37** *Temperature distributions and self-equilibrating transverse strains caused by positive temperature gradients for (a) April, (b) May, (c) June, (d) July.*

The largest transverse strain changes are indicated during the April maximum positive gradient. At the west face, the transverse compressive strain change was larger than the longitudinal strain change calculated earlier in this chapter. The transverse tensile strain changes located near the interior faces of the pier's walls were also larger than the longitudinal strains calculated there. The largest differences in temperature across the wall thickness produced the largest transverse self-equilibrating strains. This is consistent with the observations made concerning the longitudinal strain changes earlier in this chapter.

### 6.5.3.2 Negative Gradients

Figures 6.38(a) through 6.38(d) show the temperature and computed transverse stress distributions through the pier walls for each monthly maximum negative gradient. The cooler outside temperatures cause tensile stresses to develop at the outer faces of the pier walls, consistent with the stresses induced in the longitudinal direction under such loading.

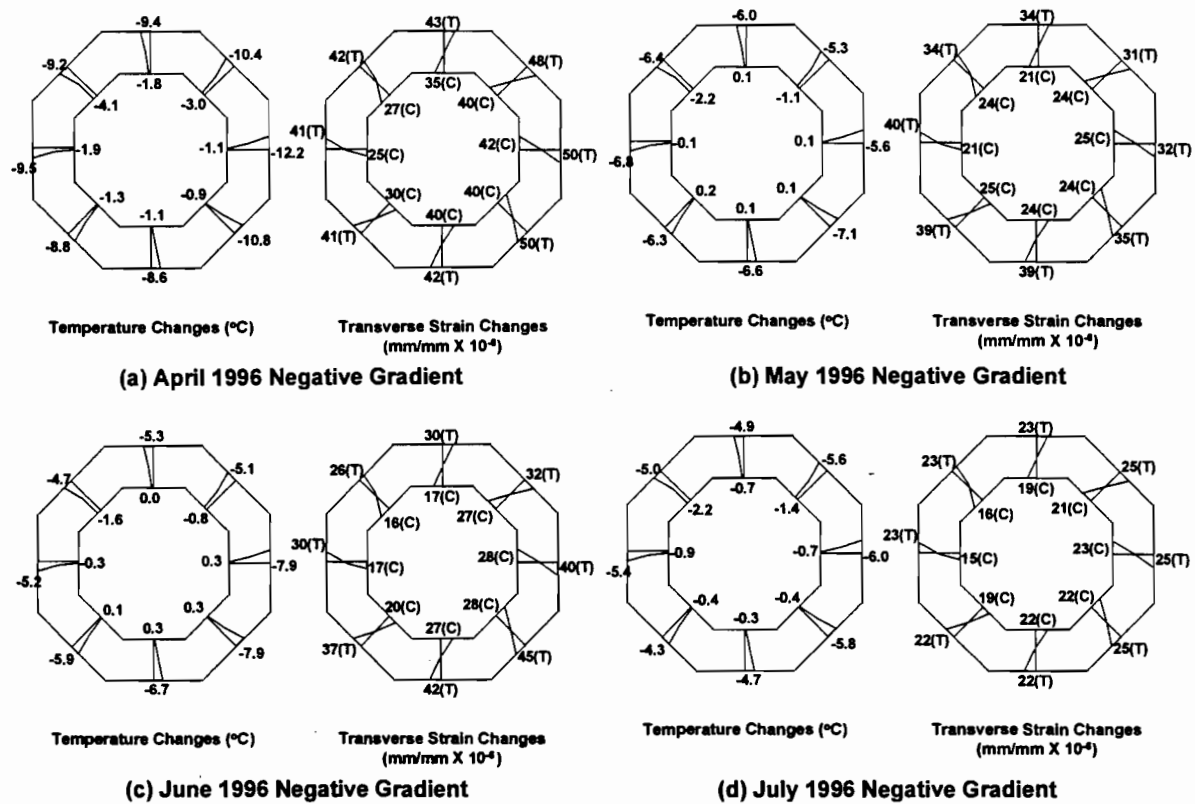


**Figure 6.38** *Temperature distributions and self-equilibrating transverse strains caused by negative temperature gradients for (a) April, (b) May, (c) June, (d) July.*

Transverse strains induced by the negative thermal gradients through the wall thickness indicate tensile strain changes at the outer faces of the pier that were larger than those previously calculated in the longitudinal direction. The April maximum negative temperature gradient loading produced the highest tensile strain changes which were computed at the west face of the pier. However, the largest strain changes were not always indicated at the west face for the four months monitored, and did not always coincide with the largest temperature gradients present in the walls. This is due to the pier's redistribution of stresses to maintain equilibrium. Thus, the location of the maximum transverse tensile strain for a given temperature loading cannot be assumed to coincide with the largest temperature changes. The maximum strain location is a function of both the geometry of the member cross-section and the distribution of temperatures across the section.

## 6.6 Finite Element Analysis

Finite element modeling can be extremely useful for analyzing a wide variety of complex structures. Most commercial finite element packages available today are capable of handling many types of loads on a structure; response due to temperature loading is a common application. Overviews of the theory behind finite element modeling have been presented elsewhere [42, 43] and are beyond the scope of this project.

During the course of this project, a finite element model of the large ramp pier P16 was constructed using the commercial finite element program ANSYS 5.0a. This model was used with input data consisting of measured temperatures. The objective of the analysis was to provide a comparison with measured strains and with stresses and strains determined from generally accepted hand calculation methods. Analysis of and comparison with the field data was limited due to the number and location of gauges installed in the pier. Longitudinal strains were well represented, but a lack of transverse strain measurements made the determination of stresses more difficult. Generally accepted hand calculation methods consisted of separate analyses of the longitudinal and transverse stresses. The finite element model provided a means to analyze three-dimensional temperature response with fewer simplifying assumptions.

### 6.6.1 Pier Geometry Input

Pier P16 consists of a hollow, octagonal cross-sectional column with a solid capital segment. The pier is post-tensioned with tendons running through the pier's height and anchoring the column segments firmly to the foundation. Some assumptions concerning pier geometry were made to reduce the complexity of the computer model and decrease the solution time.

The computer model was constructed under the assumption that the completed, post-tensioned pier would act as a monolithic member. It has been shown that segmentally constructed, post-tensioned members behave monolithically [44]. The pier's post-tensioning and epoxied joints provide excellent continuity across segment interfaces, particularly at the low service limit state stresses induced by the temperature distributions.

For comparison with the hand calculations, only strain and stress *changes* due to temperature load *changes* were required. The field measurements of strains induced by temperature gradients did not include strains due to gravity loading or post-tensioning operations. Thus, the finite element model ignored the self-weight of the structure and post-tensioning loads. The post-tensioning forces will change slowly over time due to creep, shrinkage, and tendon relaxation, but this loading should not change significantly over the short time period of daily temperature fluctuations.

The strains stresses induced by temperature gradients across the hollow cross-section were the primary concern of this computer analysis. Thus, the monolithic capital segment was not included in the finite element model. This served to greatly simplify the model, as the capital segment has complex geometrical features of little importance to the structure's response.

Figures 6.39(a) through 6.39(e) show a comparison between the actual pier geometry and the finite element model geometry. As shown in Figures 6.39(d) and 6.39(e), the hollow cross-sectional shape and size was reproduced closely in the computer model. For simplicity, the pier's base was assumed to be rigidly fixed and the top was allowed to freely deflect and rotate. Only the pier height consisting of the octagonal cross-section was modeled [see Figure 6.39(b)]. Thus, the computer model was approximately 15.6 meters in length, while the actual pier height of 20.7 meters included part of the cast-in-place base and the monolithic capital segment.

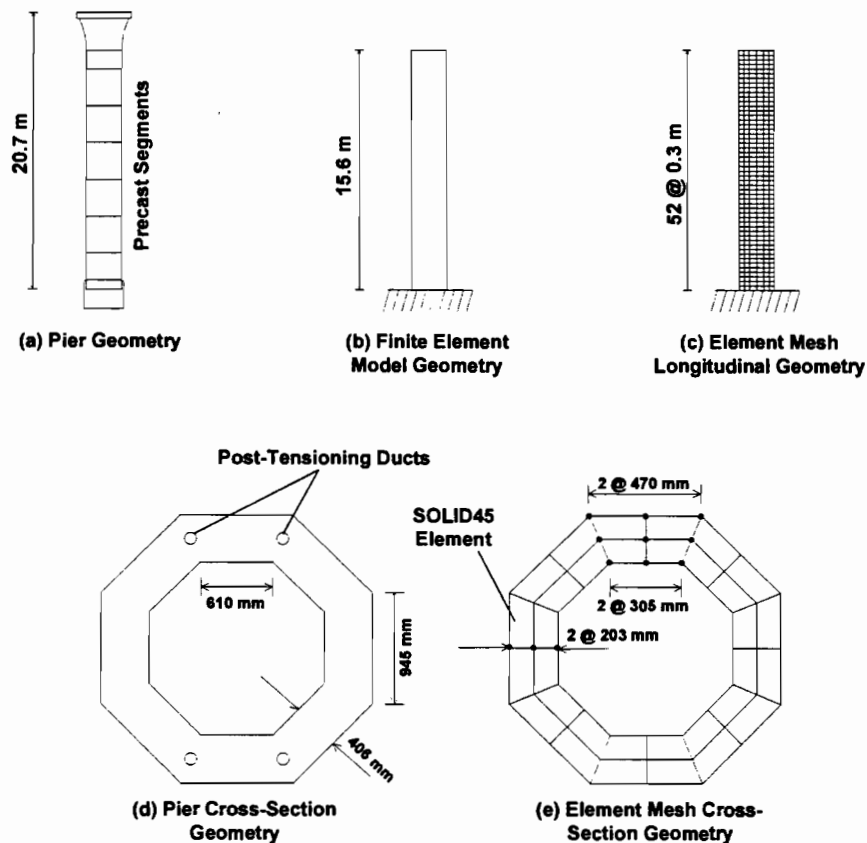


**Figure 6.39** (a) Actual pier geometry, (b) finite element model geometry, (c) element mesh longitudinal geometry, (d) actual cross-section geometry, and (e) element mesh cross-section geometry.

### 6.6.2 Material Properties Input

ANSYS required certain material property information to accurately model structural response to temperature loading. Both the modulus of elasticity and the coefficient of thermal expansion were determined in laboratory tests of concrete prism specimens cast simultaneously with the pier segments. From these tests, the modulus of elasticity was determined to be approximately 38.7 GPa. This relatively high number reflected the high compressive strength of the concrete used to construct the pier segments. The coefficient of thermal expansion found in temperature variation tests was approximately  $9.36 \times 10^{-6}/^{\circ}\text{C}$ . Typical values for concrete with limestone aggregate range from  $7.0 \times 10^{-6}/^{\circ}\text{C}$  to  $10.0 \times 10^{-6}/^{\circ}\text{C}$  [45].

Poisson's ratio was determined by comparing the longitudinal and transverse strain changes measured during post-tensioning operations. The average ratio was calculated from measurements at several points in the pier's shaft. A value of  $\nu=0.21$  was used for the ANSYS computer model. A shear modulus of  $G = 14.8$  GPa was calculated from the relation [46]:

$$\frac{E}{2G} = 1 + \nu \quad (6.4)$$

### 6.6.3 Temperature Loading Input

Temperature changes were referenced to initial temperatures at a given time. Thus what are referred to as "temperatures" here are really temperature changes from the referenced temperature state. As discussed previously, temperatures were measured at 24 locations across the cross-section of segment PC16-5. These locations were an important consideration during selection of structural elements to be used for analysis; ANSYS requires temperatures to be assigned to node points corresponding to the corners of solid elements. The simplest element mesh that most closely represented the actual temperatures measured is shown in Figure 6.39(e).

Element corners were set so that wall midpoints coincided with thermocouple locations in each of the eight walls of the pier's cross-section. However, temperatures at element corners at the interfaces between walls were not directly measured. To provide a more complete set of input data, temperature changes at these locations were linearly interpolated between measured temperature changes around the perimeter of each of three "octagonal shells" (see Figure 6.40). This method provided a more realistic estimation than if temperatures were to be interpolated *through* the wall thickness: temperature distributions through concrete are highly non-linear due to the material's poor thermal conductivity.

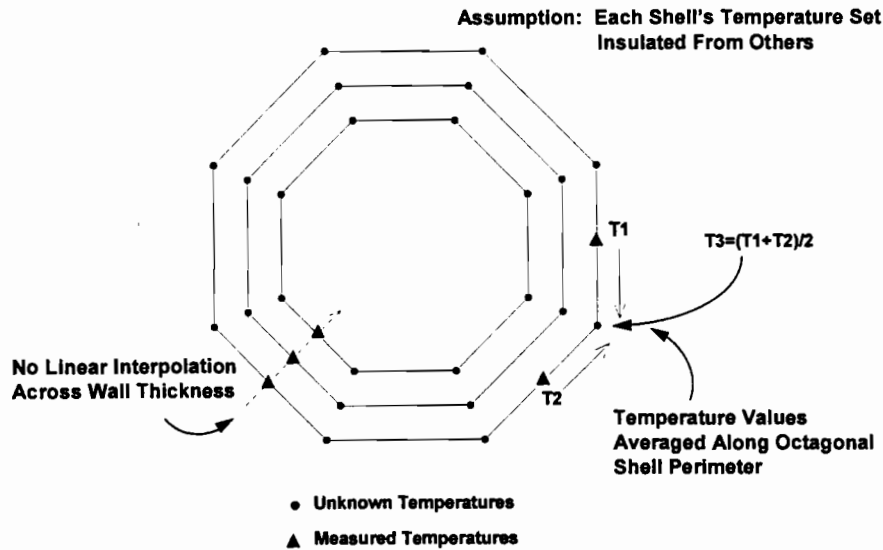


**Figure 6.40** “Octagonal shell” method of temperature estimation.

With the element corners set as in Figure 6.39e, element distribution along the length of the pier was chosen to satisfy two requirements. Most finite elements produce more accurate results when the aspect ratio (ratio of height to width) of the element is less than about 2:1 and ideally is 1:1. For three dimensional solids, a ratio of 1:1:1 is ideal. Also, element strain and stress output was required at locations matching those of actual gauges in the pier. Element heights were chosen to produce an aspect ratio of about 1.3:1.5:1.0. Thus, the element shapes were adequate to obtain reliable results, and produced stresses and strains coinciding with gauge locations.

Temperature load cases were set up to correspond with the maximum daily temperature changes. For the months of April, May, June and July the maximum daily positive and negative temperature gradients served as loading input. Actual measured temperature changes and interpolated values located at element node points for each case were used to analyze pier response. An example load case with assigned temperature changes is shown in Figure 6.41.

Positive and negative design gradients from both the *AASHTO LRFD Bridge Design Specifications* [8] and NCHRP Report 276 [17] were also input as load cases for comparison with measured temperature distributions. However, a two-dimensional temperature distribution had to be extrapolated from the one-dimensional design temperature gradients. Temperatures were assigned to model nodes as shown in the example in Figure 6.42. The temperature at each node location was interpolated from the design gradient and all temperatures at a particular cross-sectional width were assumed to be identical.



## 6.6.4 Analysis Results

### 6.6.4.1 Longitudinal Strains

#### (a) Positive Gradients

In general, longitudinal strains exhibited well defined characteristics. The higher outer face temperature changes induced large compressive strains at nodes located along the outer perimeter of the section. This behavior is consistent with the strain distributions calculated using hand methods. The areas of highest compressive strains matched the locations of high temperatures almost perfectly. Relatively low temperatures produced local regions of tensile strains. Figure 6.43 shows contour plots of temperature and strain produced by the maximum positive gradient for the month of April 1996.

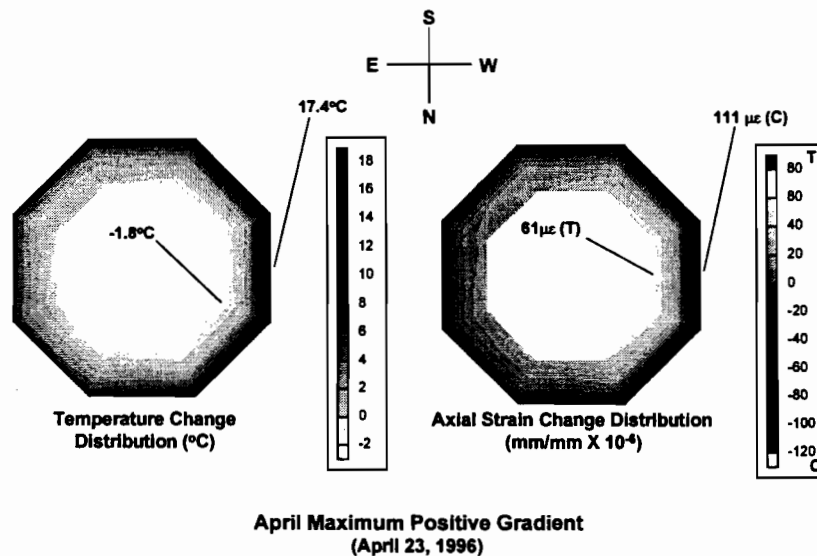


**Figure 6.43** Contour plots of temperature and longitudinal strain, April maximum positive gradient load case.

Projections of the longitudinal strain distributions onto a two-dimensional graph were performed using the octagonal shell approach. Figure 6.44 shows these strain projections on the east-west axis of the pier for the maximum monthly positive gradients. Figure 6.45 shows a comparison of the strain distributions from the largest measured temperature gradient load case and the design code gradient load cases. A summary of the maximum longitudinal strains for all positive gradient load cases can be found in Table 6.1.

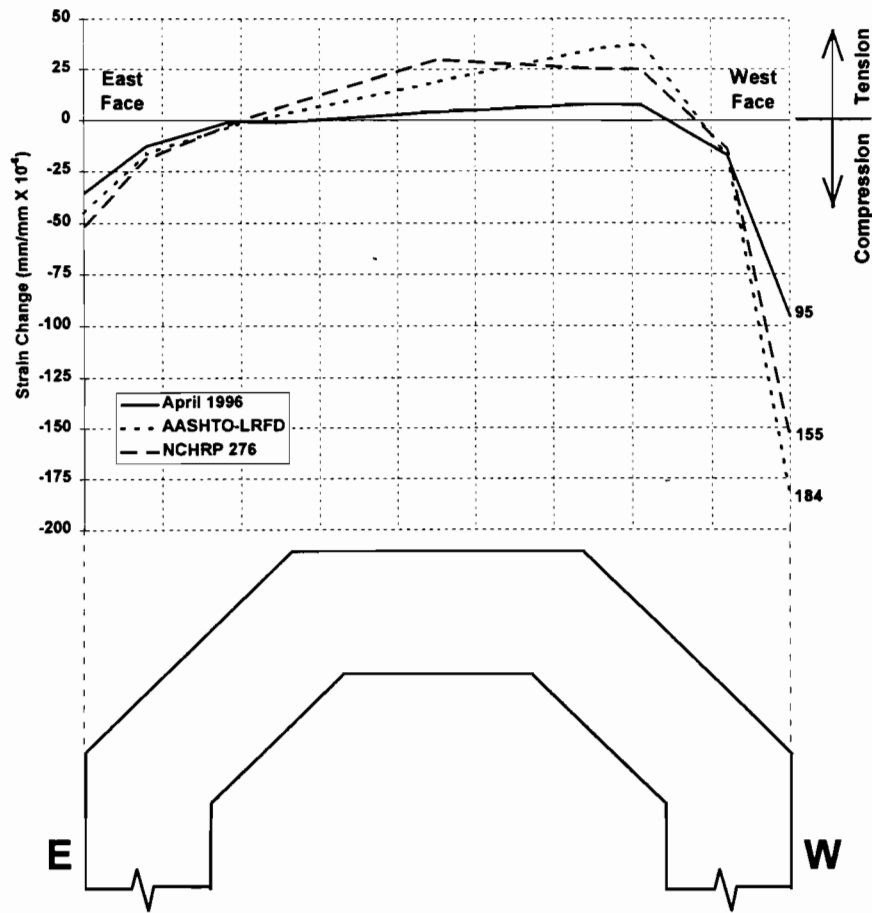


**Figure 6.44** *Finite element analyses strain projection plots on east-west cross-sectional axis from positive design temperature gradients.*

**Table 6.1** *Maximum tensile and compressive strains by load case: positive gradients.*

Positive Gradient Load Case Strain Summary		
Load Case	Max. Tensile Strain ( $\mu\epsilon$ )	Max. Compressive Strain ( $\mu\epsilon$ )
Description	Strain ( $\mu\epsilon$ )	Strain ( $\mu\epsilon$ )
April Max. Positive	61	111
May Max. Positive	51	89
June Max. Positive	54	104
July Max. Positive	50	94
AASHTO-LRFD Positive	43	184
NCHRP 276 Positive	30	155

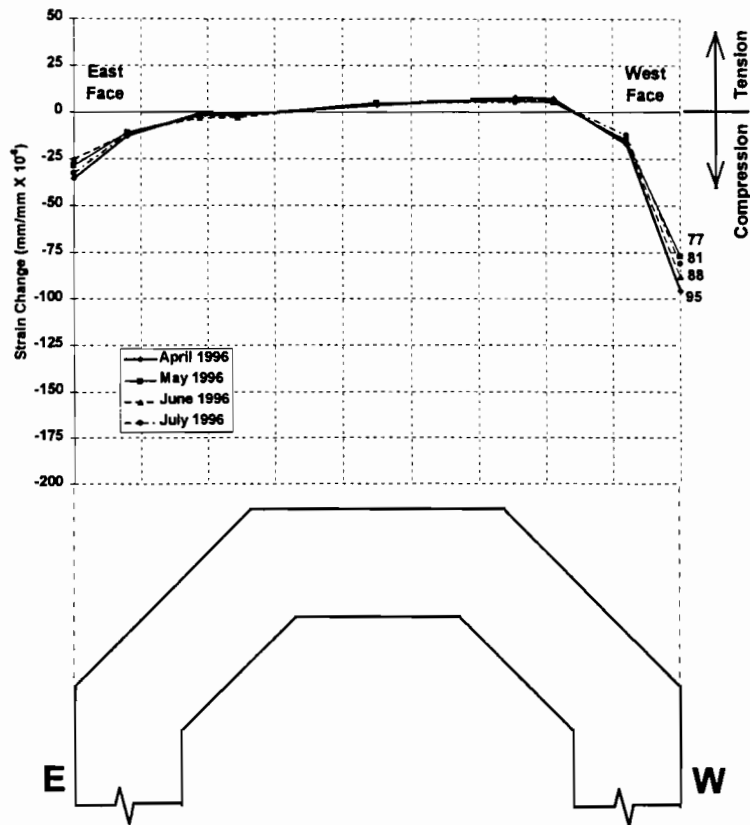


**Figure 6.45** *Finite element analyses strain projection plots on east-west cross-sectional axis from maximum monthly positive temperature gradients.*

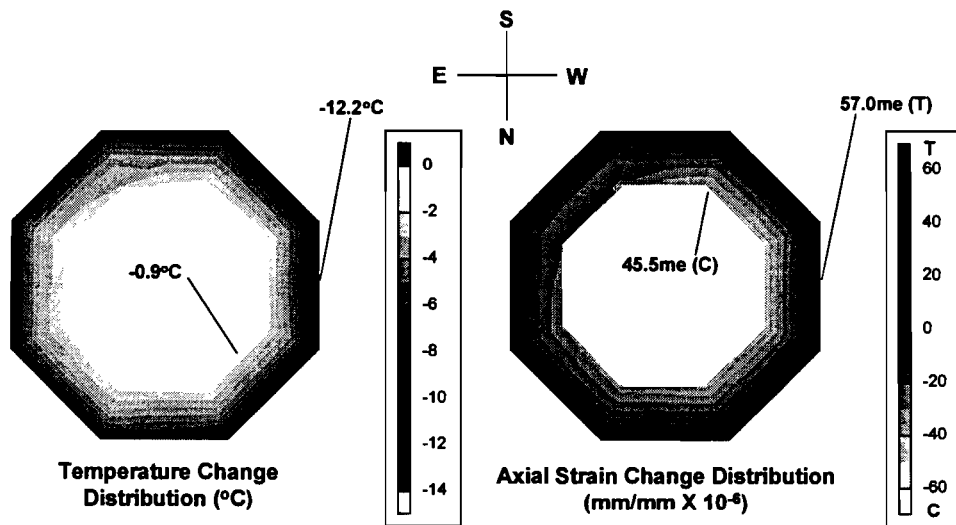
The maximum strain changes listed in Table 6.1 are slightly different than the values shown in Figures 6.44 and 6.45. The projection method used to plot the two-dimensional strain distribution on the one-dimensional east-west axis reduces the strain change magnitudes slightly because the maximum strain changes are averaged with other, slightly smaller, strain changes at the same depth in the section.

The four maximum monthly strain distributions shown in Figure 6.44 are almost identical in shape and magnitude. The strain changes from the April load case have the largest magnitude, and correspond to the largest observed monthly temperature gradient magnitudes. The April load case also exhibits the largest strain change magnitudes at any point in the cross-section for the observed load cases as listed in Table 6.1. The maximum tensile strain change of  $61 \times 10^{-6}$  mm/mm occurred at a point along the inner face of the west wall of the section. The maximum compressive strain change occurred at the outer face of the west wall.

It is apparent from Figure 6.45 that both design code temperature gradients produce resultant strain changes of much larger magnitude than even the largest strain changes due to observed temperature distributions. The maximum compressive strain change at the west face of the section due to the April positive temperature gradient load case is only 60% of the maximum compressive strain due to the AASHTO-LRFD design gradient, and 72% of the maximum compressive strain due to the NCHRP 276 positive gradient. Tensile strains from the design gradients are also larger in magnitude. In general, though, the projected strain distributions have similar shapes.

**(b) Negative Gradients**

For the negative gradient load cases, the low outer face temperatures induced large tensile strains at nodes located along the outer perimeter of the section. Similar to the previous section, the areas of highest tensile strains matched the locations of the lowest temperatures almost perfectly. Figure 6.46 shows contour plots of temperature and strain produced by the maximum negative gradient for the month of April 1996.



**April Maximum Negative Gradient  
(April 15, 1996)**

**Figure 6.46** *Contour plots of temperature and longitudinal strain, April maximum negative gradient load case.*

Octagonal shell projections are plotted in Figure 6.47. For comparison with previously calculated stress distributions, all projections were made along the east-west cross-sectional axis. A summary of the maximum longitudinal strains for all negative gradient load cases can be found in Table 6.2.

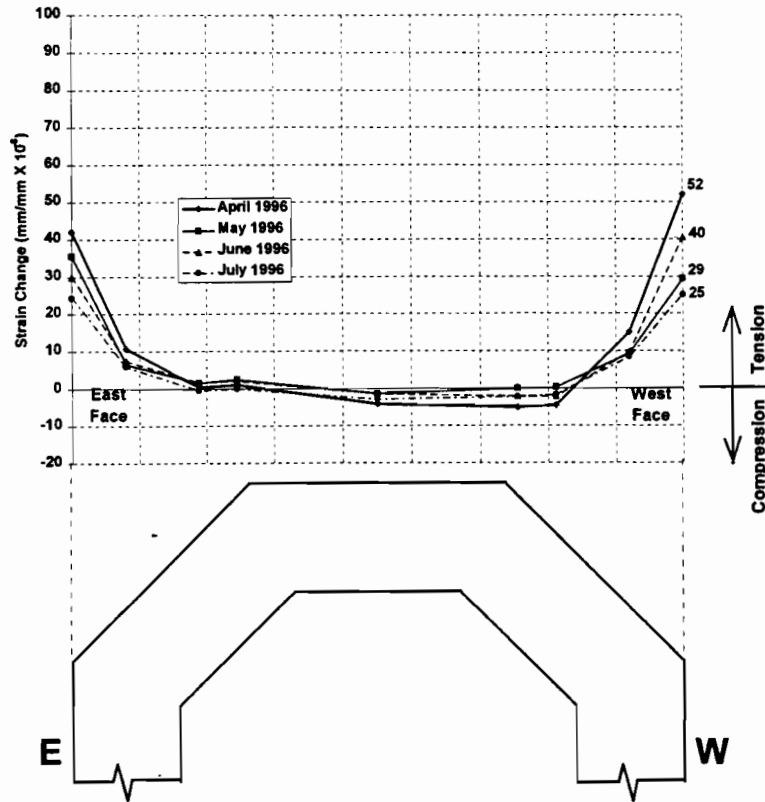


**Figure 6.47** *Finite element analyses strain projection plots on east-west cross-sectional axis from maximum monthly negative temperature gradients.*

**Table 6.2** *Maximum tensile and compressive strains by load case: negative gradients.*

Negative Gradient Load Case Strain Summary		
Load Case	Max. Tensile	Max. Compressive
Description	Strain ( $\mu\epsilon$ )	Strain ( $\mu\epsilon$ )
April Max. Negative	57	45
May Max. Negative	41	28
June Max. Negative	45	31
July Max. Negative	27	24
AASHTO-LRFD Negative	92	21
NCHRP 276 Negative	94	17

As before, the maximum strain changes shown in the strain distribution projection plots are slightly affected by the projection method (see Figure 6.47). They coincide with the values listed in Table 6.2. Note that the maximum tensile strain change for the May load case occurs on the east face of the pier, while the other observed temperature load cases

undergo the largest tensile strain changes on the west face. The April load case produced the largest strain change magnitudes among the observed load cases.

The largest tensile strain changes for the observed temperature load cases are slightly less than those found in the positive temperature gradient analyses (see Table 6.1). However, the locations of the tensile strains at the outer fibers of the section during negative gradient loading are critical for segmentally constructed members. Tensile strain changes during negative gradient loading could violate the design code requirement of zero tensile strain on the outside fibers of the section.

The design code temperature gradient load cases again produced strain changes much greater in magnitude than any observed gradient load cases (see Figure 6.48). The maximum observed load case tensile strain changes (from April 1996) were only 62% of the AASHTO-LRFD load case tensile strains, and 61% of the tensile strains due to the NCHRP 276 design negative gradient load case. The compressive strain changes from the observed temperature load cases were also much smaller than those produced by the design temperature gradients.

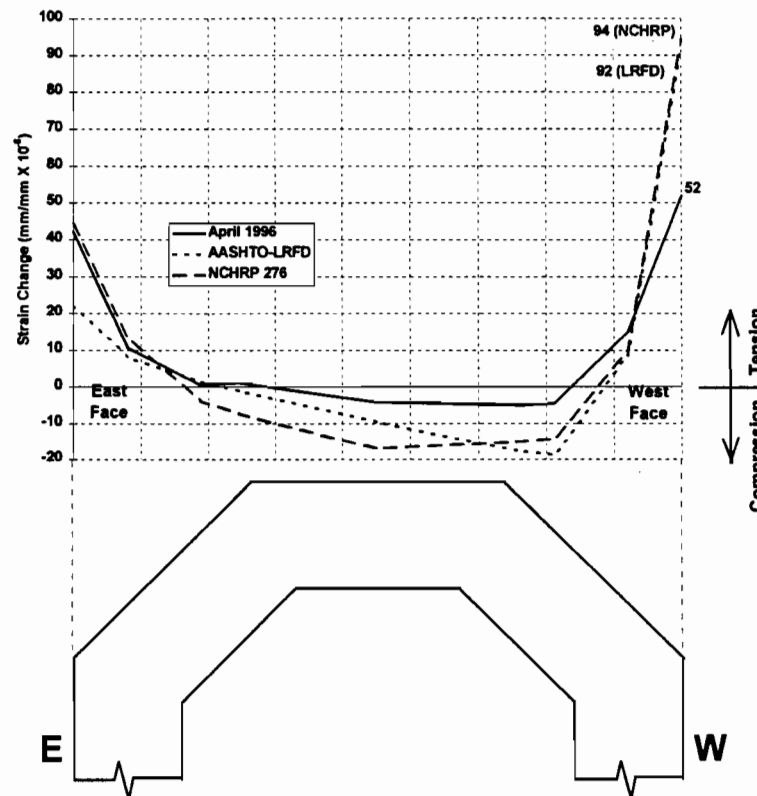


**Figure 6.48** *Finite element analyses strain projection plots on east-west cross-sectional axis from negative design temperature gradients.*

### 6.6.4.2 Transverse Strains

#### (a) Positive Gradients

The distribution of transverse strains induced by temperature changes matched those predicted by theory quite well. For positive gradient load cases, where the outer faces of the pier are much warmer than the interior, compressive strains occurred consistently along the outer face, while tensile strains were located on the interior faces where temperatures were relatively low. Figures 6.49(a) through 6.49(d) illustrate the temperature and transverse strain distributions for the maximum monthly positive temperature gradient load cases.

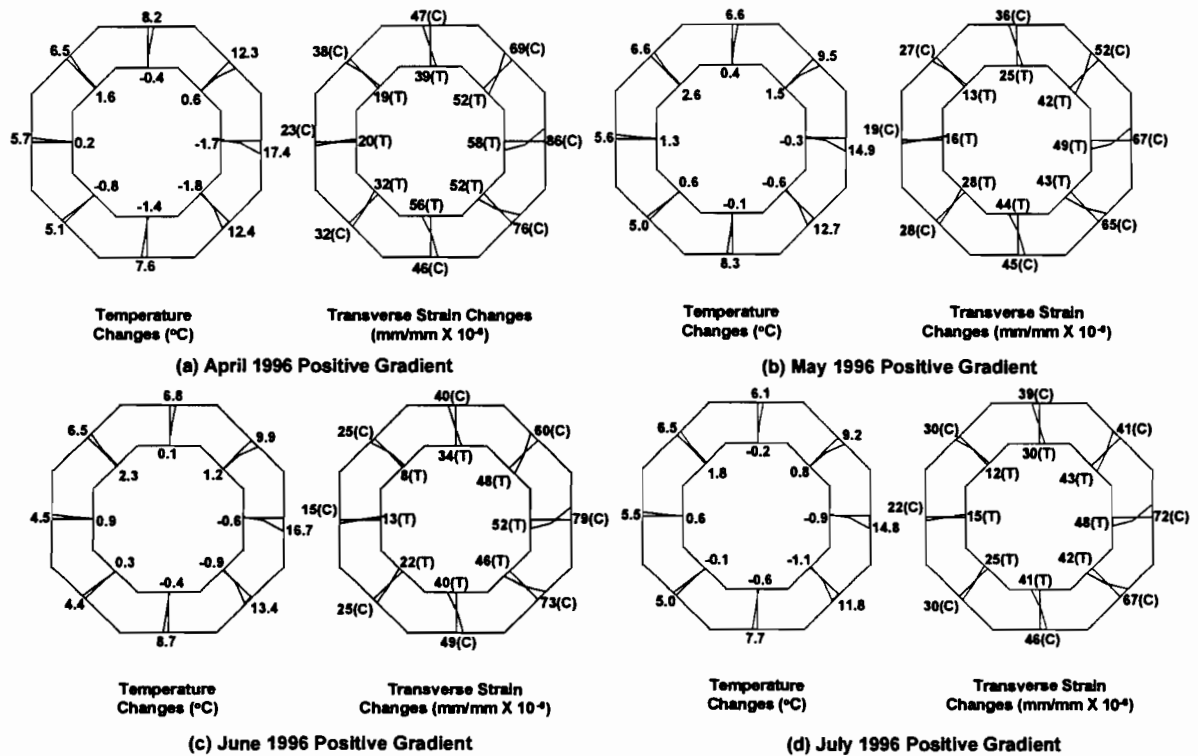


**Figure 6.49** *Temperature loading and transverse strain from finite element analysis of maximum monthly positive gradients during (a) April, (b) May, (c) June, (d) July.*

The maximum positive gradient load case from April 1996 produced the largest transverse strain changes [see Figure 6.49(a)]. Compressive strain changes coincided with temperature increases similar to the longitudinal strains discussed earlier. For the April load case, the maximum compressive strain change of  $86 \times 10^{-6}$  mm/mm occurred

at the west face of the pier. The largest tensile strain change occurred at the interior of the west wall.

The distributions of transverse strain changes were similar for subsequent months' load cases, but the strain change magnitudes were somewhat smaller. The maximum compressive and tensile strain changes occurred in the same locations for every observed load case. This follows directly from the observation that the largest temperature change for all the load cases occurred in the same location on the west face of the pier.

### **(b) Negative Gradients**

Transverse strains induced by the negative gradient load cases also matched those predicted by theory. Transverse tensile strains occurred along the outer faces of the pier where temperatures were at their lowest. Similarly, compressive strains were located at the interior of the pier. This indicates that the interior is pulled into compression by the restraint provided by the cooler outer surface concrete, similar to the longitudinal stress distributions discussed earlier. Figures 6.50(a) through (d) show the distributions of temperature and transverse stresses through each wall of the pier under the maximum monthly negative temperature gradient load cases.

Unlike the transverse strain changes produced by the positive gradient load cases, the maximum strain changes due to the negative gradient load cases do not necessarily occur in the same locations for each case. The locations of the maximum tensile strain changes did not always correspond to the largest negative temperature changes. The same holds true for the transverse compressive strain changes.

The unpredictability in the locations of the maximum strain changes is due to the distributions of temperature changes around the perimeter of the section for the negative gradient load cases. The entire outside perimeter of the pier typically undergoes almost uniform decreases in temperature [see Figures 6.50(a) through (d)]. Thus the effects due to temperature changes in any one face of the pier do not greatly change those in adjacent faces. There is less redistribution of transverse stresses around the section because the temperature loads are more uniform than that of a typical positive gradient. Positive temperature gradients are characterized by large differences in the perimeter temperature changes in the section [see Figures 6.49(a) through (d)]. More redistribution of transverse stress occurs during those temperature changes due to the highly uneven temperature loading.

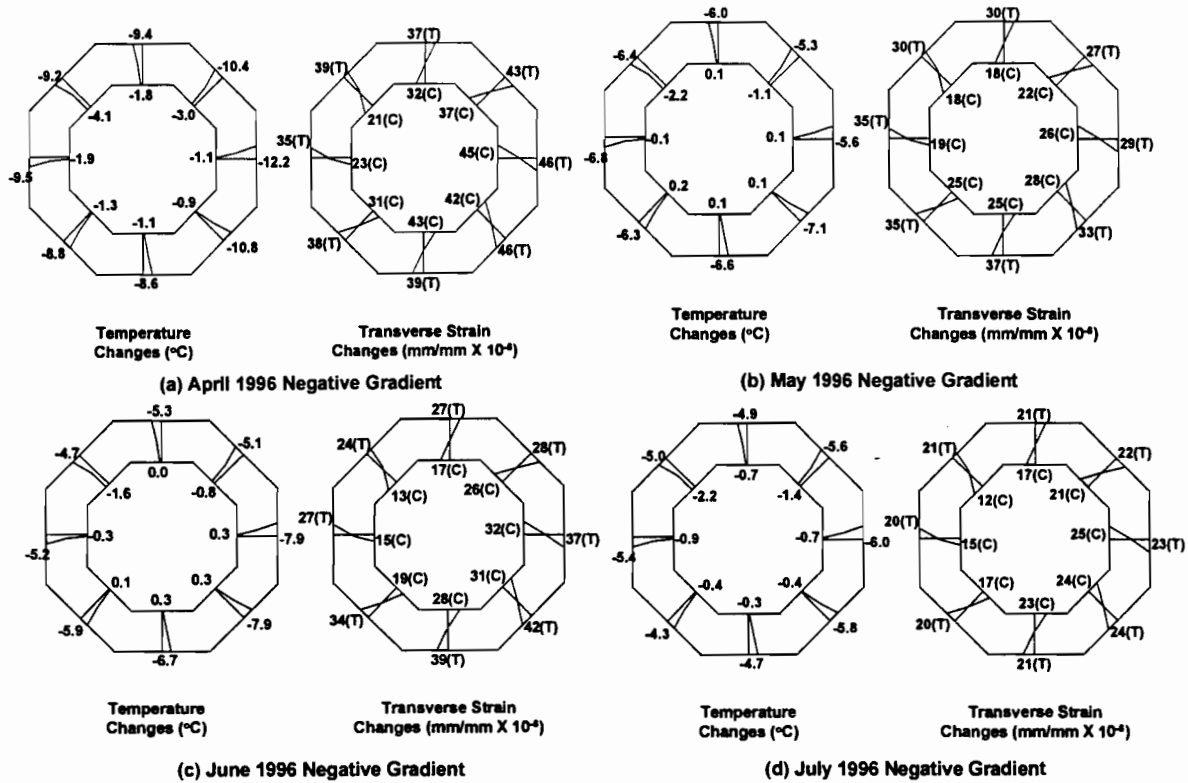


**Figure 6.50** Temperature loading and transverse strain from finite element analysis of maximum monthly negative gradients during (a) April, (b) May, (c) June, (d) July.

**6.6.5 Comments**

In general, the strain results from the finite element analyses of both observed and code-specified temperature gradient load cases matched well the behavior predicted by the conventional calculations performed in the previous sections. However, it is important to note that the finite element analyses requires modeling assumptions similar to those made during manual calculations. Both methods assumed the same modulus of elasticity, Poisson's ratio, and concrete coefficient of thermal expansion. Similarly, the manual calculations and the finite element analysis assumed linear elastic behavior throughout the pier. The pier was modeled with a constant cross-section for both methods (i.e. the capital and base were ignored). Finally, the contributions to both heat flow and the stress field present in the pier from post-tensioning tendons and imbedded rebar were ignored.

## 6.7 Measured Response of Ramp P Segmental Pier to Superstructure Construction Loads

The Ramp P superstructure was constructed in balanced cantilever with an unbalanced moment on the piers no greater than that from the weight of one unbalanced superstructure segment. Since the contractor had trouble in adequately stressing the pier tie down bars to rigidly connect the superstructure to Pier P16, this unbalanced moment was taken partially or completely by the crane used to lift the segment into place. This was possible since two ground based cranes were used to construct the five span continuous girder on Ramp P. The complicated construction sequence and limited ground access dictated the use of two cranes. Unfortunately, the maximum unbalanced moment on pier P16, as predicted in the pier's design for fully unbalanced construction, never occurred. Instead, the maximum moment in the pier from the superstructure construction occurred when segment P16-17 was placed. This was the final segment placed in cantilever near the midspan of span P16. Most importantly, this segment was placed after continuity had been made in the superstructure span P15. The cantilevering moment from segment PC16-17 was distributed to both pier P16 and to the superstructure span P15 and pier P15. The response of pier P16 was measured for this load case.

Measurements were taken by strain gauges oriented vertically at several locations along the height of pier P16. The bending moment in the pier would have been essentially constant along the height of the pier during balanced cantilevering, but since the pier was part of an indeterminant frame when segment PC16-17 was placed, the moment in the pier would change over its height. Four planes of gauges were selected for study. The first plane of gauges was in segment PC16-1 located 2.06m above the top of the footing. The second set of gauges was in segment PC16-5 located 12.17m above the top of the footing. The third set of gauges was in segment PC16-7 located 16.08m above the top of the footing. The fourth set of gauges was located on the 16 vertical tie down bars located near the top of the pier capital segment PC16-8, 19.81m above the top of the footing. The length from the top of the footing to the center of gravity of the superstructure box girder was 21.89m. The 285kN load from the placement of superstructure segment P16-17 had a cantilever arm of 25.84m to the center of gravity of the pier, yielding a bending moment of -7366kN-m to be distributed to the structure. Because of the horizontal curvature of the superstructure, a torque of 435kN-m also had to be distributed to the structure.

Figures 6.51 through 6.54 show the measured concrete stresses at the gauge locations and calculated stresses along the north-south axis. The superstructure centerline geometry was exactly parallel to the pier's north-south axis at pier P16, as well as the other ramp piers. For the purpose of comparison, a plane frame analysis was performed, ignoring torque effects, and is plotted in Figures 6.51 through 6.54. The solid line assumed fixity at the top of the footing. The dashed line assumed the point of fixity was 4.2m below the top of the footing to account for flexibility of the footing and four 1.070m drilled shafts. The 4.2m pier height increase was chosen to calibrate the model to the measured results of gauges C400, C402,

C410 and C412 in Figure 6.51 along the north-south axis of the pier. These gauges in segment PC16-1 were located near the point of inflection in the pier. Distribution of the cantilever moment of  $-7366\text{kN}\cdot\text{m}$  was  $-3263\text{kN}\cdot\text{m}$  to pier P16 and  $-4103\text{kN}\cdot\text{m}$  to span P15 when fixity was assumed at the top of the footing. Distribution was  $-3041\text{kN}\cdot\text{m}$  to pier P16 and  $-4324\text{kN}\cdot\text{m}$  to span P15 when the point of fixity was moved down  $4.2\text{m}$ .

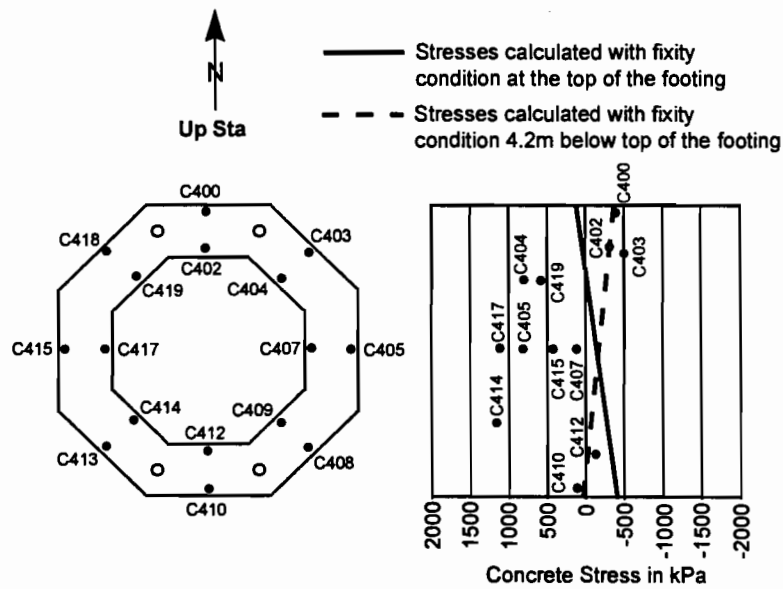


**Figure 6.51** Pier Segment PC16-1 stress changes from placement of superstructure Segment P16-17.

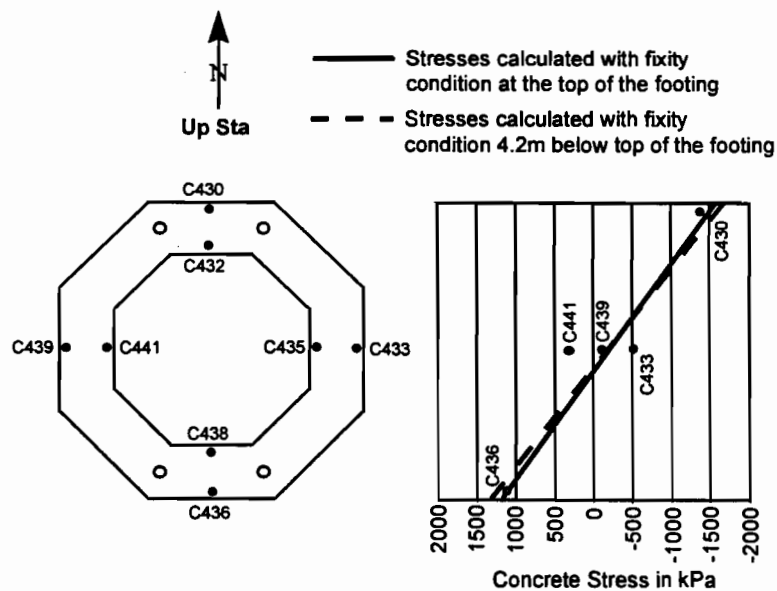


**Figure 6.52** Pier Segment P16-5 stress changes from placement of superstructure Segment P16-17.

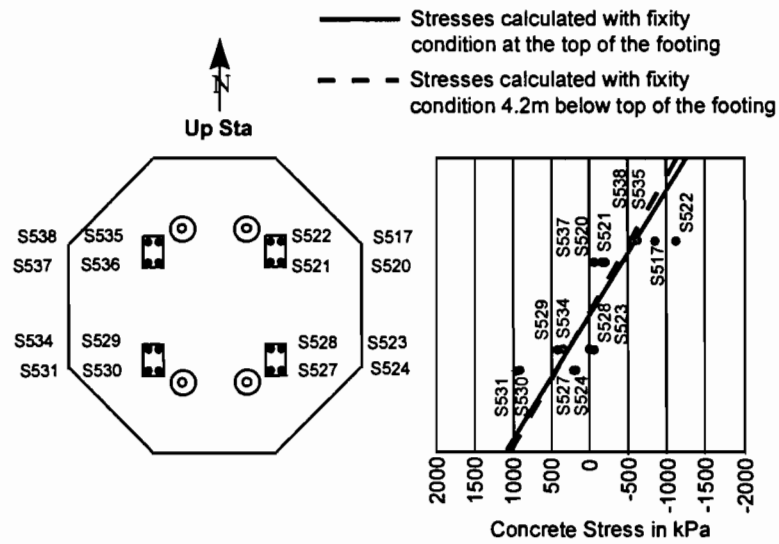


**Figure 6.53** Tie down bar stress changes at the top of pier capital Segment P16-8 from placement of superstructure Segment P16-17.

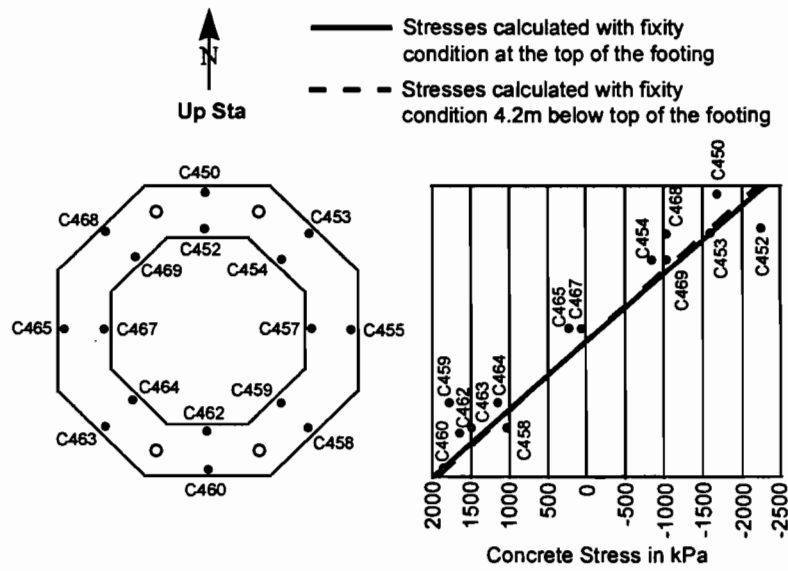


**Figure 6.54** Pier Segment P16-7 stress changes from placement of superstructure Segment P16-17.

In plan view, the torque from the superstructure would tend to cause tension in the west face of the pier. This is poorly reflected by the gauges in segment PC16-1 in Figure 6.51. This trend is consistently evident as indicated by the gauge measurements in Figures 6.52 through 6.54. If the entire torque were taken by pier P16, the change in the calculated stresses in the extreme fibers along the east-west axis, plotted in Figures 6.51 through 6.54, would be about 400kPa. The horizontal radius of the superstructure was only 218.3m, so torsional effects were included in the design of this pier.

Pier P16 was compact and regular in shape over much of its height, and appears to have behaved in a very predictable way, with stress change linear across the section. The accuracy of the design of this pier would rely more on the accuracy of the analysis, not on the sectional behavior of the pier. Accurate modeling of the foundation stiffness would be part of a good design of this pier. The post-tensioned connection of the superstructure to the pier also behaved in a predictable manner. The calculated stresses plotted in Figure 6.54 assumed that plane sections remained plane in the grout pad on top of the pier capital, and therefore the full moment of inertia of the grout pad could be used. This assumption appears to have been valid, since the measured stresses plotted in Figure 6.54 fall on either side of the calculated stresses. No tension in the connection was evident.

## **6.8 Comparison of Measured and Analytical Results**

### ***6.8.1 Longitudinal Strains***

As discussed previously, the strain gauges used during the instrumentation of pier P16 were temperature compensated so that direct linear expansions or contractions due to temperature were not measured. The strains displayed are the differential strains caused by the temperature gradients and physical member restraints which produce stresses in the members. These are referred to as self-equilibrating strains.

The octagonal shell projection method, discussed in Reference 3, was used to display two-dimensional distributions of temperature and longitudinal self-equilibrating strains on a one-dimensional axis for comparison purposes. Temperatures and strains plotted in this manner are easier to visualize, as are their effects on the member in a global sense. Comparisons between results from several strain calculation methods can be more easily made.

It should be noted that the strain projection plots presented in this section only provide a general idea of the state of self-equilibrating longitudinal strains present due to the temperature distributions throughout the pier's cross-section. Strains occurring at the outermost east and west fibers of the pier are most accurately represented. The values of strain projected onto the one-dimensional plot at these points are the averages of several strains located at the outermost edges which have similar values. Strains plotted from the interior of the cross-section are the averages of strains located at both the outer faces

and the interior, which may differ in magnitude and in direction. For this reason, strains plotted away from the outer edges on the one-dimensional graphs are generally smaller in magnitude than those actually present.

In order to gauge the relative accuracy of the three analytical methods used, strain distributions from each were compared on a one-dimensional strain projection plot. This was necessary in part because the strain results from the classical method presented by Imbsen, et al [17] were calculated from the measured temperature distribution projected onto a one-dimensional axis. Thus, the strains due to the one-dimensional temperature loading could not be extrapolated to a two-dimensional distribution.

Strain distributions were calculated for the maximum positive and negative temperature distributions for the months of April and June 1996. The temperature gradients measured during April were largest in magnitude, as were the calculated self-equilibrating strains. However, no strains were measured in the pier during April due to scheduling constraints. Therefore, results from the month of June are included here because they represent the largest temperatures and strains that were simultaneously measured.

The results from the two hand-calculation methods and the finite element analysis were adjusted for more direct comparison with the individual points of strain recorded by the gauges imbedded in the concrete of the pier. In the finite element analysis, strains were calculated at node points. This limited the number of calculated strain points at mid-length of each wall of the pier. Similarly, the strain results from the primary bending axis method were assumed to be located at the same positions as the measured temperatures in each pier wall. Discrete areas of constant temperature used to calculate strains by this method were assumed to coincide with the measured temperature locations in segment PC16-5. Although only an estimate of the strains at any depth in the pier's cross-section, the classical method of strain determination was also included during comparisons with measured strains.

A full discussion and display of all monthly maximum temperature gradients and their associated strains would be tedious and unnecessary: The temperature distributions of each month's maximum gradients vary only slightly in magnitude and are similar in shape. Ideally, strain comparisons would be made here using the largest measured gradients. However, these gradients occurred during April 1996, and the concrete strain gauges were not operational at that time. As such, comparisons with measured strains will be made with strains recorded and calculated for the maximum positive and negative gradients that occurred during the month of June 1997. These temperature distributions represent the most severe which were measured while both temperature sensors and concrete strain gauges were operational.

### 6.8.1.1 Positive Gradient

The temperature gradients used for calculations are not the static temperature distributions present in the pier at any given time. Instead, the *difference* in temperatures between the coolest, most uniform distribution and the set of temperatures showing the largest changes during the day is used to calculate the temperature gradient present in the pier. All discussions of temperature gradients made here actually refer to the largest *changes* in temperature over the course of any given day (and their associated strain changes over the same time period).

The maximum positive temperature gradient for the month of June occurred on June 20, 1996 and consisted of the difference in temperatures between 8:25 AM and 7:25 PM. The coolest and most uniform temperatures typically occur around sunrise. The temperature set exhibiting the highest temperatures with the largest differences typically occurs just after sundown. As with all of the monthly maximum positive temperature gradients measured in pier P16, the June positive gradient's highest temperatures occurred at the west face of the cross-section. Most of the associated bending of the pier due to differential heating also occurred along the east-west cross-sectional axis.

Longitudinally-oriented concrete strain gauges were positioned along the east-west and north-south axes of the pier's cross-section in all three instrumented column segments. Figure 6.55 shows the temperature changes during the maximum positive gradient for June that were recorded by thermocouples located in segment PC16-5 near mid-height of the pier. Temperatures are plotted for the six thermocouples aligned along the east-west cross-sectional axis. The thermal values from segment PC16-5 were used as input for the strain calculations in all three calculation procedures.

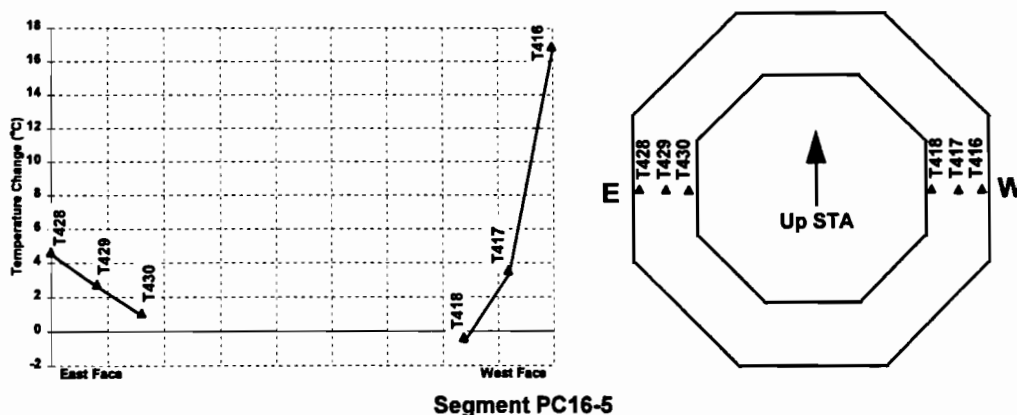


**Figure 6.55** *Temperature changes along the east-west cross-sectional axis recorded by thermocouples in segment PC16-5.*

The calculated and measured strains on the east-west axis of segment PC16-5 are plotted in Figure 6.56. Gauge C433, located near the west face of segment PC16-5, exhibits strain changes substantially below those predicted by all three calculation methods. The daily cycles of strain change recorded by gauge C433 during three days in June exhibiting regular daily temperature patterns are shown in Figure 6.57. A comparison was possible with gauge C458 located near the northwest face of segment PC16-7. From the temperature cycles discussed previously, it was shown that the west and northwest faces of the sunlit column segments experienced similar heating and cooling patterns and magnitudes. Therefore, C433 and C458 should show similar daily patterns of strain measurements. As seen in Figure 6.57, gauge C433 appears to produce somewhat more irregular cycle with magnitudes of variation smaller than those exhibited by C458. The gauge could be partially debonded. This might partially explain the lower strain change recorded by C433 that was plotted in Figure 6.569. Note that the readings from T416 tend to confirm the cyclic pattern of C458 and C433. If the value recorded by C458 was substituted for C433 in Figure 6.56, the strain change would be  $-60\text{mm/mm} \times 10^{-6}$  which would be in much better agreement with the predictions but still lower than the finite element model predictions.

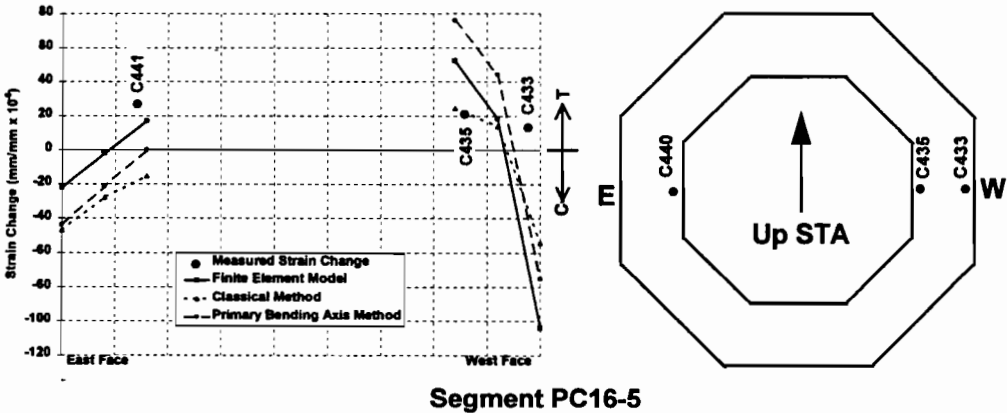


**Figure 6.56** *Calculated strain changes and strain changes recorded by concrete strain gauges in segment PC16-5, east-west cross-sectional axis.*

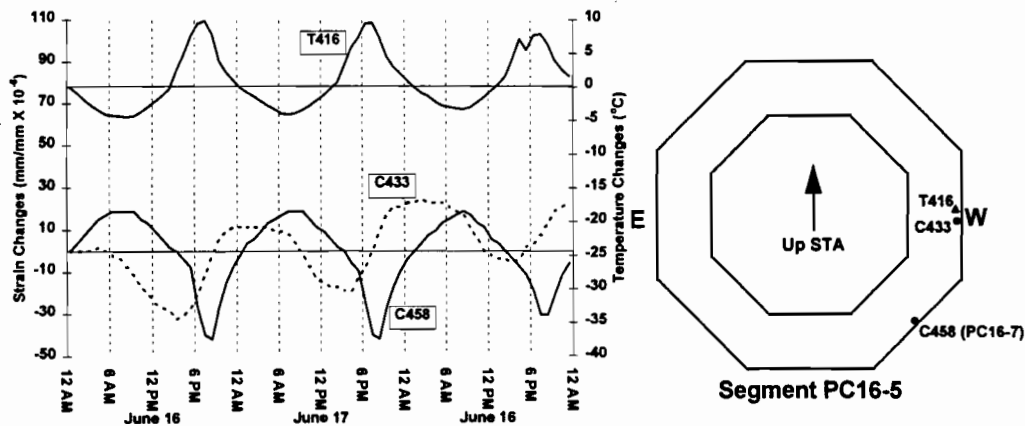


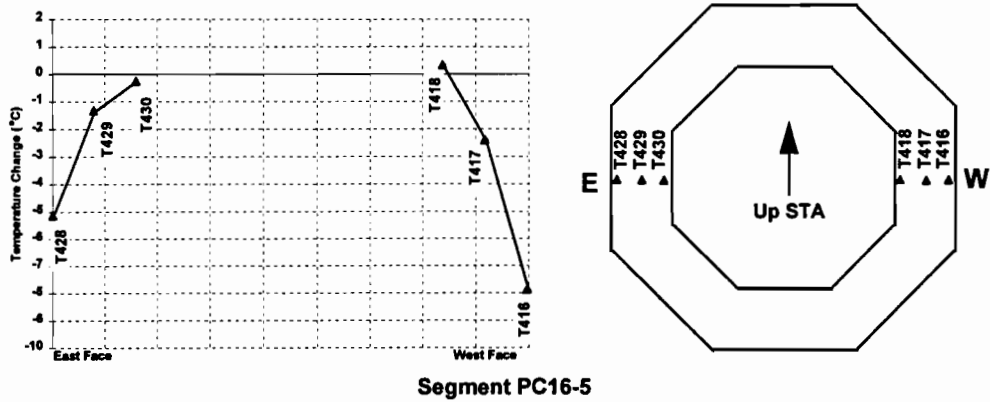
**Figure 6.57** Comparison of C433 and C458 during several daily cycles of temperature.

### 6.8.1.2 Negative Gradient

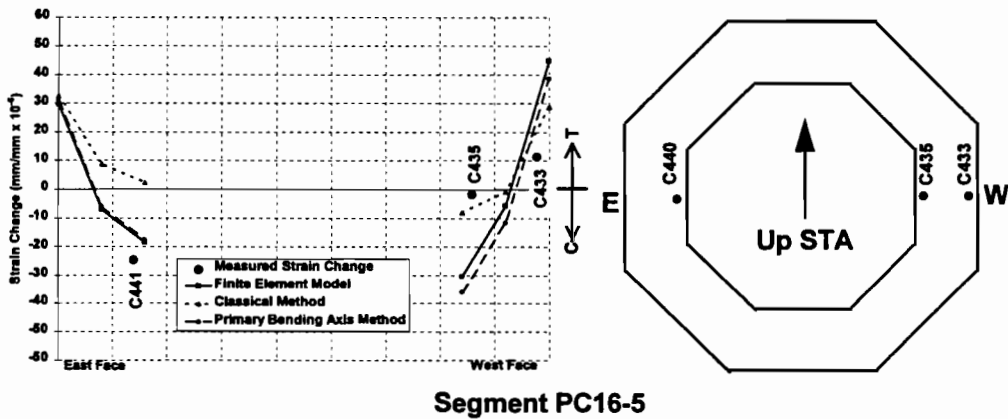
The maximum negative temperature gradient for the month of June consisted of the temperature differences between 10:25 PM on June 3 and 5:25 AM on June 4. The temperatures present at 10:25 PM were still relatively high from heating during the previous day. At that time, the outer fiber temperatures had cooled while the slow heat flow into the interior of the pier continued to raise temperatures there. Thus, the temperatures were distributed evenly through the cross-section. By 5:25 AM the outer faces had cooled rapidly relative to the interior. At that time, the largest difference in temperatures between the outer and inner faces of the pier was present.

Figure 6.58 shows the temperature changes recorded by the thermocouples located along the east-west axis of segment PC16-5 during the maximum negative gradient. Note the greater cooling of the outer fiber temperatures due to the influence of cool nighttime ambient temperatures. Again, these temperature changes were used for the calculations at all pier sections for maximum negative gradient strains. The measured and predicted changes in strain near the outer surfaces of segment PC16-5 along the east-west axis are illustrated in Figure 6.59. The measured strains along the east-west axis of segment PC16-5 do not coincide well with the calculated values, with the exception of gauge C441. As discussed earlier, gauge C433, located near the west face of the segment, is probably not totally reliable. The strain change recorded by C435, located near the interior face of the pier's west wall, appears unusually small in magnitude. Figure 6.60 shows a plot of the strain measurements recorded by C435 over the course of three regular, typical summer days. For comparison, readings from C454, located in segment PC16-7, are also included. From the figure it can be seen that the magnitudes of strain

recorded by C435 are much smaller than normally expected. The “stair-step” appearance of the data recorded by C435 indicates that the strain levels being recorded are close to the minimum strains the gauge is capable of sensing, and may be an indication that the gauge is partially debonded from its steel rod. Thus, C435 appears to be unreliable.



**Figure 6.58** Temperature changes along the east-west cross-sectional axis recorded by thermocouples in segment PC16-5.



**Figure 6.59** Calculated strain changes and strain changes recorded by concrete strain gauges in segment PC16-5, east-west cross-sectional axis.

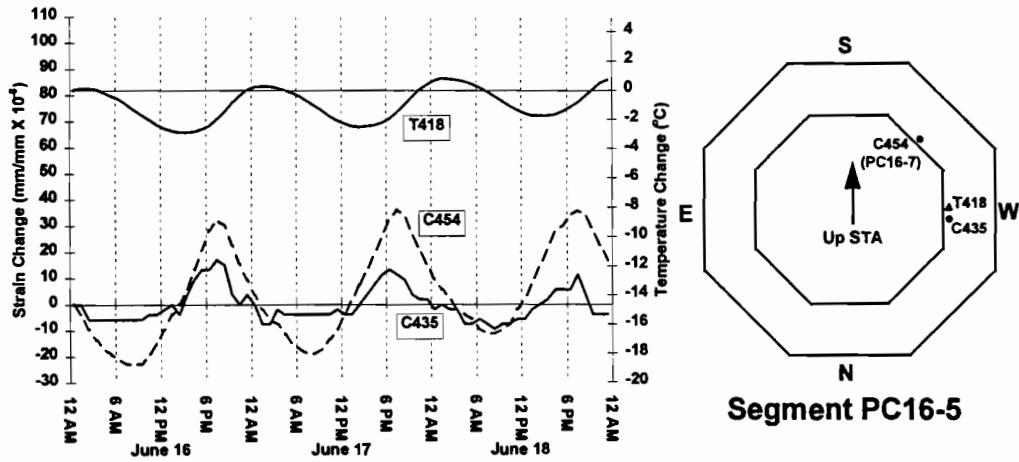


**Figure 6.60** Daily cycles of strain recorded by C435 and C454.

The temperature changes recorded by the thermocouples located along the north-south axis of segment PC16-5 during the maximum negative gradient are shown in Figure 6.61. These were used for strain calculations along the north-south axis of all column segments. In contrast to the disagreement along the east-west axis of segment PC16-5, excellent correlation between observed and calculated strains was found along the north-south axis of that segment. Figure 6.62 illustrates the similarities in measured and calculated strains. Both the finite element model and the primary bending axis method produced strains very close to those measured in the field.

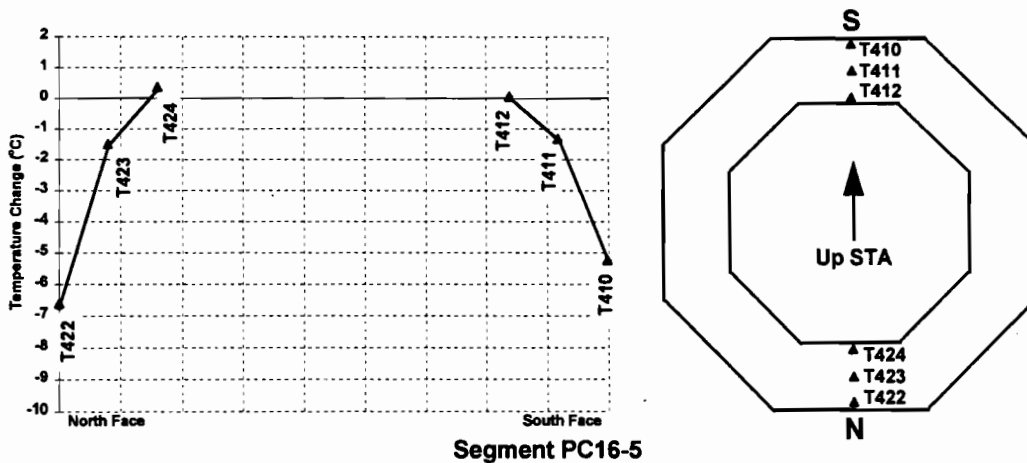


**Figure 6.61** Temperature changes along the north-south cross-sectional axis recorded by thermocouples in segment PC16-5.

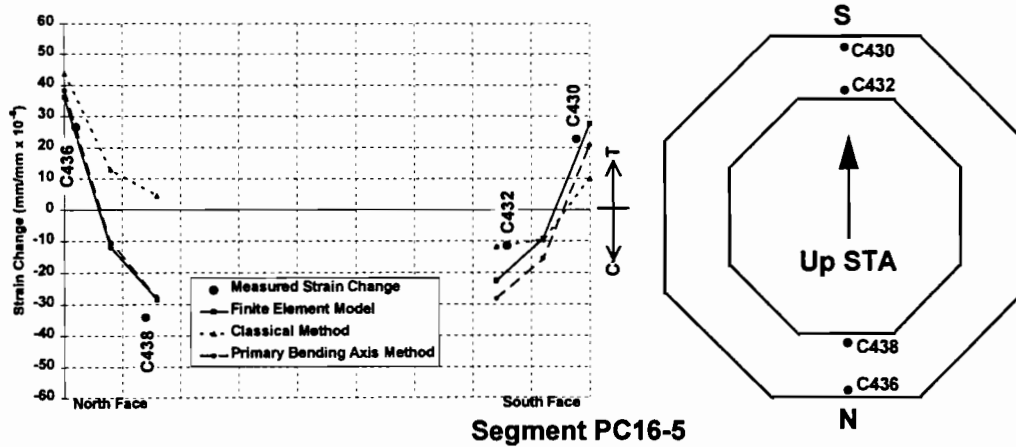


**Figure 6.62** *Calculated strain changes and strain changes recorded by concrete strain gauges in segment PC16-5, north-south cross-sectional axis.*

### 6.8.1.3 Comments on Longitudinal Strains

In many cases, calculated strains compared favorably with strains measured in the pier. Unfortunately, some questions exist concerning the reliability of several key concrete strain gauges near the west face of the pier where the largest strains were expected to occur. Calculated and measured strains correlated well in other locations. Measured and calculated strains in locations along the north-south axis of mid-height segment PC16-5 agreed much more closely, as did some of those on the east-west axes. Thus, it appears that the calculation methods used to estimate self-equilibrating strains induced in the pier by non-linear temperature gradients are generally valid, although calculated outer surface strains are greatly in excess of any strains measured on gauges which all had cover.

### 6.8.2 Transverse Strains

Self-equilibrating strains also occur in the transverse direction (normal to the longitudinal axis of the pier). They are induced by temperature gradients through the thickness of the pier's walls but also depend on the geometry of the pier's cross-section. Four strain gauges were installed in each column segment to verify the theoretical transverse strain calculations. Gauges were located in the south, west, north, and east walls at a cover of approximately 65 mm and oriented parallel to the exterior faces. For comparison with measured strains, two calculation procedures were performed. The first involved hand calculations and the use of a computer frame analysis program to determine redistribution of forces between walls of the pier's cross-section. Transverse strains were also determined using the finite element analysis. Both calculations assume that temperatures are known at three points through the thickness of the pier walls and

that they vary linearly between known temperature locations. According to Imbsen, et al [17] temperatures can be assumed to vary linearly through walls about 250 mm or less in thickness. The distance between known temperatures located at points spaced approximately 200 mm apart is well within that limit.

Calculations of transverse strains were performed to determine the strain distribution through the pier wall thickness at mid-length of the wall. This location was chosen to coincide with the positions of the strain gauges. Reference 3 shows strain distributions and points of measured strain for each of the four walls instrumented in each column segment. A typical case is shown herein.

#### **6.8.2.1 Positive Gradient**

Transverse strains calculated by the methods described previously behaved in a similar fashion to the longitudinal strains. High temperatures tend to induce regions of compressive strain and vice versa as the pier maintains equilibrium with the temperature-induced expansions and contractions of the concrete. Thus, for the maximum positive gradient load case from June, where temperature increases occurred more rapidly at the outside face of the pier, transverse self-equilibrating strains were compressive near the outer faces and tensile in the pier's interior. The finite element model and the hand calculations produced virtually identical results. Both models were calculated with the full sunlit temperature distribution measured in segment PC16-5, and assumed no external restraints on the pier cross-section.

Measured and calculated strains in the south and west walls of segment PC16-5 are similar in magnitude and direction (see Figures 6.63 and 6.64).

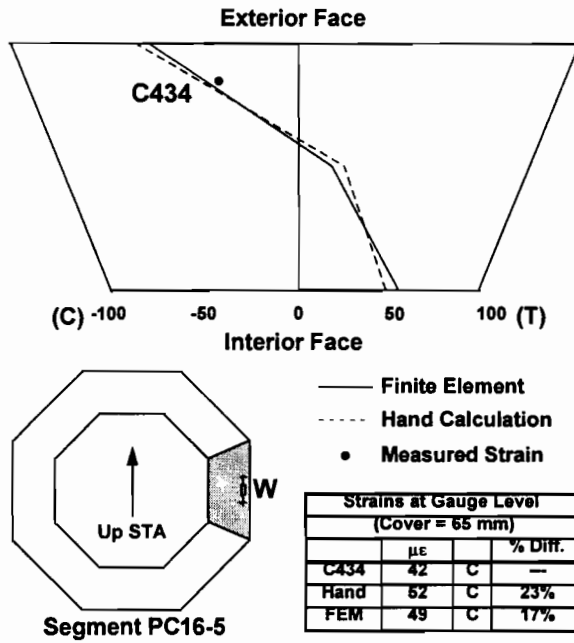


**Figure 6.63** *Transverse strain comparison in the west wall of segment PC16-5.*

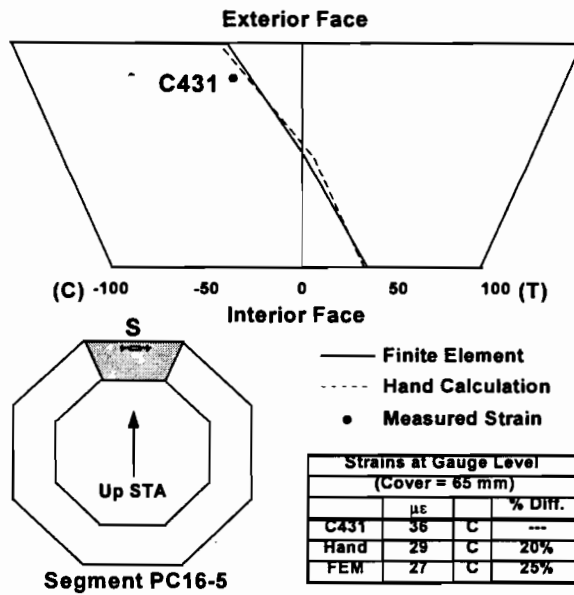


**Figure 6.64** *Transverse strain comparison in the south wall of segment PC16-5.*

### 6.8.2.2 Negative Gradient

Transverse strains caused by the negative gradient temperature change during the early morning hours of June 4, 1996 were calculated using both hand calculations and the finite element analysis. Strains were calculated from temperatures recorded in Segment PC16-5, which for the negative gradient was not exposed to the sunlight. The cooler temperatures in the exterior fibers of the pier's cross-section in theory produce tensile strains at those locations. Compressive strains occur near the interior faces of each wall of the pier. As with the transverse strains calculated for the positive gradients, the results from the hand calculations and the finite element model exhibited very close correlation.

Strain changes recorded in segment PC16-5 also agreed very well with calculated strains. Figures 6.65 and 6.66 illustrate the calculated strain distributions and the corresponding measured strains in two of the four instrumented walls of the mid-height segment. The theoretical calculations appear to predict the actual strains well, with differences ranging up to 20%.

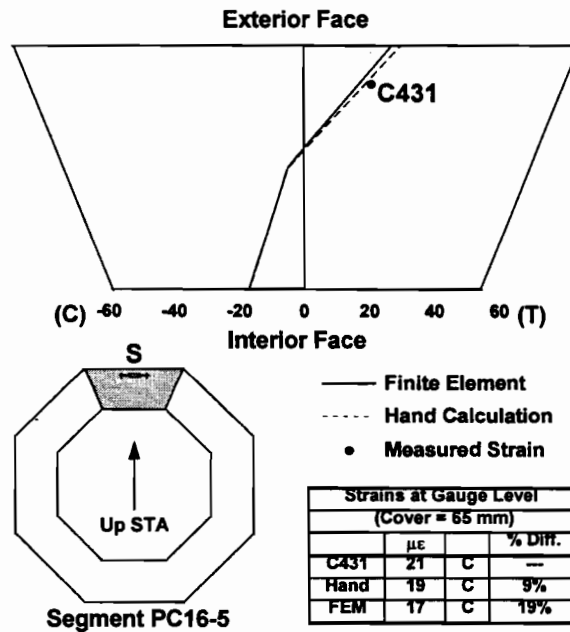


**Figure 6.65** *Transverse strain comparison in the south wall of segment PC16-5.*

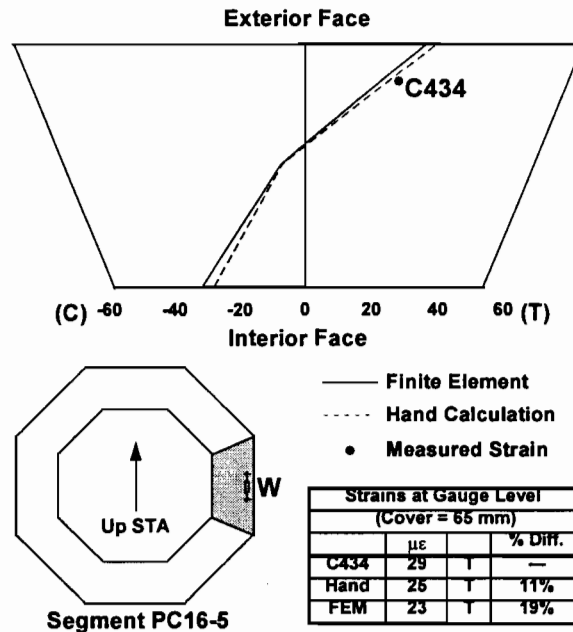


**Figure 6.66** *Transverse strain comparison in the west wall of segment PC16-5.*

### 6.8.2.3 Comments on Transverse Strains

In general, calculated transverse strains due to the positive temperature gradient seemed to match the actual measured strains. For usable gauges located in segments PC16-1 and PC16-5, measured and calculated strains agreed to within approximately 25% on average. Negative gradient strain changes in these segments were even closer, with differences averaging less than 15%. These relatively minor differences indicate that the theoretical underpinnings of the transverse strain calculations are valid and applicable to the determination of effects due to temperature loading on transverse strains in hollow piers.

### 6.8.3 General Comments Concerning Pier Thermal Gradient Effects

General trends are apparent from the comparisons of measured to calculated thermal gradient strains in pier P16. Calculations of longitudinal strains varied from measured longitudinal strains to a greater extent than strains compared in the transverse direction. The variation among analytical methods for determining longitudinal strain was also greater than the relative differences in the methods used for the calculation of transverse strains. This may reflect the difficulty of applying current methods of longitudinal strain calculations to the special case of bridge piers because the orientation of the pier with respect to solar radiation creates a much different temperature distribution than that

present in bridge superstructures. Transverse strain calculations take into account the temperature distributions through each wall of the pier, as well as the geometry of the cross-section itself. This probably provides a more accurate estimation of the strains induced by the temperature distribution.

Strain comparisons agreed more closely for the negative gradient temperature change than for the positive gradient case. This may reflect a fundamental difference between the application of temperature loads to bridge piers and superstructures. The complex distribution of temperatures through the pier's cross-section changes during the course of the maximum positive gradient loading. Certain faces of the pier experience heating *and* cooling over the time period corresponding to the maximum positive gradient temperature change (see Figure 6.2). The calculations used for this project assume that changes in strain between two times are path-independent. However, the change in actual strains in the pier from one time to another is not the same as the strain change calculated from the difference in temperatures between those same times.

If the entire pier cross-section experienced heating (albeit at different rates) between the times chosen for determination of the temperature gradient, the assumption of path-independent strains might be valid. However, because some areas of the pier undergo heating *and then cooling* during the chosen times (see Figure 6.2), a step-wise approach to the calculation of the strain differences may be necessary to more accurately estimate strain changes between the two times.

The comparison of measured to calculated strains for the negative gradient load case seems to confirm this hypothesis. During the period between the two times selected (10:25 PM and 5:25 AM) no significant rise in temperature occurs at any point in the cross-section. This is in contrast to a few locations which drop several degrees during the course of the positive gradient temperature changes. Because all of the fibers of the pier's cross-section cool during the period between the negative gradient times, less interaction between fibers occurs. Fibers are heated and, to a small extent, cooled during the course of the positive gradient temperature change, thus affecting the strain distribution in the pier as time progresses. The differences in characteristics of temperature change between the positive and negative gradient load cases may, in part, explain the more accurate calculated strains in the negative gradient case. Although the effects seem to be minor, step-wise calculations might better serve to accurately determine the effects of temperature changes over time on strains in the pier.

Strains measured in the top segment PC16-7 documented in Reference 3 present a special problem. Large differences occurred between measured and calculated strains in both the longitudinal and transverse directions which suggest that the assumptions used during calculations for this project are not valid for all locations in the pier. It is unclear whether the strains were influenced by the substantial restraint provided by the solid

capital's interface with the top segment, the flow of post-tensioning forces from the capital to the top segment, or a combination of the two effects.

Small variations in measured strains may be accounted for by slight differences in the material properties present in the pier and those assumed during calculations. Slight differences in pier geometry, particularly the presence of ducts, grout tubes, and electrical conduits could also affect the local strain fields near some of the strain gauges. However, every effort was made during instrumentation to avoid local discontinuities to minimize problems in gauge readings.

Overall, it appears that measured strain changes confirm the general validity of calculation methods used to estimate self-equilibrating strains induced in the precast, hollow, segmentally-constructed pier by non-linear temperature distributions. However, the calculations often substantially overestimated measured longitudinal strains. The accuracy of the finite element analysis was best overall. A better understanding of the behavior in certain areas of the post-tensioned pier is needed, as well as a more accurate method for determining longitudinal strain changes caused by changes in temperature over time.



# CHAPTER 7

## 7. DESIGN IMPLICATIONS

### 7.1 Mainlane Pier Indications

Several design implications can be drawn from the instrumentation of the US 183 elevated mainlane pier and the subsequent analysis of measurements made during the erection of the superstructure over the pier.

#### 7.1.1 Temperature Measurements

Observation of measurements made prior to superstructure erection provided much insight concerning the extent of and the effects of temperature change on the pier. Thermal strains induced in the pier were found to be on the same order of magnitude, in some locations, as the expected strains due to the superstructure dead load. Thus, the effects of such strains should be included in service load combinations for unusual pier designs. It would be inappropriate to include these thermal effects in strength limit state computations. Cracking would relieve these stresses.

Trends in temperature measurements and in thermal strains across sections of the concrete portion of the pier followed basic thermal principles regarding thermal stresses due to a temperature gradient across the concrete section. Due to the massive proportions of the concrete, a temperature lag was found to exist across the concrete section. As ambient temperatures increased, the outer "shell" of the concrete was immediately affected. The inner "core" of the concrete was not affected by ambient temperature changes until a later time. This temperature lag across the section induced thermal stresses in the pier.

#### 7.1.2 Superstructure Dead Load Measurements

The separation of thermal strains from total measured strains allowed determination of the strains due to the superstructure dead load. These strains due to dead load provided insight concerning the force distribution in the pier. They also provided insight concerning the field instrumentation of concrete structures subjected to low strains.

The strains measured in the structural steel pipes of the pier indicated forces which were similar to those predicted by a STM of the pier and substantially greater than the pipe forces expected from conventional elastic frame analysis of the pier. The measured compression forces in the struts were on the order of half of what was expected and required due to the superstructure dead load. These concrete strain interpretations were questionable at the low service load levels. The expected strains in the concrete due to service loads are very small. The possibility exists that these strains were so small that

the measurements were affected by small fluctuations in the resistance of the data acquisition system. Further investigation of this possibility is recommended.

### ***7.1.3 Comparison of Measured Forces with Strut-and-Tie Models***

Comparison of measured forces with strut-and-tie models of the pier provided insight concerning the use of strut-and-tie modeling with reinforced concrete design. The forces measured in the pier were compared with two strut-and-tie models. One of the strut-and-tie models was based on an angle  $\theta$  determined by the measured location of the neutral axis and hence centroid of compressive forces, while the other was based on forces predicted by an elastic frame analysis.

The strut-and-tie model based on the angle  $\theta$  determined by the measured compressive path was developed based on the known superstructure dead load and assuming uniform force distribution at the base of the pier. Although the measured forces in the concrete struts did not agree with those predicted, the force path from the point of superstructure dead load through the capital to the shaft of the pier indicated by the measured strains in the capital provided a reasonable force path. This force path was used to determine the orientation of the compressive strut in the capital of the pier. The full strut-and-tie model for the pier was then developed. The resulting tie force was in very good agreement (within 4%) with the measured tie force.

The strut-and-tie model based on forces predicted by an elastic frame analysis of the pier was developed based on the known superstructure dead load and the structural steel pipe force predicted by the frame analysis. The pipe force predicted by the frame analysis was 22% less than the measured value. The two strut-and-tie models developed provided generally similar compression force paths, indicating the ability of strut-and-tie modeling to reasonably trace the flow of forces through a structure.

Strut-and-tie modeling is a strength limit state design tool and is not intended for use in service load limit state analysis. One of the strut-and-tie models used for comparison was developed with information that a designer would not ordinarily have: measured forces and force paths. Although this information would not be known by a designer, the orientation of the compressive strut in the capital selected by an experienced designer would likely be quite close to the strut based on measured forces. However, even though this measurement program was limited to the service load limit state, the comparison of strut-and-tie models based on measured and predicted forces indicated the ability of strut-and-tie modeling to allow a designer to trace the flow of forces through a structure. Strut-and-tie models redirect the designer's focus to the overall flow of forces in a structure and provide a rational framework to aid in the visualization of structural behavior. Their use should be further encouraged within the AASHTO Bridge Design Specification. Designers should be encouraged to develop familiarity with procedures. Researchers should be encouraged to expand their usage to service limit states by

considering contributions of uncracked concrete and appropriate checks for crack control.

## 7.2 Segmental Pier Indications

### 7.2.1 Load Cases

Construction loads produce some of the largest and most important effects on segmentally constructed bridges. Balanced-cantilever construction in particular has the potential to induce large tensile stresses on the associated substructure. To gauge the significance of the effects of non-linear temperature gradients on segmentally constructed piers, an estimate was made of the maximum effects of differential temperature on pier P16 during balanced-cantilever construction of the ramp superstructure.

Section 8.4.2 of the *AASHTO Guide Specification* [7] includes several load cases and allowable stresses related to special construction situations common in segmental bridges. Two of the load cases outlined in the Guide Specification Table 8-1 deal with stresses due to the placement of an unbalanced superstructure segment during balanced-cantilever erection. For illustration purposes, load case “b” is discussed here. This load case consists of the following (all load factors = 1.0):

$$DL + U + CLL + CE + IE + (R + S + T) \quad (7.1)$$

where: DL = Dead load of structure  
U = Segment unbalance  
CLL = Construction live load  
CE = Construction equipment  
IE = Impact load from equipment  
R, S = Creep and Shrinkage  
T = Temperature effects: thermal rise and fall (TRF) and differential temperatures (DT)

$$\text{Allowable compressive stress} = 0.50 f'_c$$

$$\text{Allowable tensile stress} = 7 \sqrt{f'_c} \quad (\text{where } f'_c \text{ is in lb/in}^2)$$

The high amount of allowable tensile stress in the concrete, roughly equivalent to the modulus of rupture of concrete test prisms, reflects the extremely unlikely simultaneous occurrence of all of the factors present in the load case. It also recognizes the unusual construction procedures that the load case considers.

The largest calculated moments produced in pier P16 in the planned erection procedure would be due to an unbalanced segment during placement of the next-to-last segment in cantilever. At this point, six ramp segments cantilever from the top of pier P16 in opposite directions. The seventh segment added to one cantilever produces the maximum unbalanced moment (see Figure 7.1). The application of a typical 285.5 kN ramp segment at a moment arm of 20.1 meters produces a bending moment of approximately 5740 kN-m at the base of the pier. Prestressing forces in the pier, construction live loads, and superstructure and pier dead loads were also included in the calculation of stresses for this load case (see the appendix of Ref. 3).

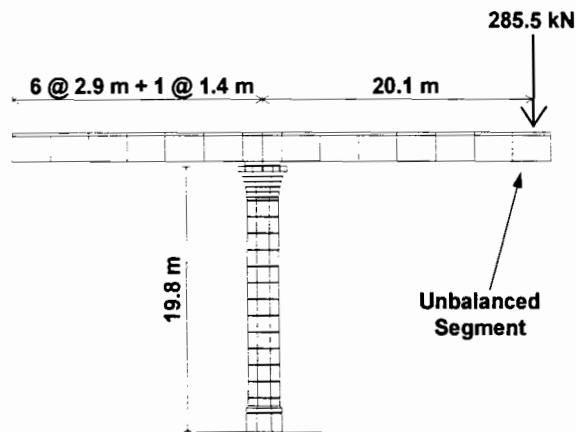


**Figure 7.1** *Unbalanced segment construction load case.*

Figure 7.2 shows the magnitudes and distributions across the pier base segment of several of the load components calculated. The compressive stress of 5.24 MPa provided by the pier's post-tensioning and dead load counters most of the tensile stress at the outer fibers of the pier produced by the unbalanced ramp segment and construction load. The section at the base of the pier remains completely in compression if temperature stresses are neglected.

Self-equilibrating stresses induced by the maximum measured positive temperature gradient for April 1996 and calculated using the finite element analysis are displayed with the other combined load effects in Figure 7.3. It should be noted that no restraint moments are induced in the pier at this point in the planned construction sequence because the structure is statically determinate. After closures are cast in the superstructure and continuity tendons have been stressed, the structure becomes indeterminate and some restraint moments due to differential temperature effects will be produced.

For comparison, the calculated stresses induced by the NCHRP Report 276 [17] positive design gradient as found using the finite element analysis are shown in Figure 7.4. To produce the maximum effect on the pier, the temperature gradients were applied to coincide with the bending moments due to the unbalanced segment.

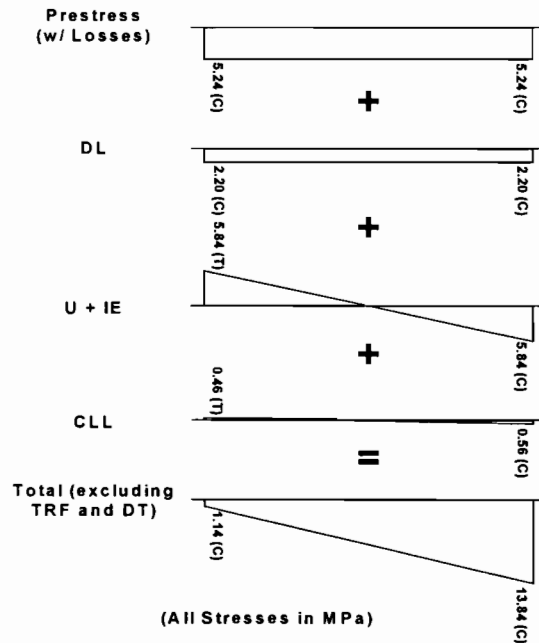


**Figure 7.2** *Stress components for load case excluding temperature effects.*

As shown in Figure 7.3, the April positive gradient stresses increase the total compressive stresses due to non-thermal causes at the outer fibers of the pier by 230% and 130%, respectively. However, those compressive stresses are still well below the maximum allowable compressive stress of 28.34 MPa. No tension is developed in the pier's section due to this load case. The NCHRP positive design gradient shown in Figure 7.4 increases the total outer fiber compressive stresses to 280% and 150% of the non-thermal stresses, respectively. Clearly, the design gradient overestimates the induced stresses in the pier. However, even for this case, the compressive stress levels are still well within the allowable limits.

Figure 7.5 illustrates the stresses induced by the maximum measured negative gradient for April, as determined using the finite element analysis. In this case, the negative gradient causes low levels of tensile stresses to develop at the outer fibers of one face of the pier. The compressive stresses at the opposite face are reduced to 87% of their previous level. The tensile stress of 1.13 MPa induced at the face of the pier is well below the design limit of 4.38 MPa for this construction load case. The maximum compressive stress for this case is also not critical.

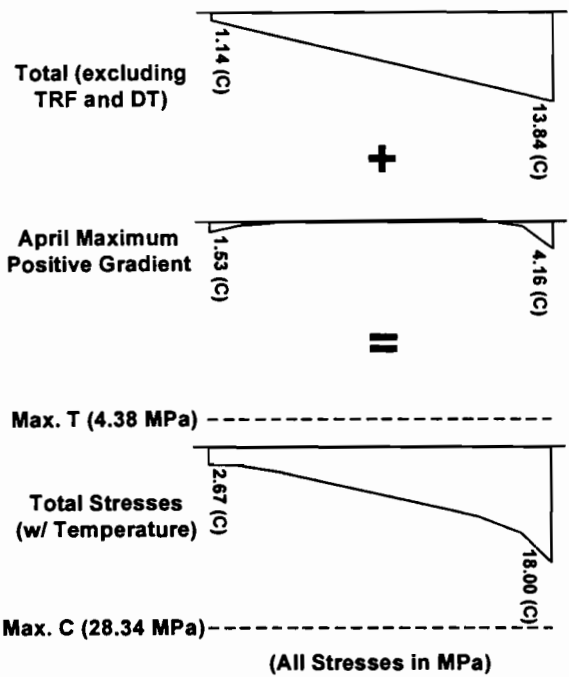


**Figure 7.3** *Additional sectional stresses due to the application of the April maximum measured positive temperature gradient.*

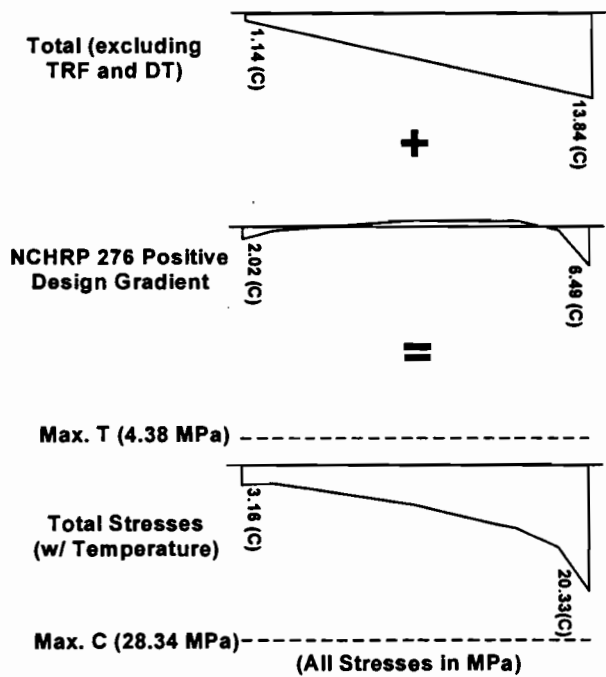


**Figure 7.4** *Additional sectional stresses due to the application of the NCHRP 276 positive design gradient.*

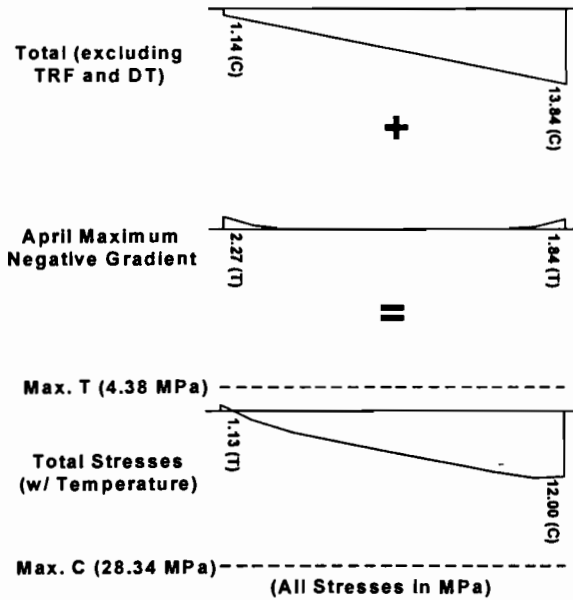


**Figure 7.5** *Additional sectional stresses due to the application of the April maximum measured negative temperature gradient.*

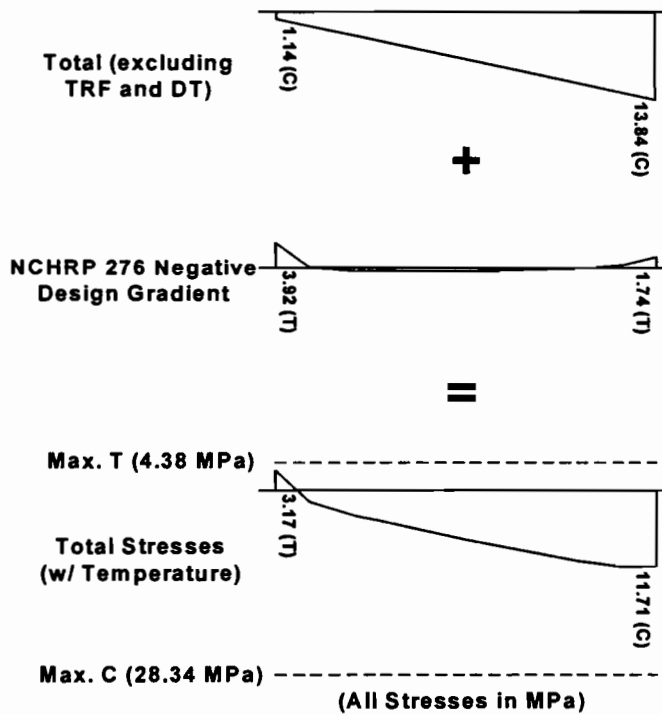


**Figure 7.6** *Additional sectional stresses due to the application of the NCHRP 276 negative design gradient.*

The application of the NCHRP negative design gradient causes much greater tensile stresses at the outer face, reaching 64% of the maximum allowable tension (see Figure 7.6). The maximum compressive stresses in this case are reduced to 43% of the allowable level. The use of the negative design gradient in this case could potentially cause problems for designers attempting to meet the maximum tensile stress requirements during construction. This need not be the case, as it has been shown herein that the design gradients specified by NCHRP Report 276 [17] greatly overestimate the actual gradients measured in pier P16.

The *AASHTO Guide Specifications* [7] also require the application of differential thermal stresses to several service limit state load cases. For load cases including live loads, the effects of differential temperature stresses may be reduced by 50%. The following service load cases include temperature effects:

$$\text{IV: } D + (L+I)_n + CF + \beta_E E + B + SF + R + S + (T + 0.5DT) \quad (7.2)$$

$$\text{V: } D + E + B + SF + R + S + (T + DT) \quad (7.3)$$

$$\text{VI: } D + (L+I)_n + CF + \beta_E E + B + SF + 0.3W + WL + LF + R + S + (T+0.5DT) \quad (7.4)$$

$$\text{Additional Thermal: } D + \beta_E E + B + SF + R + S + DT \quad (7.5)$$

- where:
- D = DL + SDL + EL
  - DL = structure dead load
  - S = shrinkage
  - SDL = superimposed dead load
  - DT = differential thermal
  - EL = erection loads
  - W = wind
  - $\beta_E E$  = earth pressure
  - LF = longitudinal live load forces
  - SF = stream flow
  - WL = wind load on live loads
  - R = creep

- B = buoyancy
- L = live loads
- I = impact factor
- CF = centrifugal force
- SF = stream flow
- T = temperature rise and fall

The maximum allowable compressive stress after all prestress losses is  $0.4 f_c$ . For segmental members with epoxied joints (designated Type A) such as those in pier P16, no tensile stresses are allowed to occur at the service limit state. The design specifications allow a 25% increase in maximum allowable stresses for load case IV, and a 40% increase for cases V and VI. The additional thermal case from the *AASHTO Guide Specifications* [7] does not include an increase in allowable stresses. Unfortunately, the *percentage* increases allowed by the code do not relieve the requirement of zero tension for segmental members.

To gauge the importance of temperature effects in bridge piers, service loads are estimated for pier P16 after all estimated prestress losses have occurred. Structure dead loads were calculated through several phases of the balanced-cantilever construction (see Figure 7.7). This is necessary because the configuration of the structure that includes pier P16 at different times during construction affects the dead loads applied to the pier.

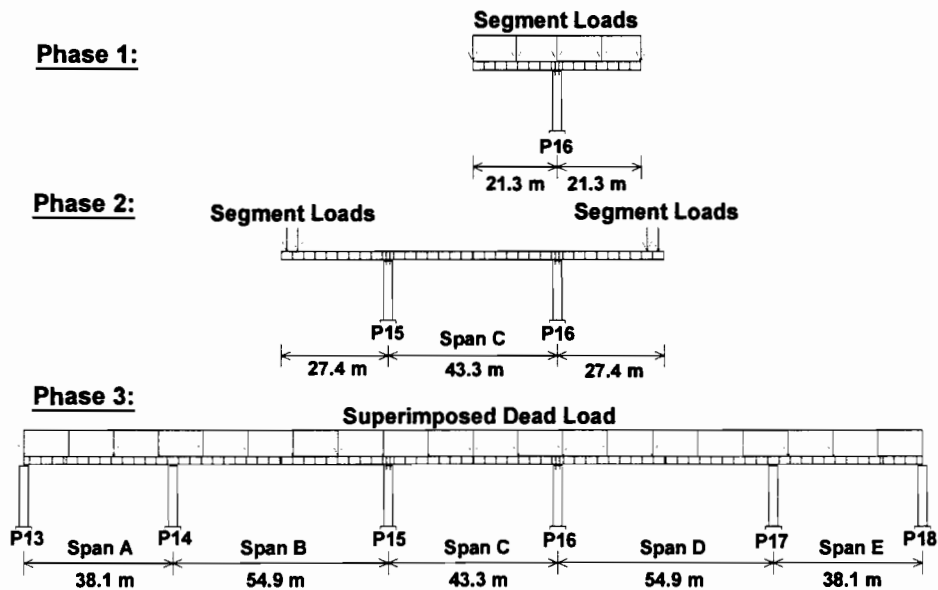


**Figure 7.7** *Dead loads at several phases during construction.*

Prestressing effects in the superstructure and pier P16 were estimated and included in the total stress distributions calculated for the service load cases. Superimposed dead loads

such as roadway overlays and barrier walls were determined, and the maximum effects due to AASHTO HS20-44 live loads were calculated. Figure 7.8 shows the estimated stress distributions across the segment at the base of pier P16 due to dead loads and prestressing as well as maximum live load effects. Note that the contribution from live loads is quite small compared to dead loads and prestressing. This is due in part to the use of balanced-cantilever construction and the large dead loads from the bridge superstructure. The maximum compressive stress on the pier's base is less than 40% of the allowable compressive stress.

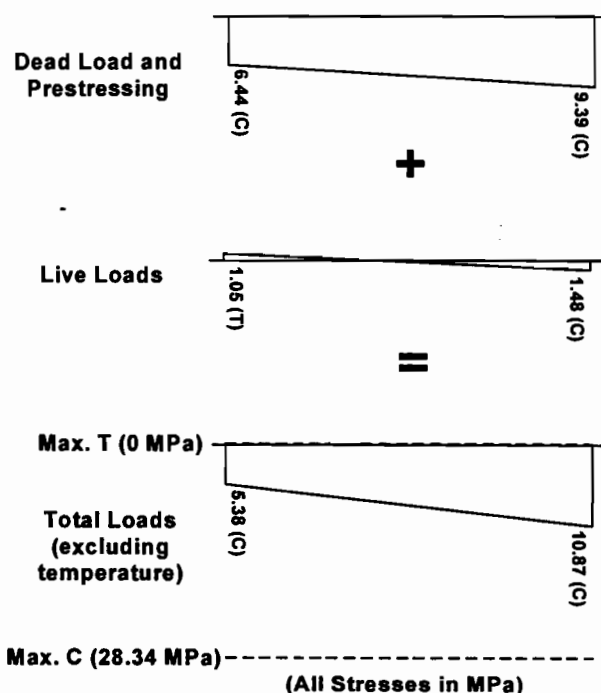


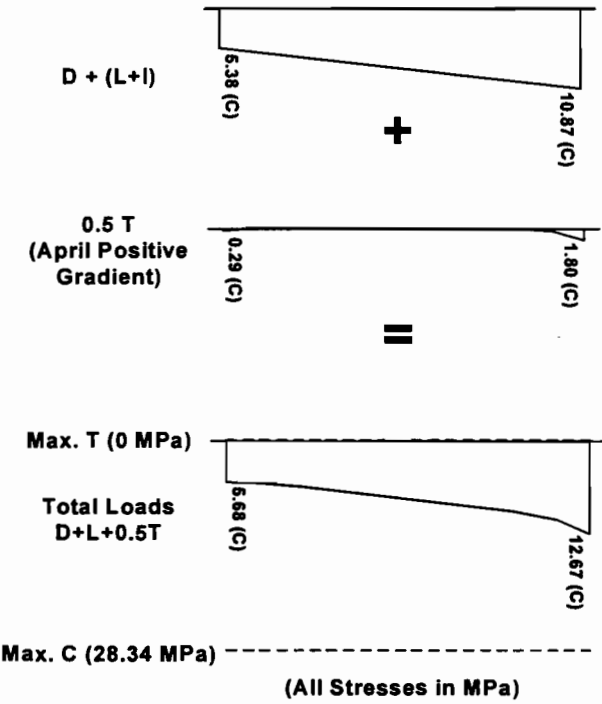
**Figure 7.8** *Relative contributions of dead and live loads to stress at the base of pier P16 for the service limit state.*

To determine the contribution of thermal gradient stresses to the stress distribution in pier P16 at service loads, restraint moments and self-equilibrating stresses found using the classical method were applied to the service load cases above. The maximum measured positive and negative gradients (from April 1996) as well as the NCHRP Report 276 [17] positive and negative design gradients were applied to two service load cases. Load case IV allows a 50% reduction in effects from temperature because it includes live and impact loads. The additional thermal case does not allow an increase in maximum stresses, but does not include live load effects.

Contributions from differential thermal gradients consisted of both self-equilibrating stresses and restraint moment stresses induced by the indeterminate nature of the five-span ramp unit to which pier P16 belongs. The magnitudes of self-equilibrating stresses

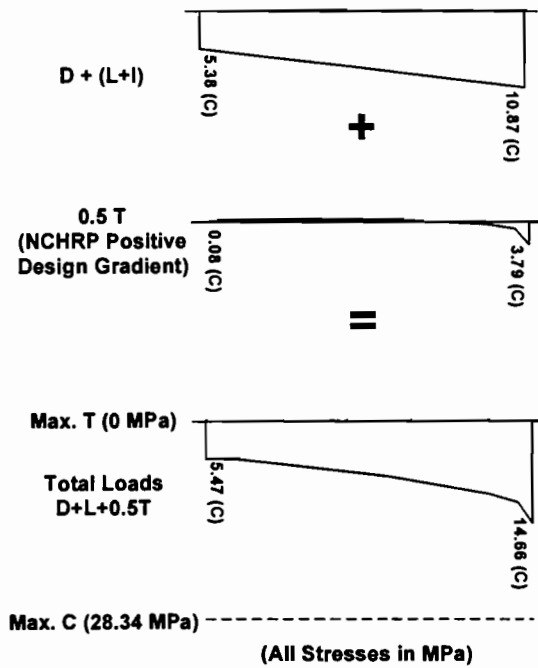
used in these cases are slightly less than those used for the construction load cases in the previous section. The classical method of self-equilibrating stress calculation produced slightly lower values of longitudinal stress than the finite element analysis.

Figure 7.9 shows the maximum measured positive gradient stresses applied to the service load case IV. The maximum compressive stresses due to thermal effects for this case are about 14% of the total compressive stress. Even with the addition of the compressive stresses induced by the thermal gradients on the pier, the maximum compressive stress is only 45% of the largest allowable stress. No tension develops due to the temperature gradient.



**Figure 7.9** Service load case IV with maximum measured positive gradient effects.

The NCHRP positive design gradient also has little effect on the pier in service load case IV (see Figure 7.10). However, the design gradient stresses overestimate the stresses calculated from the measured gradient by 210%. Thermal compressive stresses in this case contribute only 26% of the maximum compressive stress on the pier’s section. The majority of the thermal stresses occur near the outer fibers. Even with the larger thermal gradient, compressive stresses reach only 52% of the maximum allowable stress.



**Figure 7.10** Service load case IV with NCHRP positive design gradient effects.

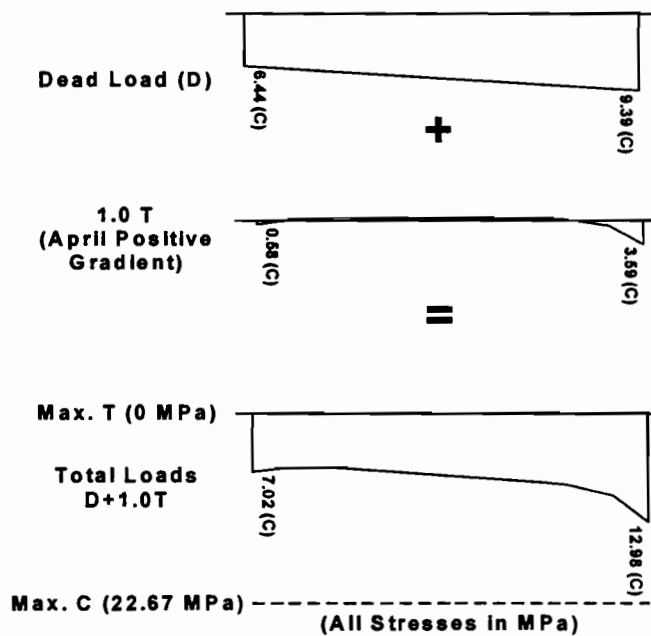


**Figure 7.11** Additional thermal case with measured positive gradient effects.

The positive thermal gradients have a somewhat greater effect on the cross-sectional stresses in the additional thermal load case. Figure 7.11 shows the increase in compressive stress due to the maximum measured positive temperature gradient. The contribution of thermal stresses to the total compressive stresses in the pier is less than 28% at the point of maximum compression. Figure 7.12 shows the contributions due to the positive design gradient on compressive stresses from the additional thermal case. Because of the steep change in temperature at the outer fiber specified by the design gradient, a relatively large amount of compressive stress occurs at that location. That stress is approximately 45% of the maximum compressive stress calculated for this load case, which is in turn about 75% of the allowable compression. Note that the allowable stress for the additional thermal service load case is lower than the value for service load case IV because no increase in maximum stress is provided by the specifications.

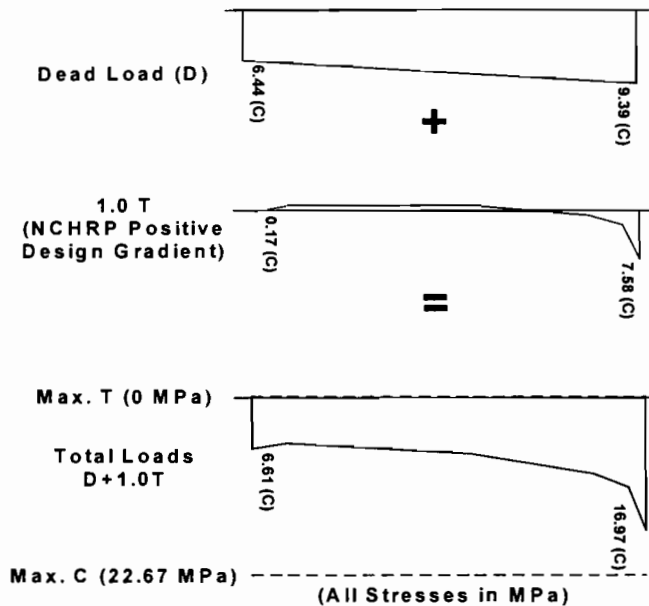


**Figure 7.12** Additional thermal case with NCHRP positive design gradient effects.

Unlike the positive gradient effects, stresses due to negative temperature gradients are primarily tensile in nature. However, the large amount of compression on the pier from the dead loads and post-tensioning forces ensures that no tension develops due to thermal gradients. Figure 7.13 shows the small decrease in compressive stresses due to the maximum negative gradient effects. The negative gradient stresses cause a 20% reduction in compressive stress where the maximum thermal tensile stresses occur. Similarly, tensile stresses from the more severe NCHRP negative design gradient also have little effect on the section for this load case (see Figure 7.14). The largest tensile stresses cause a 35% decrease in compression at the outer face. Still, neither gradient causes any tension at any depth of the section due to the large compressive stresses provided by other loads.

The additional thermal load case specified by the *AASHTO Guide Specification* [7] should produce the greatest effects on the section due to thermal gradients. Even so, neither the maximum measured negative gradient nor the much larger NCHRP negative design gradient induce any tension in the pier's cross-section (see Figures 7.15 and 7.16, respectively). The negative design gradient's maximum tensile stress does reduce the compressive stresses due to dead loads by almost 60%, but most of the effect is localized within the first several centimeters of the depth, while the rest of the pier is affected very little. This is due to the relatively steep temperature gradient present near the outside fibers in the design temperature gradient's shape.

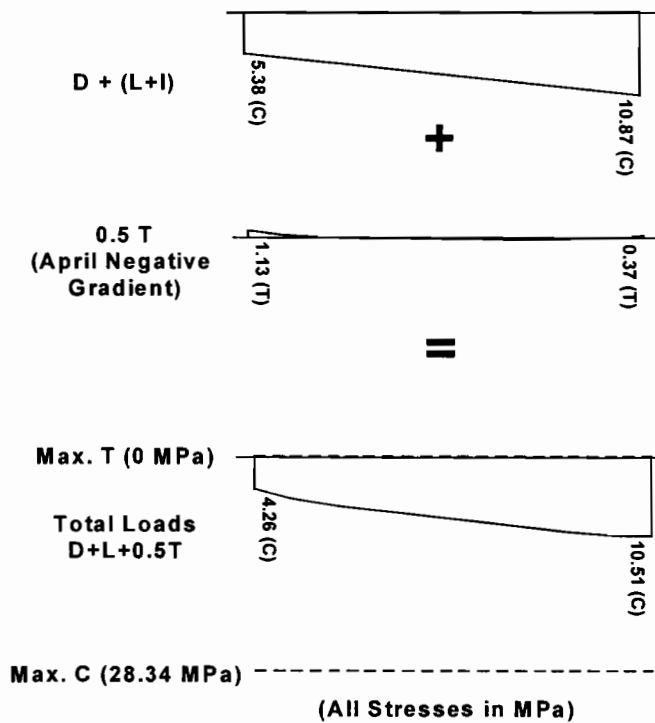


**Figure 7.13** Service load case IV with measured negative gradient effects.

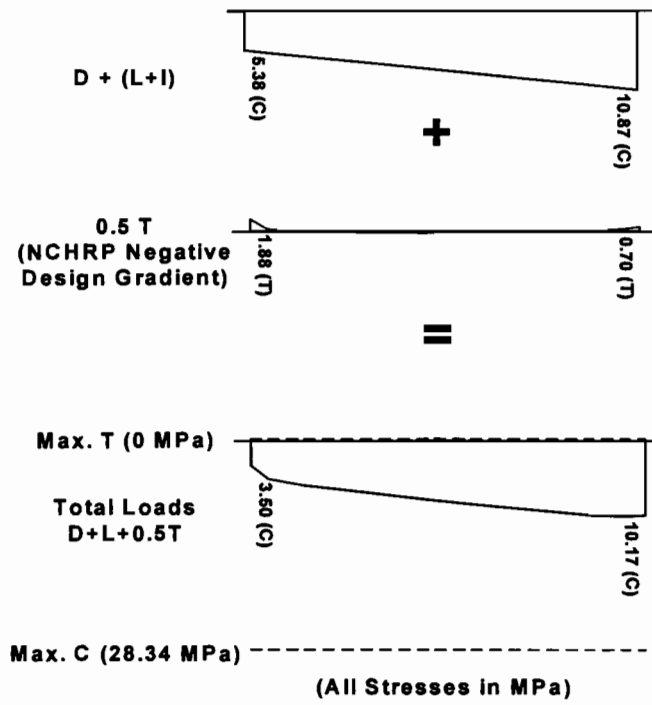


**Figure 7.14** Service load case IV with NCHRP negative design gradient effects.

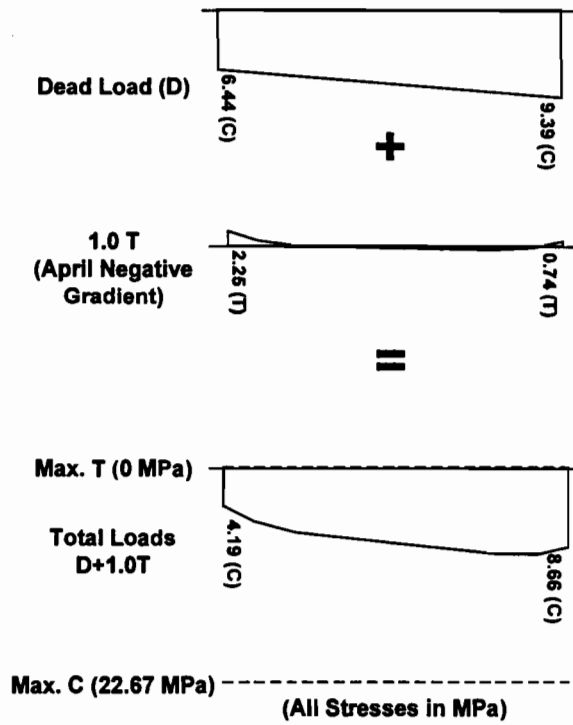


**Figure 7.15** Additional thermal case with measured negative gradient effects.

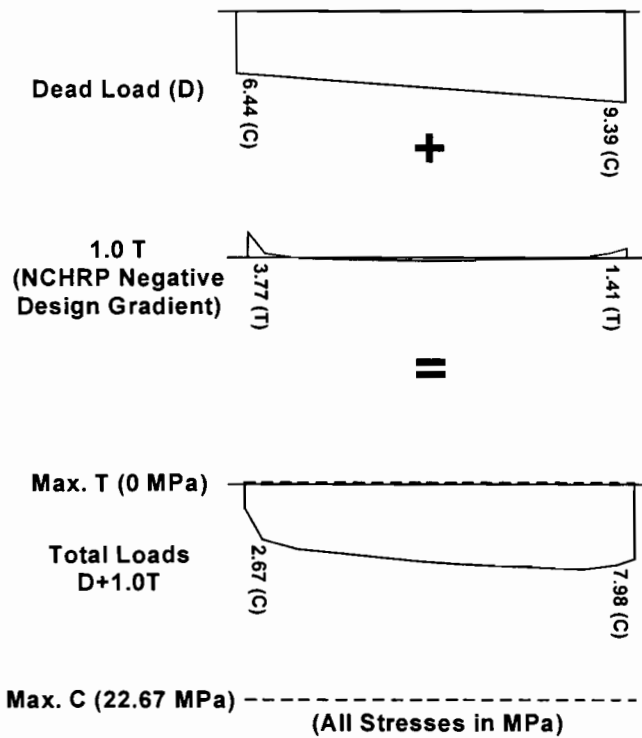


**Figure 7.16** *Additional thermal case with NCHRP negative design gradient effects.*

### 7.2.2 Comments on Load Cases

In general, the measured temperature gradients have no profound effects on the stresses present in the pier during service conditions. The pier's post-tensioning forces appear to be adequate in preventing any tension from occurring at the interfaces between pier segments. The temperature gradients specified for design based on the NCHRP Report 276 [17] produce larger effects on the pier, but no tensile stresses were calculated from the service load cases examined here. This is especially significant for the additional thermal load case, which has the greatest relative contributions due to thermal gradients and was designed to be the "worst case" service condition for the effects of temperature on a structure.

The calculations performed were only estimates of the service loads that might actually be used for design purposes. Still, it can be seen from these example load cases that the effects on cross-sectional stresses from thermal gradients are quite small in the post-tensioned pier.

On the basis of the magnitudes of stresses, it appears prudent to include the effects due to thermal gradients in the construction load cases. The measured negative gradient induced a significant amount of tensile stress in the pier's cross-section. Because the

negative gradient would likely occur during the night when most heavy urban construction work is in progress, designing for its effects is not unreasonable. The high level of allowable tension specified in Table 8-1 of the *AASHTO Guide Specifications* [7] accounts for the small likelihood of the simultaneous occurrence of the unusual construction loads and large negative thermal gradients. Compressive stresses from a positive temperature gradient in the pier would rarely significantly affect the stress distributions during construction.

### 7.3 Suggested Revisions to *AASHTO Guide Specification* [7]

#### 7.3.1 *Thermal Gradients*

Temperature distributions through the cross-section of pier P16 were measured using a comprehensive set of thermocouples. Pier temperatures were measured on an hourly basis since construction began. To date, the critical period is the spring of 1996. Based on the temperatures recorded and their distributions in the pier, conclusions can be made regarding the positive and negative design temperature gradients required for analysis by the *AASHTO Guide Specification* [7].

Measured temperature gradients projected onto a single axis for direct comparison to current superstructure design gradients appear to match the *shape* of those design gradients fairly well. However, the magnitude of the peak temperature from the maximum measured positive thermal gradient reached only 51% of the temperature specified for Austin, Texas (solar radiation Zone 2). These measurements also match very closely the shapes and magnitudes of thermal gradients measured by Roberts [19] on a segmental bridge superstructure with no asphalt topping. That fact strongly suggests that a bridge pier's vertical orientation does not necessarily protect it from large thermal gradients.

The shape of the maximum negative temperature gradient measured over the same time period also appeared to match the design gradient shape very closely. However, the magnitude of the maximum measured temperature for this case was only 53% of the specified design value. Roberts [19] found measured negative gradient magnitudes to be around 80% of those specified for use in design.

In general, the temperature distributions measured in the segmental pier appear to be applicable for use in determining appropriate shapes and magnitudes for thermal gradients in bridge piers *and* superstructures. Roberts [19] suggested the following revisions to section 7.4.4 of the *AASHTO Guide Specifications* [7] (changes in italics):

#### 7.4.4 Differential Temperature

Positive and negative differential superstructure temperature gradients *shall be taken as 80% of the values presented in Appendix A of the National Cooperative Highway Research Program Report 276 "Thermal Effects in Concrete Bridge*

Superstructures” [17]. *Alternatively, site specific thermal gradients, developed based on the climatic conditions in the area and the actual material properties of the structure, may be substituted for the current design gradients.*

The magnitudes and distributions of temperatures measured in the segmental pier support this suggested change to the segmental bridge design code for superstructures. The similarities in gradient shapes and temperature magnitudes measured by this project and by Roberts [19] suggest that the temperatures measured in the hollow box, concrete segmental pier are an excellent match to those found in hollow box , concrete bridge superstructures.

### **7.3.2 Application of Thermal Gradients to Substructures**

Currently, there is no explicit reference to segmentally constructed bridge substructures with regards to the application of thermal differential loading in the *AASHTO Guide Specification* [7] for any service limit state load conditions. Segmental substructures are listed in Table 8-1 and thermal effects are included in load combinations applicable to them. Based on the load case described earlier in this chapter, it is prudent to include thermal gradient effects in segmental substructures but only for the construction load cases. However, no guidance is provided as to the application of non-linear thermal gradients to segmental piers for service load cases. Based on the thermal gradients measured in the field, the following section should be added to the *AASHTO Guide Specification* [7] (changes in italics):

#### **8.2.3 Thermal Gradients in Substructures**

*When considering thermal gradient effects on bridge substructures, a load factor of zero (0) shall be applied to the differential temperature load (DT) for the load combination described in section 8.2.2 and other AASHTO load combinations which include differential temperature gradient effects.*

In addition, the following statement concerning column (4) in Table 8-1 should be added to the notes for that table:

*\*\*\*\*\*When considering differential thermal effects in segmental substructures, a load factor of 0.65 shall be applied to the differential thermal term (DT).*

The following section should be added to the commentary:

### **8.2.3 Thermal Gradients in Segmental Substructures**

*Preliminary field research on the magnitudes and effects of non-linear thermal gradients in bridge piers suggests that gradients similar in shape but substantially less (50%) in magnitude to those measured in bridge superstructures [7] occur in hollow box, concrete piers. However, the thermal effects appear to be minor. For construction load cases in Table 8-1, temperature gradients for substructures need be only 65% of the values recommended in Appendix A of National Cooperative Highway Research Program Report 276 "Thermal Effects in Concrete Bridge Superstructures" [5]. Generally, they need not be applied to substructures of this type for service load cases listed in section 8.0. Additional research is recommended to verify the importance of temperature gradient effects in hollow box, concrete bridge piers used for over-water crossings and piers with rectangular cross-sectional shapes.*

### **7.3.3 Suggestions for Future Study**

The field instrumentation of a segmentally constructed, hollow-box pier located on the US 183 segmental viaduct provided important insights into the nature of temperature distributions in and their effects on substructures of this type. From the analyses performed, it is clear that standard, one-dimensional assumptions of temperature variations through the pier cross-section like those typically used in the analysis of bridge superstructures are inadequate to accurately describe the self-equilibrating strains and stresses induced by the pier's temperature distribution. More accurate analysis of a pier's response to temperature changes should account for the complex, two-dimensional distribution of temperatures caused by the shape of the cross-section and the orientation of the pier to solar radiation. A simplified method of analysis accounting for the measured temperature distributions was developed, but additional development of that method is needed to verify its accuracy and increase its usefulness.

The instrumented pier was octagonal in cross-sectional shape, and its behavior was likely similar to that of a hollow, circular tube under differential temperature loading. However, most segmental piers constructed to date have rectangular cross-sections. The behavior of hollow piers with such a shape should be investigated to determine the influence of different cross-sectional shapes on the temperature distributions produced in piers and their corresponding response. In addition, many segmental piers have been constructed as part of long, over-water crossings. The influence on pier temperature gradients from reflected sunlight as well as ambient humidity should be determined by the instrumentation of a pier constructed over water.

The large strains measured in the hollow cross-section of the pier near the solid capital segment were unexpected. Further clarification of the effects of restraint provided by the interface between hollow cross-sections and solid segments would provide a better understanding of structural response to temperature gradients. Similar increases in strain likely occur near heavy end anchorage segments in superstructures as well.

The effects of temperature gradients in piers that are rigidly connected to the superstructure should be investigated to determine the magnitude of induced moments in the superstructure members. This effort could also be applied to multiple column bents with rigid connections between the columns and cross beams.

Most importantly, additional temperature and strain data should be recorded from the instruments installed in pier P16 to determine temperature characteristics during the fall and winter months at that location. Additional measurements would also aid in the verification of the magnitude and frequency of the largest temperature gradients that occur in the pier. Such measurements are being carried out in a following project.

## CHAPTER 8

### ***8. SUMMARY & CONCLUSIONS***

#### **8.1 Introduction**

This chapter presents a brief summary and conclusions from the field instrumentation of a mainlane bridge pier and a segmental ramp pier of the US 183 elevated highway located in Austin, Texas.

#### **8.2 Mainlane Bridge Pier**

The study of the force distribution through the innovative US 183 elevated mainlane bridge piers was performed in order to determine thermal effects and to further evaluate the use of strut-and-tie modeling (STM) for reinforced concrete design so as to familiarize designers with the concept of STM and its possible uses.

In order to investigate the behavior of a US 183 mainlane pier, one of these piers was instrumented during construction. The purpose of the instrumentation was to measure thermal effects and the flow of forces through the pier due to the superstructure dead load so that these forces could be compared to the forces predicted by a strut-and-tie model of the pier. Concrete strain devices and strain gages were used to measure strains in the concrete and on the structural steel pipes. Due to the limitations of STM in detecting compatibility and constraint induced stresses, temperature measurements were made using thermocouples to determine the effects of thermal gradients on the pier.

The instrumented US 183 mainlane pier was constructed several months prior to the erection of the superstructure supported by the pier. Data was therefore collected prior to, during, and subsequent to the placement of dead load on the pier.

Data collection prior to the construction of the superstructure allowed researchers to investigate the thermal strains induced in the pier. The thermal gradient across the structural steel pipes as well as the thermal gradients across the concrete sections were found to produce strains in some areas on the same order of magnitude as the strains expected from the dead load. Thermal effects were therefore considered to be of significance regarding the comparison of measured forces to a strut-and-tie model of the pier.

The construction of the superstructure extended over several days. As such, thermal induced strains had to be separated from the total strains measured during this time since the measured forces due to superstructure dead load were to be compared to strut-and-tie models. Thermal strains were separated from total measured strains. The resulting strains were due only to superstructure dead load. These strains were converted to forces and compared to two strut-and-tie models. One of the strut-and-tie models was based on measured forces, and

one was based on forces predicted by an elastic frame analysis. The measured forces, the strut-and-tie models, and a comparison of the two was presented.

### 8.3 Segmental Ramp Pier

The study of thermal and force effects on a tall, hollow segmental box section pier was performed to determine construction load and thermal effects on such a pier. In this phase, Concrete strain gauges, strain gauges attached to reinforcing bars, and thermocouples were installed in three precast column segments and one capital segment of a 20-meter high segmentally-constructed, post-tensioned, concrete, hollow box bridge pier. Data from the instruments have been recorded regularly since the pier's erection in April 1996.

A set of 24 thermocouples was installed in a cross-section of the pier near mid-height to determine the shape and magnitude of any thermal gradients present. Three thermocouples were located through the thickness of each of the eight walls of the pier's octagonal cross-section. These instruments provided excellent data concerning the distribution of temperatures through the walls of the pier as well as across the cross-section as a whole. Smaller sets of thermocouples were installed in cross-sections near the base of the pier as well as the top segment. These instruments were used to confirm the temperature measurements recorded from the mid-height segment.

Strain gauges were embedded in the concrete of each of the three column segments and the capital segment during casting operations. Gauges located in the column segments were oriented longitudinally (vertically) to provide information on longitudinal self-equilibrating strains induced by the temperature changes in the pier over daily cycles of heating and cooling. A small number of gauges were also installed in the transverse direction in each column segment to determine transverse strains due to temperature gradients through the pier walls.

Temperatures in the pier's concrete followed distinct daily cycles corresponding to both ambient air temperature changes and variations in solar radiation striking the pier's outer faces throughout the course of the day. The exterior faces of the pier experience the largest cycles of daily heating and cooling. The concrete's poor thermal conductivity prevented significant changes in the temperatures located in the interior. This also produced large thermal gradients between the inner and outer faces of the pier's walls, as well as thermal differentials between opposite faces of the pier. It was determined that solar radiation produced the largest and most rapid rises in temperature, while changes in ambient air temperature played an important, but secondary, role.

Daily fluctuations in differential or self-equilibrating strain readings also occurred due to the changing temperatures. Temperature compensated strain gauges were used to eliminate conventional linear expansion and contraction strain readings. Thus, the strain gauges reflect the stresses set up through the member by restrained thermal movements. So in general, a *rise* in temperature at the location of a strain gauge induced *compressive* strain changes in the

gauge. Temperature *drops* produced *tensile* strains. Gauges were also monitored during post-tensioning operations to track forces in the column and capital, which served as the post-tensioning anchorage zone for the pier's tendons.

From the temperature data, the maximum positive and negative temperature gradients were determined for each month. Positive gradients occurred when the outer faces of the pier were hotter than the insulated interior. The largest positive gradients typically occurred in the late afternoon as the sun almost directly struck the west face of the pier. Conversely, negative temperature gradients occurred when the outer faces of the pier were cooler than the interior. The largest of these typically occurred during the early morning hours just before sunrise. The gradients measured were considerably smaller in magnitude than the applicable values recommended for box girder superstructures by the *AASHTO Segmental Bridge Guide Specifications* [8] and by the NCHRP Report 276 [17].

The measured temperature gradients were then used to perform calculations to determine the distribution of self-equilibrating strains in the pier's cross-section. Two methods of hand calculations were used to determine longitudinal strains. A one-dimensional projection of the complex, two-dimensional temperature distribution was developed for the first hand calculation method. This "classical" method assumed that temperatures vary only through the depth of a member, even though temperatures in the pier actually varied throughout the cross-section. Therefore a second, more general, hand calculation method was developed to account for the more complicated temperature distribution associated with the maximum measured temperature gradients. Transverse strains were also calculated for each wall of the cross-section for each maximum monthly gradient.

To confirm the hand calculations, a finite element model of the pier was constructed using ANSYS 5.0a. Using the measured temperatures associated with the maximum monthly gradients as input, this computer analysis calculated self-equilibrating stresses and strains across the entire pier cross-section in both the longitudinal and transverse directions.

Finally, the three analytical determinations of self-equilibrating strains were compared with the measured longitudinal strains from the embedded strain gauges. Good correlation between measured and calculated strains was found when the measured temperature distribution was used as the input. The finite element analysis typically provided the most closely matching results. Strains measured at the top of the column near the interface with the capital segment were much larger than those calculated. This increase in apparent strain was probably due to partial restraint of the octagonal cross-section in that area by the solid capital. Transverse strains closely matched those calculated by hand as well as those from the finite element model. Transverse strain gauges located near the capital also measured larger strains than expected, further indicating possible restraint provided by the capital segment itself.

Example load cases based on load combinations from the *AASHTO Guide Specification for Design and Construction of Segmental Concrete Bridges* [7] were calculated to determine the

relative effects due to temperature-induced stresses on the pier. A construction load case and two typical service load combinations were evaluated. It was found that temperature gradients could potentially induce tensile stresses at the outer fibers of the pier's cross-section during construction. However, no net tension was calculated to occur from the service load combinations. The magnitudes of the stresses produced by temperature effects on the pier were found to be minor compared with stresses due to post-tensioning, superstructure dead loads, and design live loads.

## **8.4 Conclusions**

Based on the instrumentation and analyses of the mainlane pier and the segmental ramp pier, several conclusions and recommendations can be made:

### ***8.4.1 Mainlane Pier***

- (1) Thermal strains induced in the pier were on the same order of magnitude, in some locations, as the expected strains due to the superstructure dead load.
- (2) Trends in temperature measurements and in thermal strains across sections of the concrete portion of the pier followed basic thermal principles regarding thermal stresses due to a temperature gradient across the concrete section.
- (3) A substantial temperature lag was found to exist across the concrete section. As ambient temperatures increased, the outer "shell" of the concrete was immediately affected. The inner "core" of the concrete was not affected by ambient temperature changes until a later time. This temperature lag across the section induced thermal stresses in the pier.
- (4) The strains measured in the structural steel pipes of the pier provided forces which were similar to those predicted by a STM of the pier. The resulting tie force was in very good agreement (within 4%) with the measured tie force. They were much more realistic than those from a conventional analysis. The pipe force predicted by the frame analysis was 22% less than the measured value.
- (5) Although the measured forces in the concrete struts did not agree with those predicted, the force path from the point of superstructure dead load through the capital to the shaft of the pier indicated by the measured strains in the capital provided a reasonable force path. The two strut-and-tie models developed provided generally similar compression force paths, indicating the ability of strut-and-tie modeling to reasonably trace the flow of forces through a structure.
- (6) Strut-and-tie models redirect the designer's focus to the overall flow of forces in a structure and provide a rational framework to aid in the visualization of structural behavior.

#### 8.4.2 Segmental Ramp Pier

- (1) Temperature gradients in the hollow pier vary in magnitude and direction throughout the course of a typical day due to the changing position of the sun.
- (2) Pier temperatures fluctuate greatly at the outer surfaces of the cross-section, and do not vary as greatly in the interior.
- (3) Solar radiation produces the largest and most rapid changes in temperature at the outer faces of the cross-section. Ambient air temperature changes are a secondary mechanism of heat transfer.
- (4) Maximum differential temperature magnitudes measured in the pier were only 50% of the *AASHTO Guide Specification* [11] and the NCHRP Report 276 [5] design gradient magnitudes for both positive and negative gradients.
- (5) Maximum differential temperature magnitudes measured in the pier were similar to those found previously in bridge superstructures, suggesting that temperature distributions measured in hollow box piers can also be used to estimate temperatures in superstructures.
- (6) Unlike box girder superstructures, hollow box bridge piers experience a complex, two-dimensional distribution of temperatures throughout the cross-section. This makes conventional methods for the determination of self-equilibrating stresses inaccurate. More general methods which take into account the temperature at given points rather than discrete depths of the section should be used.
- (7) When actual measured temperature gradients were used as an input, the analytical methods predicted the measured longitudinal and transverse strains fairly well. The finite element analysis produced strain results closest to those measured in the field. Of the two hand calculation methods used, the more accurate method accounted for the two-dimensional distribution of temperatures throughout the pier cross-section.
- (8) Calculated stresses due to thermal gradients contributed only a small amount to the total estimated stress on the pier from design code service load cases.
- (9) The amount of post-tensioning present in the pier was more than enough to counteract any tensile stresses induced by negative gradients, and the additional compression from the superstructure probably ensures that no tensile stresses will occur in the pier due to temperature effects.
- (10) Measurements made in the pier during superstructure erection showed very good agreement with conventional calculations.
- (11) Specific changes to AASHTO Specifications are proposed in Section 7.3.



## REFERENCES

1. Davis, R.T., "Measurement Based Performance Evaluation of a Segmental Concrete Bridge." Ph.D. Dissertation, The University of Texas at Austin, Austin, TX. May 1999.
2. Andres, V.A., "Verification of Force Distribution in an Innovative Bridge Pier." Master's Thesis, The University of Texas at Austin, Austin, TX. December 1995.
3. Bonzon, W.S., "Thermal Gradients in Segmentally Constructed Hollow Box Bridge Piers." M.S.E. Thesis, The University of Texas at Austin, Austin, TX. December 1996.
4. Thompson, M.K., "Measured Behavior of a Balanced Cantilever Erected Curved Segmental Concrete Bridge." M.S.E. Thesis, The University of Texas at Austin, Austin, TX. January 1998.
5. Matejowsky, A., Letter to John E. Breen concerning precast substructures. March 19, 1996.
6. Breen, J.E., "Why Structural Concrete?" IABSE Colloquium: Structural Concrete. Stuttgart, Germany, 1991.
7. *AASHTO Guide Specifications for Design and Construction of Segmental Concrete Bridges*. American Association of State Highway and Transportation Officials. 1989.
8. *AASHTO LRFD Bridge Design Specifications*. 1st ed. American Association of State Highway and Transportation Officials. 1994.
9. Bergmeister, K. et al., "Detailing for Structural Concrete." Center for Transportation Research Report 1127-3F. Austin, TX. May 1993.
10. Breen, J.E., et al., "Anchorage Zone Reinforcement for Post-Tensioned Concrete Girders." NCHRP Report 356. National Academy Press. Washington, DC 1994.
11. Schlaich, J., et al., "Toward a Consistent Design of Structural Concrete." PCI Journal. Vol. 32, No. 3. Prestressed Concrete Institute. May/June 1987.
12. Leonhardt, F. and E. Monnig, "Lectures on Reinforced Concrete Structures. Part 2: Special Cases of Calculations for Reinforced Concrete Construction." 3rd ed. Springer Verlag Publishers. Berlin. 1986.
13. ACI 318-89 Building Code Requirements for Reinforced Concrete. American Concrete Institute. Detroit, MI. 1989.
14. Higdon, A. et al., *Mechanics of Materials*. 4th ed. John Wiley & Sons, Inc. New York, NY. 1985.
15. Branco, F.A. and P.A. Mendes, "Thermal Actions for Concrete Bridge Design." *Journal of Structural Engineering*. ASCE. Vol. 119, No. 8. August 1993, pp. 2313-2331.

16. Moorty, S., and C. W. Roeder., "Temperature Dependent Bridge Movements." *Journal of Structural Engineering*. ASCE. Vol. 118, No. 4. April 1992, pp. 1090-1105.
17. Imbsen, R. A., D. E. Vandershof, R. A. Schamber, and R.V. Nutt, "Thermal Effects in Concrete Bridge Superstructures." *NCHRP 276*. Transportation Research Board, Washington DC. September 1985.
18. Poston, R. W., M. Diaz, and J.E. Breen, "Design Trends for Concrete Bridge Piers." *Journal of the American Concrete Institute*. January-February 1986, pp. 14-20.
19. Roberts, C. L., "Measurement Based Revisions for Segmental Bridge Design and Construction Criteria." Doctoral dissertation, The University of Texas at Austin. December 1993.
20. Potgieter, I.C. and W.L. Gamble, "Response of Highway Bridges to Nonlinear Temperature Distributions." Report No. FHWA/IL/UI-201. University of Illinois at Urbana-Champaign. April 1983.
21. Vecchio, F. J., and J. A. Sato, "Thermal Gradient Effects in Reinforced Concrete Frame Structures." *ACI Structural Journal*. Vol. 87, No. 3. May-June 1990, pp. 262-275.
22. Hoffman, P. C., R. M. McClure, and H. H. West, "Temperature Studies for an Experimental Segmental Bridge." Research Project 75-3 Interim Report. Pennsylvania State University. June 1980.
23. Menn, Christian, *Prestressed Concrete Bridges*. Birkhäuser, Basel, Boston, 1990.
24. *AASHTO Standard Specifications for Highway Bridges*. American Association of State Highway and Transportation Officials. 1989.
25. Stephenson, D. A., "Effects of Differential Temperature on Tall Slender Columns." *Concrete and Constructional Engineering*. Vol. 56, No. 5. May 1961, pp. 175-178.
26. Gallaway, T. M., "Design Features and Prestressing Aspects of Long Key Bridge." *PCI Journal*. Vol. 25, No. 6. November-December 1980, pp. 84-96.
27. Muller, J. M., "Construction of Long Key Bridge." *PCI Journal*. Vol. 25, No. 6. November-December 1980, pp. 97-111.
28. "Closing the Gaps with Assembly Line Span Placement." *Engineering News-Record*. Vol. 207, No. 10. September 3, 1981, pp. 26-28.
29. "Dauphin Island Bridge." *PCI Journal*. Vol. 29, No. 1. January-February 1984, pp. 128-147.
30. "Sunshine Skyway Bridge Closes the Gap." *PCI Journal*. Vol. 31, No. 6. November-December 1986, pp. 168-173.

31. Muller, J. M., and J. M. Barker, "Design and Construction of Linn Cove Viaduct." *PCI Journal*. Vol. 30, No. 5. September-October 1985, pp. 38-53.
32. Podolny, W., Jr., and J. M. Muller, *Construction and Design of Prestressed Concrete Segmental Bridges*. New York: John Wiley & Sons, Inc. 1982.
33. "Viaduct." *Civil Engineering*. American Society of Civil Engineers. Vol. 54, No. 7. July 1984, pp. 34-36.
34. Carr, F.H. and M.M. Charleston, "Precast Units Barged to Bridge." *Engineering News-Record*. Vol. 219, No. 2. July 9, 1987, pp. 32-34.
35. Hurd, M.K., "Cable-Stayed Bridge Completed Across James River." *Concrete Construction*. Vol. 34, No. 9. September 1989, pp. 775-779.
36. Pate, W. D., "The Chesapeake and Delaware Canal Bridge - Design-Construction Highlights." *PCI Journal*. Vol. 40, No. 5. September/October 1995, pp. 20-30.
37. Ralls, M. L., and R. Carrasquillo, "Texas High-Strength Concrete Bridge Project." *Public Roads*. Vol. 57, No. 4. Spring 1994, pp. 1-7.
38. Texas Department of Transportation, Division of Bridges and Structures. Bridge Plan: Louetta Road Overpass. June 1993, sheets 535-536.
39. Arréllaga, J. A., "Instrumentation Systems for Post-Tensioned Segmental Box Girder Bridges." Master's thesis, The University of Texas at Austin. December 1991.
39. "Precast Segmental Cantilever Bridges: The Northumberland Strait Crossing." JMI-Bridge Engineering Consultants Informational Pamphlet. 1995.
40. Stone, William C., "Design Criteria for Post-Tensioned Anchorage Zone Tensile Stresses." Doctoral dissertation, The University of Texas at Austin. 1980.
40. "Northumberland Strait Crossing Update." *Segments*. American Segmental Bridge Institute. Vol. 25. Spring/Summer 1995, pp. 8-12.
41. National Oceanic and Atmospheric Administration. "Local Climatological Data: Monthly Summary — Austin, TX." National Climactic Data Center. Asheville, NC. 1994-95.
42. Knight, Charles E., *The Finite Element Method in Mechanical Design*. Boston: The PWS-KENT Publishing Company, 1993.
43. Bathe, Klaus-Jürgen, *Finite Element Procedures*. Englewood Cliffs: Prentice-Hall, 1996.
44. Rowell, Randall B., "Behavior of Thin-Walled, Segmentally Constructed Post-Tensioned Bridge Piers." Master's thesis, The University of Texas at Austin. Austin, Texas. May 1990.

45. Mindness, Sidney, and J. Francis Young, *Concrete*. Englewood Cliffs: Prentice-Hall, Inc., 1981.
46. Beer, Ferdinand P. and Russell Johnston, Jr., *Mechanics of Materials*. 2nd ed. New York: McGraw-Hill, Inc., 1992.